STATE-TO-STATE CROSS SECTIONS
FOR ROTATIONAL EXCITATION OF NH_3 AND OH
BY COLLISIONS WITH HE, AR AND H_2

Jean Schleipen

STATE-TO-STATE CROSS SECTIONS
FOR ROTATIONAL EXCITATION OF NH_3 AND OH
BY COLLISIONS WITH HE, AR AND H_2

STATE-TO-STATE CROSS SECTIONS
FOR ROTATIONAL EXCITATION OF NH$_3$ AND OH
BY COLLISIONS WITH HE, AR AND H$_2$

PROEFSCHRIFT

door

JOHANNES JOSEPH HUBERTINA BARBARA SCHLEIPEN

geboren op 8 april 1964
te Born

Promotor   :   Prof. Dr. J. Reuss

Co-Promotor   :   Dr. J.J. ter Meulen

'We zullen steeds verder gaan met onze onderzoekingen.
En aan het einde van al onze verkenningstochten
zullen we uitkomen bij de plaats vanwaar we vertrokken
en dan pas zullen we die plaats waarlijk kennen.'

T.S. Eliot, 'Four Quartets'

veur Pap en Mam,

aan Connie.

– Dankwoord –

Contents

Chapter 1

Introduction

1.1 Collision experiments and intermolecular potentials

The forces between two particles are the basic origin of all kinds of physical and chemical pheno-
mena One can think of microscopic properties of interacting systems, such as a chemical reaction
between two molecules or the sticking of a molecule on a solid state surface But also macroscopic
properties such as the structure and strength of a crystal, the boiling temperature of a liquid or
the compressibility of gases, they can in principle all be explained by means of interatomic and
intermolecular forces In the field of molecular physics interatomic forces are the origin for the
existence of molecules, which in turn can be studied very precisely by means of spectroscopical
techniques In this case the static behaviour of interatomic forces is studied when all molecular
nuclei are in their equilibrium position The same is true for spectroscopical studies on molecular
complexes such as van der Waals molecules Intermolecular forces are responsible for a bound
geometry between the individual constituent molecules and spectroscopy of the complex reveals
the static behaviour of these intermolecular forces The most direct way to study the dynamical
behaviour of these forces is to perform a collision experiment in which the changes of kinetic and
internal energy of the particles upon a collisional event are investigated All characteristics of the
interatomic and intermolecular forces are concealed in the interatomic and intermolecular potential
describing the energy of the respective interaction From this potential important physical and
chemical properties can be extracted

Not only earthly phenomena go often back to atomic and molecular collisions and the involved
play of interatomic or intermolecular forces Astrophysical observations indicate that collisions
between interstellar molecules play an important role in the extra-terrestrial world as well Ano-
malous non-thermal emission and absorption of NH_3 and OH microwave radiation, observed from
several galactic objects [1, 2, 3], cannot be explained assuming a complete thermal equilibrium of
the emitting or absorbing gas with its environment Several models were developed which should
be able to explain for a non thermal relaxation of the involved rotational and vibrational levels
involved of the molecule One class of these models is based on radiative processes in which the
observed molecule is exposed to ultraviolet, infrared or millimeter radiation and (de-)excited out

of its initial thermal state into some other state [4] None of these models however can adequately account for the observed anomalous emission or absorption In 1969 Cheung et al [5] were the first to propose the collision model in which the emitting molecule is excited due to collisions with surrounding interstellar molecules such as the very abundant H_2, or the He and H atoms, followed by deexcitation by spontaneous or stimulated emission In order to verify this collision model and to interpret the observed anomalous microwave radiation in terms of absolute interstellar densities and temperatures, astrophysicists need collision rates for exciting a particular molecular state $|f\rangle$ from a certain initial state $|i\rangle$ due to a collision with a specific second molecule at an interstellar temperature of typically 5-100 K In most of the cases these states $|i\rangle$ and $|f\rangle$ denote rotational states of the molecule since the energy involved in these collision processes is not high enough to excite any vibrational motion inside the molecule

A physical quantity from which these collision rates can be deduced is the differential cross section $\sigma_{if}(\Omega, E)$, which is defined as the ratio of the scattered flux of particles in state $|i\rangle$ per unit solid angle Ω to the incident flux of particles in state $|f\rangle$ per unit area at a collision energy E This cross section reflects the nature and behaviour of the intermolecular forces between the two colliding molecules and studying these collision cross sections provides valuable information on the intermolecular potential energy surface Many experiments have been performed to study these inelastic collision processes under laboratory circumstances, as will be shown in the next section The ultimate goal for an experimentalist would be to determine absolute state-to-state collision cross sections σ_{if} at a well-defined collision energy E for scattering in a solid angle Ω To control and prepare all of these parameters independently is a hard job to do experimentally and no experiment up to now has succeeded in yielding a complete set of state-to-state cross sections as a function of collision energy and scattering angle

Apart from the astrophysical interest in the development of an accurate intermolecular potential, many macroscopic properties, such as transport properties or chemical properties, can be calculated from it directly So, it is of great importance to obtain a detailed picture of the intermolecular potential Now, scattering experiments mainly provide information on the repulsive, anisotropic short range part of the potential Another technique to investigate intermolecular interactions is the study of van der Waals complexes A van der Waals molecule consists of two molecules or a molecule and an atom, hold together via the weak van der Waals bond So in this case a bound state is formed when the two constituent particles approach each other The binding forces are related to the intermolecular potential, the same as used when describing a collision event between the two monomers In the last decade the spectroscopy of van der Waals complexes extended from electronic ground state microwave and (far-)infrared spectroscopy to electronic spectroscopy in molecular jets The rovibronic spectrum of a complex conceals direct information on the intermolecular potential In fact, in this case the region around the potential well is probed As a result scattering experiments and spectroscopy of van der Waals complexes become two complementary techniques to determine intermolecular potentials as accurate as possible

In the construction of the potential energy surface from the observed collision cross sections theory plays an essential role Although the quantum mechanical description of the molecular collision dynamics is a complex matter and may not yet be fully understood, one generally believes that the close coupling scattering formalism is a quantum mechanically correct device to calculate these collision cross sections This molecular quantum scattering theory, relating collision cross sections with the actual shape of the intermolecular potential, is a rather complex theory and requires the integration of large sets of coupled second order differential equations on large computers Howe

ver, the lack of fast computer systems or computer time requires approximations to be made and hence introduces uncertainties in the outcome of these scattering calculations The results of the quantum mechanical close coupling scattering calculations are strongly dependent on the shape and the strength of the potential energy surface, which can be obtained theoretically from first principles The construction of the ab initio potential requires extensive self consisting field (SCF) and perturbation theory calculations For economy reasons these calculations are carried out on a grid in coordinate space As a result the potential is only known for a discrete set of certain relative orientations of the two colliding particles and thus will be an approximate reflection of the real physical intermolecular potential involved

As will be indicated in the next sections, scattering experiments are sufficiently sophisticated nowadays to give an important contribution to the knowledge of the intermolecular potential in case of diatomic and some small polyatomic molecules The fondest wish of an experimentalist and a theoretician will be the fitting of the calculated scattering cross sections to the observed ones, hereby using the intermolecular potential as fit parameter Unfortunately, this calculational effort will have to await the invention of still faster computer systems and till then will be music of the future

In this thesis we study the rotational excitation of the astrophysically important NH_3 and OH molecules when colliding with target particles such as the interstellar abundant H_2 and noble gas atoms He and Ar The inelastic state to-state collision cross sections obtained from this study may provide valuable information for the interpretation of various astrophysical observations The experimentally obtained cross sections for the rotational excitation of the NH_3 and OH molecules are compared with theoretical values from molecular quantum scattering calculations The com parison between experiment and theory evokes a discussion on the interpretation of the collision dynamics and on the shape of the intermolecular potential energy surface involved in the scattering event

1.2 Experimental methods

In order to illustrate the fast development of new experimental techniques and the resulting more detailed information one obtains from molecular collision experiments, a short summary is given in this section of several kinds of experiments performed in the last three decades This list is far from complete and is merely meant to give an overview of the different experimental techniques used to extract collision cross sections or collision rates from laboratory experiments Furthermore, the references used to illustrate these techniques are restricted to experiments involving NH_3 and OH scattering

The first collision experiments were performed in bulk media A gas mixture, containing the two interacting molecular species was studied in a cell at different pressures Collision interactions result in shifting of energy levels and quenching of populations, which can be measured and interpreted in terms of collision cross sections The disadvantages of this technique are manifold First of all the experiments are usually performed at room temperature and hence many rotational and vibrational states are populated, making a state-to-state experiment impossible Secondly in bulk circumstances the molecules possess a broadband velocity distribution and consequently the scattering signals are averaged over a wide collision energy range, yielding collision rates in stead of cross sections The third disadvantage of bulk experiments is the difficulty in controlling the collision process the measured effects are a combination of multiple elastic, inelastic and wall col lisions which makes it impossible to interpret the measured data in terms of state-to-state collision
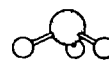
cross sections Furthermore, no differential cross sections can be obtained since no initial or final collision angle is defined

To overcome these problems the molecular beam technique is introduced in scattering experiments A molecular beam is produced by expanding a gas into vacuum through a small hole, the nozzle It has the advantage that all molecules travel in the same direction with nearly the same velocity By using two molecular beams an initial collision angle is defined and the collision energy is well known Furthermore the beam density is low such that the mean free path length for a collision inside the beam is high and the molecules can be considered as being isolated The collision region is confined to the intersection of both molecular beams and hence wall effects are absent By changing the backing pressure of the gas behind the nozzle, the beam density can be controlled and the occurrence of multiple collisions can be studied and eliminated Especially the use of pulsed molecular beams enables a very efficient cooling of rotational and vibrational motions of the molecule in a supersonic expansion, facilitating initial state preparation

In order to obtain state-to-state collision cross sections, one single initial state $|i\rangle$ of the molecule has to be prepared Here $|i\rangle$ stands for a complete set of quantum numbers describing the internal motion of the molecule During the collision process molecules in state $|i\rangle$ become excited into a final state $|f\rangle$ and the probability of this excitation is related to the cross section $\sigma_{if}(E\ \Omega)$ There are several ways for preparing an initial state $|i\rangle$

- Rotational and vibrational states can be selectively populated by pumping molecules to a specific level $|i\rangle$ by means of an externally applied (microwave or infrared) radiation field

- The supersonic expansion of a molecular beam results in an adiabatic cooling of the internal degrees of freedom of the molecule Effective rotational temperatures of ≈ 10 K can easily be obtained For NH_3, as well as OH, this means that the lowest rotational level in the vibronic ground state contains over 90 % of all population

- By means of electrostatic multipoles it is possible to focus molecules state specifically towards the molecular beam axis For this purpose the molecules must possess a dipole moment in order to make the Stark force active, which is responsible for this state specific deflection in a multipole electrostatic field

Once the collision process has taken place the final state distribution has to be probed For this purpose a state specific detection device is necessary for measuring the density of molecules in state $|f\rangle$ Again three techniques are most commonly used

- An electrostatic lens can be used in order to focus molecules in state $|f\rangle$ onto a mass spectrometer The sensitivity is determined by the 'sharpness' of the focus for a particular molecular state $|f\rangle$ and is restricted by the small acceptance angle and strong chromatic aberrations of the multipole state selector

- In time of flight (TOF) measurements the final state distribution is probed by making use of the different velocities for different $|f\rangle$ state scattered molecules By measuring the intensity of scattered molecules in a specific solid angle Ω with time resolution, the individual quantum states $|f\rangle$ can be resolved, yielding state-to-state cross sections However, the sensitivity in this case is determined by the time resolution of the TOF apparatus which is only sufficient for resolving individual vibrational states

- By using spectroscopical techniques in the microwave, infrared, visible and ultraviolet spectral range, the rotational and vibrational populations can be probed before and after the collision process Furthermore, a complete species selectivity can be achieved For OH as well as NH_3, microwave techniques have been applied to study the Λ-doublet and inversion doublet transitions respectively A complete picture of the rotational and vibrational population distribution can be obtained using electronic spectroscopy For OH the laser induced fluorescence (LIF) technique can be used, whereas NH_3 is a good candidate for applying resonance enhanced multi photon ionization (REMPI)

In Figure 1 1 the various methods are illustrated by means of some diagrams Experimental information about the collisional excitation of NH_3 has been obtained from line broadening measurements in the microwave [6], submillimeter [7] and infared [8, 9] region, from microwave-microwave and infrared-microwave double resonance experiments [10, 11, 12, 13], from microwave beam maser experiments [14] and from differential cross section measurements using molecular beams [15, 16] In case of OH scattering information is obtained from double resonance experiments [17, 18] and crossed molecular beam experiments [18]

In line broadening experiments (Figure 1 1 a) total inelastic cross sections are obtained for a particular state, but state-to-state collisional excitation rates cannot be extracted since the measured effect, $\Delta\omega_i$, includes the simultaneous interaction of state $|i\rangle$ with all possible molecular states $|k\rangle$ The microwave double resonance experiments (Figure 1 1 b) are close to state-to-state experiments By changing the population in the $(J+1)$-rotation inversion doublet, the competition of parity changing and parity conserving collisional population transfer to the J-rotation inversion doublet will result in an increase or decrease of the probe signal Although the results of these experiments are qualitatively interesting, they are difficult to interpret in terms of real state-to-state cross sections, because different radiative and collisional processes occur simultaneously in the absorption cell The double resonance relaxation experiments (Figure 1 1 c) became possible with the invention of tunable, narrow band, pulsed radiation sources, such as pulsed CO_2 and dye lasers At time t=0 the microwave or infrared pump populates a specific rotational or rovibrational level $|i\rangle$ in the electronic ground state From then on this population is collisionally transferred to all other rovibrational levels $|f\rangle$ By probing these levels $|f\rangle$ at different times $t > 0$ with a pulsed visible or UV laser, collisional relaxation rates are obtained for a large number of selected initial states $|i\rangle$ and final states $|f\rangle$ However, due to the bulk character of these experiments multiple collisions cannot be excluded This is certainly better in the microwave beam maser experiments (Figure 1 1 d), where single collision conditions are obtained, facilitating the interpretation of experimental results The combination of an electrostatic state selector and a microwave pump preferentially populates the + or - parity component of the J'-rotation inversion doublet The effect of switching the pump on and off is collisionally transferred to the J-rotation inversion doublet and can be measured in the signal cavity A disadvantage here is that due to the small acceptance angle of the microwave signal cavity, the measurement of complete integral cross sections is not possible in case of weak interactions In the differential cross section measurements (Figure 1 1 e) use is made of two molecular beams and a rotatable particle detector Final state selectivity is achieved by applying a time of flight (TOF) detector due to collision kinematics, scattered molecules in different final states $|f_i\rangle$ possess different velocities $v(f_i)$ However, in the differential cross section measurements of NH_3 scattering [15, 16] rotational state-to-state results cannot be obtained, since single rotational state selectivity requires a TOF resolution that is not in the reach of the experiments performed thus far
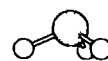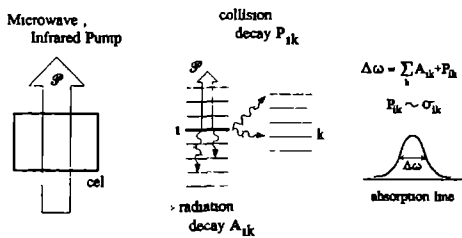
Collision Broadening
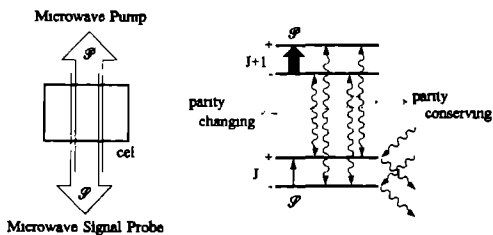
Microwave Double Resonance
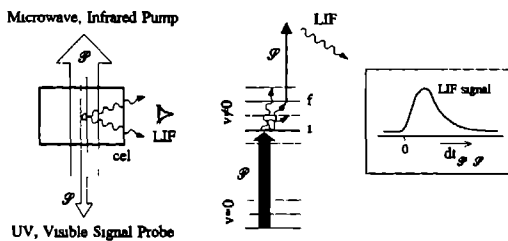
Double Resonance Relaxation
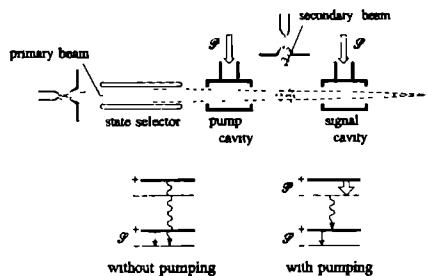
Molecular Beam Maser
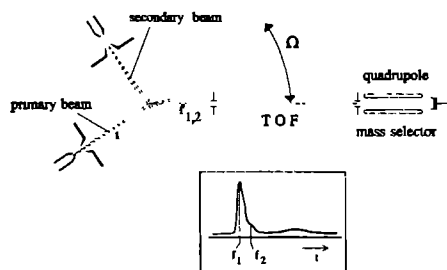
Molecular Beam TOF

Figure 1.1 : *Various experimental methods for obtaining information about rotational energy transfer in molecules due to collisions with some target species.*

    1.1.a. *Line broadening experiment*
    1.1.b. *Microwave double resonance experiment*
    1.1.c. *Relaxation experiment*
    1.1.d. *Microwave beam maser experiment*
    1.1.e. *Differential time-of-flight experiment.*
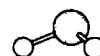
1.3 The present investigation

Our main goal in constructing the collision experiment described in this thesis is the determination of relative rotational state-to-state cross sections This means that the molecules under study, NH$_3$ and OH, have to be prepared in a single well defined rotational state before they are exposed to interactions with their collision partners For reasons mentioned in the previous section we decided to use a pulsed crossed molecular beam set-up

Two molecular beams intersect at right angles with a certain relative velocity v_r yielding a well defined initial collision angle Ω_i and collision energy E By changing the primary or secondary beam velocity the collision energy E can be varied Initial state preparation is achieved by rotational cooling of the molecules in a pulsed supersonic expansion Furthermore a hexapole state selector is used to select only one parity substate and hence parity resolved rotational state-to-state cross sections can be obtained The way this initial state preparation is reached in the present investigation brings on a relatively low primary beam density As a result the intensity of scattered primary beam molecules into solid angle Ω is low and only integral state-to-state cross sections $\int \frac{d\sigma}{d\Omega} d\Omega$ can be measured

The rotational state distribution of the primary beam molecules before and after the collision process is monitored by spectroscopical means With the invention of high power, narrow band, tunable lasers in the visible and the ultraviolet spectral region, it has become possible to use electronic spectroscopy as a tool for probing the rotational state distribution in the electronic ground state of the scattered molecules For the detection of the NH$_3$ molecule the 2+1 REMPI technique is used, whereas for the OH radical the LIF technique is applied For this purpose a pulsed laser beam is crossed at right angles with the two colliding molecular beams, hereby probing the primary beam rotational state distribution with complete state selectivity

The relative state-to-state cross sections obtained in this investigation are compared with theoretical data available from molecular scattering calculations Several calculational techniques are applied to attack the scattering problem, ranging from semi-classical trajectory calculations to the quantum mechanically exact close coupling formalism The quality of agreement between theory and experiment is discussed in terms of the intermolecular potential used in the scattering calculations, the calculational technique in order to solve the scattering equations, and experimental parameters such as initial state preparation and multiple collision conditions

Chapter 2 of this thesis gives a general overview of the NH$_3$ and OH collision experiments The molecular beam machine is described in some detail and some radical production techniques are discussed Furthermore a short explanation is given of the NH$_3$-REMPI and OH-LIF spectroscopy, necessary for analyzing the scattering spectra

Chapter 3 describes a collision experiment dealing with the rotational excitation of ortho- and para-NH$_3$ in collision with He and normal H$_2$ In Chapter 4 we were able to separate ortho-H$_2$ from the para-H$_2$ species The scattering experiment is repeated with the astrophysically important para-H$_2$ as collision partner Quantum scattering calculations on ab initio potential energy surfaces for the NH$_3$ – para-H$_2$ and NH$_3$ – ortho-H$_2$ interaction are performed and the theoretical cross sections are compared with the experimental values

Chapters 5 and 6 deal with the rotational excitation of ortho- and para-NH$_3$ in collision with Ar In Chapter 5 the experiment is described in detail In this case the collision energy can be varied by changing the primary beam velocity The resulting collision cross sections are compared with the theoretical data obtained from quantum scattering calculations, described in Chapter 6

Here, the close coupling formalism is used in order to extract the collision cross sections from an ab initio potential energy surface, containing the NH_3 tunneling coordinate explicitly.

In Chapter 7 the OH scattering experiment is described Relative state-to-state cross sections are obtained for rotational excitation of the single $X^2\Pi_{3/2}(J = \frac{3}{2}, f)$ Λ-doublet state due to collisions with secondary beam targets He, Ar and H_2 The results are compared with theoretical scattering data and with the outcome of other experiments involving rotational energy transfer in the electronic ground state of the OH radical

In view of the common element in OH-rare gas scattering and spectroscopy of OH-rare gas van der Waals complexes, i e the potential energy surface describing the interaction between the OH radical and the rare gas atom, Chapter 8 deals with a spectroscopical study on the OH-Ar van der Waals complex. The complex is produced in a pulsed molecular beam set-up and is studied by means of LIF spectroscopy The use of a narrow-band PDA laser system resulted in the determination of accurate rotation and distortion constants for the complex.

Chapter 2
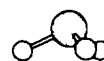
The NH₃ and OH collision experiment

2.1 Experimental set-up

An artists view of the experimental set-up is presented in Figure 2 1 Two pulsed molecular beams are crossed at right angles in a vacuum machine The molecular beam machine consists of three chambers The primary beam chamber and the scattering chamber are pumped separately by two 8000 mbar l s⁻¹ oil diffusion pumps The secondary beam is differentially pumped by a third 5500 mbar l s⁻¹ oil diffusion pump, giving vacuum pressures of ≈ 5 10^{-7} mbar During operation of both valves the pressure inside the scattering chamber remains well below 10^{-5} mbar The primary beam molecules undergo a supersonic expansion where their internal energy is converted into translational motion along the molecular beam axis The beam is narrowly collimated by a skimmer 20 mm downstream in order to avoid collisions with the rods of a state selector mounted between skimmer and the scattering region

In order to reach an efficient reduction of vibrational and rotational motion the molecules are seeded in a carrier gas, which is argon or xenon In the case of NH₃ scattering, 1% of ammonia is seeded in Ar and Xe respectively, and the gas mixture is fed to the primary beam valve with a backing pressure of 1 bar In the OH scattering experiment, the OH radicals have to be produced first Since the OH molecule is a chemically unstable species, it can be best produced under vacuum conditions There are several ways to produce radicals inside a molecular beam and these will be discussed in the next section In the OH scattering experiment we used an electrical discharge to dissociate water molecules, yielding a very efficient OH production

For monatomic gases it follows from hydrodynamic considerations that the kinetic temperature of the expanding gas at a position x downstream the nozzle orifice, as long as the expansion takes on, is given by [19]

$$\frac{T(x)}{T_N} = \left[\frac{x}{D}\right]^{-\frac{4}{3}} \tag{2 1}$$

where T_N is the nozzle temperature and D is the diameter of the nozzle orifice Detailed experiments on pulsed beam kinetics and hydrodynamics showed that the adiabatic cooling of internal gas energy stops at a distance of roughly 10-20 nozzle diameters from the nozzle orifice From here
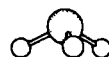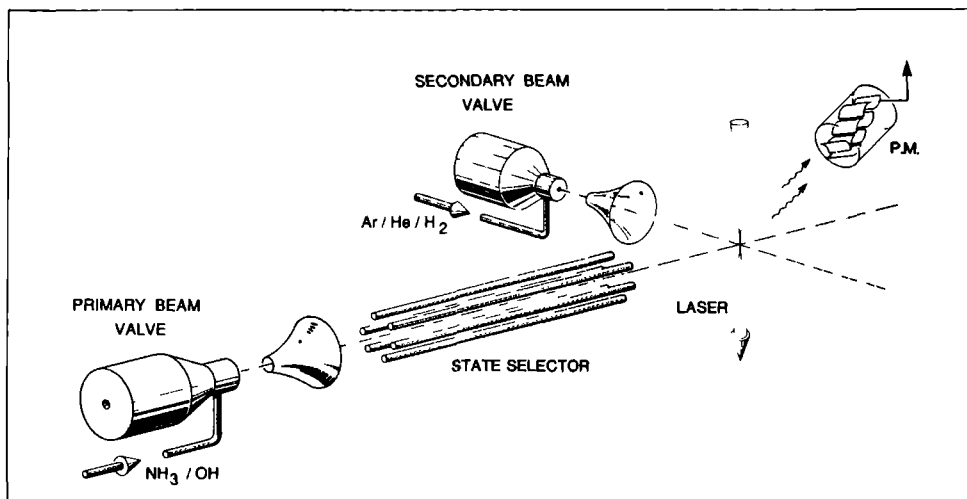
Figure 2.1 : *Artists impression of crossed molecular beam machine*

on, no collisions take place any more which are responsible in first instance for the conversion of internal energy into translational motion of the molecules and hence the hydrodynamic expansion is succeeded by a free molecular flow. The final kinetic temperature of the beam is then given by Equation (2 1) to be typically 10 K, assuming a nozzle temperature of 300 K room temperature. By cooling the nozzle even lower beam temperatures can be achieved.

After the expansion the rotational motion of the NH_3 and OH molecules is reduced to a minimum. For para-NH_3 and ortho-NH_3 over 90 % of the total vibronic ground state population is contained in the lowest rotational state $|J_0\rangle$. For OH about 80 % is populated in the rotational ground state $|J_0\rangle$. In the case of para-NH_3, the inversion tunneling motion inside the ammonia molecule is responsible for a doubling of each rotational level into two parity components $|J_0^+\rangle$ and $|J_0^-\rangle$ as will be discussed in section 2 3. Also for OH, an interaction of the electronic angular momentum and the rotation of the nuclear frame, known as Λ-doubling (section 2 4), gives rise to a splitting into two parity components $|J_0^\pm\rangle$. Now molecular scattering calculations predict strong parity propensity rules for a specific rotational excitation. That is to say, a strong preference exists for some rotational excitations to preserve parity, whereas for other rotational transitions the parity is changed during the collision. Since these propensity rules are of great importance also for the interpretation of astrophysical observations such as interstellar maser activity, there is a need for experimental verification of these parity propensities. The most elegant way to measure these propensity rules is to prepare the primary beam molecules in only one parity substate, $|J_0^+\rangle$ or $|J_0^-\rangle$, and see whether the parity will change or will be conserved during a collision with the secondary beam molecules. For this purpose a hexapole is positioned on the primary beam axis which acts as an electrostatic state specific lens for the NH_3 and OH molecules. The sign of the

24

Stark force exerted on the molecule is dependent on the parity of the molecular quantum state and hence only one parity component of the $|J_0^{\pm}\rangle$ doublet is retained in the molecular beam when it reaches the scattering volume

Before and after the collision process the NH$_3$ and OH rovibrational state distribution is monitored by means of electronic spectroscopy A pulsed, tunable laser beam is focused inside the scattering volume, 400 mm downstream the primary beam valve, and probes the vibrational and rotational state distribution of the electronic ground state primary beam molecules The NH$_3$ molecule is ideally suited for applying the 2+1 REMPI spectroscopical technique Two laser photons with a wavelength of approximately 332 nm are absorbed by the $\tilde{X}$ ground state NH$_3$ molecule, to reach the second electronically excited $\tilde{B}$ state at 59200 cm^{-1}(1 eV = 8049 7 cm^{-1}) An additional third photon is absorbed by the $\tilde{B}$ state molecule and as a result it becomes excited into the first NH$_3$ ionic state The subsequent NH$_3^+$ ions are collected by a particle multiplier giving the 2+1 REMPI signal In the case of OH a LIF detection scheme is applied where one single laser photon with a wavelength of about 308 nm is used to excite the $X^2\Pi_i$ electronic ground state of OH into the first electronically excited $A^2\Sigma^+$ state at 32400 cm^{-1} The A state OH molecule has a finite lifetime and it will relax to the electronic ground state under spontaneous emission of a photon, yielding the LIF signal Consequently, the indication $P\,M$ in Figure 2.1 should be read as *photon multiplier* in the case of OH scattering, respectively *particle multiplier* in the case of the NH$_3$ collision experiment From the measured REMPI and LIF spectra, which will be discussed in sections 2 3 and 2 4 , the electronic ground state rotational and vibrational population distribution of the primary beam molecules can be obtained before and after the collision process rather straightforwardly Next, relative state-to-state cross sections can be derived from these measured population differences via simple formulae, derived in Chapter 3

Since the population distribution of the scattered primary beam molecules is probed directly in the scattering volume, these cross sections represent integral state-to-state cross sections Since no absolute beam densities could be measured in the present experimental set-up, only relative state-to-state cross sections were obtained However, a rough estimate can be made for the primary and secondary beam densities in the scattering center and hence the measured scattering signals can be interpreted in terms of absolute state-to-state cross sections For this purpose we use the following simple formula for the density of molecules, assuming the expansion takes place in a spherically symmetric cone around the beam axis [19]

$$n(x) = \frac{P_N}{k_B\,T_N}\left[\frac{D}{x}\right]^2 \qquad (2\,2)$$

Here x is the position from the nozzle orifice along the beam axis, P_N is the gas stagnation pressure, T_N is the gas temperature before the expansion takes place and D is the nozzle diameter A typical state-to-state cross section $\sigma(i \to f)$ describing the scattering of primary beam molecules out of an initially prepared state $|i\rangle$ into state $|f\rangle$, due to collisions with the secondary beam target atoms, is given by (see Chapter 3, section 3 1)

$$\sigma(i \to f) \simeq \frac{\delta n_{scat}(i \to f)}{n(i)}\frac{1}{n_{sec}}\frac{1}{l_{cr}} \qquad (2\,3)$$

Here n_{sec} represents the secondary beam density at the scattering center, l_{cr} the length of the collision region and $\eta(i \to f) \equiv \delta n_{scat}(i \to f)/n(i)$ the percentage of initially prepared molecules in state $|i\rangle$, scattered into final state $|f\rangle$ This latter quantity $\eta(i \to f)$ is directly obtained from the
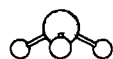
primary beam	secondary beam
$P_N = 760 \; Torr \;\; ; \;\; T_N = 300 \; K$	$P_N = 200 \; Torr \;\; ; \;\; T_N = 300 \; K$
$D = 1 \; mm$	$D = 1 \; mm$
$x_{scat} = 0.4 \; m$	$x_{scat} = 0.06 \; m$
$n_{prim} = 1.6 \cdot 10^{20} \; m^{-3}$	$n_{sec} = 1.8 \cdot 10^{21} \; m^{-3}$

$$l_{cr} = 4 \; mm$$
$$\eta(1_1^- \rightarrow 2_1^-) \simeq 3\%$$

$$\sigma(1_1^- \rightarrow 2_1^-) \simeq 0.42 \mathring{A}^2$$

Table 2.1 : *Experimental estimation of the absolute value for the state-to-state cross section $\sigma(1_1^- \rightarrow 2_1^-)$ for the NH_3-He collision system*

scattering experiments. In Table 2.1 the absolute magnitude of the NH_3-He inelastic collision cross section $\sigma(1_1^- \rightarrow 2_1^-)$ is estimated. The relative collision cross sections for the NH_3-He scattering experiment are given in Chapter 3. The absolute cross section is calculated using Equations (2 2) and (2.3). From the experiment we obtained a value for $\eta(1_1^- \rightarrow 2_1^-)$ of $\approx 3\%$. The estimated experimental value for the absolute collision cross section $\sigma(1_1^- \rightarrow 2_1^-)$ of 0.42 $\mathring{A}^2$ is in reasonably good agreement with the theoretical value of 0.76 $\mathring{A}^2$ obtained by Meyer et al. [15].

2.2 Radical production techniques

In this section some production techniques for radicals, which were investigated for their applicability in the collision experiments are described briefly. Since a radical is a chemically unstable species, it has to be produced under mild circumstances, e.g. in vacuum environment. It can be produced by using chemical reactions or dissociation reactions, starting with a stable parent molecule and ending up with the desired radical. We did not attempt to study in detail the reaction kinetics of the different production methods. Our main goal was merely to produce the radicals as efficiently as possible and to control their production under several conditions.

In the Nijmegen laboratory chemical reactions and microwave discharges have been applied extensively in the past in order to produce radicals in a cw molecular beam setup [20, 21]. For the OH radical production the exothermal reaction

$$H \;+\; NO_2 \;\rightarrow\; OH \;+\; NO$$
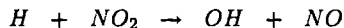
in a glass flow reaction tube may be used. For this purpose H-atoms are produced in an electrodeless microwave discharge in H_2O. The NO_2 is added to the flow of H-atoms just before the nozzle exit hole where the reaction occurs, yielding the OH radical. A second way to produce the hydroxyl radical is to make use of a coaxial microwave discharge in water. The microwave cavity is placed

around the H_2O gas inlet tube and by applying 100 Watts of broadband radiation ($\approx$ 2 5 GHz) a discharge is generated in which the OH radical is produced Both methods can only be applied at low pressures ($\sim$ mbars) Consequently they can not be used in a pulsed molecular beam experiment operating with high stagnation pressures ($\geq$ 1 bar)

In this thesis we used two alternative methods to produce the OH radical in a supersonic pulsed beam setup, the photodissociation technique and a DC electric discharge

Photodissociation

Every stable molecule also possesses dissociative states, in which the electronic wavefunction contains an anti-bonding molecular orbital configuration If, by some means, the stable ground state molecule is excited to a dissociative state, a chemical bond will be destroyed and the molecule will fall apart into smaller fragments This fragmentation can be either direct, when the excited state potential energy curve is a pure dissociative state, or indirect, when the fragmentation is caused by an excited state interaction with a nearby dissociative state or by tunneling through a small potential energy barrier In the latter case we speak of predissociation, rather than dissociation of the molecule
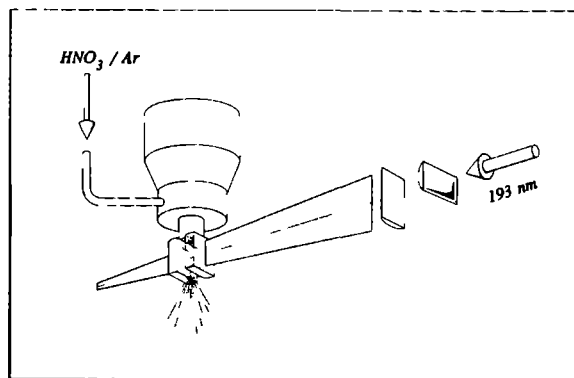
Figure 2.2 : *Photolysis set-up The 193 nm output of an ArF excimer laser is focused through a quartz channel confining the molecular gas flow Dissociation of the parent molecules results in an efficient radical source*

In order to produce the OH radical with this photodissociation technique several parent molecules may be used In the 200 nm region nitric acid (HNO_3) shows a strong broad band photon absorption Bercess et al [22] and Johnston et al [23] studied the photolysis of HNO_3 in the near ultraviolet region and the main process governing the fragmentation of the nitric acid molecule at these wavelengths, is

$$HNO_3 \xrightarrow{h\nu} OH(X^2\Pi) + NO_2$$
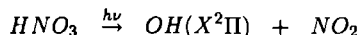
According to them this dissociation into the electronic ground state OH radical has a quantum
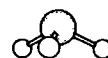
yield of unity in the 200 - 300 nm region and consequently the photolysis of nitric acid is a good candidate for an OH radical source

A laser system providing these short wavelength UV photons is the ArF excimer laser This laser system emits photons with a wavelength of 193 nm and typical output powers of 100 mJ/15 nsec pulse In Figure 2 2 the experimental setup is shown for the photodissociation of the HNO_3 molecules The nitric acid parent molecules are seeded in a carrier gas Ar Directly behind the pulsed valve a quartz channel, $10 \times 1 \times 1$ mm^3, is mounted through which the gas pulse flows before it expands into vacuum Through the quartz windows of the channel the output of the ArF excimer laser is focused with a f=50 cm lens The focus is positioned about 10 cm behind the second quartz window, in order not to damage the quartz plates and to irradiate the gas pulse inside the capillary over the largest possible area The expanding gas pulse then contains the photofragments OH which can be studied by means of conventional spectroscopical techniques In Chapter 8 we used this photodissociation technique for the production of the OH radical and the OH-Ar van der Waals complex

Electric discharge

In 1983 Droege and Engelking [24] reported radical production in a cw molecular beam setup using an electrical discharge The discharge was burning from an electrode inside the gas inlet tube, through the nozzle, towards a second electrode or a skimmer on earth potential Recently, Bramble and Hamilton [25] applied this technique in a somewhat modified form to a pulsed molecular beam setup

The discharge geometry we used in the collision experiments is presented in Figure 2 3 The parent molecule is seeded in argon which in this case also initiates the discharge Downstream the pulsed valve a small ring is mounted, centered on the molecular beam axis The ring is typically 6 mm in outer diameter and is made of 1 mm in diameter stainless steel wire The distance from ring to nozzle is 1-3 mm The pulsed valve is on earth potential, whereas a negative high voltage is applied to the electrode ring Under vacuum conditions, i e with the valve closed, there is no discharge between nozzle and electrode However, when the valve opens a gas pulse expands through the electrode ring and a discharge occurs In this discharge the parent molecules are fragmented either by the bombardment with fast electrons and ions or by a photolysis process where UV photons emitted by electronically excited Ar atoms are responsible for dissociation of the parent molecules

The discharge remains very stable as long as the stagnation pressure of the gas mixture behind the nozzle does not exceed 4-5 bars The magnitude of the high voltage applied to the electrode ring depends on the distance from electrode to valve and for Ar as carrier gas a typical value of 500 V/mm is needed to initiate the discharge Higher voltages result in higher discharge currents and a more effective dissociation of the parent molecules

We used this very efficient (and cheap) radical source for the production of the hydroxyl radical in the OH collision experiment, described in Chapter 7 For details such as the rotational temperature of the OH fragments we refer to this chapter
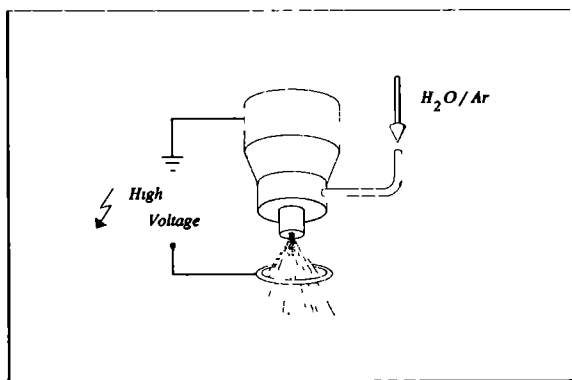
Figure 2.3 : *Discharge radical source. A high voltage is applied to an electrode ring underneath the pulsed valve exit hole During the expansion a discharge occurs between valve and electrode in which radicals are produced.*

2.3 REMPI spectroscopy of the NH₃ molecule

2.3.1 Ground state energy levels

In the electronic ground state of NH₃ the 10 electrons of the molecule are distributed among their molecular orbitals in such a way that the NH₃ molecule has a pyramidal structure. Figure 2.4 shows the potential energy barrier for the nitrogen atom to tunnel through the plane of the three H atoms. Due to the inversion motion of the NH₃ molecule the vibronic wavefunction splits into a symmetric (l) and antisymmetric (u) component. The vibronic ground state is henceforth designated as $\tilde{X}(0)$ for the symmetric component and $\tilde{X}(1)$ for the antisymmetric component, following the convention of Bunker [26]. The tunneling through the barrier with a height of 2023 cm^{-1} is responsible for an energy splitting of 0.79 cm^{-1} between the symmetric and antisymmetric component, $\tilde{X}(0)$ and $\tilde{X}(1)$ respectively.

The C_{3v} symmetry of the pyramidal structure, together with the tunneling inversion symmetry operation of the molecule, require the D_{3h} symmetry group in order to give a complete symmetry classification of the molecular rovibronic wavefunction. In this D_{3h} symmetry group the vibronic ground state has symmetry labels $\Gamma_{ev}[\tilde{X}(0)] = A_1'$ and $\Gamma_{ev}[\tilde{X}(1)] = A_2''$, the subscript e, v denoting the vibronic character of the molecular wavefunction.

Although the NH₃ molecule is a floppy molecule it is allowed to describe the rotational energy levels with the Hamiltonian of a rigid oblate symmetric top molecule:

$$\hat{H}_v^{rot} = B_v \cdot \vec{J}^2 + (C_v - B_v) \cdot J_z^2 \qquad (2.4)$$

with $\vec{J}$ the total angular momentum of the molecule, J_z the projection of $\vec{J}$ onto the D_{3h} molecular symmetry axis and B_v and C_v the effective rotational constants for the particular vibronic state. Allowing for additional centrifugal distortion terms in the Hamiltonian, the electronic ground state

29

Inversion Potential
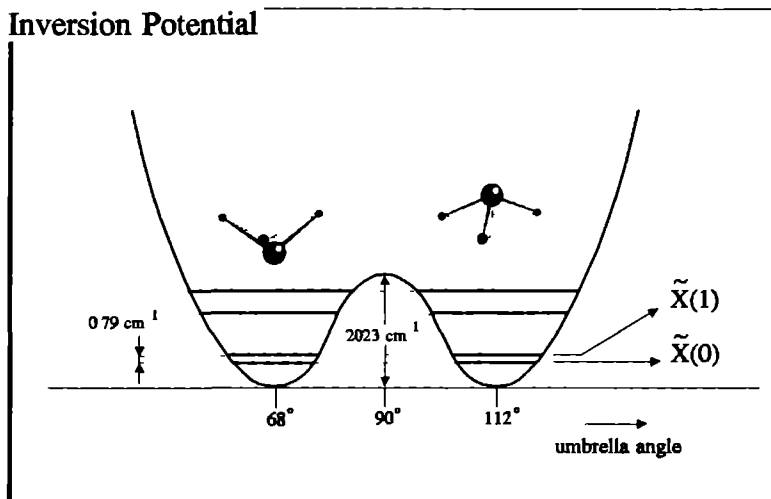
Figure 2.4 : *Potential energy curve for the electronic ground state of NH_3 as a function of the umbrella angle Due to tunneling through the potential barrier each vibrational level is split in a symmetric (e g $\tilde{X}(0)$) and antisymmetric (e g $\tilde{X}(1)$) component with respect to the inversion operation*

energy levels can be described by the following formula

$$E_v(J, K) = T_v + B_v \; J(J+1) + (C_v - B_v) \; K^2 \tag{2 5}$$
$$-D_{JJ\,v} \; J^2(J+1)^2 - D_{JK\,v} \; J(J+1) \; K^2 - D_{KK\,v} \; K^4$$

The rotational constants B_v and C_v and the centrifugal distortion constants $D_{JJ\,v}, D_{JK\,v}$ and $D_{KK\,v}$ can be found in Table 2 2   Here T_v denotes the inversion splitting between the $\tilde{X}(0)$ and $\tilde{X}(1)$ inversion doublets of the vibronic ground state

The eigenfunctions of the rotational Hamiltonian are the Wigner rotation matrices $D^{(J)}_{KM}(\theta, \phi, \chi)$ [28] The Euler angles θ, ϕ and χ specify the orientation of the NH_3 nuclear frame in a space fixed reference frame The rotational eigenstates are designated

$$|JKM, \epsilon\rangle = \frac{1}{\sqrt{2}} \left[|JKM\rangle + \epsilon \; |J - KM\rangle \right] \tag{2 6}$$

Here ϵ is called the parity index and according to Green [29] the relation between the parity index ϵ and the parity p, i e the symmetry of the molecular wavefunction under the inversion operation E^*, is given by

$$p = \epsilon \; (-1)^{J-K+1} \tag{2 7}$$

It is evident that in a field free region the energy levels are independent of the space fixed projection quantum number M and hence the rotational state J_K is $(2J+1)$-fold degenerate The

	T_v	B_v	C_v	D_{JJv} ×10⁶	D_{JKv} ×10⁶	D_{KKv} ×10⁶
$\tilde{X}(0)$	0 0	9 94655	6 22675	849 4	1577 0	810 2
$\tilde{X}(1)$	0 7932	9 94160	6 22950	831 4	1529 0	880 6

Table 2.2 : *Molecular constants (in cm⁻¹) for the vibronic ground state of NH₃ The constants are taken from Ashfold et al [27]*

D_{3h} symmetry classification Γ_r of the rotational eigenstates $|JKM, \epsilon\rangle$ is given in Table 2 3 and is of importance when considering the overall symmetry $\Gamma_{evr} = \Gamma_{ev} \otimes \Gamma_r$ of the rovibrational wavefunction The rotational energy level diagram of the ground state of NH₃, including symmetry classification Γ_{evr} and parity index ϵ, is given in Figure 2 5

As can be seen from this figure some levels are missing in the $K = 0$ ladder The reason for this is the Pauli exclusion principle which states that the overall molecular wavefunction, including nuclear spin, should be antisymmetric with respect to interchange of two hydrogen atoms (Fermions), i e the overall molecular wavefunction must have D_{3h} symmetry $\Gamma_{evrn} = A'_2$ or A''_2 Now, the ammonia molecule consists of two nuclear species, ortho-NH₃ having nuclear spin $I_H = \frac{3}{2}$ ($\Gamma_n = A'_1$) and para-NH₃ with spin $I_H = \frac{1}{2}$ ($\Gamma_n = E'$) Consequently, for ortho-NH₃ only those rovibrational levels exist that fulfil the relationship

$$A'_2, A''_2 \in \Gamma_{evrn} = A'_1 \otimes \Gamma_{evr} \tag{2 8}$$

For K=0 this implies that in the $\tilde{X}(0)$ state, with vibronic symmetry $\Gamma_{ev} = A'_1$, all even-J states are Pauli forbidden The same argument holds for the $\tilde{X}(1)$ state where for the $K = 0$ ladder all odd-J levels are absent A second consequence of the Pauli exclusion principle is that ortho NH₃ can only have A_1 or A_2 rotational wavefunctions, i e $K_{ortho} = 0, , 3n$, whereas para-NH₃ is accompanied with E-type rotational wavefunctions, i e $K_{para} = 6n \pm 1, 2$

2.3.2 $\tilde{B}$ state energy levels

The $\tilde{B}$ state of NH₃ possesses a flat geometry due to the excitation of a $2pa''_2$ ground state electron to a $3pe'$ molecular orbital The overall electronic wavefunction has $\Gamma_e = E''$ symmetry and is twofold degenerate In our experiments we examine the two photon transition $\tilde{B}(v_2) \leftarrow \tilde{X}(0, 1)$ in which the ν_2 umbrella vibration is excited in the $\tilde{B}$ state The symmetry of this ν_2 umbrella vibration is obtained from normal mode analysis to be A''_2 [30, 31]

Due to the flat equilibrium structure of the molecule there is no tunneling barrier and consequently the inversion splitting will be absent However, for molecules with a twofold degenerate E type vibronic state, strong rotation-vibration interactions can show up, as is the case for the $\tilde{B}$ state of the NH₃ molecule Coriolis coupling effects and vibrational l-type doubling give a considerable contribution to the molecular Hamiltonian and cause additional shifts and splittings of the rigid rotor energy levels The rotational energy levels can be adequately described using a
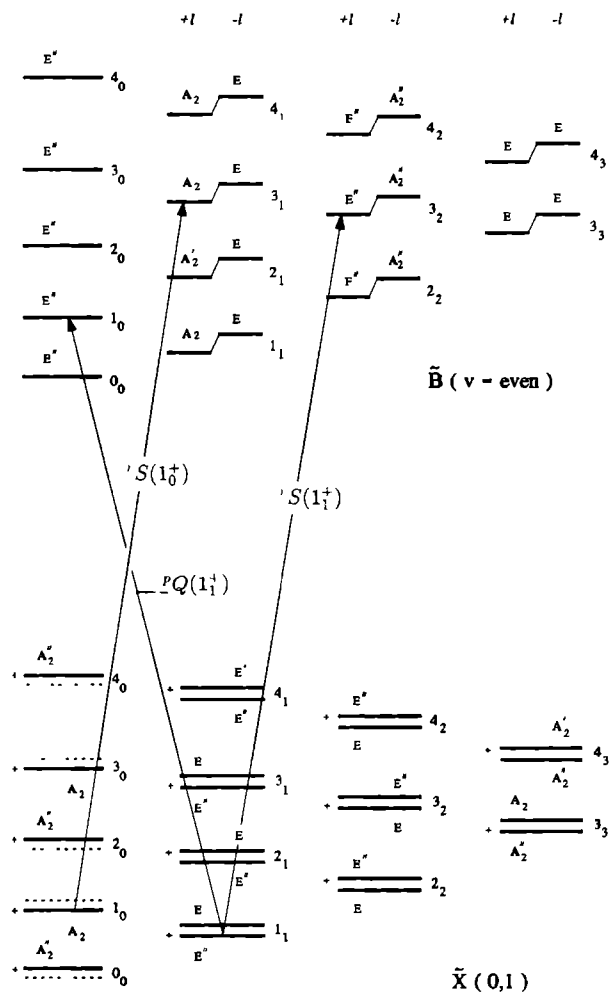
Figure 2.5 : *Rotational energy level diagram for the $\tilde{X}$ and $\tilde{B}$ electronic states of NH_3 Each level is characterized by the rotational quantum numbers J_K and the D_{3h} symmetry label Γ_{evr} of the rovibronic wavefunction In the electronic ground state the parity index number ϵ is given for completeness Some $\tilde{B} \leftarrow \tilde{X}$ two-photon transitions are indicated by the solid arrows*

32

conventional symmetric top Hamiltonian, including the effects of rotation-vibration coupling [30]

$$
\begin{aligned}
\hat{H}_v^{rot} = {} & T_v + B_v \ \vec{J}^2 + (C_v - B_v) \ J_z^2 \\
& - D_{JJ\,v} \ \vec{J}^4 - D_{JK,v} \ \vec{J}^2 \ J_z^2 - D_{KK,v} \ J_z^4 \\
& - 2C_v \zeta_v \ \vec{l} \ \vec{J} + \frac{1}{2} q_v \left\{ \vec{l}_+^{\,2} \ \vec{J}_-^{\,2} + \vec{l}_-^{\,2} \ \vec{J}_+^{\,2} \right\}
\end{aligned}
\tag{2 9}
$$

T_v is term value of the vibronic state, $B_v, C_v, D_{JJ\,v}, D_{JK\,v}$ and $D_{KK\,v}$ are the effective rotational and centrifugal distortion constants for the $\tilde{\text{B}}$ state, ζ_v is the strength of the Coriolis type interaction and q_v gives the strength of the rotation-vibration interaction causing the vibrational l-type doubling

In this formalism the wavefunction can be written as a product of the pure rotational part $|JKM\rangle$ and a vibrational part $|l\rangle$ Here l represents the vibrational angular momentum along the molecular symmetry axis and takes on the values 0 for the electronic ground state and ± 1 for the $\tilde{\text{B}}$ state We adopt the convention of Herzberg who connects the $l = +1$ label with the symmetric rotation vibration coupling, i e $\vec{J}$ and $\vec{l}$ pointing in the same direction [32]

The molecular constants for the $\tilde{\text{B}}$ state are presented in Table 2 4 The rovibronic symmetries of the energy levels are calculated according to $\Gamma_{evr} = \Gamma_e \otimes \Gamma_v \otimes \Gamma_r$ and are given in Figure 2 5 Again, those levels that do not obey the Pauli exclusion principle are spin forbidden and are excluded from the figure

K	$\Gamma_r[\ |J,K\rangle\ ]$
0 , J even	A_1'
0 , J odd	A_2'
$6n \pm 1$	E''
$6n \pm 2$	E'
$6n \pm 3$	$A_1'' \oplus A_2''$
$6n \pm 6$	$A_1' \oplus A_2'$

Table 2.3 : D_{3h} *symmetry classification of rigid rotor symmetric top wavefunctions* $|J,K\rangle$
See reference [26]

2.3.3 Two photon selection rules and line strengths

In order to assign the measured REMPI spectra we have to know the two photon electric dipole selection rules for the $\tilde{\text{X}} \to \tilde{\text{B}}$ rovibrational transitions Furthermore, the populations in the ground state of NH₃ can be extracted from these spectra once we know the transition moment matrix elements for these transitions The operator responsible for this two photon transition is defined as $\hat{P}_{2h\nu}$ and can be written in terms of the one photon dipole operator $P_{h\nu} = \vec{\tilde{\mu}}_{BF} \ \vec{E}_{SF}$

	T_v	B_v	C_v	$D_{JJ,v}$ $\times 10^6$	$D_{JK,v}$ $\times 10^6$	$D_{KK,v}$ $\times 10^6$	ζ_v	q_v
$\tilde{B}(0)$	59225.4	10.4844	5.1565	1065.0	-1613.0	645.0	0.8260	0.8868
$\tilde{B}(1)$	60123.6	9.9552	5.2099	534.0	-1077.0	551.0	0.8311	0.7303

Table 2.4 : *Molecular constants (in cm^{-1}) for the electronic $\tilde{B}$ state of NH_3 The constants are taken from Ashfold et al. [27]*

where $\vec{\mu}$ is the dipole moment in body fixed coordinates and $\vec{E}_{SF}$ the space fixed laser electric field causing the transition:

$$\hat{P}_{2h\nu} = \hat{P}_{h\nu} \cdot \hat{P}_{h\nu} = |E|^2 \cdot \hat{\mu}_\zeta^2 \qquad (2.10)$$

Here ζ denotes the polarization axis of the laser field and is one of the X, Y, Z space fixed axes. From this formula it can be immediately seen that the transition moment probability , defined as the square of the transition moment matrix element $\mathcal{M}_{fi}$ between initial state $|i\rangle$ and final state $|f\rangle$

$$\mathcal{M}_{fi} = \langle f|\hat{P}_{2h\nu}|i\rangle \qquad (2.11)$$

will be proportional to the square of the laser power which is an important result for the analysis of the two-photon REMPI spectra. For the evaluation of the matrix element $\mathcal{M}_{fi}$ the space fixed ζ component of the dipole moment operator is written in terms of body fixed components $\hat{\mu}_\alpha$ ($\alpha = 0, \pm 1$), with D_{3h} symmetry $\Gamma(\hat{\mu}_0) = A_2''$, $\Gamma(\hat{\mu}_{\pm 1}) = E'$, and the direction cosine matrices $\lambda_{\alpha\zeta}$ [28]. Separation of the molecular wavefunction Φ into an electronic, vibrational and rotational part yields the following expressions for the 2-photon dipole moment matrix element:

$$\mathcal{M}_{fi} \propto \sum_j \sum_{\alpha,\beta} \langle \Phi_f^{evr}|\lambda_{\alpha,\zeta}\mu_\alpha|\Phi_j^{evr}\rangle\langle \Phi_j^{evr}|\lambda_{\beta,\zeta}\mu_\beta|\Phi_i^{evr}\rangle \qquad (2.12)$$

$$= \sum_j \sum_{\alpha,\beta} \langle \Phi_f^{rot}|\lambda_{\alpha,\zeta}|\Phi_j^{rot}\rangle\langle \Phi_j^{rot}|\lambda_{\beta,\zeta}|\Phi_i^{rot}\rangle \times$$

$$\langle \Phi_f^{vib}|\langle \Phi_f^{elec}|\mu_\alpha|\Phi_j^{elec}\rangle|\Phi_j^{vib}\rangle\langle \Phi_j^{vib}|\langle \Phi_j^{elec}|\mu_\beta|\Phi_i^{elec}\rangle|\Phi_i^{vib}\rangle \qquad (2.13)$$

From this last equation the product of the two rotational one photon matrix elements indicate that the angular momentum vector $\vec{J}$ may change by at most 2 quanta, as is expected for a two photon transition and hence $\Delta J = 0, \pm 1, \pm 2$.

'Electronic' selection rules

For the initial state $\tilde{X}$ we have electronic symmetry $\Gamma[\Phi_i^{elec}] = A_1'$ whereas for the $\tilde{B}$ state $\Gamma[\Phi_f^{elec}] = E''$. Substituting this in Equation (2.13) it follows that the only combination (α, β) giving a non-zero contribution to $\mathcal{M}_{fi}$ is $(0, \pm 1)$ or $(\pm 1, 0)$ with $\Gamma[\Phi_j^{elec}] = E'$. Writing out the rotational matrix elements in Equation (2.13) and using the fact that $|\alpha - \beta| = 1$, immediately

implies that we have to do with a perpendicular band, i.e.

$$\Delta K = \pm 1$$

and hence only P and R branches are allowed for this two photon $E'' \leftarrow A_1'$ electronic transition. According to the convention used by Herzberg [32] these $\Delta K = \pm 1$ transitions are accompanied by a change in vibrational angular momentum of

$$\Delta l = \pm 1$$

'Vibronic' selection rules

Using the same arguments as for the electronic selection rules and bearing in mind that $\Gamma_{ev}[\tilde{X}(0)] = A_1', \Gamma_{ev}[\tilde{X}(1)] = A_2'', \Gamma_{ev}[\tilde{B}(v_2 = \text{even})] = E''$ and $\Gamma_{ev}[\tilde{B}(v_2 = \text{odd})] = E'$, we obtain the following results for the vibronic selection rules:

$$\begin{array}{ccccccc}
\tilde{B}(v_2 = \text{even}) & \leftarrow & \tilde{X}(0) & ; & \tilde{B}(v_2 = \text{odd}) & \not\leftarrow & \tilde{X}(0) \\
\tilde{B}(v_2 = \text{odd}) & \leftarrow & \tilde{X}(1) & ; & \tilde{B}(v_2 = \text{even}) & \not\leftarrow & \tilde{X}(1)
\end{array}$$

This implies that the upper levels of the electronic ground state inversion doublets must be probed in a $\tilde{B}(v_2 = \text{odd})$ band, whereas the lower inversion doublets can only be measured in a $\tilde{B}(v_2 = \text{even})$ band. A consequence of this is that in order to probe the complete vibronic ground state population distribution, one even and one odd $\tilde{B}(v_2)$ vibrational band has to be measured.

'Rovibronic' selection rules

The overall rovibronic selection rule is obtained from Equation (2.12). The dipole moment operator $\lambda_{\alpha,\zeta} \cdot \mu_\alpha$ is invariant under all D_{3h} symmetry operations except the inversion operator $E^\star$. As a result its D_{3h} symmetry is $\Gamma[\lambda_{\alpha,\zeta} \cdot \mu_\alpha] = A_1''$. Applying the non-vanishing-integral rule on the two matrix elements in Equation (2.12) yields the rovibronic selection rules :

$$\begin{array}{ccccccc}
\Gamma[\Phi_f^{evr}] & = & A_2'(A_2'') & \leftarrow & \Gamma[\Phi_i^{evr}] & = & A_2'(A_2'') \\
\Gamma[\Phi_f^{evr}] & = & E'(E'') & \leftarrow & \Gamma[\Phi_i^{evr}] & = & E'(E'')
\end{array}$$

In other words, the rovibrational symmetry of the levels involved in a two photon transition stays the same.

From Equation (2.13) the transition probability $\mathcal{M}_{fi}^2$ can be calculated and consists of a vibronic part, known as the Franck-Condon factor, and a rotational part, henceforth designated as $S^{\updownarrow\updownarrow}(\Phi_f^{rot}; \Phi_i^{rot}) = S^{\updownarrow\updownarrow}(J'K'; J''K'')$. The superscript $^{\updownarrow\updownarrow}$ indicates that we deal with a two photon transition where both absorbed photons are linearly polarized and have the same polarization direction. Chen and Yeung [33] calculated these two photon rotational matrix elements $S^{\updownarrow\updownarrow}(J'K'; J''K'')$ for a symmetric top molecule. However, in our case a non-negligible rotation-vibration coupling exists in the $\tilde{B}$ state of NH$_3$ and the rigid rotor rotational quantum numbers J' and K' are no good quantum numbers any more. The rigid rotor eigenfunctions are mixed and the real rotational eigenfunction $\Phi_{J'K'}$ becomes a linear combination of $|J', K'\rangle$ and $|J', K' + 2\rangle$. The corresponding mixing coefficients are obtained from diagonalization of the molecular Hamiltonian

J_K^ϵ	$\Delta K\,\Delta J$	wavelength	$\mathcal{L}_{f_i}$	$\tilde{B}(i)$	J_K^ϵ	$\Delta K\,\Delta J$	wavelength	$\mathcal{L}_{f_i}$	$\tilde{B}(i)$
Ortho NH₃					Para NH₃				
0_0^+	^rS	332 409	8 00	$\tilde{B}(1)$	1_1^+	^pQ	337 665	1 20	$\tilde{B}(0)$
1_0^+	^rQ	337 771	2 40	$\tilde{B}(0)$	1_1^+	^rR	337 646	1 52	$\tilde{B}(0)$
1_0^+	^rR	337 511	1 33	$\tilde{B}(0)$	1_1^+	^pR	337 426	1 82	$\tilde{B}(0)$
1_0^+	^rS	337 199	4 27	$\tilde{B}(0)$	1_1^+	^rS	337 290	3 00	$\tilde{B}(0)$
2_0^+	^rP	332 943	2 40	$\tilde{B}(1)$	1_1^+	^pS	337 065	0 47	$\tilde{B}(0)$
2_0^+	^rQ	332 738	0 57	$\tilde{B}(1)$	1_1^-	^pQ	332 632	1 20	$\tilde{B}(1)$
2_0^+	^rR	332 371	1 60	$\tilde{B}(1)$	1_1^-	^rR	332 612	1 49	$\tilde{B}(1)$
2_0^+	^rS	331 997	3 43	$\tilde{B}(1)$	1_1^-	^rS	332 284	2 96	$\tilde{B}(1)$
3_0^+	^rO	338 339	0 69	$\tilde{B}(0)$	1_1^-	^pS	332 079	0 51	$\tilde{B}(1)$
3_0^+	^rP	338 079	2 29	$\tilde{B}(0)$	2_1^+	^rQ	332 833	1 64	$\tilde{B}(1)$
4_0^+	^rP	333 142	2 22	$\tilde{B}(1)$	2_1^+	^rS	332 069	2 76	$\tilde{B}(1)$
4_0^+	^rO	333 510	1 02	$\tilde{B}(1)$	2_1^-	^pO	338 013	0 80	$\tilde{B}(0)$
3_3^+	^pP	337 849	1 43	$\tilde{B}(0)$	2_1^-	^rQ	337 872	1 63	$\tilde{B}(0)$
3_3^+	^rR	337 668	2 50	$\tilde{B}(0)$	2_1^-	^rS	337 046	2 81	$\tilde{B}(0)$
3_3^+	^pQ	337 490	1 67	$\tilde{B}(0)$	3_1^+	^pO	338 233	0 91	$\tilde{B}(0)$
3_3^+	^rS	337 073	1 66	$\tilde{B}(0)$	3_1^+	^rP	338 214	0 78	$\tilde{B}(0)$
3_3^-	^pP	332 806	1 43	$\tilde{B}(1)$	3_1^-	^pO	333 182	0 91	$\tilde{B}(1)$
3_3^-	^rR	332 638	2 50	$\tilde{B}(1)$	3_1^-	^rP	333 164	0 79	$\tilde{B}(1)$
3_3^-	^rS	332 090	1 66	$\tilde{B}(1)$	3_1^-	^rP	333 275	0 90	$\tilde{B}(1)$
4_3^+	^pO	333 248	1 11	$\tilde{B}(1)$	4_1^+	^pP	333 069	0 86	$\tilde{B}(1)$
4_3^+	^rR	332 529	0 64	$\tilde{B}(1)$	4_1^-	$^{a)}$			
4_3^-	^pO	338 304	1 11	$\tilde{B}(0)$	2_2^+	^pP	332 768	0 80	$\tilde{B}(1)$
4_3^-	^rQ	338 122	1 41	$\tilde{B}(0)$	2_2^+	^pQ	332 548	1 71	$\tilde{B}(1)$
4_3^-	^pQ	337 465	1 48	$\tilde{B}(0)$	2_2^+	^pR	332 217	1 08	$\tilde{B}(1)$
6_6^+	^pP	332 991	2 42	$\tilde{B}(1)$	2_2^+	^rS	332 181	2 11	$\tilde{B}(1)$
6_6^+	^rR	332 759	3 06	$\tilde{B}(1)$	2_2^-	^pP	337 811	0 80	$\tilde{B}(0)$
6_6^-	^pP	338 038	2 42	$\tilde{B}(0)$	2_2^-	^pQ	337 572	1 71	$\tilde{B}(0)$
6_6^-	^rR	337 786	3 07	$\tilde{B}(0)$	2_2^-	^rS	337 176	2 12	$\tilde{B}(0)$
					3_2^+	^pO	338 151	1 14	$\tilde{B}(0)$
					3_2^+	^pQ	337 552	1 12	$\tilde{B}(0)$
					3_2^-	^pO	333 099	1 14	$\tilde{B}(1)$
					3_2^-	^rS	331 966	2 36	$\tilde{B}(1)$
					4_2^+	^pO	333 320	1 27	$\tilde{B}(1)$
					4_2^-	^pO	338 367	1 27	$\tilde{B}(0)$
					4_4^+	^pP	332 857	1 87	$\tilde{B}(1)$
					4_4^+	^rR	332 668	2 74	$\tilde{B}(1)$
					4_4^+	^rS	332 009	1 37	$\tilde{B}(1)$
					4_4^-	^pP	337 899	1 87	$\tilde{B}(0)$
					4_4^-	^rR	337 695	2 76	$\tilde{B}(0)$
					5_5^+	^rR	337 736	2 93	$\tilde{B}(0)$
					5_5^+	^pQ	337 363	1 38	$\tilde{B}(0)$
					5_5^-	^pP	332 918	2 18	$\tilde{B}(1)$
					5_5^-	^rR	332 708	2 92	$\tilde{B}(1)$

Table 2.5 : *Line strengths and wavelengths of isolated lines of the $\tilde{B} \leftarrow \tilde{X}$ two photon spectrum of NH₃ J_K^ϵ is the state probed by the spectral line ΔK and ΔJ denote the change in K and J respectively and are assigned O, P, Q, R and S for a change of -2,-1,0,1 and 2 respectively The one photon wavelength is given in nanometers and $\mathcal{L}_{f_i}$ is the line strength of the transition The last column shows whether the state is probed in the $\tilde{B}(0)$ or $\tilde{B}(1)$ vibrational band.*

$^{a)}$ No isolated lines

NH$_3$ REMPI SPECTRA
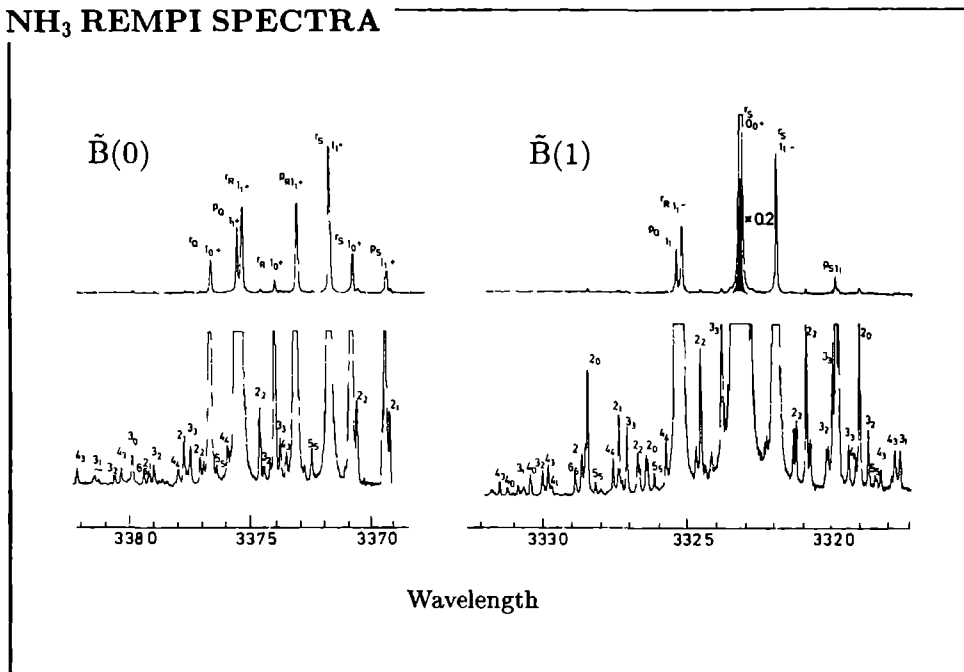
Figure 2.6 : *Measured 2+1 REMPI spectra of the $\tilde{B}(0) \leftarrow \tilde{X}(0)$ and $\tilde{B}(1) \leftarrow \tilde{X}(1)$ vibronic transitions of NH$_3$ Plotted is the ion yield (arb units) versus wavelength (in nm) For the strongest lines in the spectra the type of transition $^{\Delta K}\Delta J(J_K^\epsilon)$ is indicated In the lower part of the figure the vertical scale is multiplied with a factor of 25 The weaker transitions arising from higher rotational states are now identified by their ground state rotational quantum numbers J_K.*

of Equation (2.9). The real linestrengths belonging to a rotational transition $\Phi_{J'K'} \leftarrow \Phi_{J''K''}$ are obtained by properly weighing the matrixelements $S^{11}(J'K'; J''K'')$ with these mixing coefficients and are called $\mathcal{L}(J'K'; J''K'') \equiv \mathcal{L}_{fi}$ [27]

In Figure 2.5 some rotational two photon transitions for the $\tilde{B}(v_2 = \text{even})$ electronic transition are indicated by the solid arrows. The type of transition is designated as $^{\Delta K}\Delta J(J_{K''}^{\epsilon''})$, where the conventional definition of O, P, Q, R and S is used for $\Delta K, \Delta J = -2, -1, 0, 1, 2$ transitions. In Table 2 5 the transition type, the wavelength and the linestrength is given for those transitions in the $\tilde{B}(0) \leftarrow \tilde{X}$ and $\tilde{B}(1) \leftarrow \tilde{X}$ vibronic bands that are of interest in the analysis of the NH$_3$ scattering spectra

In Figure 2.6 the measured two-photon REMPI spectra of the $\tilde{B}(0)$ and $\tilde{B}(1)$ vibronic bands of NH$_3$ are presented. All lines can clearly be identified according to the assignments given in Table 2.5 . The top part of the figure gives a complete overview of the two bands, illustrating the
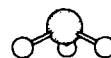
good rotational cooling yielding an effective rotational temperature of $T_o = 9$ K for ortho-NH_3 and $T_p = 13$ K for para-NH_3. In the lower part of the figure the vertical scale of the spectra is magnified with a factor 25 in order to show the high J_K rotational transitions which are labeled by their ground state J_K value. Note that in the $\tilde{B}(0)$ band all lines designated with J_K denote the lower inversion doublet component $J_K^{(l)}$, whereas in the $\tilde{B}(1)$ band J_K stands for $J_K^{(u)}$. The corresponding parity of the $J_K^{(l,u)}$ ground state levels can be obtained from Equation (2.7).

2.4 LIF spectroscopy of the OH molecule

The spectroscopy of the $\tilde{A} \leftarrow \tilde{X}$ electronic transition of the OH radical has been discussed extensively in literature [34, 35] and will be discussed here only briefly.

2.4.1 Ground state energy levels

The electronic ground state of OH has a non-zero electronic angular momentum about its internuclear symmetry axis. The projection of the electronic angular momentum $\vec{L}$ onto the internuclear axis is $\Lambda = \pm 1$ and hence the electronic wavefunction is designated $X^2\Pi$, having electronic spin angular momentum $S = \frac{1}{2}$.

For low rotational angular momentum the coupling of $\vec{L}, \vec{S}$ and the nuclear rotational angular momentum $\vec{R}$, giving a resultant total angular momentum $\vec{J}$, follows a Hund's case (a) coupling scheme [34, 36]. In this scheme the electronic spin angular momentum $\vec{S}$ and electronic orbital momentum $\vec{L}$ are strongly coupled to the internuclear axis. As a result the projection of $\vec{S}$ on this axis, Σ, and the projection of $\vec{L}$, designated as Λ, are good quantum numbers. The allowed values of Λ and Σ, being ± 1 and $\pm\frac{1}{2}$ respectively, result in two electronic states: the $^2\Pi_{3/2}$ state where $\Omega \equiv |\Lambda + \Sigma| = \frac{3}{2}$ and the $^2\Pi_{1/2}$ state where $\Omega = \frac{1}{2}$. Now the total angular momentum of the molecule $\vec{J}$ is formed by coupling the electronic angular momentum Ω to the rotational angular momentum $\vec{R}$:

$$\vec{J} = \vec{\Omega} + \vec{R} \qquad (2.14)$$

Since the projection of $\vec{R}$ onto the internuclear axis is zero by definition, the projection of $\vec{J}$ gives the values $\Omega = \frac{1}{2}$ or $\Omega = \frac{3}{2}$ and the rotational energy levels start from $J = \frac{1}{2}$ in the $^2\Pi_{1/2}$ state and from $J = \frac{3}{2}$ in the $^2\Pi_{3/2}$ state. A strong $\vec{L} \cdot \vec{S}$ coupling, known as the spin-orbit interaction, is responsible for an energy splitting between the two $^2\Pi$ electronic states, being equal to the spin-orbit constant A.

The rotational Hamiltonian for a $^2\Pi$ diatomic rotor, including the spin-orbit interaction, can be written as [36]:

$$\begin{aligned} \hat{H}_v^{rot} &= A_v \vec{L} \cdot \vec{S} + B_v \left[\vec{J} - \vec{L} - \vec{S} \right]^2 \\ &\cong A_v \vec{L} \cdot \vec{S} + B_v (\vec{J}^2 - J_z^2) - B_v(J_+S_- + J_-S_+) \end{aligned} \qquad (2.15)$$

where A_v is the spin-orbit coupling constant and B_v the rotational constant for the electronic ground state. These constants are given by Dieke and Crosswhite [35]:

$$\begin{aligned} A_{v=0} &= \text{-139.73 cm}^{-1} \\ B_{v=0} &= \text{18.515 cm}^{-1} \end{aligned}$$

For the OH radical the strong spin-orbit interaction is responsible for the uncoupling of the electron spin angular momentum from the internuclear axis and hence a transition occurs from a pure Hund's case (a) to an intermediate (a)-(b) Hund's case. Hill and van Vleck [37] were the first to calculate the rotational term values of a $^2\Pi_i$ state for an intermediate Hund's case:

$$E(^2\Pi_{\frac{1}{2}}, J) = B_v \left[(J + \frac{1}{2})^2 - 1 + \frac{1}{2}\sqrt{4(J + \frac{1}{2})^2 + Y(Y - 4)} \right] \qquad (2.16)$$

$$E(^2\Pi_{\frac{3}{2}}, J) = B_v \left[(J + \frac{1}{2})^2 - 1 - \frac{1}{2}\sqrt{4(J + \frac{1}{2})^2 + Y(Y - 4)} \right] \qquad (2.17)$$

In these formulae $Y \equiv B/A$ is a measure of the strength of the electron spin coupling to the internuclear axis. If the spin-orbit coupling constant A is large, $Y \to 0$ and the angular momentum coupling approaches a Hund's case (b). For weak spin-orbit coupling, $Y \to \infty$ and Hund's case (a) is regained.

Since the spin orbit coupling constant A is negative, the $^2\Pi_{3/2}$ electronic state is lower in energy than the $^2\Pi_{1/2}$ state. The $^2\Pi_{3/2}$ state is henceforth referred to as the F1 component whereas the $^2\Pi_{1/2}$ state is designated as the F2 component of the inverted $^2\Pi_i$ manifold. The molecular eigenfunctions are written as a product of a rotational part $|JM\Omega\rangle$ and a vibronic part $|v; \Lambda S\Sigma\rangle$ where v is the vibrational quantum number and M the space fixed projection quantum number of $\vec{J}$. The proper eigenstates of the molecular Hamiltonian are a linear combination of $|J\Omega M\rangle$ and $|J - \Omega M\rangle$ states:

$$|JM|\Omega|, \epsilon\rangle = \frac{1}{\sqrt{2}} [|JM\Omega\rangle|\Lambda, \Sigma\rangle + \epsilon \cdot |JM - \Omega\rangle| - \Lambda, -\Sigma\rangle] \qquad (2.18)$$

with $\Sigma = \Omega - \Lambda$. Here $\epsilon = \pm 1$ is the parity index and the labels 'f' and 'e' are used to refer to states with $\epsilon = +1$ and -1 respectively. The relation between the parity p of the wavefunction and the parity index ϵ is discussed by Alexander and Dagdigian [38] and is given by:

$$p = \epsilon \cdot (-1)^{J-S} \qquad (2.19)$$

When the rotational angular momentum J increases the electron spin $\vec{S}$ becomes less coupled to the internuclear axis and the coupling scheme tends towards a Hund's case (b) situation. Here the electron spin $\vec{S}$ is coupled to the vector sum of $\vec{\Lambda}$ and $\vec{R}$ and Ω is not a good quantum number any more. The rotational eigenfunctions belonging to the intermediate Hund's case can be written as linear combinations of Hund's case (a) wavefunctions $|JM\Omega = \frac{3}{2}, \epsilon\rangle$ and $|JM\Omega = \frac{1}{2}, \epsilon\rangle$:

$$\Phi^\epsilon_{\frac{3}{2}, J} = c^\epsilon_J \cdot |JM\frac{3}{2}, \epsilon\rangle - d^\epsilon_J \cdot |JM\frac{1}{2}, \epsilon\rangle$$

$$\Phi^\epsilon_{\frac{1}{2}, J} = d^\epsilon_J \cdot |JM\frac{3}{2}, \epsilon\rangle + c^\epsilon_J \cdot |JM\frac{1}{2}, \epsilon\rangle \qquad (2.20)$$

From the diagonalization of the rotational Hamiltonian in Equation (2.15), the mixing coefficients c^ϵ_J and d^ϵ_J can be calculated and expressed in terms of A, B and J [39].

A general feature for $\Lambda \neq 0$ diatomic molecules is the 'Λ doubling' of rotational states. The interaction between the electronic angular momentum $\vec{L}$ and nuclear rotational angular momentum $\vec{R}$ causes the otherwise degenerate $\epsilon = \pm 1$ levels to split into two substates. For a Hund's case (a)
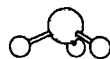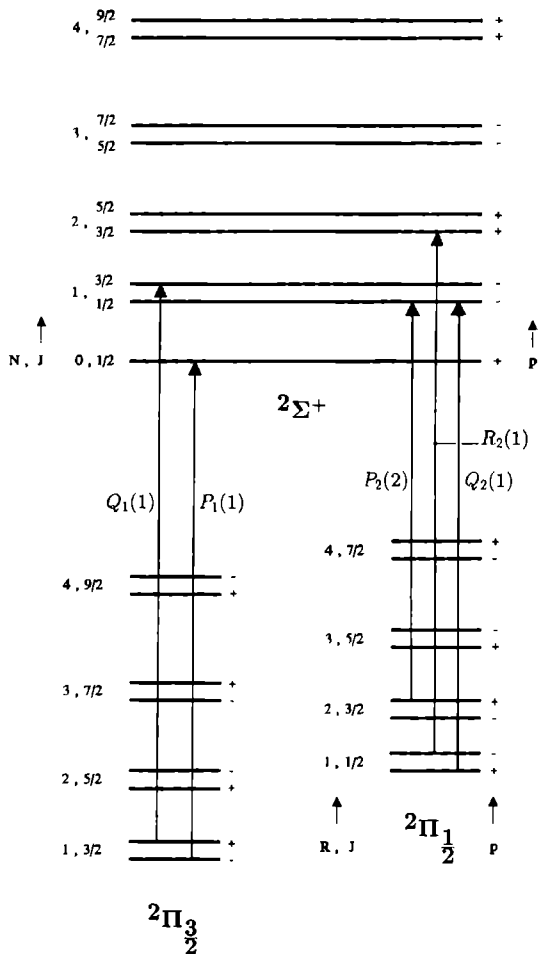
Figure 2.7 : *Rotational energy level diagram for the $X^2\Pi_i$ and $A^2\Sigma^+$ electronic states of OH. Each level is characterized by its rotational quantum numbers R, J ($^2\Pi$) and N, J ($^2\Sigma$), and the parity p. Some $A^2\Sigma^+ \leftarrow X^2\Pi_i$ one-photon transitions are indicated by the solid arrows*

molecule the $\epsilon = -1$ level becomes higher in energy than the $\epsilon = +1$ level. The splitting for the lowest rotational state of OH $^2\Pi_i$ is about 0.05 cm^{-1} and increases with increasing J.

A complete energy level diagram for the $X^2\Pi_i$ ground state of OH is presented in Figure 2.7. Note that for high J values ($J \geq \frac{9}{2}, \Omega = \frac{1}{2}$), as the molecule reaches the Hund's case (b) limit, the Λ doubling splitting between the two $\epsilon = \pm 1$ levels changes sign and the $\epsilon = -1$ component has the lowest energy.

2.4.2 $A^2\Sigma^+$ state energy levels

The first electronically excited state of OH has a $^2\Sigma^+$ electron configuration. The projection of the electronic orbital angular momentum on the internuclear axis is zero and hence the angular momentum coupling follows a Hund's case (b) scheme. Furthermore, an additional interaction $\gamma \cdot \vec{N} \cdot \vec{S}$ between the electron spin angular momentum and the rotational angular momentum $\vec{N}$ causes each rotational level to split. This splitting is traditionally referred to as ρ-doubling and is discussed in detail by Herzberg [34]. The rotational term values for the $A^2\Sigma^+$ are given by:

$$E_{F1}(N = J - \frac{1}{2}) = B_v \cdot N(N+1) + \frac{1}{2}\gamma_v \cdot N \tag{2.21}$$

$$E_{F2}(N = J + \frac{1}{2}) = B_v \cdot N(N+1) - \frac{1}{2}\gamma_v \cdot (N+1) \tag{2.22}$$

where the notation F1 and F2 refers to the component of the ρ-doublet with $J = N + \frac{1}{2}$ and $J = N - \frac{1}{2}$ respectively. For the vibrational ground state in the electronic A state the molecular constants are given by Ref. [35]:

$$B_{v=0} = 16.961 \text{ cm}^{-1}$$
$$\gamma_{v=0} = 0.224 \text{ cm}^{-1}$$

The parity of the rotational wavefunction in the $^2\Sigma^+$ state is given by:

$$p = (-1)^N \tag{2.23}$$

as is indicated in Figure 2.7.

2.4.3 Transitions and linestrengths

The selection rules for a one photon $^2\Sigma^+ \leftarrow {}^2\Pi$ transition are well known [34] and are given by:

$$\pm \leftarrow \mp \quad ; \quad \pm \nleftarrow \pm$$
$$\Delta J = 0, \pm 1$$

i.e.: the overall parity of the molecular wavefunction has to change and the total angular momentum J may change by at most 1 quantum. The type of transition is designated as

$$^{\Delta N}\Delta J_{F_f F_i}(N'') \tag{2.24}$$

with the conventional notation O, P, Q, R and S for $\Delta N, \Delta J = -2, -1, 0, 1, 2$ transitions. Furthermore F_i and F_f denote the $F_{1,2}$ component in the initial, respectively final state. If $\Delta N = \Delta J$ and $F_f = F_i$ the indication of ΔN and F_f is omitted from the spectroscopical notation, hence $Q_1(1)$ stands for the transition $^QQ_{11}(1)$.

41
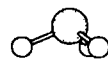
$A^2\Sigma^+ \leftarrow X^2\Pi_{3/2}$			$A^2\Sigma^+ \leftarrow X^2\Pi_{1/2}$		
Transition	Wavelength	$\mathcal{L}_{f_\imath}$	Transition	Wavelength	$\mathcal{L}_{f_\imath}$
$Q_1(1)$	307.933	9.0	$Q_2(1)$	309.136	5.3
$Q_1(2)$	308.084	17.0	$Q_2(2)$	309.075	11.0
$Q_1(3)$	308.243	25.3	$Q_2(3)$	309.075	18.2
$Q_1(4)$	308.417	33.7	$Q_2(4)$	309.125	26.1
$Q_1(5)$	308.608	42.2	$Q_2(5)$	309.225	34.4
$P_1(1)$	308 255	9.4	$P_2(1)$	-	-
$P_1(2)$	308.728	12.7	$P_2(2)$	309.724	4.4
$P_1(3)$	309.208	16.5	$P_2(3)$	310.048	8.6
$P_1(4)$	309.701	20.5	$P_2(4)$	310.423	12.9
$P_1(5)$	310.212	24.5	$P_2(5)$	310.845	17.4
$R_1(1)$	307.289	2.6	$R_2(1)$	308.494	2.7
$R_1(2)$	307.120	6.1	$R_2(2)$	308.112	5.7
$R_1(3)$	306.959	10.1	$R_2(3)$	307.791	8.9
$R_1(4)$	306 812	14 2	$R_2(4)$	307 525	12.8
$R_1(5)$	306.686	18.4	$R_2(5)$	307.308	16.7

Table 2.6 : *Line strengths and vacuum wavelengths of the strongest rotational lines of the $A^2\Sigma^+(v'' = 0) \leftarrow X^2\Pi_\imath(v' = 0)$ vibronic transition of OH The wavelength is given in nanometers and $\mathcal{L}_{f_\imath}$ is the line strength of the transition*

The rotational linestrength $\mathcal{L}_{f_\imath}$ for a one photon electric dipole transition can be obtained by evaluating the dipole moment matrix element between initial and final rotational state. In this case the Hönl-London factors [28] have to be properly weighed with the mixing coefficients c_j^r and d_j^r of the intermediate Hund's case ground state [35].

In Figure 2.7 some rotational transitions for the $A^2\Sigma^+(v' = 0) \leftarrow X^2\Pi_\imath(v'' = 0)$ vibronic band are indicated. In Table 2.6 the strongest rotational transitions up to $N = 5$ are presented, including wavelength and linestrength.

Chapter 3

State-to-State Cross Sections
For Rotational Excitation Of Ortho And Para NH$_3$
By Collisions With He And H$_2$

J Schleipen and J J ter Meulen
Department of Molecular and Laser Physics, University of Nijmegen,
Toernooiveld, 6525 ED Nijmegen, The Netherlands

Parity resolved state-to-state cross sections for rotational excitation of ortho- and para-NH$_3$, colliding with He and H$_2$, have been obtained in a crossed molecular beam experiment State preparation of the 0_0^+ state for ortho-NH$_3$ and the 1_1^- state for para-NH$_3$ is achieved by adiabatic expansion of ammonia, seeded in argon, followed by electrostatic state selection in a hexapole electric field The NH$_3$ rotational state distribution is probed by 2+1 REMPI spectroscopy via the $\tilde{B}$ state A comparison with calculated cross sections shows a reasonably good agreement for pure rotational excitation However, strong deviations from predicted parity propensity rules are observed
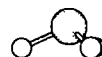
3.1 Introduction

The rotational excitation of ammonia by collisions with He and H_2 has been the subject of many experimental and theoretical investigations (see [62] and references [1] to[16] therein) The ultimate goal of these studies is to determine the intermolecular potential of both collision partners It has become clear that this goal can only be reached by the measurement of pure state-to-state cross sections, i e the collision process has to be studied between a selected pure initial state $|i\rangle$ and a single final state $|f\rangle$ From the specific shape of the potential energy surface of the two colliding molecules, quantum or semi-classical scattering calculations [40] directly yield state-to-state cross sections, σ_{if}, for rotational excitation of one of the collision partners To this purpose the intermolecular potential can in principle be obtained from ab initio studies on the intermolecular forces which however usually require great computational efforts and calculational approximations On the other hand, when knowing the state to-state inelastic collision cross sections σ_{if} from experiment, the intermolecular potential can be constructed by fitting the calculated cross sections to the experimental values This potential modelling and consequent scattering calculations give a clear insight into the intermolecular forces which come into play during the collision and in the collision dynamics in general For NH_3-H_2 collisions the cross sections σ_{if} also have important astrophysical relevance They can be translated into collision rates, in order to describe the anomalous non-thermal microwave radiation observed from interstellar clouds [1, 2]

The first state-to-state-like collision data were obtained by Oka and coworkers [10] who performed MW-MW and IR-MW double resonance experiments yielding information on collision-induced transitions between two specific J_K inversion doublets However, their results were difficult to interpret in terms of real state-to-state cross sections, due to the fact that the experiments were performed in bulk circumstances and hence multiple collision processes could not be excluded

Single collision processes were studied in a microwave beam maser experiment by Klaassen t al [14], using molecular beams Here the collision process could be controlled because, due to the use of molecular beams, the scattering volume was well defined and secondary or higher order collisions could be eliminated by controlling the secondary beam intensity However, due to the limited opening angle of the microwave cavity, only molecules scattered in nearly forward direction could be detected, yielding incomplete integral cross sections A molecular beam experiment aimed at the differential cross section measurement for NH_3-He collisions is performed by Buck and coworkers [15] The limited TOF resolution of their apparatus did not allow the determination of state-to-state cross sections also in this case Furthermore, their angular detection range was limited to backward scattering, and hence mainly the repulsive part of the potential was probed The inelastic collision cross sections, however, are determined by the total anisotropy of the potential and are sensitive to the attractive part of the interaction potential as well

Recently we reported an experiment [41] in which state-to-state collision measurements have been performed, free of the difficulties mentioned above Relative state-to-state cross sections for rotational excitation of ortho-NH_3 by He and H_2 were presented, whereas for para-NH_3 an average of two state-to-state cross sections was obtained, due to the preparation of both 1_1 parity states In the present experiment we succeeded in separating the two 1_1 parity states by means of electrostatic state selection, which yields parity resolved state-to-state cross sections for para-NH_3 In addition improved state-to-state cross sections were obtained for ortho-NH_3, which are in better agreement with theory than the previous data For ortho-NH_3 the 0_0^+ state is selected, whereas for para-NH_3 only the 1_1^- state contributes to the collision process

The preparation of only one single rotational state of each NH_3 species made it possible to

investigate the parity propensity rules predicted by theory for both ortho- and para-NH$_3$ For ortho-NH$_3$ parity-index (section 2 2) conserving $|\Delta K| = 3$ transitions are predicted to be very weak using semi-classical scattering theory [42] or even forbidden when the more accurate coupled states technique is applied [15, 44] Also for para-NH$_3$ both theories predict a strong parity propensity rule especially for the $1_1^- \rightarrow 2_2^\pm$ transition

The experimental data can be compared with results obtained from theoretical studies on the NH$_3$-He and NH$_3$-H$_2$ collision processes For He scattering Meyer et al [15] performed a coupled states calculation using an experimentally modelled intermolecular potential based upon differential cross section measurements A second approach for the NH$_3$-He scattering is provided by Billing et al [42] who performed semi classical trajectory calculations using the ab initio potential of Diercksen [43] For the H$_2$ scattering the calculations of Ebel et al [44] and Offer and Flower [46, 47] can be compared to our experimental results Ebel et al use coupled states quantum calculations whereas Offer and Flower perform the more accurate quantum mechanical close coupling calculations to attack the dynamical scattering problem Both calculations make use of ab initio potential energy surfaces However, using the potential of Billing and Diercksen [48], Ebel et al freeze out the ϕ_2 dependence, i e the rotation of the H$_2$ molecule around the intermolecular axis, whereas the scattering calculations of Offer and Flower explicitly contain this angle ϕ_2 and thus provide a better description of the physical reality

The chapter is organized as follows In section 3 2 the experiment is described The way to translate the scattering signals into parity resolved state-to-state inelastic cross sections is explained in section 3 3 The experimentally determined cross sections are presented in section 3 4 Finally, a comparison is made with theoretically available state to-state cross sections which will be discussed in section 3 5

3.2 Experimental

3.2.1 Experimental set-up.

The pulsed crossed-beam experiment is an extended version of the one described in a previous paper [41] An artists view of the set-up is given in Figure 3 1 The primary molecular beam (NH$_3$) is produced by expanding the ammonia gas through a 1 mm diameter nozzle into vacuum, using a modified Bosch-type pulsed valve The vacuum chamber is pumped by a 8000 mbar l s^{-1} oil diffusion pump and the background pressure during operation is well below 10^{-5} mbar

Rotational cooling of the NH$_3$ molecule is achieved by seeding the ammonia in argon Optimum cooling conditions are obtained using 1% NH$_3$ in Ar and a stagnation pressure of about 1 bar During operation the valve can be electronically and mechanically adjusted in order to optimize the molecular pulse profile The beam is narrowly collimated by a skimmer about 20 mm downstream in order to avoid collisions of the molecules with the rods of the state selector, mounted between the skimmer and the scattering region The skimmer is electroformed of hard nickel as described in reference [51] The 5 mm diameter opening of the skimmer is very sharp-edged in order to minimize the interactions between the skimmer and beam molecules which may warm up the rotationally cold NH$_3$ molecules The molecular pulse width is monitored by a fast ionization gauge positioned on the primary beam axis and adjusted to be about 1 millisecond FWHM By varying the distance between the nozzle-skimmer assembly and the ionization gauge, we measured the velocity of the primary beam molecules and found $v_{NH_3} = 670(30)$ m/sec

After the skimmer the NH$_3$ molecules undergo an electrostatic state selection process For this
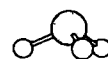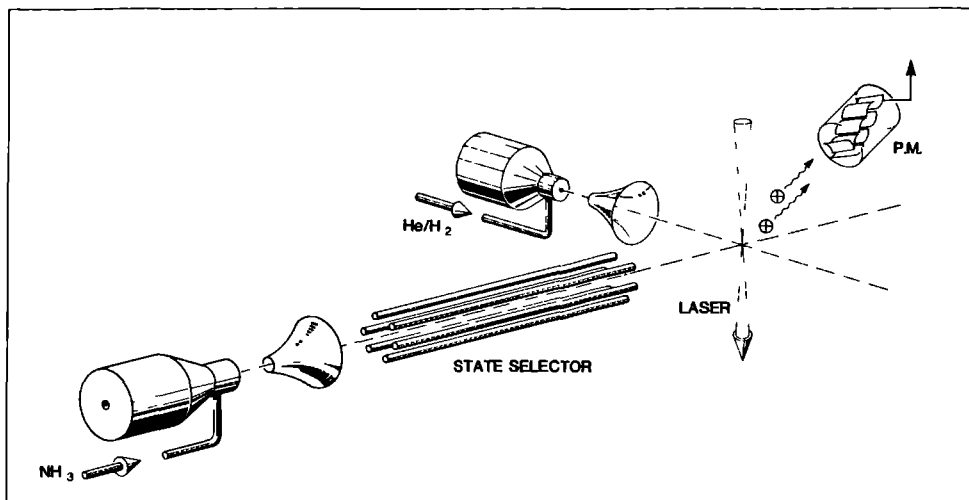
Figure 3.1 : *Artists impression of the experimental set-up*

purpose a hexapole, operating at voltages up to 25 kV, is inserted between the nozzle-skimmer assembly and the scattering region The rods of the hexapole are 230 mm long and 2 mm in diameter The spacing between two neighbouring rods is about 2 mm The distance from the skimmer to the entrance opening of the hexapole is 40 mm and is chosen in such a way as to collect as many NH_3 molecules as possible The whole nozzle-skimmer-hexapole system can be translated along the six-pole axis in order to adjust the focus of the state selector at the scattering region The optimum distance from the hexapole exit opening to the scattering region at the operating voltage of 25 kV is 80 mm The focus of the 1_1^- state molecules is spread out over several mm along the axis, depending on the focusing voltage At the exit of the state selector a metal diaphragm is placed on the molecular beam axis for shielding off stray electric fields arising from the hexapole This shielding was necessary in order not to disturb the detection of the NH_3^- ions produced by the REMPI (Resonance Enhanced Multi Photon Ionization) process downstream

For calibration purposes (see later), a microwave cavity can be inserted between the hexapole and the scattering center cavity is of a cylindrical type with a length of 50 mm and a diameter of 8 93 mm and resonates in the TM_{01} mode on the frequency of the 1_1 doublet microwave transition, $\Delta\nu_{1_1} = 23\,969$ GHz [52] The Q-factor of the cavity is kept low in order to obtain a broad cavity absorption band of several 100 MHz In this way the frequency of the radiation can be scanned without changing the cavity diameter Due to transit-time broadening all hyperfine levels of the 1_1^- state can be excited by the narrow band microwave radiation simultaneously The microwave frequency is phase-locked and stabilized by the 5 MHz reference signal from a Rb-atomic clock standard

In the scattering region, positioned about 400 mm downstream from the primary nozzle, the

NH$_3$ molecular beam is crossed perpendicularly with the secondary beam, containing the collision partners He or H$_2$ The secondary beam is produced in a differentially pumped (5500 mbar l s^{-1}) vacuum chamber using the same type of valve as used for the NH$_3$ beam Backing pressures up to 500 mbar were used, low enough to avoid secondary collision effects Again the expanded beam is shaped by a 4 mm electroformed skimmer, positioned 20 mm downstream from the nozzle orifice In this way the background pressure in the scattering chamber is not influenced by operating the second valve and remains below 10^{-5} mbar Furthermore the geometry of the scattering region is well defined and the occurrence of secondary collision processes can be avoided The distance from the secondary nozzle to the scattering region is 60 mm A second ionization gauge mounted on the secondary beam axis is used to determine the velocities of the collision partners He and H$_2$ The results are $v_{He} = 1560(65)$ m/sec and $v_{H_2} = 2720(110)$ m/sec

Before and after collisions take place, the rotational state distribution of the NH$_3$ molecules is monitored by 2+1 REMPI spectroscopy Two laser photons are used to make a resonant absorption to the electronic $\tilde{B}$ state of NH$_3$, followed by the absorption of an additional third photon to promote the excited $\tilde{B}$ state molecule above its ionization potential For this purpose a probe laser is crossed at right angles with the two molecular beams The laser probes the $\tilde{B}(v_2'=0) \leftarrow \tilde{X}(v_2''=0)$ and $\tilde{B}(v_2'=1) \leftarrow \tilde{X}(v_2''=0)$ vibrational bands of NH$_3$, at 337 nm and 332 nm respectively The radiation at these wavelengths is generated by a dye laser (Lambda Physik FL2002) operating at PTP dye, pumped by a pulsed XeCl excimer laser (Lambda Physik EMG201MSC) The dye PTP lases between 330 nm and 350 nm and possesses a high efficiency and lifetime The output power has to be attenuated in order not to saturate the first two-photon step in the 2+1 REMPI process This was done by checking the quadratic power dependence of the resonant two-photon step in the 2+1 REMPI process This quadratic power dependence indicates that the ionization step from the excited $\tilde{B}$ state in the REMPI process is saturated Typical powers used in the experiment are about 6 mJ for the $\tilde{B}(0)$ band and about 1 mJ for the $\tilde{B}(1)$ band The resolution of our spectra is determined by the laser bandwidth which is about 0 7 cm^{-1} The probe laser is focused into the scattering region by a f=+25 cm lens, which was attached to a 3-dimensional translational device in order to scan the focus through the scattering region in all three dimensions

The REMPI process produces NH$_3^+$ ions which are detected with great sensitivity by a venetian blind-type particle multiplier tube A repeller plate was used to direct the ions into the multiplier The multiplier signal is then processed by a boxcar averager and a stripchart recorder During the scattering measurements the baseline subtraction mode (BSM) of the boxcar is used In this mode the secondary beam is toggled and the boxcar subtracts the NH$_3$ signal measured with secondary beam off (no collisions), from the NH$_3$ signal measured with the secondary beam on The resulting difference signal is then averaged and the boxcar output gives directly the difference spectrum of NH$_3$ due to collisions with secondary beam molecules Simultaneously the UV power is registered so that afterwards the signal intensity can be corrected for fluctuations of the laser power

Both valves and the laser are triggered by one central clock, followed by three parallel delay units First the laser delay unit is preset to such a value that the laser probes the early part of the NH$_3$ primary beam pulse Next, the secondary beam pulse is brought into overlap with the primary beam and the laser pulse by adjusting the secondary beam delay unit The clock is also used to trigger an A/D converter In this way the scattering signal, as well as the laser power can be stored in and manipulated by a computer In order to eliminate long term fluctuations in the scattering signal and to check for reproducebility, several scans of the same spectral range were recorded successively During each scan the signal was averaged over 30 samples by the boxcar
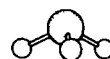
averager in order to eliminate short term fluctuations. The results obtained from different scans under the same experimental conditions were averaged to give the final scattering data.
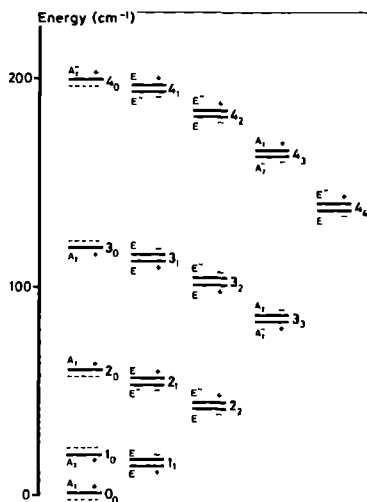
Figure 3.2 : *Energy level diagram for the $\tilde{X}$ state of NH_3 For each level J_K the D_{3h} symmetry label is indicated, together with the parity-index ϵ*

3.2.2   State selective detection of NH_3.

The rotational state distribution in the electronic vibrational ground state of the ammonia molecule is probed by means of the 2+1 REMPI spectroscopic technique [27, 53, 54, 55, 56, 57]. For symmetry reasons two vibrational $\tilde{B} \leftarrow \tilde{X}(0)$ transitions must be excited in order to probe all individual rotational states. Use is made of the $\tilde{B}(0)$ and $\tilde{B}(1)$ vibronic bands of ammonia which have their band origins in the far UV at around 60000 cm^{-1}.

The ground state ammonia molecule has a pyramidal structure and the rotational eigenfunctions are described by oblate symmetric rotor expressions. The eigenvalues of the Hamiltonian are characterized by two quantum numbers, J and K, in which J denotes the total angular momentum $|\vec{J}|$ of the rotating molecule and K the projection of $\vec{J}$ onto the molecular C_{3v} symmetry axis. In addition to pure rotation of the nuclear frame, the ammonia molecule possesses a relatively small potential energy barrier for the three H-atoms to tunnel e.g. from a position in a plane above the N-atom to an equivalent position in a plane below the N-atom. This inversion tunneling gives rise to a splitting of all rotational levels into doublets. The inversion splitting is about 0.8 cm^{-1}

in the ground vibrational state which is smaller than the rotational constants of ammonia. Due to this inversion tunneling the energy levels are classified according to the D_{3h} symmetry group. A diagram of the rotational energy level scheme in the vibronic ground state is given in Figure 3.2, together with the overall rovibronic-inversion symmetry of the wavefunctions and a symmetry label $\epsilon = \pm$, called the parity-index, in order to classify the individual states belonging to either inversion doublet. We will adopt the notation of Billing et al [49] and henceforth the parity-index ϵ is used to denote a specific rotational state J_K^ϵ. The parity of this state J_K^ϵ, i.e. the symmetry of the overall NH₃ molecular wavefunction under the operation of E^*, according to Green [29] is then given by ϵ $(-1)^{K-J+1}$, as is reflected in the D_{3h} symmetry label. In the following one has to be careful not to confuse the parity-index ϵ and the parity of the overall wavefunction. Energy levels having rovibronic-inversion symmetry A_1' or A_1'' are Pauli-forbidden and this is the reason why for the K=0 ladder always one of the J_K^ϵ levels belonging to an inversion doublet is missing.

Due to the alternating vibronic symmetry in the $\tilde{B}$ state (Γ^{ve}=E",v even, Γ^{ve}=E',v odd), the lower inversion doublets have to be probed in the even $\tilde{B}$ vibronic bands, whereas the upper inversion doublets are probed in the odd $\tilde{B}$ vibronic bands. Using PTP dye which lases directly in the UV between 330 nm and 350 nm, we chose the $\tilde{B}(0)$ and $\tilde{B}(1)$ bands to probe the ground state inversion doublets. In this way, measuring both parity states belonging to a specific rotational state J_K in two different vibronic bands, we were able to distinguish spectroscopically between the two inversion doublet levels, although their energy separation is comparable to the laser bandwidth.

Using the Hamiltonian and constants of Ashfold et al [27] and the two-photon linestrengths of Chen and Yeung [33] to describe the $\tilde{B} \leftarrow \tilde{X}$ two-photon spectrum of NH₃ we calculated the wavelengths and transition strengths of all lines appearing in the spectrum. A simulation of the experimental spectra gives a clear identification of all lines. Some of them are overlapping and cannot be used in our data analysis. However, for every J_K^ϵ state two or more isolated lines can easily be found in the spectra, giving a reliable value for the population in this rotation-inversion level. For the NH₃ molecular constants and the relevant spectroscopic data for unraveling the spectra, we refer to Chapter 2, section 3.

3.2.3 Initial state preparation.

A first step in the initial state preparation is made by rotational cooling of the NH₃ molecules in the molecular beam expansion. Analysis of the rotational structure in the $\tilde{B}(0)$ and $\tilde{B}(1)$ bands shows for the ortho-NH₃ that more than 90 % is found in the single 0_0^+ state and about 8 % in the 1_0^+ state. For para-NH₃ the $J_K = 1_1$ doublet contains more than 95 % of the total para-NH₃ distribution. From the ratio of populations in the 0_0^+ and 1_0^+ states for ortho-NH₃ and the 1_1^+ and 2_1^- states for para-NH₃ a rotational temperature of $T_{ortho} \approx 10$ K and $T_{para} \approx 15$ K is obtained for the ortho and para species respectively. The construction of a Boltzmann-plot indicates that the rotational energy distribution is non-thermal. Similar rotational relaxation features are observed in other experiments [41, 54].

For para-NH₃ the prepared $J_K = 1_1$ level is doubled due to the inversion splitting and consequently two states of different parity are prepared after rotational cooling. The two parity states are separated in such a way that only one state, in this case the 1_1^- state, reaches the scattering center. This is achieved by applying state-specific electrostatic deflection and (de-)focusing of the NH₃ molecules in a hexapole electric field. While travelling through the hexapole field, an electrostatic force is exerted on the molecules due to the interaction of the electric field with the dipole moment of the molecule. Due to the positive radial field gradient, molecules possessing a positive
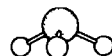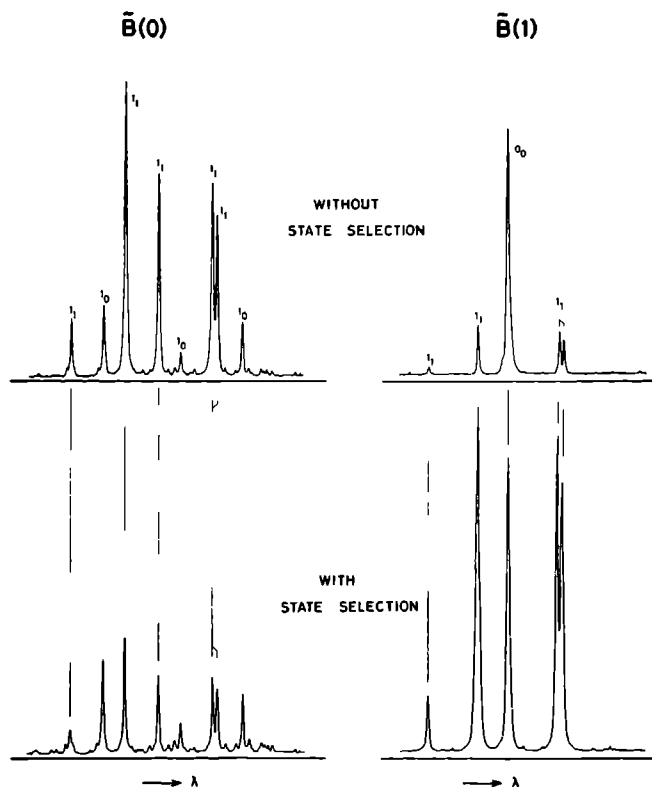
Figure 3.3 : *REMPI spectra of the NH$_3$ primary beam The $\tilde{B}(0)$ and $\tilde{B}(1)$ band spectra are recorded with different sensitivity The upper part shows both bands without voltage applied to the state selector In the lower part the state selection is active giving a decrease of 1_1^+ signal in the $\tilde{B}(0)$ band and an increase of 1_1^- signal in the $\tilde{B}(1)$ band*

Stark effect are deflected towards the molecular beam axis, whereas those having a negative Stark effect are deflected away from the beam axis For ammonia this means that molecules in the upper doublet levels are focused into the scattering region, whereas the lower doublet molecules are removed from the scattering region This second-order Stark force exerted on a NH₃ molecule in a specific rotational state J_K, can be described in terms of the dipole moment μ, the 1_1 doublet transition frequency $\Delta\nu_{1_1}$, the external electric field $E(\vec{r})$ with $\vec{r}$ the radial distance and the quantum numbers J, K and M where M denotes the projection of $\vec{J}$ onto the electric field axis

$$\vec{F}_{Stark} \;=\; -\,\vec{\nabla} W_{Stark} \tag{3 1}$$

with

$$W_{Stark} \;=\; \pm\sqrt{\frac{1}{4}\,\Delta\nu_{1_1}^2 + (\mu\;E(\vec{r}))^2}\;\frac{M\;K}{J(J+1)} \tag{3 2}$$

The plus sign applies to molecules having a positive Stark effect, i e to the upper doublet level 1_1^-, while the minus sign applies to the negative Stark effect, i e to the lower doublet level 1_1^+.

In Figure 3 3 the effect of the state selection process is illustrated for both the $\tilde{B}(0)$ and $\tilde{B}(1)$ band of NH₃ In the $\tilde{B}(0)$ band the 1_1^+ signals are decreased due to deflection of 1_1^+ state molecules away from the molecular beam axis, on the other hand in the $\tilde{B}(1)$ band the 1_1^- signals are increased due to focusing the 1_1^- state molecules into the scattering and detection region Figure 3 4 shows the focusing efficiency for both the 1_1 doublet levels We measured the $^R S(1_1^+)$ ($\tilde{B}(0)$ band) and $^R S(1_1^-)$ ($\tilde{B}(1)$ band) intensities as a function of the applied voltage For the sake of comparison the population of both states at zero voltage is normalized to 1 0 From the figure it follows that the gain for the 1_1^- state population does not reach a maximum within the present voltage range We did not exceed the 25 kV limit in order to avoid electrical breakdown At a value of 25 kV the 1_1^- population in the detection area is increased by a factor of about 7, whereas the 1_1^+ population has decreased by a factor of about 3 From the figure it is clear that this latter factor 3 is a saturated value This can be understood from Equation (3 2) Molecules in the $M = 0$ sublevels of the $J_K = 1_1$ level are not influenced by the Stark force and consequently follow their way through the state selector, undisturbed by the hexapole field For the 1_1^+ rotational state one out of three substates has $M = 0$, which accounts for this factor 3

For the $K = 0$ molecules no inversion doublets exist and consequently the expression for the Stark force as given in Equation (3 2) cannot describe the deflection of these molecules in an adequate way Experiment indeed shows that the K=0 levels are affected only slightly by the electrostatic state selection process As a result, all ortho-NH₃ scattering measurements are performed with the state selector removed from the molecular beam machine

3.3 Data analysis.

3.3.1 Single state-to-state collisional cross sections.

The rotational state-to-state cross section $\sigma(i \to f)$ is related to the increase of population $\delta n(f)$ in a specific rotational state $|f\rangle$ due to scattering from the prepared initial states $|i\rangle$

$$\delta n(f) \;=\; \sum_{i \neq f} \sigma(i \to f)\;n(i)\;n_T\;F\;l_{cr} \tag{3 3}$$
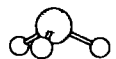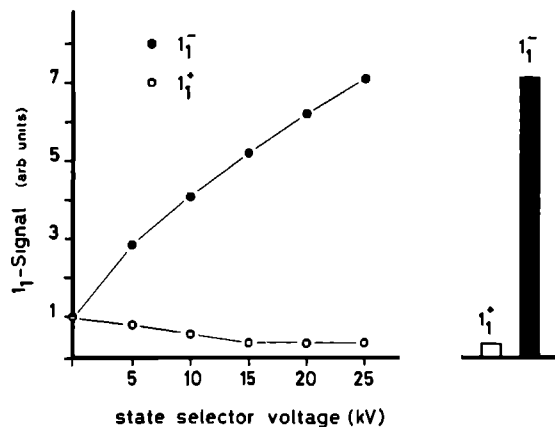
Figure 3.4 : $J_K = 1_1$ *signal as a function of state selector voltage The 1_1^- state molecules are focused, whereas the 1_1^+ state molecules are defocused by the state selection process At a voltage of 25 kV the separation factor of both states is more than 20*

where the summation runs over all initial states contributing to the scattering process, $n(i)$ is the density of NH$_3$ molecules in the initial state $|i\rangle$, n_T the density of the collision partner He or H$_2$, and l_{cr} the length of the collision region

The flux-density transformation F [58] has to be performed because we are monitoring the density of the molecules and not the flux The evaluation of this flux-density transformation in crossed molecular beam experiments is discussed by several authors [58, 59, 60] Recently Sonnenfroh and Liu [60] developed a method to calculate this flux-density transformation in a rather straightforward manner However, the approximations they performed only hold for some special beam set-ups, which is not the case in our experiment A determination of the flux-density transformation for the NH$_3$-He/H$_2$ scattering experiment described in this paper, would require a complete knowledge of the differential state-to-state cross sections $\sigma_{if}(\Omega)$, which are not known at present Joswig et al [58] performed a NO-Ar scattering experiment using a similar experimental set-up as ours Their theory for the NO-Ar scattering provided differential cross sections and they were able to perform the flux-density transformation in a correct way The effect of this transformation on the NO-Ar cross sections was only a minor one In fact they saw a small decrease in cross sections as higher rotational states were populated In the NO-He scattering experiment the contribution from the flux-density transformation is even smaller because of the relative larger center of mass velocity In general, for any heavy projectile - light target collision system, such as the NH$_3$-He/H$_2$ scattering, the laboratory velocity of the heavy (NH$_3$) projectile is merely determined by the center of mass velocity, which of course does not change during the collision Therefore this transformation F is assumed to take on almost the same value for

52

all rotational states in our experiment and is consequently not of importance here because only relative cross sections are determined

As confirmed by several experiments [54, 61] no ortho-to-para conversion is allowed during the collision process That is to say, the nuclear spin of the ammonia molecule cannot be changed during the interaction with the collision partner As a result Equation (3 3) separates into two formulae, one describing the collisions for the ortho ammonia species and the other for the para species Furthermore, in the present experiment for each species only one single state is effectively populated before collisions take place, and consequently the summation in these formulae can be replaced by the contribution of one state only For ortho ammonia we have

$$\delta n(f_o) \;=\; \sigma(0_0^+ \to f_o) \;\; n(0_0^+) \;\; n_T \;\; F \;\; l_{rc} \tag{3 4}$$

and for para ammonia

$$\delta n(f_p) \;=\; \sigma(1_1^- \to f_p) \;\; n(1_1^-) \;\; n_T \;\; F \;\; l_{cr} \tag{3 5}$$

Knowing the increase in population of all ortho and para states $|f_o\rangle$ and $|f_p\rangle$ we can directly derive the corresponding cross sections from these two formulae

The REMPI signal intensity observed for a transition from a specific rotational state $|f\rangle$ to a rotational state $|f'\rangle$ in the resonant intermediate state $\tilde{B}(v')$ is equal to

$$S_{ff'} = n(f) \;\; \mathcal{L}_{ff'} \;\; P_{ff'}^2 \;\; q_{v'} \;\; E_{v'} \tag{3 6}$$

The change of the REMPI signal intensity, due to collisions, is called the scattering signal $\delta S_{ff'}$ and is related to $\delta n(f)$ via

$$\delta S_{ff'} = \delta n(f) \;\; \mathcal{L}_{ff'} \;\; P_{ff'}^2 \;\; q_{v'} \;\; E_{v'} \tag{3 7}$$

In these formulae $\mathcal{L}_{ff'}$ represents the two photon rotational linestrength of the transition, taken from [33], $q_{v'}$ is the Franck-Condon factor for the vibronic transition $\tilde{B}(v') \leftarrow \tilde{X}(v'' = 0)$, where $v' = 0$ or 1, $P_{ff'}^2$ is the square of the laser power at the specific transition frequency and $E_{v'}$ represents the experimental sensitivity determined by the gain of the particle multiplier and the sensitivity of the boxcar In going from the $\tilde{B}(0)$ to the $\tilde{B}(1)$ band, the sensitivity $E_{v'}$ had to be increased because less laser power was available in the $\tilde{B}(1)$ band wavelength region

The collision cross sections can be obtained combining Equations (3 4), (3 5) and (3 7),

$$\sigma(\imath \to f) = \frac{\delta S_{ff'}}{n(\imath) \;\; \mathcal{L}_{ff'} \;\; P_{ff'}^2 \;\; q_{v'} \;\; E_{v'}} \;\; [n_T \;\; F \;\; l_{cr}]^{-1} \tag{3 8}$$

Here $\imath$ denotes the prepared state 0_0^+ in case of the ortho species and 1_1^- for the para species Because we are determining relative cross sections, the last factor in this equation can be omitted to give the following formulae

$$\sigma(0_0^+ \to f) \propto \frac{\delta S_{ff'}}{n(0_0^+) \;\; \mathcal{L}_{ff'} \;\; P_{ff'}^2 \;\; q_{v'} \;\; E_{v'}} \qquad , v' = 0,1, f \in ortho\, NH_3 \tag{3 9}$$

$$\sigma(1_1^- \to f) \propto \frac{\delta S_{ff'}}{n(1_1^-) \;\; \mathcal{L}_{ff'} \;\; P_{ff'}^2 \;\; q_{v'} \;\; E_{v'}} \qquad , v' = 0,1, f \in para\, NH_3 \tag{3 10}$$
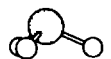
For each rotational state $|f\rangle$ both parity states must be probed by measuring the $\tilde{B}(0)$ and $\tilde{B}(1)$ band. For a comparison of the cross sections involving both parity states, the ratio R is determined,

$$R = \frac{[q_{v'} \quad E_{v'}]_{v'=1}}{[q_{v'} \quad E_{v'}]_{v'=0}} \tag{3 11}$$

The way this calibration is done is explained in the next section

3.3.2 Microwave-UV double resonance calibration experiment.

In our previous work [41] the ratio R was obtained under the assumption that the states 1_1^+ and 1_1^- are equally populated in the primary beam. In order to check this assumption we performed a microwave-UV double resonance experiment. The hexapole state selector was not active in this case. After rotational cooling the NH_3 molecules travel through a microwave cavity in which they are exposed to the microwave field resonant with the 1_1 doublet transition. The molecules in the 1_1^+ state are pumped into the 1_1^- state, and vice versa, due to absorption and stimulated emission of microwave photons. When, before entering the cavity more molecules were present in the 1_1^+ state, the REMPI signal arising from a 1_1^+ state is decreased when microwave power is fed to the cavity, due to a net decrease in density of 1_1^+ state molecules. Similarly, when the laser probes the 1_1^- state, the REMPI signal would increase during microwave irradiation. Indeed we observed an increase of the 1_1^- population and an equal decrease of the 1_1^+ population which means that the 1_1^+ state is more populated after the expansion than the 1_1^- state. Because of overlapping hyperfine transitions due to transit time broadening and the spread in velocity of the NH_3 primary beam molecules, no Rabi oscillations are observed when the microwave power is varied. Instead we observed saturation of the $1_1^{\pm}$ transition with increasing microwave power. From this we conclude that at maximum microwave power the density of molecules in both 1_1 parity states is the same. Thus in case of saturation the density $n_{1_1^{\pm}}$ of $1_1^{\pm}$ state molecules before entering the cavity, is changed by the microwave field into $n_{1_1^{\pm}}^S$,

$$n_{1_1^+}^S = n_{1_1^-}^S = \frac{1}{2} \ (n_{1_1^+} + n_{1_1^-}) \tag{3 12}$$

It follows then,

$$\frac{n_{1_1^+}}{n_{1_1^-}} = 2 \ \frac{n_{1_1^-}^S}{n_{1_1^-}} - 1 = \left[2 \ \frac{n_{1_1^+}^S}{n_{1_1^+}} - 1 \right]^{-1} \tag{3 13}$$

From the experimentally determined saturation values a value for $n_{1_1^+}/n_{1_1^-}$ of 1 33(13) is obtained. The lower 1_1^+ level is overpopulated with respect to the upper 1_1^- level. This factor is larger than the value of 1 14 predicted by the Boltzmann distribution, assuming a rotational temperature of 15 K. From this we may conclude that the relaxation process within one inversion doublet is faster compared to the pure rotational relaxation within a specific K-ladder. We measured the population difference for the 1_1 doublet states at several different beam formation conditions. It turned out that the observed factor 1 33 is not much influenced if the primary backing pressure is varied from 0 5 to 2 bar.

The ratio R is determined by measuring the $^rS(1_1^+)$ transition in the $\tilde{B}(0)$ band and the $^rS(1_1^-)$ transition in the $\tilde{B}(1)$ band. From Equation (3 6) the following equation relating the ratio $n_{1_1^+}/n_{1_1^-}$

with the unknown R is obtained,

$$\frac{n_{1_1^+}}{n_{1_1^-}} = R \frac{S_{rS(1_1^+)}}{S_{rS(1_1^-)}} \frac{\mathcal{L}_{rS(1_1^-)}}{\mathcal{L}_{rS(1_1^+)}} \frac{P^2_{rS(1_1^-)}}{P^2_{rS(1_1^+)}} \tag{3 14}$$

In this equation all quantities are known and thus R can be calculated, taking the value of 1 33 for the ratio $n_{1_1^+}/n_{1_1^-}$ Consequently, in our data analysis we multiply all experimental data from $\bar{B}(0)$ band measurements by this factor R in order to scale them with the results obtained from the $\bar{B}(1)$ band data

3.3.3 Secondary collisions.

A necessary condition for the translation of our experimental scattering data into single state-to-state cross sections is the requirement that during scattering the NH₃ molecules undergo only one collision before they are probed If a second or even more collisions occur, the formulae describing the scattering process would become too complex and a determination of the single state-to-state cross sections $\sigma(0_0^+ \rightarrow J_K^\epsilon)$ and $\sigma(1_1^- \rightarrow J_K^\epsilon)$ is no longer possible Therefore, in order to be sure that we are justified to use the formulae for single collision conditions, elaborate checks upon secondary collision processes have been made The experimental parameter we used to make these checks is the secondary beam density, which is proportional to the stagnation pressure

In case of single collision conditions we may write from Equations (3 4) and (3 5) ,

$$\delta n(J_K^\epsilon) \quad \propto \quad \sigma(\imath \rightarrow J_K^\epsilon) \; n(\imath) \; n_T \tag{3 15}$$

where $\imath$ denotes the initially prepared state

When higher order collision processes are coming up an additional contribution $\delta n^{sec}(J_K^\epsilon)$ to the scattering signal is produced by a second collision

$$\delta n^{sec}(J_K^\epsilon) \quad \propto \quad \sigma(\imath \rightarrow J_K^\epsilon) \; \bar{n}(\imath) \; n_T + \sum_{\imath' \neq \imath} \sigma(\imath' \rightarrow J_K^\epsilon) \; n(\imath') \; n_T \tag{3 16}$$

where, for small effects,

$$\bar{n}(\imath) \quad \propto \quad n(\imath) - \sum_{J_K^\epsilon \neq \imath} \sigma(\imath \rightarrow J_K^\epsilon) \; n(\imath) \; n_T \tag{3 17}$$

and

$$n(\imath') \quad \propto \quad \sigma(\imath \rightarrow \imath') \; n(\imath) \; n_T \tag{3 18}$$

It follows that as soon as higher order collision processes come into play, the scattering signal includes terms proportional to n_T^2 and is no longer linearly proportional to the secondary beam density

In order to determine the maximum allowable secondary beam density for single collision conditions we carefully checked the dependence of the scattering signal upon the backing pressure of the secondary beam We made this check for both collision partners He and H₂ and for scattering of NH₃ into several rotational states In Figure 3 5 the behaviour of some rotational states J_K is demonstrated under variation of the stagnation pressure with H₂ as collision partner From the figure

we conclude that as long as the H_2 stagnation pressure is below 400 Torr (1 Torr = 1.32 mbar), we are working in the linear regime and secondary collisions can be neglected. For He this critical pressure is somewhat higher. From these results we decided to measure our scattering spectra at a secondary stagnation pressure of 300 Torr for H_2 and 400 Torr for He.
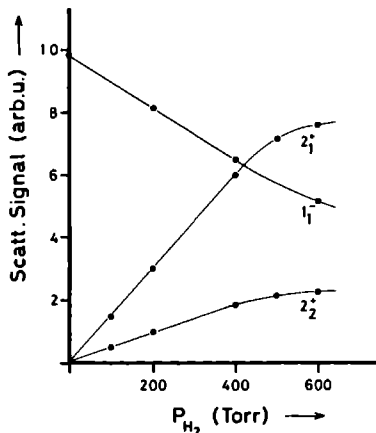
Figure 3.5 : *Linearity check of the scattering signal with secondary H_2 backing pressure for some rotational states J_K^c. Secondary collisions are showing up at pressures higher than 450 Torr. For H_2 the actual scattering experiments are performed at a pressure of 400 Torr.*

We performed a second check for secondary collisions by varying the interaction length of the collision process. To this purpose the laser focus is moved in three dimensions through the scattering region. For instance, if the focus is in the plane of the two molecular beams we can translate the laser focus, and thus the probe volume, along the primary beam axis, starting at a position closest to the primary nozzle. Due to the well defined geometry of the scattering region no scattering signal is observed at first instance; by moving the focus towards the secondary beam axis, the probe volume enters the scattering region and an increase of the scattering signal is observed. We recorded several scattering spectra at different positions in the scattering region and all spectra showed the same intensity distribution. This again is a strong indication that no higher order collision processes are disturbing our measurements.

3.4 Results and interpretation.

3.4.1 Scattering spectra.

In Figure 3.6 typical scattering spectra of the $\tilde{B}(0)$ and $\tilde{B}(1)$ bands are shown for collisions with H_2 when the state selector is active. Both spectra are recorded in the baseline subtraction mode (BSM). For some of the lines the ground state J_K^c identification is given. The upper part of the

figure shows the $\bar{B}(0)$ scattering spectrum One can see a strong increase of most para lines due to scattering into these states from the electrostatically prepared 1_1^- state Also the 1_1^+ state gains population due to scattering from the 1_1^- state, which is reflected in a positive scattering signal for the 1_1^+ transitions However, the 1_1^+ scattering intensities obtained from these spectra are not reliable, due to overload of the boxcar integrator at the strong absolute 1_1^+ signals when operating in BSM mode
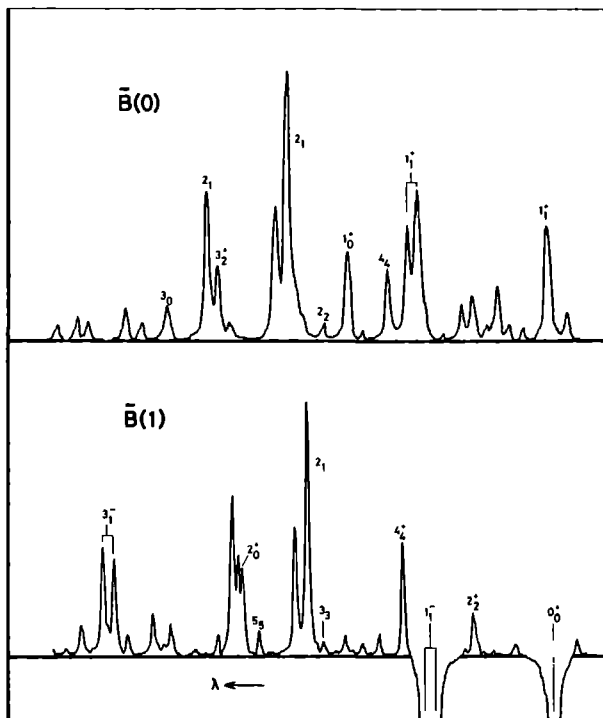
Figure 3.6 : *H$_2$ scattering spectra of the $\bar{B}(0)$ and $\bar{B}(1)$ band with the state selector operating at 25 kV All lines can be clearly identified For some of them the rotational quantum numbers are given A positive signal represents scattering into a specific state J_K^t, a negative signal corresponds with scattering out of the prepared 0_0^+ and 1_1^- states*

The lower part of the figure shows the $\tilde{B}(1)$ scattering spectrum One can clearly see the decrease of 1_1^- and 0_0^+ population due to scattering out of these initially prepared states, which is now reflected in a negative BSM signal for the transitions originating at the 1_1^- and 0_0^+ levels A check for elastic scattering out of the 1_1^- and 0_0^+ states can now be made In order to be sure that elastic collision processes do not influence the scattering results, we performed careful absolute measurements on the ortho- and para-NH$_3$ scattering signals Next we compared the decrease
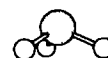
of $0_0^+(1_1^-)$ population with the (measured) increase of all other ortho (para) populations. Good agreement was obtained for this balance for both ortho and para populations to within 8 % . From this we may conclude that there are as many molecules elastically scattered into the detection area as there are molecules scattered out of this zone. Throughout the experiment the UV power is recorded simultaneously. After correcting the scattering signal δS for the quadratic UV power dependence and the two-photon linestrength $\mathcal{L}_{ff'}$, the cross sections $\sigma(0_0^+ \to J_K^\epsilon)$ and $\sigma(1_1^- \to J_K^\epsilon)$ are obtained according to Equations (3.9) and (3.10) .

The scattering signals $\delta S_{ff'}$ are measured by averaging several BSM spectra, recorded under the same experimental conditions. By recording several lines originating at the same J_K^ϵ rotational state two or more independent values for a specific cross section $\sigma(i \to J_K^\epsilon)$ are obtained. These values are also averaged and, as a result, the experimental error is merely determined by the standard deviation in these averages. For most data an experimental error of 10 % can be specified. However, for some para rotational states a somewhat larger statistical uncertainty in the cross sections of about 20 % arises, due to the fact that for the para-NH_3 measurements the state selector is inserted between the primary nozzle and the scattering center and hence the absolute signals are not as strong as for ortho-NH_3.

In the following we discuss two types of experiments. In the first type of experiment the hexapole state selector is not used and the two 1_1 parity states are both prepared. In comparing our new data with the old ones [41] we observed deviations for some cross sections, which will be discussed. The second experiment deals with the hexapole state selection. New state-to-state cross sections for rotational excitation of para-NH_3 will be presented and discussed.

3.4.2 State-to-state cross sections.

Without electrostatic state selection the state preparation is similar to the one applied in our previous work [41]. The two 1_1 parity states are both present in the scattering center and the population changes measured for the para-NH_3 species are actually the result of two different cross sections,

$$\delta n(J_K^\epsilon) \quad \propto \quad \left[\sigma(1_1^+ \to J_K^\epsilon) \cdot n(1_1^+) + \sigma(1_1^- \to J_K^\epsilon) \cdot n(1_1^-)\right] \cdot n_T \tag{3.19}$$

In [41] it was assumed that after rotational cooling in the expansion both 1_1 parity states are equally populated, and the calibration of the $\tilde{B}(0)$ band on the $\tilde{B}(1)$ band was based on this assumption. However, in section 3.2 we showed that the lower 1_1^+ state is 33 % more populated than the upper 1_1^- state. Since the primary beam in both experiments is produced under nearly identical conditions it may be assumed that the same overpopulation in the 1_1^+ state was present in the previous experiment [41], which means that the reported cross sections have to be corrected. Furthermore, for the para-NH_3 species, Equation (3.19) has to be used with $n(1_1^+)$ set equal to $1.33 \cdot n(1_1^-)$,

$$\delta n(J_K^\epsilon) \quad \propto \quad \left[1.33 \cdot \sigma(1_1^+ \to J_K^\epsilon) + \sigma(1_1^- \to J_K^\epsilon)\right] \cdot n(1_1^-) \cdot n_T \tag{3.20}$$

We remeasured the data with both 1_1 parity states prepared in the scattering center, i.e. with no state selection active. However, a comparison with the previous data showed still considerable discrepancies for several cross sections. Despite elaborate efforts we did not succeed in finding the origin of the observed deviations. As described in Chapter 2 the previous set-up was different from the present one. The beam skimmers used now provide a better definition of the scattering volume. Measurements under many different collision conditions, in some of which also secondary collisions

by the Ar atoms in the primary beam were considered, yielded results which are consistent with the present data. We also checked the effects of impurities in the secondary beam gas supply. It turned out that only the presence of a relatively large amount of polar molecules such as H_2O, in the secondary beam could explain the previous results, a supposition which seems very unlikely. As will be discussed in the next chapter the present data on He collisions are in reasonably good agreement with the results of Meyer et al. [15]. We conclude that the old measurements should be discarded.

	Ortho-NH₃; $\sigma(0_0^+ \to J_K^\epsilon)$				Para-NH₃; $\sigma(1_1^- \to J_K^\epsilon)$		
J_K^ϵ	Billing et al [42] 524 cm⁻¹	Meyer et al [15] 789 cm⁻¹	present results 435 cm⁻¹	J_K^ϵ	Billing et al [42] 524 cm⁻¹	Meyer et al [15] 789 cm⁻¹	present results 435 cm⁻¹
1_0^+	4 75	1 01	2 00	2_1^+	4 58	3 162	2 72
2_0^+	6 20	5 16	4 53	2_1^-	3 23	0 860	2 62
3_0^+	1 37	1 03	1 29	3_1^-	1 91	1 931	1 62
4_0^+	0 59	0 50	0 53	3_1^+	0 670	0 693	0 86
6_0^+	-	-	0 38	4_1^+	0 248	0 293	0 31*
3_3^-	2 69	6 68	4 11	4_1^-	0 366	0 419	0 69
3_3^+	0 04	0 00	1 30	2_2^+	1 12	3 121	2 55
4_3^+	0 04	0 00	0 62	2_2^-	0 026	0 0007	0 59
4_3^-	3 16	4 48	3 46	3_2^-	0 449	0 930	1 00
6_6^+	-	1 15	0 59	3_2^+	1 28	1 887	1 34
6_6^-	-	0 00	-	4_2^+	0 443	0 263	-
				4_2^-	0 551	0 763	0 69*
				4_4^+	2 04	3 073	2 27
				4_4^-	0 960	0 500	0 65
				5_4^-	-	0 063	0.38*
				5_4^+	-	1 753	0 83
				5_5^-	-	0 942	0 45*
				5_5^+	-	0 006	0 21*

Table 3.1 : *Relative state-to-state cross sections for NH₃-He collisions The experimental error is 10% Cross sections marked with an asterisk have an error of 20%*

The inelastic collision cross sections for NH₃-He and NH₃-H₂ obtained in this study are presented in Tables 3.1 and 3.2. The first table gives the state-to-state cross sections for rotational excitation of ortho- and para-NH₃ with He as collision partner, whereas in Table 3.2 the H₂ scattering results are presented. Results from several theoretical studies are also given For the helium scattering a comparison is made with calculated values of Billing et al. [42] and experimentally modelled values of Meyer et al. [15]. For the H₂ scattering the present data are compared with the

Ortho-NH$_3$; $\sigma(0_0^+ \to J_K^\epsilon)$				Para-NH$_3$; $\sigma(1_1^- \to J_K^\epsilon)$			
J_K^ϵ	Ebel et al [44] 604 cm^{-1}	Offer and Flower [47] 604 cm^{-1}	present results 596 cm^{-1}	J_K^ϵ	Ebel et al [44] 604 cm^{-1}	Offer and Flower [47] 64 cm^{-1}	present results 596 cm^{-1}
1_0^+	13.82	15 9	12.1	2_1^+	2 13	3 33	2 72
2_0^+	3 94	5.31	5 33	2_1^-	5 38	5.30	5 69
3_0^+	1.86	1.34	2 72	3_1^-	0 95	-	2 15
4_0^+	0 36	0.61	0.70	3_1^+	0 97	-	1 03
6_0^+	0.06	-	0 40	4_1^+	0 22	-	0 43*
3_3^-	7.63	3.63	2 69	4_1^-	0 43	-	0 76
3_3^+	0 000	1.79	3.18	2_2^+	2 47	0 82	0 79*
4_3^+	0.000	0 84	1.12	2_2^-	0 004	0 56	0 79*
4_3^-	3.91	2 15	3 32	3_2^-	0.86	-	0 76
6_6^+	-	-	-	3_2^+	1.27	-	0 93
6_6^-	-	-	-	4_2^+	0 364	-	-
				4_2^-	0 637	-	0.53*
				4_4^+	3 148	-	1 59
				4_4^-	0 351	-	0 89
				5_4^-	0.131	-	0 69
				5_4^+	1 042	-	0.63*
				5_5^-	0.473	-	0 23*
				5_5^+	0 004	-	0 17

Table 3.2 : *Relative state-to-state cross sections for NH$_3$-H$_2$ collisions The experimental error is 10%. Cross sections marked with an asterisk have an error of 20%*

results of Ebel et al. [44] and the calculations of Offer and Flower [46, 47].

So far we have not yet performed calibration measurements in order to obtain absolute cross sections, as pointed out in section 3.1 . Consequently all data presented in Tables 3.1 and 3.2 are relative values, normalized in such a way that the sum of the cross sections for ortho-NH$_3$, as well as for para-NH$_3$, is the same for experiment and theory.

For the H$_2$ scattering we were not yet able to separate the ortho from the para hydrogen. This will be done in a future experiment. As a result, we cannot distinguish between the collision effects of both species. Due to the rotational cooling during the expansion, only the $J = 0$ state for para-H$_2$ and the $J = 1$ state for ortho-H$_2$ and to a small amount (< 1 %) the $J = 2$ (para) state are populated in the secondary beam. Because theory gives cross sections for scattering with H$_2$ ($J = 0$) and H$_2$ ($J = 1$) separately, these cross sections must be averaged with nuclear statistical weights 1:3 for the para:ortho species in order to obtain a value which can be compared with the experimental results. These weighted calculated cross sections for NH$_3$-H$_2$ are presented in Table

3 2

Furthermore, in our experiment the collision energy is 435 cm^{-1}for NH$_3$-He and 596 cm^{-1}for NH$_3$-H$_2$ scattering, whereas theoretical studies use different energies, as can be seen in Tables 3 1 and 3 2 Although the relative inelastic collision cross sections are not expected to vary drastically with collision energy, one must be careful comparing our experimental results and the corresponding theoretical values

3.5 Discussion.

Based on symmetry arguments, collision theory for the NH$_3$-He and NH$_3$-H$_2$ systems predicts that the cross sections for parity conserving transitions as well as those for parity changing transitions are the same [40, 42]

$$\sigma(1_1^+ \rightarrow J_K^+) = \sigma(1_1^- \rightarrow J_K^-) \qquad (3\ 21)$$

$$\sigma(1_1^+ \rightarrow J_K^-) = \sigma(1_1^- \rightarrow J_K^+) \qquad (3\ 22)$$

Because we prepare only the $J_K^\epsilon = 1_1^-$ parity component of the 1_1 doublet, this theoretical statement cannot be proved in this experiment Attempts to prepare the 1_1^+ state as well by pumping all electrostatic prepared 1_1^- state molecules into the 1_1^+ state, in a microwave field resonant on this 1_1 doublet transition, were not successful For this purpose the microwave cavity had to be positioned directly behind the state selector Although 1_1^- state molecules were effectively pumped into the 1_1^+ state, it was not possible to create a complete population inversion between the two 1_1 states, probably because the TM$_{01}$ microwave radiation was entering the state selector and disturbed the focusing efficiency of the state selection process

A second problem, causing our state-to-state scattering experiment not to be an ideal one, is the fact that the initial state preparation for the ortho-NH$_3$ is not as good as for the para species Together with the 0_0^+ state molecules, a small amount of 1_0^+ state molecules (about 8 %) is still present in the primary beam Scattering out of this 1_0^+ state can give a certain contribution to the scattering signals $\delta n(f)$ However, assuming the absolute cross sections for scattering out of the 1_0^+ state being in the same order of magnitude as the cross sections for scattering out of the 0_0^+ state, the contribution to the scattering signal arising from scattering out of the 1_0^+ state is estimated to be at most 10 % of the 0_0^+ state scattering, which is within the experimental accuracy

3.5.1 NH₃-He results.

In Figure 3 7 the cross sections, both experimental and theoretical, are presented graphically for the NH$_3$ He experiment At the collision energy of 435 cm^{-1}excitation of rotational states up to $J_K = 6_6$ can be observed For every J_K, except for the $K = 0$ states, two bars are plotted for the two parity states The height of the bars gives the magnitude of the corresponding cross sections Also plotted are the calculated values of Meyer [15] and Billing [42] As can be seen from the figure, apart from the parity propensity rules there is a reasonably good qualitative agreement between both calculations and our experiment For the ortho-NH$_3$ indeed we measure the $\sigma(0_0^+ \rightarrow 2_0^+)$ to be larger than $\sigma(0_0^+ \rightarrow 1_0^+)$, as theory predicts The experimental ratio of both cross sections is in between both calculated values Meyer et al use a relatively high collision energy of 789 cm^{-1}and probably this is the reason that their results are in favour of the high $J_K = 3_3, 4_3$ excitations, whereas the cross section for collisional excitation into the lower $J_K = 1_0$ state is less pronounced than in the calculations of Billing and in our experiment Also for para-NH$_3$ the pure rotational

(i.e. parity averaged) energy transfer measured in our experiment is fairly well in agreement with theory.
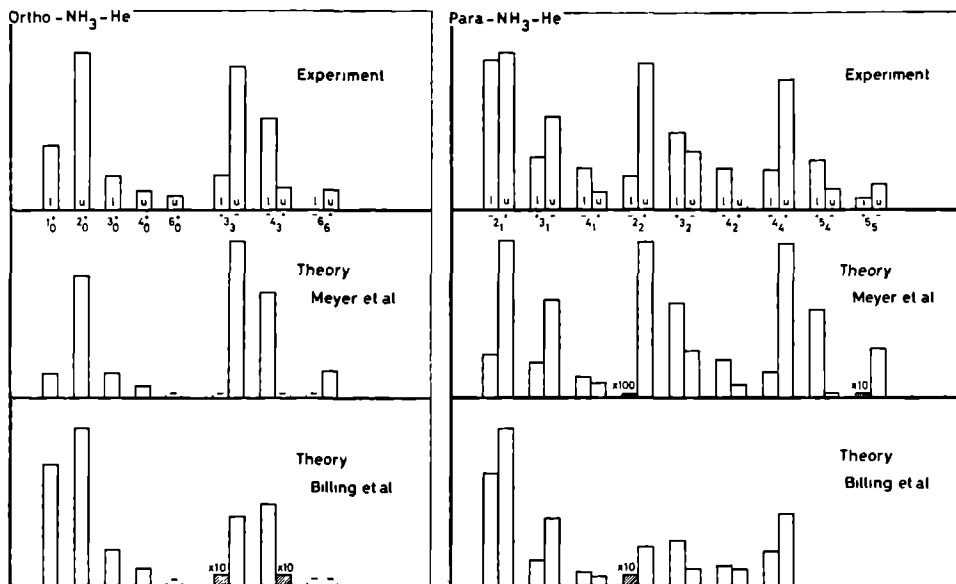
Figure 3.7 : *Relative state-to-state cross sections* $\sigma(0_0^+ \rightarrow J_K^\epsilon)$ *for scattering of ortho-* NH_3 *and* $\sigma(1_1^- \rightarrow J_K^\epsilon)$ *for scattering of para-NH_3 by He. Each bar corresponds with one rotational state* J_K^ϵ *The character l(u) denotes the lower (upper) level of the* J_K *doublet. The experimental results are compared with theoretical values from Meyer et al [15] and Billing et al. [42]*

Deviations show up when one considers how the probability of rotational excitation is shared between the two parity states belonging to a specific J_K rotational level. Theory predicts strong parity propensity rules. For example, for the $J_K = 2_2$ rotational level the $1_1^- \rightarrow 2_2^+$ collisional excitation has a high probability whereas the $1_1^- \rightarrow 2_2^-$ excitation is almost forbidden by theory. However, we still see a considerable contribution to our scattering spectra arising from collisional excitation into this 2_2^- state, even comparable in magnitude with the $1_1^- \rightarrow 2_2^+$ scattering signal. The same is true for ortho-NH_3. Here the parity propensity rule concerning the $J_K = 3_3$ and 4_3 levels does not show up so strongly in our experiment, as we would expect from theory. For all measured transitions a weak parity propensity is observed but it is much less pronounced than predicted by theory.

The reason that the two calculations yield different results is not only the difference in collision energies. In the calculations of Billing only 524 cm^{-1} can be transferred from kinetic energy of both collision partners into internal energy of the NH_3 molecule. The 789 cm^{-1} available in the calculations of Meyer, favours excitation of higher J_K rotational states. Apart from collision energies, both

theoretical frameworks are essentially different For the dynamical scattering calculations Meyer et al apply the coupled states approximation, using an intermolecular potential fitted to measured data, whereas Billing et al use a semiclassical approach to the problem Furthermore, the intermolecular potential used for the NH_3-He scattering calculations is different in both theories Although the same SCF repulsive part of the potential [43] is used, different numerical techniques are applied in connecting the short-range part of the potential with the long-range part

For both ortho- and para-NH_3 theory predicts a strong propensity towards parity-index changing transitions for some $|\Delta K| = 3$ excitations A possible explanation for the fact that in this experiment this propensity rule is not obeyed could be the tunneling motion within the NH_3 molecule causing it not to be rigid Up to now, all theoretical approaches neglect the tunneling motion of the NH_3 molecule in describing the interaction potential, as was first pointed at in a paper of Davis and Boggs [50] The tunneling motion is included only in the description of the molecular wavefunctions as a symmetric or antisymmetric combination of two symmetric top wavefunctions, centered at the equilibrium position of the nitrogen nucleus The justification of this simplification is based on the assumption that during the collision interaction, which lasts about 10^{-12} seconds (interaction length $\approx 10\AA$), the NH_3 molecule is regarded as a rigid rotor in which the 50 % probability to find the 3 H-atoms on either side of the N-atom is conserved during $\approx 4 \ 10^{-11}$ sec The experimental results that the parity propensity rules are much less pronounced than predicted by theory, may indicate that the intermolecular potential should include the inversion motion explicitly in order to correctly describe the physics of these collision processes

3.5.2 NH₃-H₂ results.

In Figure 3 8 the cross sections from the NH_3-H_2 collision experiment are plotted in the same manner as for the NH_3-He scattering Comparing the experimental results with the calculations of Ebel et al [44] we see that the agreement is not as good as for the NH_3-He scattering experiment As can be seen, the strong parity propensity rules predicted for the $J_K = 3_3, 4_3$ and $2_2, 5_5$ states, are not reflected in our experiment The cross sections obtained by Ebel et al [44] were calculated using the coupled states approximation In this CS framework some parity cross sections are per definition zero, yielding an incorrect distribution of the $i \rightarrow J_K$ rotational excitation probability among the two parity substates J_K^ϵ When however the summed cross sections $\sigma(i \rightarrow J_K^+) + \sigma(i \rightarrow J_K^-)$ are considered, we conclude that, except for the $J_K = 3_1, 4_1$ and 2_2 states, the agreement between calculated and experimentally determined parity averaged cross sections is reasonably good The deviations are smaller than 25%

The theory behind the NH_3-H_2 calculations differs from the NH_3-He theory principally in two aspects First of all the dynamical scattering calculations for the NH_3-H_2 system demand much more computational efforts than the NH_3-He system Due to the internal degrees of freedom of the hydrogen molecule many more entrance channels are contributing to the coupled states scattering calculations in order to get reliable cross sections Furthermore, the interaction potential for the NH_3-H_2 system is more complex than the NH_3-He system, because of the rotation of the hydrogen molecule itself during the collision interaction, which introduces two extra coordinates in describing the potential

Comparing theory with experiment we notice that most of the calculated cross sections which show poor agreement, represent a $|\Delta K| = 3$ excitation, which corresponds to a rotational excitation around the $C_{3v}(D_{3h})$ symmetry axis of the NH_3 molecule Usually the intermolecular potential is expressed in a product series of two spherical harmonics, one describing the orientation of the

63
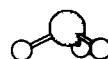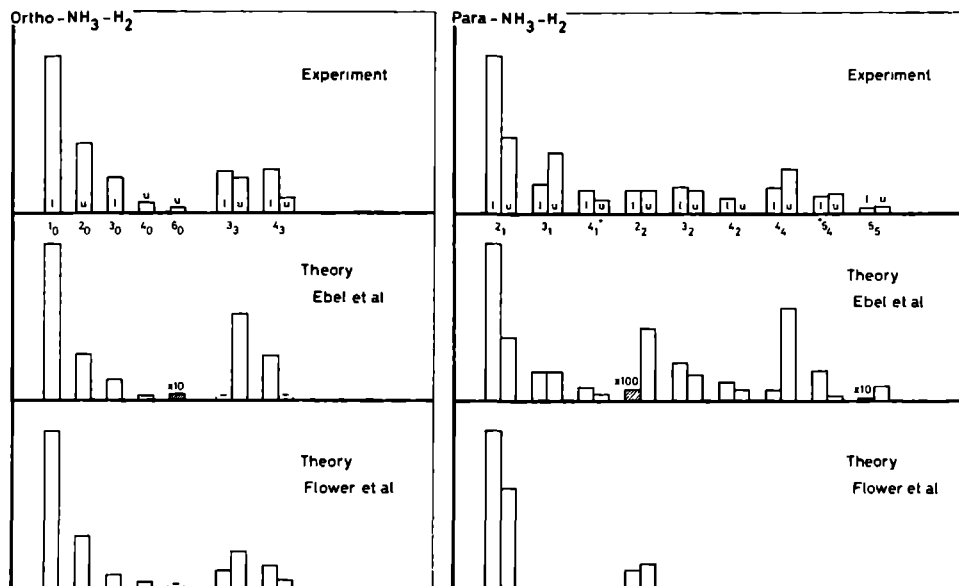
Figure 3.8 : *Same as Figure 3 7, but for NH_3-H_2 Theories are from Ebel et al [44] and Offer and Flower [46, 47]*

hydrogen molecule and the other describing the orientation of the NH_3 molecule with respect to a space-fixed axes system It is shown by Offer and Flower [46, 47] that this description is not correct since terms are neglected which describe the ϕ orientation of both the NH_3 and the H_2 molecule Presuming the potential terms describing the internal orientation of the NH_3 molecule give rise to the $|\Delta K| = 3$ excitations just mentioned, it is obvious that theory cannot fully account for the $|\Delta K| = 3$ collisional excitations we observe in the experiment

Offer and Flower performed close coupling calculations for the NH_3-H_2 collision system, in which they expand the potential in a correct way They described the orientation of the NH_3 molecule not by means of a spherical harmonic, but by a Wigner rotation matrix $D_{KM}^{(J)}(\alpha, \beta, \gamma)$, thus taking into account the complete set of Euler angles (α, β, γ), specifying the orientation of the NH_3 molecule Also terms in the potential describing the rotation of the H_2 molecule around the intermolecular axis were properly taken into account Their results are also given in Figure 3 8 As can be seen, the strong parity propensity rule for the $|\Delta K| = 3$ cross section $\sigma(1_1^- \rightarrow 2_2^\pm)$ predicted by Ebel et al is no longer valid Offer and Flower calculated the cross sections only for $1_1^- \rightarrow 2_1^\pm, 2_2^\pm$ collisional excitation We contacted Dr Flower for calculating the remaining cross sections for the para-NH_3 species, but due to intensive (computer)time consuming calculations it was not possible to get these results In order to make a comparison with the close coupling calculations possible for all cross sections that can be measured, we are preparing now measurements at lower collision

energies

3.6   Conclusions

We obtained the first parity resolved state-to-state cross sections for rotational excitation of para-NH$_3$ by He and H$_2$ In a crossed molecular beam experiment preparation of the 1_1^- state is achieved by rotational cooling, followed by electrostatic state selection in a hexapole electric field In addition, improved values were obtained for the state-to-state cross sections of ortho-NH$_3$ Probing of the rotational state distribution before and after collisional excitation by 2+1 REMPI spectroscopy via the electronic $\tilde{B}$ state of NH$_3$ has proven to be a sensitive detection technique We performed careful checks for secondary collision processes A linear behaviour of the scattering signal with the secondary backing pressure indicated that only single collisional events are contributing to the scattering process

In a comparison of the experimental cross sections with theoretical values from quantum scattering calculations a reasonably good agreement is obtained for the rotational excitation in He scattering, whereas for the H$_2$ scattering deviations show up The preparation of only one single parity state for ortho- as well as for para-NH$_3$ made it possible to investigate the parity propensity rules predicted by theory In general the experiment shows only a weak propensity, indicating that theory still needs further improvement in order to describe these scattering experiments in a correct way

Preparations are under way to separate ortho- and para H$_2$ in order to obtain inelastic rotational cross sections for NH$_3$ – ortho H$_2$ and NH$_3$ – para H$_2$ scattering, which should provide interesting input for theoretical studies on the complex NH$_3$-H$_2$ scattering system

3.7   Acknowledgement

Chapter 4
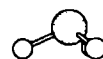
State-to-State Cross Sections
For Rotational Excitation Of Ortho And Para NH$_3$
By Collisions With Ortho and Para H$_2$
—
Experiment versus Theory

J Schleipen and J J ter Meulen
Department of Molecular and Laser Physics, University of Nijmegen,
Toernooiveld, 6525 ED Nijmegen, The Netherlands

A R Offer
Sterrewacht Leiden, Huygens Laboratory, University of Leiden,
P O Box 9513, 2300 RA Leiden, The Netherlands

State-to-state cross sections for inversion-rotational excitation of ortho and para- NH$_3$, colliding with para-H$_2$, have been obtained in a crossed molecular beam experiment State preparation of the 0_0^+ state for ortho-NH$_3$ and the 1_1^- state for para-NH$_3$ is achieved by adiabatic expansion of ammonia followed by electrostatic state selection in a hexapole electric field The NH$_3$ rotational state distribution is probed by 2+1 REMPI spectroscopy via the $\tilde{B}$ state From a comparison with previous NH$_3$-normal-H$_2$ scattering results relative cross sections are obtained for both NH$_3$-para-H$_2$ and NH$_3$-ortho-H$_2$ collisions The experimental values are compared with the results from close coupling and coupled states calculations using ab initio potentials It is demonstrated that the collisional behaviour of para-H$_2$ is strongly different from the scattering by He
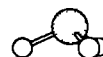
4.1 Introduction

In Chapter 3 we reported the study of rotational excitation of the NH_3 molecule in collision with helium and molecular hydrogen. Many experimental and theoretical studies have been performed to obtain inelastic cross sections and collision rates for these collision processes. Several experimental methods were applied such as the microwave double resonance technique [10], line broadening experiments [9], the molecular beam maser [14], IR-IR [12] and IR-UV [13] double resonance relaxation measurements and differential TOF measurements [15]. As already mentioned in Chapter 1 of this thesis we use the laser crossed molecular beam method in order to obtain single state-to-state inelastic cross sections for the collision systems under study. Theoretical state-to-state collision rates and cross sections have been calculated semi-classically [48, 63] and quantum mechanically in the coupled states approximation [44] and the exact close coupling formalism [45, 46, 47]. The accuracy of these calculations is mainly determined by two factors. Firstly, the rotational excitation of NH_3 in collisions with H_2 involves the complex dynamics of two rotating interacting nuclear frames, which are treated as rigid rotors. In fact the ammonia molecule is a floppy molecule and the accuracy of the collision calculations depends on the extent to which the NH_3 inversion motion, along with the higher rotational levels of both molecules can be neglected. The second item determining the reliability of the scattering calculations is the accuracy with which the intermolecular potential describing the interaction between the two colliding molecules is known. This potential energy surface is often constructed from theoretical ab initio calculations. Detailed collision experiments can give an important contribution to the understanding of the collision dynamics and provide valuable information on the intermolecular potential involved in the scattering event.

Apart from the knowledge we obtain from these collision experiments about the intermolecular potential, there is a considerable interest in the collision cross sections from astrophysicists. In 1968 interstellar NH_3 was detected for the first time by Cheung et al [1]. They observed microwave emissions arising from the metastable $J_K = 1_1$ and 2_2 rotation inversion doublets in the vibrational ground state of NH_3. In a second paper [5] they pointed out that the observed emission intensities of these metastable lines are inconsistent with a single rotational temperature. Furthermore this rotational temperature was found to be smaller than the kinetic temperature of the emitting NH_3 gas cloud. In the years thereafter observations of higher J_K inversion transitions were reported [65] up to rotational excitations of the high $J_K = 11_9$ level [66] which should not even be populated at interstellar temperatures of 10 300 K. In 1983 Walmsley and Ungerechts [67] predicted from theoretical arguments that under certain interstellar conditions the $J_K = 3_3$ transition can show maser activity. Only two months after this publication Guilloteau et al [68] observed maser emission from the NH_3 $J_K = 3_3$ inversion doublet in the interstellar source DR21. This observation was followed by many others reporting maser activity in the metastable level $J_K = 3_3$ [69] and the non-metastable levels $J_K = 9_6$ and 6_3 [70] and $J_K = 5_4, 7_5, 9_8$ and 10_8 [66].

The anomalous emission arising from high J_K inversion transitions and the maser activity in some of these levels, show clearly that the emitting NH_3 molecule cannot be in thermal equilibrium with its environment and is disturbed by some kind of inversion-rotation cooling or pumping mechanism. The generally accepted model used nowadays to explain this non-thermal emission of interstellar ammonia is based on three different physical processes. 1 thermal relaxation of excited J_K levels, 2 (IR) pumping of the thermally relaxed levels, and 3 rotational excitation or relaxation due to collisions with the abundant molecular hydrogen. The dipole allowed transitions $\Delta K = 0, \Delta J = \pm 1$ result in thermal relaxation of population inside a specific $|K|$-manifold. The

Einstein coefficients for this spontaneous decay process are in the order of $0.1\ s^{-1}$ and hence is a fast process in comparison with the collision induced transitions among the individual $|K|$-manifolds having collision rates of typically $10^{-7}\ s^{-1}$ As a result all $J > |K|$ molecules accumulate in the $|K| = J$ metastable levels In order to calculate the NH_3 level populations resulting from these different relaxation and excitation processes, a set of rate equations has to be solved, known as the *equations of statistical equilibrium* [71] For this purpose reliable state-to-state collision cross sections are needed One of the outcomes of these calculations is the relationship between rotational temperature of the NH_3 molecule and the collision energy Once knowing the rotational temperature from observations the kinetic temperature of the interstellar gas cloud can be calculated In order to explain the maser activity in some of the NH_3 rotation inversion doublets, a parity selective pump mechanism must be responsible for selectively populating the upper inversion levels Assuming the collisions with H_2 are responsible for this pump mechanism, parity resolved state-to-state cross sections are required for the NH_3-H_2 collision system

Molecular hydrogen consists of two species para-H_2 having nuclear spin $I = 0$ and ortho-H_2 with nuclear spin $I = 1$ In astrophysics it is generally believed that the H_2 molecules are produced in a 3 1 ortho to para ratio From then on, magnetic interactions such as reactions with interstellar ions H^+, H_3^+ and HCO^+ are responsible for a conversion from the ortho- to the para-H_2 species, until thermal equilibrium is reached for the low kinetic temperatures ($T \stackrel{<}{\sim} 100K$) in interstellar clouds The time constants belonging to these conversion processes are estimated from calculations [72, 73] The study of collisional induced rotational excitation of NH_3 by the two H_2 species in an interstellar cloud reveals information on the ortho to para H_2 density ratio As a result, knowing the relative ortho- to para-H_2 ratio in an interstellar cloud at present and assuming the 3 1 ortho-to para-H_2 ratio is correct when the cloud was formed, it is possible to estimate the age of such cloud

Ground state para-H_2, with zero total angular momentum, behaves very differently as a collision partner in NH_3-H_2 collisions than rotationally excited para-H_2 The leading long range term in the intermolecular potential for NH_3-H_2 is the dipole-quadrupole interaction which falls off as R^{-4} In the case of ground state para-H_2 collisions this contribution vanishes, and as a result, the dipole allowed transitions of NH_3 ($\Delta k = 0, \Delta j_1 = \pm 1$) might be expected to be less likely in NH_3 ground state para-H_2 collisions than in collisions with rotationally excited H_2 (In this chapter we designate the total angular momentum of the NH_3 molecule by j_1, its projection on the NH_3 symmetry axis by k and the total angular momentum of the H_2 molecule by j_2) In addition, because ($j_2=0$)-para-H_2 is spherically symmetric, terms in the potential which depend on the orientation of the H_2 molecule do not contribute directly to the scattering (at least if the H_2 molecule remains in the $j_2=0$ state) This can lead to qualitative differences in the behaviour of the NH_3 rotational transitions induced by collisions with ortho-H_2 and ground state para-H_2 For example, the recent quantum calculations of Offer and Flower [46] predict that there is a strong parity propensity for the $j_1 k \epsilon = 00+ \rightarrow 33-$ transition when para-H_2 is the collider whereas for ortho-H_2 a weak propensity is expected for excitation to the 33+ state Once knowing the inelastic cross sections for the NH_3 para-H_2 and NH_3-ortho-H_2 collision system a comparison between experimental and theoretical results may indicate which potential energy terms are important for the rotational excitation of the NH_3 molecule yielding a more complete picture of the intermolecular potential

Due to the absence of a dipole-quadrupole interaction when ground state para-H_2 ($j_2=0$) is the collider, ($j_2=0$)-para-H_2 is often considered to be equivalent to a He atom and the collision effects induced by ($j_2=0$)-para-H_2 are believed to be similar to those induced by helium Green [29, 40]
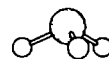
performed quantum scattering calculations on the NH_3-He collision system and obtained state-to-state collision rate coefficients at different kinetic temperatures Often this work on NH_3-He scattering is referred to in astrophysical papers and the NH_3-He inelastic collision rate coefficients are used in the rate equations describing the NH_3-H_2 collision process In this study we show that for some NH_3 rotational levels ground state para-H_2 behaves very differently from helium, which may have important astrophysical consequences

In this study we present parity resolved state-to-state inelastic cross sections for rotational excitation of the NH_3 molecule in collisions with ortho- and para-H_2, obtained from experiment and theory The experimental values were obtained using a molecular beam machine in combination with a state selective laser detection technique The quantum scattering calculations involved solving the close coupled and coupled states equations for the NH_3-H_2 collision system using ab initio intermolecular potentials In section 2 the experiment is described briefly In section 3 the quantum scattering calculations are described in detail Section 4 presents the experimental and theoretical cross sections and the two sets of data are compared and discussed in section 5 In section 6 we finish with some conclusions

4.2   Experimental

The experiment has been described in detail in Chapters 2 and 3 of this thesis Two pulsed molecular beams are crossed at right angles The primary NH_3 molecular beam is produced by expanding a 1 % NH_3 in Ar mixture into vacuum with a backing pressure of 1 bar The vacuum pressure during operation of both valves does not exceed 1 10^{-5} mbar Initial state preparation is achieved by rotational cooling of the NH_3 molecules during the expansion, followed by state selection in an electrostatic hexapole field For ortho-NH_3 90 % of all population is in the ground state $j_1k\epsilon = 00+$, whereas for para-NH_3 almost 95 % of all population is contained in the $11-$ state In this way we succeed in preparing only one rotational state in the scattering volume for each NH_3 species Due to collisions with the secondary beam molecules translational energy is transferred to rotation of the NH_3 molecules and higher rotational states of the ammonia molecule become populated

The secondary beam is operated with a backing pressure of 500 mbar and is produced in a differentially pumped vacuum chamber This secondary target beam consists of molecular hydrogen with a well determined ortho- to para-H_2 ratio Both beams are skimmed in order to get a well defined scattering volume of $\approx$ 8x8x8 mm^3 Measuring the velocity of both molecular beams enables us to determine the collision energy involved in the NH_3-H_2 scattering process, yielding E_{coll} = 605 cm^{-1} In the scattering volume the rotational state distribution in the electronic ground state of the NH_3 molecule is probed before and after the collision process by means of 2+1 REMPI via the $\tilde{B}$ state of ammonia For this purpose the output of a XeCl pumped dye (PTP) laser is focused into the scattering volume and subsequent NH_3 ions produced by the REMPI process are detected by a venetian-blind type particle multiplier The signal is then processed by a boxcar averager and an AT computer The two-photon spectrum of the $\tilde{B} \leftarrow \tilde{X}$ electronic transition of ammonia is well understood [27, 41, 57] and from these spectra it is possible to extract the rotational population distribution before and after collisions have taken place From the population differences thus obtained the relative state-to-state cross sections can be deduced using simple formulas derived and discussed in Chapter 3

In order to produce the para-H_2 on-line during the collision experiment we use a liquid-He flow cryostat operating at liquid H_2 temperature ($\approx$ 20 K) Underneath the cryostat a reservoir

is connected containing several layers of the catalytic ferric oxyd pallets. Allowing the normal-H_2 to flow over the magnetic field gradients of the FeO powder causes a nuclear spin flip in the H_2 molecule, accelerating the rotational relaxation to a 20 K Boltzmann equilibrium, which ultimately results in almost exclusively $j_2=0$ (para) molecular H_2 [76]. The FeO reservoir is 6 cm in diameter, and 5 cm long. The normal-H_2 enters the top of the reservoir just under the cold plate of the cryostat. It diffuses through the catalyst and at the bottom of the FeO container the converted para-H_2 is collected and directly fed to the secondary beam valve. The catalyst operates best just above liquid-H_2 temperature. The temperature of the container is regulated by adjusting the flow of liquid helium through the cryostat and can be stabilized with an accuracy of about 0.5 K .
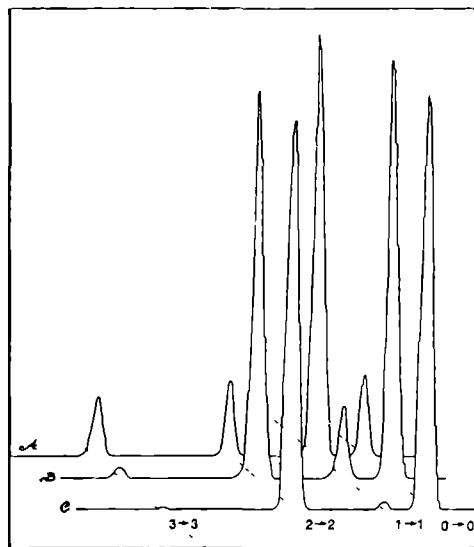
Figure 4.1 : $X^1\Sigma_g^+(v' = 1, j' \leftarrow v'' = 0, j'')$ *Q-branch Raman spectra of molecular hydrogen samples The lines can be identified as the Q(1) to Q(4) rotational transitions Curve A shows the spectrum of a normal-H_2 sample In curve B a converted H_2 sample was collected during the actual collision measurements at moderate flow velocity Curve C gives the Raman spectrum of a converted H_2 sample, using a low flow velocity*

When the secondary beam valve is operated the backing pressure must be constant. The pressure can be regulated accurately by two needle valves; the first one at the normal-H_2 entrance opening of the convertor and a second one directly after the para-H_2 outlet of the convertor. The efficiency of the conversion process, and thus the quality of the para-H_2 sample, is checked several times during the measurements by collecting samples and taking Raman spectra of each of them. For this purpose the Q-branch of the $v'' = 0 \rightarrow v' = 1$ excitation in the electronic ground state of H_2 around 4150 cm^{-1} is measured in an intracavity Raman spectrometer. The influence of
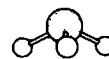
magnetic field gradients inside the pulsed solenoid valve on a possible back conversion from para-H_2 to ortho-H_2 is checked by taking H_2 samples at the outlet of the pulsed valve. No changes of the para-H_2 purity are observed.

In Figure 4.1 the results obtained from the Raman measurements on the H_2 samples are shown. All lines can be clearly identified as the $Q_1(1)$ to $Q_1(4)$ rotational transitions of the $X^1\Sigma_g^+(v' = 1 \leftarrow v'' = 0)$ vibronic band of H_2. From symmetry considerations it follows that the transitions starting at the $j_2 = 0, 2$ levels belong to the para-H_2 species, whereas the $j_2 = 1$ and 3 lines correspond to the ortho-H_2 species. The A curve of Figure 4.1 shows the Raman spectrum of a normal-H_2 sample at room temperature, whilst curve B shows a sample of the converted para-H_2 which was collected during the actual collision experiment. Curve C shows measurements for a para-H_2 sample which was obtained by allowing the normal-H_2 to flow very slowly over the surface of the catalyst. In the case of curve B a larger H_2 flow was necessary in order to maintain a secondary backing pressure of 500 mbar, resulting in a lower conversion efficiency, compared to the situation in curve C. From the analysis of the intensities [77] the ortho- to para-H_2 ratio is deduced. The converted H_2 sample in the case of a small H_2 flow as in Figure 4.1, curve C, can easily reach a purity of 98 % . However, during the collision experiment the hydrogen flow was too high to reach this purity. Several samples of the converted para-H_2 were collected during the scattering experiment on several days and measured in the Raman spectrometer. The quality of the samples reproduced perfectly and as a result the averaged purity of the para-H_2 samples yields 91 ± 2 %.

4.3 Theory

4.3.1 Scattering formalism

The formulation of the theoretical calculation of cross sections for the rotational excitation of NH_3 with a spherically symmetric collision partner such as ground state para-H_2 was originally described by Green [40], and this has since been extended to include rotationally excited H_2 [47]. For the latter the close coupled (CC) equations are derived in a space fixed frame of reference by expanding the total wavefunction as:

$$\Psi_{\beta l}^{JM} = \sum_{\beta' l'} \frac{F_{\beta' l'}^{JM\beta l}(R)}{R} |JM\beta' l'\rangle \tag{4.1}$$

$$|JM\beta l\rangle = \sum_{\substack{m_1 m_2 \\ m_{12} m_l}} C_{m_1 m_2 m_{12}}^{j_1 \ j_2 \ j_{12}} C_{m_{12} m_l M}^{j_{12} \ l \ J} \left(\frac{2j_1+1}{8\pi}\right)^{1/2} (D_{km_1}^{j_1}(\hat{\Omega}_1') + \epsilon D_{-km_1}^{j_1}(\hat{\Omega}_1')) Y_{m_2}^{j_2}(\hat{R}_2') Y_m^l(\hat{R}')$$

Here $\beta \equiv (j_1 k \epsilon j_2 j_{12})$, $|j_1, k\rangle$ denotes the rotational state of the NH_3 molecule, the parity index $\epsilon = \pm 1$ gives the symmetry of the inversion doublet state, j_2 is the rotational angular momentum of the H_2 molecule, j_{12} is the vector sum of j_1 and j_2, l is the relative orbital angular momentum, and J the total angular momentum involved in the collision process. The subscript '1' refers to the NH_3 molecule and '2' to the H_2 molecule. Both molecules are treated as rigid rotors.

Substituting this into the Schrödinger equation leads to the close coupled equations:

$$\left[\frac{d^2}{d\bar{R}^2} - \frac{l'(l'+1)}{R^2} + 2\mu(E - E_{j_1k\epsilon} - E_{j_2})\right] F_{\beta'l'}^{JM\beta l}(R) =$$

$$2\mu \sum_{\beta''l''} \langle JM\beta'l'|V(R\hat{\Omega}_1'\hat{R}_2')|JM\beta''l''\rangle F_{\beta''l''}^{JM\beta l}(R) \tag{4.2}$$

where μ is the reduced mass of the two collision partners. The integral on the right hand side is evaluated by writing the potential as a spherical expansion:

$$V(R\hat{\Omega}_1'\hat{R}_2') = \sum_{\substack{\lambda_1\lambda_2 \\ \lambda\mu}} v_{\lambda_1\lambda_2\lambda\mu}(R) \sum_{n_1n_2n} C_{n_1n_2n}^{\lambda_1\lambda_2\lambda} D_{\mu n_1}^{\lambda_1}(\hat{\Omega}_1') Y_{n_2}^{\lambda_2}(\hat{R}_2') Y_n^{\lambda*}(\hat{R}) \tag{4.3}$$

When the angular integration is done the integral on the right hand side of Equation (4.2) becomes:

$$\langle JM\beta l|V|JM\beta'l'\rangle = \sum_{\substack{\lambda_1\lambda_2 \\ \lambda\mu\geq0}} v_{\lambda_1\lambda_2\lambda\mu}(R) \frac{(1+\epsilon\epsilon'(-1)^{\lambda+\lambda_2+j_1+j_1'+\mu})}{2[(1+\delta_{k0})(1+\delta_{k'0})]^{1/2}}(\omega F_{kk'\pm\mu} + \epsilon F_{-kk'\mu}) \tag{4.4}$$

where $\omega = 1$ and $F_{kk'\mu}$ contributes to the first term if $(k' - k) \geq 0$, $\omega = (-1)^{\lambda_1+\lambda_2+\lambda+\mu}$ and $F_{kk'-\mu}$ contributes otherwise, and:

$$F_{kk'\mu} = (-1)^{j_1'+j_2'+j_{12}'+k'-J}\left(\frac{2\lambda+1}{4\pi}\right)[(2j_1+1)(2j_1'+1)\times$$

$$(2j_2+1)(2j_2'+1)(2j_{12}+1)(2j_{12}'+1)(2l+1)(2l'+1)(2\lambda_2+1)]^{1/2} \times$$

$$\begin{pmatrix} l & l' & \lambda \\ 0 & 0 & 0 \end{pmatrix}\begin{pmatrix} j_2 & j_2' & \lambda_2 \\ 0 & 0 & 0 \end{pmatrix}\begin{pmatrix} j_1 & j_1' & \lambda_1 \\ k & -k' & \mu \end{pmatrix} \times$$

$$\left\{\begin{matrix} l' & l & \lambda \\ j_{12} & j_{12}' & J \end{matrix}\right\}\left\{\begin{matrix} j_{12} & j_2 & j_1 \\ j_{12}' & j_2' & j_1' \\ \lambda & \lambda_2 & \lambda_1 \end{matrix}\right\} \tag{4.5}$$

Because of the large number of channels required to give convergence of the cross sections, the number of coupled equations rapidly becomes large, and the solution of the set of CC equations can be very time consuming. A frequently used and well tested approximation is the coupled states (CS) approximation. The CS equations are derived from the CC equations in a body fixed frame in which the z-axis lies along the intermolecular vector. In this body fixed frame the wavefunction can be expanded as:

$$\Psi_{\beta\Omega}^{JM} = \sum_{\beta'\Omega'} \frac{G_{\beta'\Omega'}^{JM\beta\Omega}(R)}{R} \sum_{m_1m_2} C_{m_1m_2m_{12}}^{j_1\,j_2\,j_{12}}\left(\frac{2j_1+1}{8\pi}\right)^{1/2}(D_{km_1}^{j_1}(\hat{\Omega}_1) + \epsilon D_{-km_1}^{j_1}(\hat{\Omega}_1))Y_{m_2}^{j_2}(\hat{R}_2) \tag{4.6}$$

where Ω is the projection of J (and j_{12}) on the body-fixed z-axis. In this frame the orbital angular momentum couples states with $\Omega' = \Omega \pm 1$ as well as states with $\Omega' = \Omega$. The coupled

73
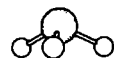
states approximation is derived by neglecting the centrifugal coupling between states of different Ω and approximating the remaining terms by $\langle\beta\Omega|1^2|\beta'\Omega\rangle \approx J(J+1)$ The coupled states equations then become

$$\left[\frac{d^2}{dR^2} - \frac{J(J+1)}{R^2} + 2\mu(E - E_{J_1 k\epsilon} - E_{J_2})\right] G^{JM\beta\Omega}_{\beta'\Omega'}(R) = 2\mu \sum_{\beta''} \langle\beta'\Omega'|V|\beta''\Omega'\rangle G^{JM\beta\Omega}_{\beta''\Omega'}(R) \quad (4\ 7)$$

The body fixed equivalent of Equation (4 3) is

$$V(R\hat{\Omega}_1\hat{R}_2) = \sum_{\substack{\lambda_1\lambda_2 \\ \mu\nu}} v_{\lambda_1\mu\lambda_2\nu}(R)D^{\lambda_1}_{\mu\nu}(\hat{\Omega}_1)Y^{\lambda_2}_{-\nu}(\hat{R}_2) \tag{4 8}$$

where $\hat{\Omega}$ and $\hat{R}$ are the angular coordinates with respect to the body fixed frame and $v_{\lambda_1\mu\lambda_2\nu}(R)$ the radial part of the potential matrix elements

$$v_{\lambda_1\lambda_2\lambda\mu}(R) = \left(\frac{4\pi}{2\lambda+1}\right) \sum_{\nu\geq0} \frac{C^{\lambda_1\lambda_2\lambda}_{\nu-\nu0}}{(1+\delta_{\nu0})} \left(v_{\lambda_1\mu\lambda_2\nu}(R) + (-1)^{\lambda_1+\lambda_2+\lambda}v_{\lambda_1\mu\lambda_2-\nu}(R)\right) \tag{4 9}$$

After integration the $\langle\beta\Omega|V|\beta'\Omega\rangle$ reduce to an expression of the form of Equation (4 4) but with the $F_{kk'\mu}$ now given by

$$F_{kk'\mu} = (-1)^{J_1'+J_2'+J_{12}'-k'-\Omega} \begin{pmatrix} 2\lambda+1 \\ 4\pi \end{pmatrix}$$
$$[(2J_1+1)(2J_1'+1)(2J_2+1)(2J_2'+1)(2J_{12}+1)(2J_{12}'+1)(2\lambda_2+1)]^{1/2}$$
$$\begin{pmatrix} J_2 & J_2' & \lambda_2 \\ 0 & 0 & 0 \end{pmatrix} \begin{pmatrix} J_1 & J_1' & \lambda_1 \\ k & -k' & \mu \end{pmatrix} \begin{pmatrix} J_{12} & J_{12}' & \lambda \\ \Omega & -\Omega & 0 \end{pmatrix} \begin{Bmatrix} J_{12} & J_2 & J_1 \\ J_{12}' & J_2' & J_1' \\ \lambda & \lambda_2 & \lambda_1 \end{Bmatrix} \tag{4 10}$$

4.3.2 Interaction Potential

Two interaction potentials were considered in the current study Both potentials contain the same SCF part described by Danby et al [45] supplemented by calculations at the additional geometries required to evaluate the $\nu = 1$ terms in Equation (4 8) [78] The first potential has a dispersion contribution calculated using second order perturbation theory [45] Following the nomenclature of Danby and Valiron [64] this will be refered to as the SCF+EK potential The second potential, referred to as the SCF+MBPT potential, has a dispersion contribution taken from a fourth order many body perturbation calculation [48, 63] Unfortunately the data were not available at a sufficient number of orientations to allow determination of the $\nu = 1$ terms in the body fixed potential expansion These terms were taken from the second order perturbation theory calculation

The two potentials have been discussed in the context of NH_3 – ground state para-H_2 calculations by Danby and Valiron [64] where only the $\lambda_2 = 0$ terms contribute They pointed out that the two potentials differ most in the $\lambda_1\lambda_2\lambda\mu = 2020$ term The significance of this difference to the current calculations will be discussed further

ortho-NH_3 , E = 605 cm^{-1}			para-NH_3 , E = 60 cm^{-1}		
transition $jk\epsilon \rightarrow j'k'\epsilon'$	CC ref [46]	CS	transition $jk\epsilon \rightarrow j'k'\epsilon'$	CC ref [47]	CS
$0_0^+ \rightarrow 1_0^+$	16 4	17 1	$1_1^+ \rightarrow 2_1^+$	12 6	9 46
$0_0^+ \rightarrow 2_0^+$	6 97	6 40	$1_1^+ \rightarrow 2_1^-$	9 97	8 26
$0_0^+ \rightarrow 3_0^+$	1 59	1 65	$1_1^+ \rightarrow 2_2^+$	1 74	2 05
$0_0^+ \rightarrow 4_0^+$	0 74	0 68	$1_1^+ \rightarrow 2_2^-$	1 70	1 72
$0_0^+ \rightarrow 3_3^+$	2 39	2 49	$2_1^+ \rightarrow 2_1^-$	23 8	30 6
$0_0^+ \rightarrow 3_3^-$	3 07	3 18	$2_1^+ \rightarrow 2_2^+$	3 59	2 95
$0_0^+ \rightarrow 4_3^+$	1 12	1 10	$2_1^+ \rightarrow 2_2^-$	4 55	4 99
$0_0^+ \rightarrow 4_3^-$	1 65	1 76	$2_2^+ \rightarrow 2_2^-$	44 2	58 3

Table 4.1 : *Calculated state-to-state cross sections (in units of 10^{-16} cm^2) for rotational excitation of ortho- and para-NH_3 in collision with ortho-H_2 constrained to $j_2 = 1$ comparison between close coupled results and the coupled states approximation*

4.3.3 Calculations

To compare with the experimental results calculations were done with both potentials at a relative collision energy of 605 cm^{-1} for ortho- and para-NH_3 colliding with ortho- and para-H_2 The cross sections for the ortho-H_2 collisions were calculated using the coupled states approximation and in order to interpret the results it is important to know how well the coupled states calculations reproduce the results obtained with full close coupled calculations For ortho-NH_3 –ortho-H_2 collisions close coupled calculations at an energy of 605 cm^{-1} have been published [46] These calculations used the 'SCF+EK' potential and a basis set consisting of the 14 energetically lowest NH_3 rotational states ($E_{j_1 k\epsilon} \leq E_{66\pm}$) and the $j_2 = 1$ rotational state of H_2 To test the accuracy of the CS approximation for this system these ortho-NH_3 –ortho-H_2 calculations were repeated using the same potential and the same basis sets For para-NH_3 - ortho-H_2 CC calculations at 605 cm^{-1} have not been done, so CS calculations were performed at 60 cm^{-1} to compare with previously published CC results at this lower energy [47] The results are given in Table 4 1 and in general the agreement between the CC and CS cross sections is good The level of agreement is less good for the 60 cm^{-1} calculations, but the CS approximation is expected to improve with increasing energy

In the case of ortho-NH_3 - para-H_2 collisions the cross sections $\sigma(00+ \rightarrow j_1'3+)$ are identically zero in the CS approximation when $j_2 = j_2' = 0$ regardless of the potential surface used, whilst they are non vanishing for the CC calculations The same is true for the $(00+ \rightarrow j_1'6-)$ cross sections For these transitions the potential matrix element responsible for direct transitions from j_1 to j_1' vanishes for all j_1' and the transition is driven only through centrifugal coupling which is neglected in the coupled states approximation For para-NH_3 –para-H_2 collisions a similar problem

occurs for the $11\pm \rightarrow 22\pm$ transition where once again the direct coupling terms vanish although in this case the cross section is non-zero as the transition can be driven indirectly through terms in the potential with $\lambda_1 > 3$ As the experimental cross sections were not negligible for these transitions, full close coupled calculations were done for para H_2 collisions to avoid ambiguity in the interpretation of the results

An important consideration in the calculations is the size of the rotational basis set used At an energy of 605 cm^{-1} the $j_2 = 2$ level of para-H_2 is energetically accessible, and it is possible for both molecules to be simultaneously excited Although the cross sections for this process are small it is desirable to include $j_2 = 2$ para H_2 states in the basis for all NH$_3$ levels of interest For the para NH$_3$ – para-H_2 calculations a (24,10) basis was used consisting of the 24 $|j_1(j_2 = 0)k\epsilon\rangle$ levels with $E_{j_1 k\epsilon} < E_{61\pm}$, and the 10 energetically lowest $|j_1(j_2 = 2)k\epsilon\rangle$ states For the ortho-NH$_3$ – para-H_2 calculations a (14,9) basis was used For the ortho-H_2 calculations only $j_2 = 1$ was included in the H_2 basis set, and NH$_3$ basis sets consisting of the energetically lowest 14 ortho NH$_3$ levels and the energetically lowest 24 para-NH$_3$ levels were used Tests showed that these basis sets gave converged cross sections for the transitions of interest

The coupled equations were integrated using the MOLSCAT computer code [79] modified to treat linear rotor symmetric top collisions For reasons of economy calculations were limited to every second partial wave for the ortho-NH$_3$ – para H_2 calculations and fourth partial wave for the remainder (where here the partial waves are labelled by total angular momentum) This only introduces a very small error at this energy where partial cross sections are smoothly and slowly varying with total angular momentum

4.4 Results and interpretation

4.4.1 · Calculated cross sections

The results of the calculations are given in Tables 4 2 and 4 3 for transitions out of the $j_1 k\epsilon = 00+$ and the $j_1 k\epsilon = 11-$ states For the ortho-H_2 species the calculations have been performed in the CS approximation whereas for para-H_2 the exact close coupling results are given In both cases the cross sections are given for collisions with ortho-H_2 ($j_2 = 1$) or para-H_2 ($j_2 = 0$), but for para-H_2 collisions j_2' is no longer confined to zero The relative sensitivity of the cross sections for ortho- and para-H_2 collisions to the differences between the two potentials can be seen immediately from the tables NH$_3$ rotational transitions in NH$_3$–ortho-H_2 collisions are driven by terms in the potential expansion with $\lambda_2 = 0$ and 2 so a large number of terms can contribute to the sum in Equation (4 4) As a result the coupling matrix elements, and consequently the cross sections, are relatively insensitive to the choice of the potential However, coupling matrix elements between states with $j_2' = j_2 = 0$ only contain terms with $\lambda_2 = 0$, so cross sections for para-H_2 collisions are far more sensitive to changes in the potential It has already been noted that the SCF+MBPT potential has a larger $v_{\lambda_1 \lambda_2 \lambda_\mu}(R) = v_{2020}$ term than the SCF+EK potential, and the effect of this on the cross sections for collisions with para-H_2 can easily be seen To first order the v_{2020} term drives the $00+ \rightarrow 20+$ and the $11- \rightarrow 21+$ transitions The relative sizes of the cross sections for these transitions increase when the SCF+MBPT potential is used

transition $jk\epsilon \to j'k'\epsilon'$	para-H_2				ortho-H_2	
	SCF+EK $j'_2 = 0$	$j'_2 = 2$	SCF+MBPT $j'_2 = 0$	$j'_2 = 2$	SCF+EK $j'_2 = 1$	SCF+MBPT $j'_2 = 1$
$0_0^+ \to 1_0^+$	17 017	0 100	12 029	0 130	17 895	18 999
$0_0^+ \to 2_0^+$	0 459	0 064	1 812	0 106	6 402	8 843
$0_0^+ \to 3_0^+$	0 464	0 023	0 976	0 024	1 647	1 254
$0_0^+ \to 4_0^+$	0 631	0 001	0 262	0 002	0 678	0 873
$0_0^+ \to 3_3^+$	0 016	0 021	0 006	0 026	2 492	2 540
$0_0^+ \to 3_3^-$	4 161	0 085	4 899	0 095	3 176	2 876
$0_0^+ \to 4_3^+$	0 002	0 003	0 009	0 005	1 103	0 869
$0_0^+ \to 4_3^-$	4 152	0 020	2 944	0 030	1 757	1 661
$1_0^+ \to 2_0^+$	11 322	0 085	8 254	0 112	11 065	11 209
$1_0^+ \to 3_0^+$	0 736	0 031	1 049	0 046	3 014	4 125
$1_0^+ \to 4_0^+$	0 265	0 005	0 515	0 006	0 754	0 650
$1_0^+ \to 3_3^+$	3 199	0 058	3 804	0 077	2 856	2 522
$1_0^+ \to 3_3^-$	1 067	0 050	0 695	0 051	2 148	2 155
$1_0^+ \to 4_3^+$	1 954	0 015	1 393	0 019	1 674	1 529
$1_0^+ \to 4_3^-$	1 310	0 026	1 318	0 027	1 779	1 542

Table 4.2 : *Calculated state-to state cross sections (in units of 10^{-16} cm^2), obtained in the CC and CS approximation, for the rotational excitation of ortho NH_3 in collision with ground state para-H_2 (CC) and ortho-H_2 (CS) at an energy of 605 cm^{-1}*

4.4.2 Measured cross sections

In Figure 4 2 a part of a REMPI scattering spectrum is presented Each line is identified by the rotational state in the electronic ground state and represents the signal due to scattering into this specific state The top part of the figure shows the results for collisions with normal-H_2, whilst the lower part shows results for collisions with para-H_2 Secondary backing pressures and experimental sensitivities were the same in both spectra As can be seen from the figure the scattering signals decrease for all states, except the 44+ state, when changing the collision partner from normal- to para-H_2

Although the purity of the para-H_2 sample did not reach 100 %, we are able to determine relative state-to-state cross sections for the NH_3-para-H_2 collision system by using previously obtained scattering results for the NH_3-normal-H_2 collision experiment, described in Chapter 3 Since normal-H_2 consists of 75 % ortho-H_2 and 25 % para-H_2 and the H_2 sample used in this experiment consists of 91 % para-H_2 and 9 % ortho-H_2, we have two series of measurements
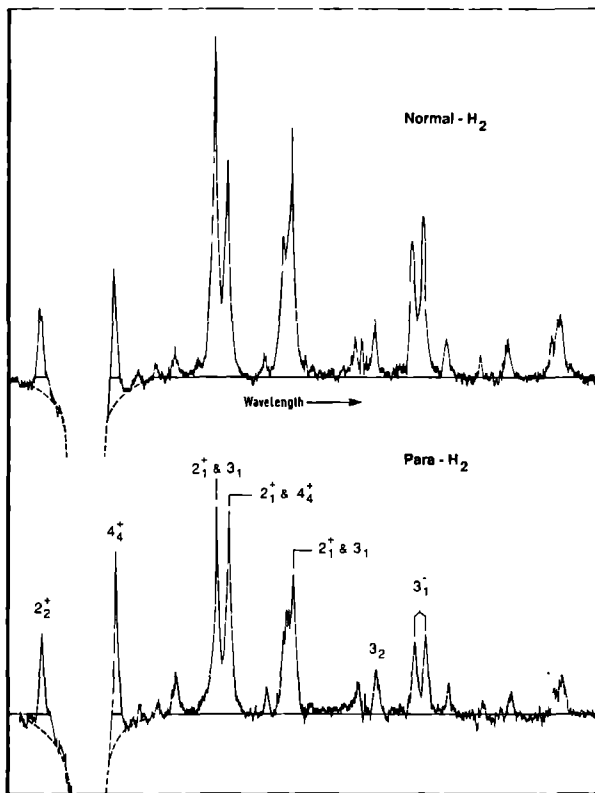
Figure 4.2 : *REMPI scattering spectra of the NH$_3$-normal-H$_2$ and NH$_3$-para-H$_2$ collision event. All lines are identified according to their initial rotational state in the electronic ground state. Both spectra were recorded with 400 mbar secondary gas backing pressure and the same experimental sensitivity.*

transition $jk\epsilon \rightarrow j'k'\epsilon'$	para-H$_2$				ortho-H$_2$	
	SCF+EK $j_2'=0$	$j_2'=2$	SCF+MBPT $j_2'=0$	$j_2'=2$	SCF+EK $j_2'=1$	SCF+MBPT $j_2'=1$
$1_1^- \rightarrow 2_1^+$	0 362	0 031	0 962	0 068	4 240	5 621
$1_1^- \rightarrow 2_1^-$	8 583	0 056	6 082	0 066	8 030	8 242
$1_1^- \rightarrow 2_2^+$	1 673	0 030	1 947	0 041	1 486	1 315
$1_1^- \rightarrow 2_2^-$	0 013	0 021	0 003	0 021	0 848	0 928
$1_1^- \rightarrow 3_1^+$	0 287	0 022	0 460	0 026	0 912	0 667
$1_1^- \rightarrow 3_1^-$	0 313	0 019	0 593	0 028	1 880	2 660
$1_1^- \rightarrow 3_2^+$	1 592	0 020	1 074	0 024	0 930	0 903
$1_1^- \rightarrow 3_2^-$	0 588	0 017	0 642	0 017	0 831	0 704
$1_1^- \rightarrow 4_4^+$	1 945		2 228		1 749	1 589
$1_1^- \rightarrow 4_4^-$	0 343		0 251		1 213	1 383

Table 4.3 : *Calculated state-to state cross sections (in units of 10^{-16} cm^2), obtained in the CC and CS approximation, for the rotational excitation of para NH$_3$ in collision with ground state para-H$_2$ (CC) and ortho-H$_2$ (CS) at an energy of 605 cm^{-1}*

involving the same set of cross sections $\sigma_{o-H_2}(i \rightarrow f)$ and $\sigma_{p-H_2}(i \rightarrow f)$ where i denotes the initially prepared state, i e 00+ for ortho-NH$_3$ and 11- for para-NH$_3$ Since the scattering signal $\delta S_{ff'}$ is linearly dependent on secondary beam density, which is the same for ortho- and para-H$_2$, and on the cross sections $\sigma_{o-H_2}(i \rightarrow f)$ and $\sigma_{p-H_2}(i \rightarrow f)$ (see Chapter3, section 3 1), we obtain the following set of equations

$$0\ 75 \ \ \sigma_{o-H_2}(i \rightarrow f) + 0\ 25 \ \ \sigma_{p-H_2}(i \rightarrow f) \ \ \propto \ \ S_{ff'}^I \qquad (4\ 11)$$

$$0\ 09 \ \ \sigma_{o-H_2}(i \rightarrow f) + 0\ 91 \ \ \sigma_{p-H_2}(i \rightarrow f) \ \ \propto \ \ S_{ff'}^{II} \qquad (4\ 12)$$

Here f denotes the NH$_3$ collisionally excited rotational state and the superscripts I and II refer respectively to the scattering signals obtained in Chapter 3, using normal-H$_2$ as collision partner, and to this work Solving this set of equations yields the relative cross sections for rotational excitation of NH$_3$ for both ortho- and para-H$_2$ species as collision partner These relative cross sections are given in Table 4 4 for ortho-NH$_3$ and Table 4 5 for para-NH$_3$, normalized in such a way that the sum of all given ortho- and para-H$_2$ cross sections is one for each NH$_3$ species The experimental error for the cross sections obtained from Equations (4 11) and (4 12) is estimated to be 14%

To compare the theoretical cross sections with the experimental results a correction has to be made to allow for the 8% of the ortho NH$_3$ initially in the $j_1k\epsilon = 10+$ state and the 5% of para-NH$_3$ initially in the $j_1k\epsilon = 11+$ state The measured cross section for excitation into the $j_1k\epsilon$ states is then given by

$$\sigma(i \rightarrow j_1k\epsilon) \ = \ 0\ 92 \ \ \sigma(00+ \rightarrow j_1k\epsilon) + \ 0\ 08 \ \ \sigma(10+ \rightarrow j_1k\epsilon) \qquad (4\ 13)$$

Ortho-NH$_3$ – ortho-H$_2$ $\sigma(i \to j_k^\epsilon)$				Ortho-NH$_3$ – para-H$_2$ $\sigma(i \to j_k^\epsilon)$			
j_k^ϵ	SCF+EK	experiment	SCF+MBPT	j_k^ϵ	SCF+EK	experiment	SCF+MBPT
1_0^+	0 229	0 214	0 269	1_0^+	0 245	0 173	0 169
2_0^+	0 133	0 102	0 164	2_0^+	0 025	0 053	0 044
3_0^+	0 032	0.051	0 027	3_0^+	0 009	0 032	0 018
4_0^+	0 013	0 013	0 015	4_0^+	0 011	0 010	0 005
3_3^+	0 044	0 058	0 046	3_3^+	0 005	0 040	0 006
3_3^-	0 054	0 041	0 051	3_3^-	0 073	0 058	0 084
4_3^+	0 021	0 020	0 017	4_3^+	0 003	0 015	0 002
4_3^-	0 030	0 051	0 030	4_3^-	0 072	0 072	0 052

Table 4.4: *Relative state-to-state cross sections for rotational excitation of ortho-NH$_3$ (92 % in 0_0^+ and 8 % in 1_0^+) in collision with ortho- and para-H$_2$ The experimental error is 14% The theoretical data are corrected for the initial state preparation of the ortho-NH$_3$ molecules (see section 4 2) All data represent relative cross sections, such that the sum of all ortho- and para-H$_2$ cross sections for each NH$_3$ species equals 1 0*

$$\sigma(i \to 10+) = 0.92 \cdot \sigma(00+ \to 10+) - 0.08 \cdot \sum_{j_1'k'\epsilon' \neq 10+} \sigma(10+ \to j_1'k'\epsilon')$$

for ortho-NH$_3$ and.

$$\sigma(i \to j_1 k\epsilon) = 0.95 \cdot \sigma(11- \to j_1 k\epsilon) + 0 05 \; \sigma(11+ \to j_1 k\epsilon) \tag{4 14}$$

for para-NH$_3$. Here i stands for the ensemble of initially prepared states The calculated values of these cross sections, normalized in the same way as the experimental values, are also given in Tables 4.4 and 4.5 for ortho- and para-NH$_3$ respectively, for both potential energy surfaces.

4.5   Discussion

To facilitate the comparison between the experimental cross sections and the calculated values, the relative cross sections of Tables 4.4 and 4.5 are presented graphically in Figures 4.3 and 4.4 respectively. For each excited state three bars are shown, with heights proportional to the cross section $\sigma(i \to j_1 k\epsilon)$. The left and right hand bars represent the calculated cross sections, as defined in Equations (4.13) and (4 14), obtained using the SCF+EK and SCF+MBPT ab initio potential respectively. The central bars represent the measured cross sections obtained from Equations (4.11) and (4.12).

Para-NH$_3$ – ortho-H$_2$ $\sigma(i \to j_k^\epsilon)$			Para-NH$_3$ – para-H$_2$ $\sigma(i \to j_k^\epsilon)$			
j_k^ϵ	SCF+EK	experiment	SCF+MBPT	j_k^ϵ	SCF+EK	experiment	SCF+MBPT
2_1^+	0 117	0 099	0 150	2_1^+	0 020	0 052	0 032
2_1^-	0 207	0 201	0 212	2_1^-	0 216	0 125	0 152
2_2^+	0 038	0 027	0 034	2_2^+	0 042	0 021	0 049
2_2^-	0 023	0 027	0 025	2_2^-	0 003	0 019	0 003
3_1^+	0 025	0 037	0 020	3_1^+	0 008	0 022	0 012
3_1^-	0 048	0 079	0 067	3_1^-	0 008	0 037	0 015
3_2^+	0 024	0 033	0 023	3_2^+	0 041	0 019	0 027
3_2^-	0 022	0 026	0 019	3_2^-	0 017	0 018	0 017
4_4^+	0 046	0 048	0 041	4_4^+	0 049	0 059	0 056
4_4^-	0 033	0 032	0 036	4_4^-	0 011	0 018	0 009

Table 4.5 : *Same as Table 4 4, but now for para NH$_3$ (95 % in 1_1^- and 5 % in 1_1^+) – ortho-, para-H$_2$ scattering*

4.5.1 NH$_3$ – para-H$_2$ cross sections

For para-H$_2$ as the collision partner we see from Figures 4 3 b and 4 4 b that the overall rotational energy transfer, i e the cross sections for rotational excitation to state $j_1 k\epsilon$ averaged over both parity components $\epsilon = \pm 1$, is predicted correctly by theory For ortho-NH$_3$ indeed $\sigma(00+ \to 10+)$ is the strongest cross section in theory and experiment Furthermore for the $k = 0$ manifold the experimental cross section decreases exponentially with angular momentum transfer in good agreement with the SCF+MBPT potential calculation

Apart from pure rotational energy transfer we are also dealing with parity conserving and changing transitions starting from the 00+ and 11− states For ortho-NH$_3$ – ground state para-H$_2$ scattering theory predicts strong parity propensity rules for transitions to the $k = 3$ levels, i e the rotational excitation from the 00+ level to the $j_1 3-$ levels is strongly favoured over excitation to the $j_1 3+$ levels The reason for this is that the potential matrix elements in Equation (4 4) for $\Delta k = 3, \Delta j_1$ transitions with para-H$_2$ ($j_2 = 0$) as collider has a strong diagonal contribution if the parity index ϵ changes sign The small non-zero cross sections for the parity index conserving transitions to the $j_1 3+$ levels come from off-diagonal contributions to the matrix element due to centrifugal coupling terms which are not neglected in the close coupling scattering formalism Now experiment shows clearly a non-zero cross section for the parity index conserving $\Delta k = 3, \Delta j_1$ transitions The same problem is encountered in NH$_3$ He scattering (Chapter 3) and NH$_3$-Ar scattering, to be discussed in Chapters 5 and 6

For the para-NH$_3$ – para-H$_2$ collision system the strongest rotational excitations are observed for the $j_1 k\epsilon = 11- \to 21-$ and $11- \to 44+$ transitions, as is predicted by theory The experimentally

81
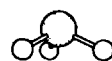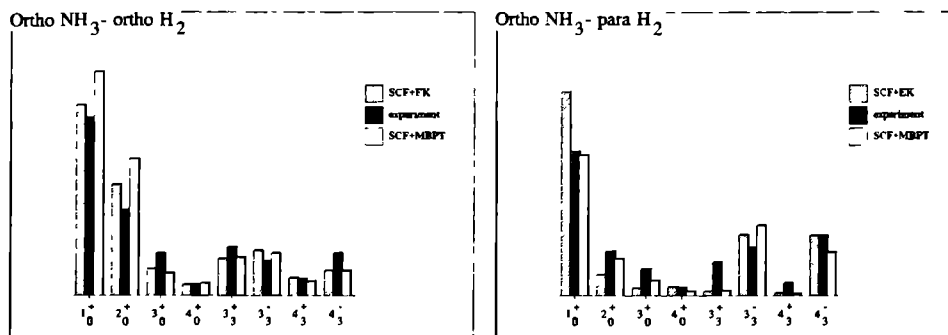
Figure 4.3 : *Relative state-to-state cross sections $\sigma(i \to j_1 k\epsilon)$ for scattering of ortho-NH$_3$ with ortho-H$_2$ (Figure 4.3.a) and para-H$_2$ (Figure 4.3.b) at a collision energy of 605 cm^{-1}. For each rotational state $j_1 k\epsilon$ three bars are given. The middle bar gives the experimentally obtained cross section. The left bar represents the cross section from the SCF+EK potential calculation, whereas the right bar gives the results using the SCF+MBPT potential. The experimental error is about 14 %.*

observed parity propensities roughly agree with the calculated propensities, except for the $11- \to 22\pm$ transition where the agreement is worse. Here, the matrix element of Equation (4.4) only has a strong contribution for the parity index changing $\Delta j_1 = 1, \Delta k = 3$ transition when $j_2 = 0$. Experiment however indicates that both transitions, parity changing as well as parity conserving, are equally strong. This same phenomenon, into somewhat less extent, was also observed for NH$_3$-He scattering.

4.5.2   NH$_3$ – ortho-H$_2$ cross sections

For the NH$_3$ – ortho-H$_2$ collision system the agreement between experiment and theory is surprisingly good, as can be seen from the figures. For both ortho-NH$_3$ and para-NH$_3$ not only the measured rotational energy transfer, but now also the parity propensities are in good agreement with the theoretical values. For ortho-NH$_3$ the $j_1 k\epsilon = 00+ \to 30+$ and $00+ \to 40+$ experimental cross sections are slightly too strong with respect to the $00+ \to 10+$ and $00+ \to 20+$ cross sections in comparison with both sets of calculated values. The strong parity propensity rules which were predicted for $|\Delta k| = 3$ transitions in ground state para-H$_2$ scattering, are absent for ortho-H$_2$. Due to the $j_2 = 1$ ground state of the ortho-H$_2$ molecule, $\lambda_2 = 2$ terms can contribute to the matrix element of Equation (4.4), and it no longer vanishes for $00+ \to j_1 3+$ transitions. Consequently, transitions from the NH$_3$ ground state to both the upper and lower components of the $k = 3$ inversion doublets become allowed and are observed experimentally. The size of the observed propensities is in good agreement with the calculated values, except that the $43-$ level is measured slightly too strong compared to theory.

For para-NH$_3$ the agreement between experiment and theory is also satisfying. The excitations to the low $j_1 k\epsilon = 21\pm$ and $22\pm$ energy levels are predicted somewhat stronger with respect to
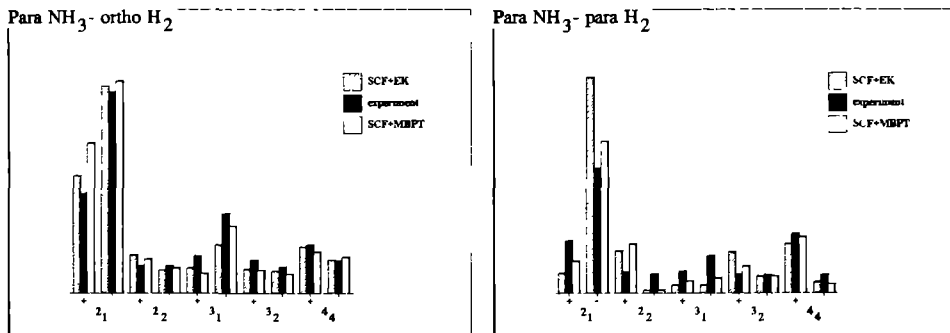
Figure 4.4 : *Same as Figure 4.3, but now for para-NH₃.*

the higher $j_1 k\epsilon = 31\pm$ and $32\pm$ levels as compared to the experimental results. Furthermore all theoretically predicted parity propensities are confirmed by the experiment. The observed propensity for the $j_1 k\epsilon = 21\pm$ level is only slightly stronger than the theoretical value.

4.5.3 NH₃-ortho-H₂ versus NH₃-para-H₂ cross sections

When comparing the ortho-H₂ and para-H₂ cross sections for a specific NH₃ species, one common feature can be noticed for all NH₃ rotational states $j_1 k\epsilon$. An increase (or decrease) of the theoretical cross sections, when going from ortho-H₂ to para-H₂ as perturber, corresponds to an increase (resp. decrease) of the experimental cross sections. In order to study this change of cross section when changing the H₂ species, the following quantity may be defined:

$$\Delta\sigma(j_1 k\epsilon) = \frac{\sigma_{o-H_2}(i \to j_1 k\epsilon) - \sigma_{p-H_2}(i \to j_1 k\epsilon)}{\sigma_{o-H_2}(i \to j_1 k\epsilon) + \sigma_{p-H_2}(i \to j_1 k\epsilon)} \tag{4.15}$$

For the cross sections obtained using the SCF+MBPT potential this quantity $\Delta\sigma(j_1 k\epsilon)$ has the same sign as the corresponding experimental values for all ortho- and para-NH₃ states, except for the 22+ and 32+ states. This illustrates that an increase (resp. decrease) of the theoretical cross section when changing from ortho-H₂ to para-H₂ as the perturber, corresponds with an increase (resp. decrease) of the experimental values. In general the value for $\Delta\sigma(j_1 k\epsilon)$ is positive and hence the cross sections for ortho-H₂ scattering are stronger than for para-H₂ scattering. This is in agreement with the results of Broquier et al. [9]. They were the first to demonstrate the difference between para-H₂ and normal-H₂ colliders upon rotational energy transfer in the NH₃ molecule by means of pressure broadening experiments. The outcome of their experiments showed a preferentially stronger NH₃ rotational excitation by the ortho-H₂ species.

4.5.4 NH₃-para-H₂ versus NH₃-He cross sections

As already mentioned in the introduction it is assumed in astrophysical models that the relative state-to-state cross sections for NH₃-para-H₂ ($j_2 = 0$) collisions, which are thought to be the most
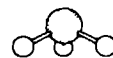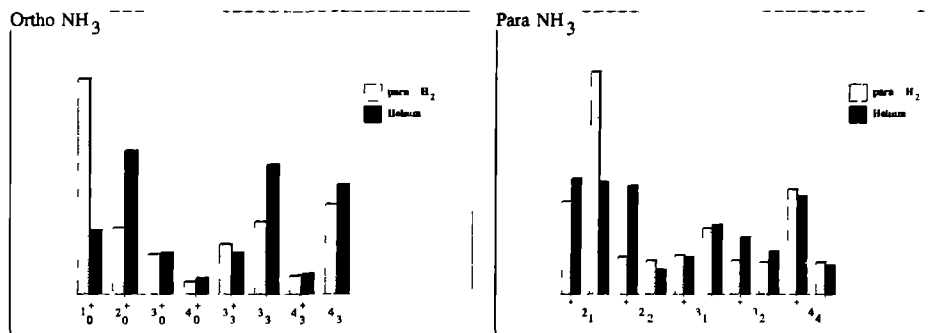
Figure 4.5 : *Relative state-to-state cross sections $\sigma(\imath \rightarrow \jmath_1 k\epsilon)$ for scattering of ortho-NH3 (Figure 4 5 a) and para-NH3 (Figure 4 5 b) with para-H2 and He at a collision energy of 605 cm^{-1} For each rotational state $\jmath_1 k\epsilon$ the left bar represents the para-H2 collision cross sections and the right bar the He cross sections, obtained from [62] The experimental error is about 14 %*

likely in the cold interstellar medium, are similar to the relative cross sections for NH_3 rotational excitation in collisions with He atoms In the past many astrophysical studies have referred to the work of Green [29] in which state to-state collision rate coefficients were calculated for NH_3 He collisions at several kinetic temperatures

In Figure 4 5 the state-to-state cross sections for NH_3-He scattering [62], are compared with the experimental values for NH_3-para H_2 scattering obtained in this study Since no absolute determination of the cross sections is possible, they are normalized in such a way that the sum over all states of the ortho- or para-NH_3 cross sections is the same for para-H_2 and He scattering As can be seen from the figure large differences between both collision partners show up For para-NH_3 a parity propensity is observed for excitation to the $\jmath_1 k\epsilon = 21-$ state in the case of para H_2 scattering, which is absent when He is the collider The opposite is true for the $\jmath_1 k\epsilon = 22\pm$ level Here a strong parity propensity is observed only in the case of He scattering For the higher $\jmath_1 k\epsilon$ levels the para-H_2 and He collision cross sections indeed look very similar For ortho-NH_3 the similarity between para-H_2 and He scattering is also less clear for the low lying $\jmath_1 k\epsilon = 10+$ and 20+ states Furthermore, a less pronounced propensity is observed for excitation to the $\jmath_1 k\epsilon = 33-$ state in the case of para-H_2 scattering when compared to the NH_3-He collision experiment

Whilst it is tempting to draw some conclusions about the relative strengths of particular terms in the NH_3-H_2 and NH_3-He potential expansions these observations could equally well be explained by the fact that para-H_2 is not an atom and treating it as a purely spherically symmetric collision partner in the collision calculations (i e including only $\jmath_2 = 0$ terms in the H_2 basis set) is an approximation As can be seen from Figure 4 5 , for both para- and ortho-NH_3 results the dipole allowed transitions, 00+ $\rightarrow$ 10+ and 11- $\rightarrow$ 21-, are much enhanced when para-H_2 is the collision partner A similar enhancement of the (theoretical) cross sections for these transitions was found in the low energy close coupled results of reference [47] when calculations using a $(\jmath_2 = 0, 2)$ H_2

basis set were compared to calculations using ($j_2 = 0$) only This illustrated that the $\lambda_2 = 2$ terms in the potential can have an important effect even at energies well below the threshold for excitation of the $j_2 = 2$ level of para-H$_2$, and it is possible that we see a similar effect here This would imply that care should be taken not only when using NH$_3$-He rate coefficients, but also in interpreting the results of NH$_3$ – ($j_2 = 0$)-H$_2$ scattering calculations

The observation that the theoretically expected parity propensities towards excitation of the $j_1 k\epsilon = 33-, 43-$ and $22+$ are more evident for He collisions than for para-H$_2$ collisions may also be an indication that for ground state para-H$_2$ coupling to higher rotational states should not be ignored

These differences, especially for ortho-NH$_3$, between para-H$_2$ and He scattering might have important consequences for the interpretation of the observed interstellar $j_1 k = 33$ maser If also at lower kinetic temperatures the rate of collisional pumping into the upper 33− level is less strong in the case of para-H$_2$ scattering than it is for helium scattering, inversion should be reached less easily than when He is the collision partner Applying state-to-state cross sections for NH$_3$ –para-H$_2$ scattering instead of the NH$_3$-He values to the interstellar rate equations should have its impact also on threshold interstellar H$_2$ densities and the relation between he observed rotational temperature and the kinetic temperature of the emitting gas Collisions with ortho-H$_2$ will not be efficient in the production of population inversion between the 3$_3$ doublet states At the present collision energy an anti-inversion would be obtained due to the preference of exciting the 43− state that will decay spontaneously to the 33+ state Measurements are being prepared to establish the parity propensities at lower collision energies

4.6 Conclusions

In this chapter we report parity-resolved state-to-state cross sections for rotational excitation of NH$_3$ in collision with ortho- and para- H$_2$ In a crossed molecular beam experiment the NH$_3$ initial state preparation is achieved by rotational cooling in a supersonic expansion into vacuum, followed by an electrostatic state selection process In this way we succeeded in preparing almost exclusively the 0_0^+ state for ortho-NH$_3$ and the 1_1^- state for para-NH$_3$ Before and after the scattering event the rotational state distribution in the vibronic ground state of the ammonia molecule was probed by means of 2+1 REMPI spectroscopy via the electronic $\bar{B}$ state of NH$_3$

The experimentally obtained inelastic cross sections are compared with calculated values derived from CS and CC quantum scattering calculations based on two different ab initio potential energy surfaces for both NH$_3$-ortho-H$_2$ and NH$_3$-para-H$_2$ collision systems A comparison of the parity averaged state-to-state cross sections between experiment and theory yields good agreement for both ortho-H$_2$ and para-H$_2$ as collider Theory predicts strong parity propensity rules for NH$_3$-para-H$_2$ scattering, which are observed in experiment only to a slight extent The results for the NH$_3$-para-H$_2$ collisions are compared with the state-to-state collision cross sections for NH$_3$-He scattering, obtained from a previous study Considerable differences between para-H$_2$ and He are observed for collisional excitation to the lowest rotational states of NH$_3$, which has important consequences for the calculation of astrophysical rate coefficients

4.7 Acknowledgement

Chapter 5
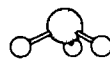
State-to-State Cross Sections
For Rotational Excitation Of Ortho And Para NH$_3$
By Collisions With Ar

J Schleipen and J J ter Meulen
Department of Molecular and Laser Physics, University of Nijmegen,
Toernooiveld, 6525 ED Nijmegen, The Netherlands

G C M van der Sanden, P E S Wormer and A van der Avoird
Institute of Theoretical Chemistry, University of Nijmegen,
Toernooiveld, 6525 ED Nijmegen, The Netherlands

Parity resolved state-to-state cross sections for rotational and tunneling inversion excitation of ortho- and para- NH$_3$, colliding with Ar, have been obtained in a crossed molecular beam experiment State preparation of the 0_0^+ state for ortho-NH$_3$ and the 1_1^- state for para-NH$_3$ is achieved by adiabatic expansion of ammonia followed by electrostatic state selection in a hexapole electric field The NH$_3$ rotational state distribution is probed by 2+1 REMPI spectroscopy via the $\tilde{B}$ state The scattering experiments have been performed at two collision energies, 282 cm^{-1} and 451 cm^{-1}, by varying the NH$_3$ molecular beam velocity The experimental values for the relative cross sections are compared with the results from close coupling calculations using an ab initio potential Also a modified potential scaled to spectroscopic data for the NH$_3$-Ar complex is considered For ortho-NH$_3$ observed parity propensities are in good agreement with theoretical predictions In the case of para-NH$_3$ discrepancies are present For the parity averaged rotational excitation a reasonably good agreement between experiment and theory is obtained
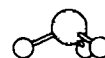
5.1 Introduction

The study of rotational energy transfer in atom - molecule and molecule - molecule collision processes has been the subject of many experimental and theoretical investigations The interest in this energy transfer problem has particularly intensified since non-thermal microwave absorption and emission of radiation and even maser emission has been observed from several important, small molecules inside our galaxy, such as molecular hydrogen, the hydroxyl radical, formaldehyde and ammonia [1, 2, 68] In order to account for the anomalous optical behavior of these molecules models have been developed based on collision induced rotational energy transfer In these models radiative and collisional decay of a molecule is in competition with collisional excitation of rotational states, arising from the interaction with its surrounding molecules, mainly molecular hydrogen In order to test and verify these models there is a need for rate constants for rotational energy transfer In other words, energy dependent collision cross sections are needed for excitation to specific rotational levels of the molecule under study

Many experiments have been performed the last twenty years in order to measure these rate constants or cross sections for several small molecules like the ones mentioned above Depending on the type of experiment different information was obtained on the energy transfer process The first experiments were performed in the bulk gas phase and yielded temperature dependent rate constants By the application of molecular beam techniques it was possible to obtain the first energy dependent cross sections State specific cross sections could be measured first by means of microwave double resonance experiments And only in the last decade it has become possible to use narrow band laser radiation in order to probe individual rotational states and measure differential and integral state-to-state rotational cross sections

Together with these experiments theoreticians were active in calculating these cross sections starting from first principles, that is from the intermolecular potential governing the microworld of the two approaching molecules Especially the development of larger and faster computers the last decade has accelerated these theoretical investigations enormously In this way the outcome of scattering experiments was not only input for the astrophysicist, but also for the development of a quantum mechanically correct molecular scattering theory

From this scattering theory we know that the rotational energy transfer is mainly governed by the anisotropic repulsive part of the potential energy surface So, measuring cross sections for rotational energy transfer provides additional information on the repulsive wall of the potential Additional in the sense that the potential energy surface can already be probed experimentally by means of spectroscopy When the two interacting particles come close together and the energy in the NH_3-Ar scattering event is low enough, a van der Waals bond between the ammonia molecule and the Ar atom can be established In this way the attractive part of the potential energy surface is probed and spectroscopic data can give us information on this part of the potential Microwave and (far-) infrared spectroscopy on the NH_3-Ar van der Waals molecule [80, 81, 82, 83] has been used in the past to model an empirical intermolecular potential which in turn could be used to predict unknown spectroscopical features However, this empirical potential is based only on data probed in the attractive well region of the intermolecular potential Now state-to-state collision experiments in combination with scattering theory can be used as two complementary techniques to construct an intermolecular potential as accurately as possible

The rotational energy level scheme of the NH_3 molecule is that of an oblate symmetric top, i e for increasing K, the projection of $\vec{J}$ onto the NH_3 molecular symmetry axis, the rotational energy decreases Due to the tunneling motion inside the NH_3 molecule all rotational levels J_K

are split into two states J_K^ϵ ($\epsilon = \pm 1$), in which ϵ denotes the symmetry of the rotation-inversion wavefunction with respect to this tunneling motion. The parity of the overall molecular wavefunction is then given by $\epsilon \cdot (-1)^{K-J+1}$ [29]. In Chapters 3 and 4 of this thesis we reported collision experiments on the NH₃ - He and NH₃ - H₂ systems in which a single initial state of NH₃ was prepared, $J_K^\epsilon = 0_0^+$ for ortho-NH₃ and 1_1^- for para-NH₃ [62]. The experiments yielded relative parity-resolved integral state-to-state cross sections for rotational excitation of ammonia upon collisions with helium and molecular hydrogen. An interesting feature in performing these scattering experiments is the study of theoretically predicted parity-propensity rules: for some rotational excitations a strong preference for exciting one specific parity state is expected [84]. In our previous experiment we found that the experimentally observed parity propensity was much weaker than the theoretical propensities or did not even exist. However, no quantum mechanically correct theory was available at that time for the relatively high collision energy we used and the comparison with theory had to be made with great care. In this study we present the results of a similar state-to-state scattering experiment carried out for the NH₃-Ar system. Furthermore we performed a quantum mechanically exact close coupling calculation on this system, using a NH₃-Ar ab initio intermolecular potential and a potential scaled to data obtained from far-infrared spectroscopy on the NH₃-Ar van der Waals molecule.

In section 5.2 the experiment is described in short. Where necessary we refer to an earlier experiment [62] for details. In section 5.3 the experimental data are presented and compared with cross sections obtained from the close coupling scattering calculations. Details of the scattering calculations are published in a Chapter 6.

5.2 Experimental

The experimental set-up has been described in full detail in Chapter 3. Two pulsed molecular beams are crossed at right angles, using two modified Bosch-type fuel injectors with a pulse width (FWHM) of about 1 millisecond. The primary NH₃ molecular beam is produced by expanding 1 % NH₃ in a carrier gas Ar, respectively Xe, at a backing pressure of 1 bar. During operation of both molecular beam valves the pressure inside the vacuum chamber did not exceed 10^{-5} mbar. The use of Ar and Xe as a carrier gas results in a different velocity of the expanding primary beam molecules and hence collision experiments can be performed at different collision energies. It can be shown [85] that for small seeding ratios the beam velocity is inversely proportional to the square root of the mass of the carrier gas. We measured the velocity of the primary beam in both cases by means of a fast ionization gauge positioned on the beam axis. By varying the distance from nozzle to ionization gauge and measuring the corresponding flight times we estimated the velocities to be $v_{NH_3} = 670(30)$ m/s when seeding in argon and $v_{NH_3} = 280(16)$ m/s when seeding in xenon. From an analysis of the shape of the molecular pulse in timespace we estimated the spread in the velocity distribution to be $\Delta v_{FWHM}/\bar{v} \approx 20$ %.

Once the expansion has taken place the NH₃ molecular pulse is shaped into the primary beam by a skimmer about 20 mm downstream from the nozzle orifice. Next, the NH₃ molecules travel through an electrostatic state selector positioned on the primary beam axis. Use is made of a hexapole which acts as an electrostatic positive lens for those NH₃ molecules possessing a positive Stark effect and as a negative lens for the ones having a negative Stark effect. The state selector we used is 230 mm long and consists of six 2 mm diameter rods at a distance of 2 mm from each other. The hexapole is operated at voltages up to 25 kV, well below electrical breakdown. The focus of the state selector occurs about 80 mm behind the exit opening of the hexapole and coincides with
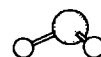
the scattering volume and detection region

The secondary beam of Ar atoms is produced in a differentially pumped vacuum chamber, separated from the scattering chamber by a 5 mm diameter skimmer. By the two skimmers the scattering region is geometrically confined to within a volume of about 8x8x8 mm³. Careful checks [62] have been performed in order to be sure that collisional effects are linear with secondary beam density. In order to avoid secondary or higher order collisions the backing pressure of the secondary beam was kept below 500 mbar.

In the scattering volume the ammonia molecules are detected state selectively by means of a 2+1 REMPI process via the $\tilde{B}$ electronic state of NH_3. For details on the NH_3 2+1 REMPI spectroscopy we refer to the extensive work of Ashfold et al. [27] and Glownia et al. [57]. All the relevant spectroscopic data such as wavelengths and line strengths can be found in Chapter 2 of this thesis.

In order to probe the individual rotational states, two vibrational bands $\tilde{B}(0) \leftarrow \tilde{X}(0)$ and $\tilde{B}(1)$ $\leftarrow \tilde{X}(0)$ in the NH_3 molecule at one-photon wavelengths 337 nm and 332 nm respectively, have to be measured. For this purpose the output of a XeCl excimer laser pumped dye laser is focused into the scattering region with a f=25 cm lens. The dye laser operates at PTP dye, lasing between 330 and 350 nm. The ions produced in the REMPI process are extracted from the scattering volume by means of a conventional particle multiplier in combination with a repeller plate. The signal is then processed by a boxcar averager and directed to a recorder and AT computer. During the measurements the UV power is recorded simultaneously so that afterwards the scattering signal can be corrected for the quadratic laser power dependence.

Initial state preparation is achieved by the supersonic expansion and subsequent cooling of the internal degrees of freedom of the NH_3 molecules. The rotational temperature of the NH_3 molecules is somewhat lower for a NH_3/Xe mixture than for a NH_3/Ar mixture. In the latter case, for ortho-NH_3 the lowest rotational state, $J_K^\epsilon = 0_0^+$, contains almost 90 % of all ortho population. About 8 % is populated in the next higher rotational state, $J_K^\epsilon = 1_0^+$. For para-NH_3 the two lowest rotational states $J_K^\epsilon = 1_1^\pm$ are almost equally populated after the expansion (see Chapter 3, section 3.2) and contain about 92 % of the total para population. The net effect of the electrostatic state selection is that the 1_1^- population is increased by a factor of 20 with respect to the 1_1^+ population. We thus succeeded in preparing a single rotational state $J_K^\epsilon = 1_1^-$ also for para-NH_3. For details on the state selection procedure we refer to Chapter 3 of this thesis.

5.3 Results and interpretation

As shown in Chapter 3 the single state-to-state collision cross section σ_{if} for scattering out of state $|i\rangle$ into state $|f\rangle$ can be deduced from the scattering spectra in a rather straightforward manner if single collision conditions are fulfilled. The final state in the scattering process $|f\rangle$ is probed by means of a two-photon transition to state $|f'\rangle$ in the vibronically excited $\tilde{B}(v')$ state of the NH_3 molecule, yielding the 2+1 REMPI signal $S_{ff'}$. The scattering signal $\delta S_{ff'}$ represents the change in signal $S_{ff'}$ upon collisions with the secondary beam molecules. From these scattering signals $\delta S_{ff'}$ the cross sections $\sigma(i \rightarrow f)$ can be deduced from the following formulae

$$\sigma(0_0^+ \rightarrow f) \propto \frac{\delta S_{ff'}}{n(0_0^+)\ \mathcal{L}_{ff'}\ P_{ff'}^2\ q_{v'}\ E_{v'}} \qquad , v' = 0, 1, f \in ortho - NH_3 \qquad (5.1)$$

$$\sigma(1_1^- \to f) \propto \frac{\delta S_{ff'}}{n(1_1^-) \cdot \mathcal{L}_{ff'} \cdot P_{ff'}^2 \cdot q_{v'} \cdot E_{v'}} \quad ; v' = 0, 1; f \in para - NH_3 \qquad (5.2)$$

In these formulae $\mathcal{L}_{ff'}$ represents the two-photon rotational linestrength of the transition, taken from [33], $q_{v'}$ is the Franck-Condon factor for the vibronic transition $\tilde{B}(v') \leftarrow \tilde{X}(0)$, where $v' = 0$ or 1, $P_{ff'}^2$ is the square of the laser power at the specific transition frequency and $E_{v'}$ represents the experimental sensitivity determined by the gain of the particle multiplier and the sensitivity of the boxcar. The product of Franck-Condon factor and experimental sensitivity, $q_{v'} \cdot E_{v'}$, could not be determined and hence only relative collision cross sections have been obtained. For further details we refer to section 3 of Chapter 3.

Ortho-NH₃; $\sigma(0_0^+ \to J_K^\epsilon)$ E = 282 cm⁻¹				Ortho-NH₃; $\sigma(0_0^+ \to J_K^\epsilon)$ E = 451 cm⁻¹			
J_K^ϵ	Experiment	Theory unscaled	Theory scaled	J_K^ϵ	Experiment	Theory unscaled	Theory scaled
1_0^+	6.07	11.06	3.82	1_0^+	4.33	7.92	5.53
2_0^+	6.73	8.45	13.20	2_0^+	5.72	10.10	11.02
3_0^+	2.19	4.16	2.51	3_0^+	2.38	3.94	1.77
4_0^+	0.48	0.35	2.44	4_0^+	1.73	0.46	3.04
6_0^+	-	-	-	6_0^+	1.01*	0.07	0.12
3_3^-	12.23	9.04	10.65	3_3^-	14.23	11.70	13.12
3_3^+	3.43	1.54	0.70	3_3^+	1.68	1.32	0.83
4_3^-	5.77	3.38	1.87	4_3^-	4.90	2.52	2.07
4_3^+	1.31	0.23	0.44	4_3^+	2.70	0.65	0.82

Table 5.1 : *State-to-state cross sections for ortho-NH₃-Ar collisions [in Å²]. The experimental error is 10%. Experimental data are compared with the corresponding theoretical cross sections, obtained using the unscaled ab initio potential V_I and the scaled potential V_{II}. Cross sections marked with an asterisk have an experimental error of 20 %. The experimental data represent relative cross sections, the sum of which is set equal to the sum of the theoretical cross sections obtained from the unscaled potential.*

From the scattering spectra the parity resolved state-to-state cross sections σ_{if} were obtained using the relations between the collision induced signal δS and σ_{if} as given in Equations (5.1) and (5.2). In Tables 5.1 and 5.2 the cross sections for the collisional excitation by Ar are presented for ortho- and para-NH₃, respectively. The experimental error is given by the standard deviation obtained from averaging typically 15 to 20 scattering results for the same cross section. This averaging procedure resulted in an experimental error of 10 % for most cross sections. However,
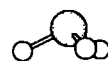
some cross sections have to be specified with a somewhat larger error of about 20 %; these are marked with an asterisk. In Figures 5.1 and 5.2 the cross sections σ_{if} are presented graphically for both NH_3 species. Figures 5.1.a and 5.1.b show the ortho- and para-NH_3 results respectively for the low energy experiment. In Figures 5.2.a and 5.2.b the results are derived from the high energy experiment.

A first inspection of the experimental results leads to the following conclusions. For ortho-NH_3 first of all we see a definite parity propensity for the cross sections for exciting the $K = 3$ levels. Scattering into states 3_3^- and 4_3^- is strongly preferred over scattering into the opposite parity states 3_3^+ and 4_3^+. This same behaviour was observed earlier for the NH_3-He collision experiment. These parity propensity rules seem to be sensitive to the collision energy in the scattering process. When increasing the collision energy the parity propensity for the $J_K = 3_3$ state grows stronger whereas the propensity for the $J_K = 4_3$ state is now less pronounced. For the $K = 0$ manifold we see that the cross section $\sigma(0_0^+ \rightarrow 1_0^+)$ is somewhat decreasing in going from the low to the high energy scattering. When comparing the cross sections with the results obtained for He collisions [62], we notice that relative to $\sigma(0_0^+ \rightarrow 1_0^+)$ the cross section for excitation to the 2_0^+ state is about a factor of 2 smaller, whereas the excitation to the 3_3^- state is clearly more efficient. For para-NH_3 we see a strong parity propensity for excitation to the $J_K = 2_2$ rotational level which is also observed in the NH_3-He collision experiment. This propensity is strongest for the low energy experiment. A remarkable feature for para-NH_3 is the observed reversal of a (weak) parity propensity for excitation to the $J_K = 2_1$ level when changing the collision energy from 282 cm^{-1} to 451 cm^{-1}. In comparison with the para-NH_3 - He results the cross sections for $\Delta K = 0$ transitions are smaller relative to the cross sections for $\Delta K = 3$ excitations to the $K = 2$ states.

In the next two sections the experimental data are compared to the theoretical values for the cross sections. In performing the dynamical scattering calculations the quantum mechanical close coupling formalism is used in order to extract the collision cross sections from the intermolecular potential. The calculations were carried out with the Hibridon inelastic scattering code [1]. For the NH_3-Ar interaction the potential energy surface V_I is based on ab initio calculations performed by Bulski et al. [86]. Furthermore, a second scattering calculation uses a scaled potential V_{II}, in which the short range contribution to the anisotropic term V_{33} is scaled in order to reproduce far-infrared spectroscopic data for the NH_3-Ar van der Waals complex [87]. Both potential energy surfaces V_I and V_{II} account for the NH_3 tunneling motion. Up to now it is generally believed that the tunneling motion inside the NH_3 molecule can be considered as being frozen during the comparatively short collision time and hence the inelastic collision cross section is not expected to depend on the inversion motion [50]. In this study the tunneling motion of the NH_3 molecule during the collision interaction is explicitly taken into account by means of this tunneling potential depending on the inversion coordinate ρ [86]. To our knowledge this theoretical study is the only one available up to now for the NH_3-Ar collisional system. The dynamical scattering calculations are carried out at both the experimental energies of 282 cm^{-1} and 451 cm^{-1}. The full details and results of the calculational efforts are given in Chapter 6.

In Tables 5.1 and 5.2 the experimental and theoretical data are compared for both collision energies. There are two columns with theoretical values, depending on the potential used in performing the scattering calculations. In the first theoretical column the unscaled ab initio potential

---

[1]Hibridon is a package of programs for the time-independent quantum treatment of inelastic collisions and photodissociation, written by M.H. Alexander, D. Manolopoulos, H.-J Werner and B. Follmeg, with contributions by P.F. Vohralik, G. Corey, B. Johnson and P. Valiron.
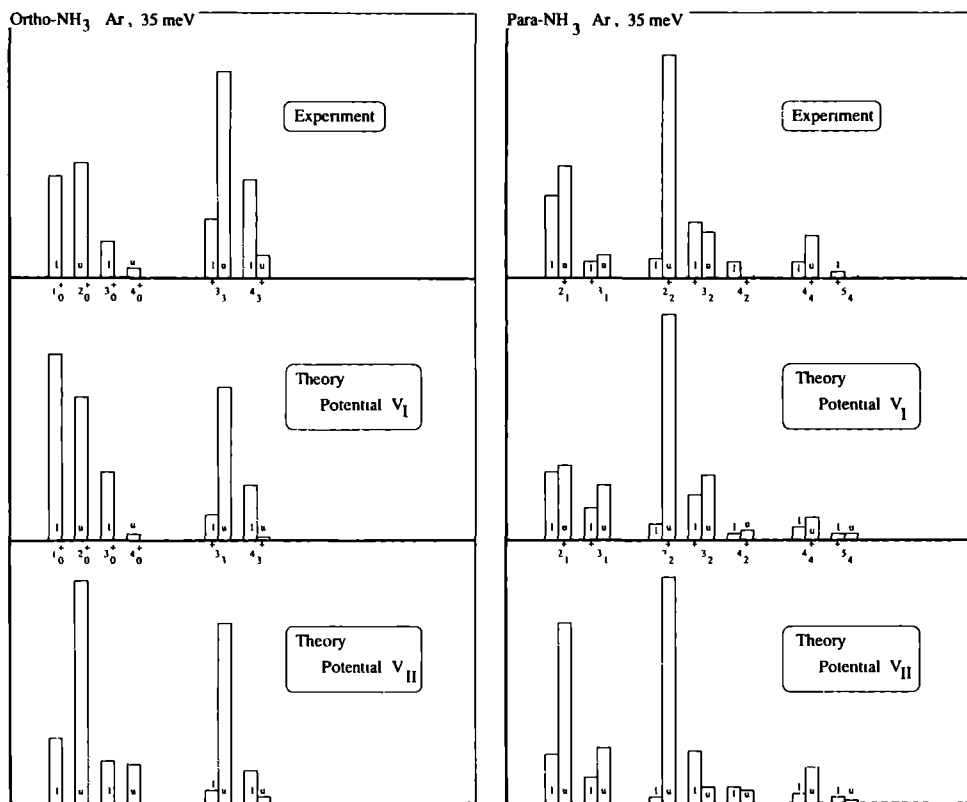
Figure 5.1 : *Relative state-to-state cross sections $\sigma(0_0^+ \rightarrow J_K^\epsilon)$ for scattering of ortho-NH₃ (Figure 5 1 a) and $\sigma(1_1^+ \rightarrow J_K^\epsilon)$ for scattering of para-NH₃ (Figure 5 1 b) by Ar for the low collision energy $E_{coll} = 282$ cm^{-1} Each bar corresponds with one rotational state J_K^ϵ The character l(u) denotes the lower (upper) level of the J_K doublet The experimental results are compared with the data obtained from close coupling calculations using an ab initio potential V_I and a potential V_{II} scaled to spectroscopical data for the NH₃-Ar van der Waals complex*
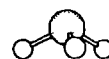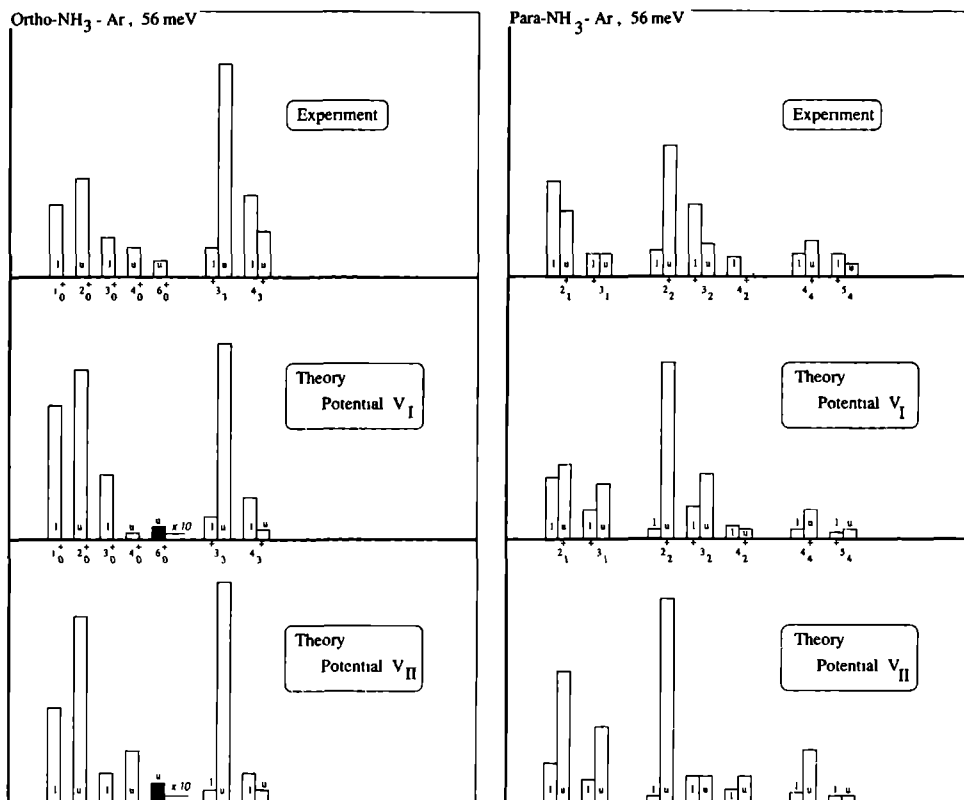
Figure 5.2 : *Same as Figure 5 1, but now for the high collision energy experiment with*
$E_{coll} = 451 \; cm^{-1}$.

V_I is used whereas in the second column the scaled potential V_{II} was applied. All collision cross sections are normalized in such a way that the sum of the cross sections over all states equals the sum of the calculated cross sections using V_I. This is allowed due to the fact that our experiment only yields relative values for the state-to-state cross sections.

5.3.1   Ortho-NH$_3$

For ortho-NH$_3$ a comparison of the experimental data with theoretical data obtained from the unscaled potential V_I shows a reasonable overall agreement for both energies. However, a few discrepancies have to be noticed. In going from the high to the low collision energy experiment the cross section for excitation to the 1_0^+ state grows stronger with respect to e.g. $\sigma(0_0^+ \to 2_0^+)$; the relative increase of $\sigma(0_0^+ \to 1_0^+)$, defined as

$$I = \frac{\sigma(0_0^+ \to 1_0^+;\ 282\ \text{cm}^{-1}) - \sigma(0_0^+ \to 1_0^+;\ 451\ \text{cm}^{-1})}{\sigma(0_0^+ \to 1_0^+;\ 451\ \text{cm}^{-1})} \tag{5.3}$$

is about the same for theory ($I = 0.396$) and experiment ($I = 0.402$).

With respect to the $K = 3$ manifold we see that for both collision energies the collisional excitations to states $J_K^\epsilon = 4_3^-$ and $J_K^\epsilon = 3_3^-$ are measured a factor of two stronger compared to the $K = 0$ state cross sections than would be expected from theory. As in the previous experiments on the NH$_3$-He and NH$_3$-H$_2$ systems we observe a substantial population transfer from the 0_0^+ state into the 3_3^+ and 4_3^+ states. For the NH$_3$-He collisions the available calculations which are based on the coupled states approximation predict cross sections equal to zero for these transitions. In the present approach the 3_3^+ and 4_3^+ states are populated and even a remarkably good agreement is obtained with experiment for the ratios $P(3_3)$ and $P(4_3)$. Here $P(J_K)$ is a quantitative measure for the parity propensity involving collisional excitation to state J_K and is defined as:

$$P(J_K) = \frac{\sigma(i \to J_K^+) - \sigma(i \to J_K^-)}{\sigma(i \to J_K^+) + \sigma(i \to J_K^-)} \tag{5.4}$$

where i denotes the initially prepared state 0_0^+ or 1_1^-. For the low collision energy $P_{exp}(3_3) = -0.56$ for experiment and $P_{th}(3_3) = -0.71$ for the unscaled ab initio calculations. For $J_K = 4_3$ we obtain $P_{exp}(4_3) = -0.63$ and $P_{th}(4_3) = -0.87$. In case of the high collision energy experiment we have $P_{exp}(3_3) = -0.79$, $P_{th}(3_3) = -0.79$ and $P_{exp}(4_3) = -0.29$, $P_{th}(4_3) = -0.59$. The breakdown of the parity selection rules, where $P(J_K)$ would be -1, is due to Coriolis type interactions which are neglected in the coupled states approximation. This is confirmed by close coupling calculations of Offer and Flower on the more complicated NH$_3$-H$_2$ system [46, 47].

5.3.2   Para NH$_3$

Also for para-NH$_3$ the overall agreement with theory is quite reasonable. Here, a similar problem with respect to the parity propensity shows up as is pointed at in our previous work on NH$_3$ - He and NH$_3$ - H$_2$ collisional excitation [62]. In coupled states calculations a strong parity propensity is predicted for excitation to the $J_K^\epsilon = 2_2^+$ state whereas the experiment shows that still a sizable excitation takes place to the 2_2^- state. In the present study, however, the relative size of the theoretical cross sections for the $1_1^- \to 2_2^-$ transition in comparison with the $1_1^- \to 2_2^+$ excitation is in good agreement with the experiment. For the other states the parity propensity is more or less

	Para NH$_3$, $\sigma(1_1^- \to J_K^\epsilon)$ $E = 282$ cm^{-1}				**Para NH$_3$, $\sigma(1_1^- \to J_K^\epsilon)$** $E = 451$ cm^{-1}		
J_K^ϵ	Experiment	Theory unscaled	Theory scaled	J_K^ϵ	Experiment	Theory unscaled	Theory scaled
2_1^+	6 49	4 40	10 73	2_1^+	3 84	4 39	7 72
2_1^-	4 82	4 22	2 82	2_1^-	5 62	3 62	2 23
3_1^+	0 91	2 00	1 57	3_1^+	1 38	1 65	1 26
3_1^-	1 39*	3 35	3 27	3_1^-	1 40	3 24	4 55
2_2^+	13 29	13 48	13 30	2_2^+	7 86	10 52	12 13
2_2^-	1 22	0 99	0 47	2_2^-	1 53	0 62	0 44
3_2^+	3 33	2 64	3 06	3_2^+	4 35	1 96	1 46
3_2^-	2 63	3 90	1 05	3_2^-	1 99	3 94	1 56
4_2^+	-	0 59	0 75	4_2^+	-	0 71	1 58
4_2^-	1 00	0 52	0 97	4_2^-	1 21*	0 79	0 71
4_4^+	2 49	1 25	2 15	4_4^+	2 15*	1 72	3 10
4_4^-	0 82*	0 69	0 52	4_4^-	1 27	0 56	0 49
5_4^+	0 45*	0 39	0 39	5_4^+	1 28*	0 44	0 37
5_4^-	-	0 42	0 22	5_4^-	0 77	0 49	0 31

Table 5.2 : *State-to-state cross sections for para NH$_3$-Ar collisions [in Å^2] The experimental error is 10% Experimental data are compared with the corresponding theoretical cross sections, obtained using the unscaled ab initio potential V_I and the scaled potential V_{II} Cross sections marked with an asterisk have an experimental error of 20 % The experimental data represent relative cross sections, the sum of which is set equal to the sum of the theoretical cross sections obtained from the unscaled potential*

confirmed by experiment. However, when comparing the absolute magnitude of the propensity $P(J_K)$ the agreement between theory and experiment is rather poor. Reversal of the predicted parity propensity rules is even observed for excitation to the states $J_K = 2_1$ and 3_2.

In order to check the pure rotational energy transfer for para-NH_3 we summed all individual cross sections $\sigma(1_1^- \rightarrow J_K^\epsilon)$ over both parity states ($\epsilon = \pm 1$), yielding parity averaged rotational cross sections $\sigma(1_1^- \rightarrow J_K)$. In Figure 5.3 a graphical presentation of these cross sections is given for both energies. From this figure it is clear that the parity averaged cross section for exciting a J_K rotational state is decreasing faster as a function of rotational energy transfer for the low collision energy experiment. Of course, this is what one would expect from a simple energy gap law: the higher the collision energy, the larger the probability of excitation to a high-energy rotational state. This collision energy dependence is also reflected in both calculations. Furthermore we see that for the $K = 1$ manifold the cross section for excitation to the 3_1 rotational state, compared to the one for excitation to the 2_1 state, is predicted stronger in comparison with experiment for both collision energies. For all other states the agreement between experimentally and theoretically determined parity averaged cross sections is fairly good.

5.3.3 Discussion

In Chapter 3 we suggested that in order to get a better agreement with experiment, the inversion coordinate should be explicitly taken into account in the scattering calculations. In this study the theoretical collision cross sections are obtained using potentials V_I and V_{II}, including the inversion motion within the NH_3 molecule via the inversion coordinate ρ. Calculation of the cross sections in this case involved solving the ρ-dependent tunneling wavefunctions and subsequent integration over ρ. We also performed a close coupling calculation using both potentials V_I and V_{II} without the inclusion of the inversion coordinate explicitly. In this case the model of Green [40, 88] is used to describe the NH_3 tunneling motion using delta-functions for the inversion wavefunctions, localized at the equilibrium positions $\rho = \pm\rho_e$. In the next chapter we compare both calculations and as a result we may conclude that, at least for the NH_3-Ar system, the inclusion of the inversion coordinate in the close coupling calculations has only a minor effect on the collision cross sections.

From the comparison between experiment and theory involving the potential energy surfaces V_I and V_{II} it is evident that the ultimate potential is not yet found. A comparison of both sets of theoretical data shows some remarkable differences between the unscaled ab initio potential V_I and the spectroscopically scaled potential V_{II}. For ortho-NH_3 the scaled potential V_{II} does not reflect certain characteristics of the experimental data. For instance, for the low energy experiment the cross sections $\sigma(0_0^+ \rightarrow 2_0^+)$ and $\sigma(0_0^- \rightarrow 4_0^+)$ are overestimated. The same is true for the high energy calculations; here $\sigma(0_0^- \rightarrow 4_0^+)$ is even stronger than $\sigma(0_0^- \rightarrow 3_0^+)$, which is not observed in the experiment and would be in contradiction with a simple energy gap law for the $K = 0$ manifold. Also for para-NH_3 scaling of the V_{33} term in the potential energy expansion series has a strong effect on the cross sections for transitions to the $J_K = 2_1$ and 3_2 states, yielding a worse agreement with experiment. Concluding we can state that a comparison of the experimental cross sections with both sets of theoretical data gives clearly a preference to the unscaled potential V_I. This is in contradiction with the spectroscopic results which can not be explained when applying the unscaled potential.

It is evident that the individual potential energy terms V_{lm} have a strong effect on the individual state-to-state cross sections. However, because of the complexity of the scattering formalism it is difficult to get a clear physical understanding of the individual potential terms. Furthermore,
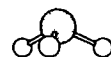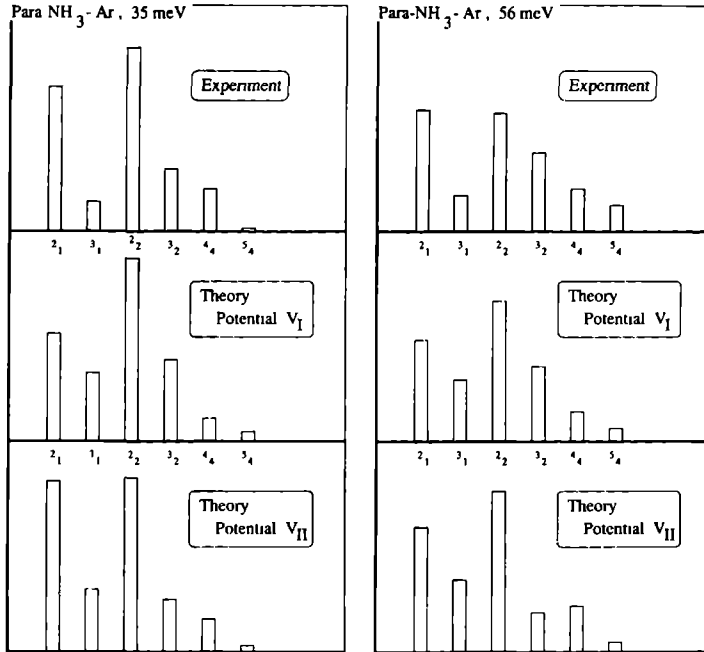
Figure 5.3 : *Parity averaged cross sections $\sigma(1_1^- \rightarrow J_K)$ for scattering of para-NH_3 by Ar Each bar corresponds with one averaged cross section $\bar{\sigma}(1_1^- \rightarrow J_K)$ The left part of the figure shows the cross sections for the low energy experiment whereas the right part gives the high energy cross sections The experimental data are compared with the calculated values using both potential energy surfaces V_I and V_{II}*

98

the potential terms V_{lm} not only give rise to the direct rotational excitation $\Delta J = l, \Delta K = m$, but due to the mixing of wavefunctions in the intermediate NH$_3$-Ar complex state, they can also give an important indirect higher-order contribution to excitations with $\Delta J \neq l$ or $\Delta K \neq m$. Assuming the close coupling scattering calculation being converged, the intermolecular potential can be refined by fitting the potential energy terms V_{lm} to the experimentally observed cross sections. However, this will be a hard job and the computational efforts needed to achieve this goal will be immense. Of course, the intermolecular potential obtained that way would also have to predict the experimental spectroscopic data.

As mentioned before, 8% of all ortho population is present in the 1_0^+ state after the initial state preparation. Consequently, this 1_0^+ state may give a contribution to the measured scattering signals. Assuming the cross sections $\sigma(1_0^+ \rightarrow J_K^\epsilon)$ are in the same order of magnitude as the cross sections for excitation out of the 0_0^+ state, it is a reasonable assumption that this contribution can be neglected within our experimental accuracy. However, it may show up whenever the cross section $\sigma(0_0^+ \rightarrow J_K^\epsilon)$ is small. The same is true for para-NH$_3$. Here the 1_1^+ state is slightly populated in the primary beam ($\approx 5\%$) and can give a contribution to the measured cross sections. The effects due to the initial population in excited states can be taken into account when comparing experiment with theory because the cross sections $\sigma(1_0^+ \rightarrow J_K^\epsilon)$ and $\sigma(1_1^+ \rightarrow J_K^\epsilon)$ are also known from the scattering calculations. When we assume that two states are initially prepared, the measured cross sections $\sigma(p \rightarrow J_K^\epsilon)$ are composed of two contributions. For ortho-NH$_3$ the measured cross section is not exactly equal to $\sigma(0_0^+ \rightarrow J_K^\epsilon)$ but in fact:

$$\sigma(p \rightarrow J_K^\epsilon) = 0.92 \cdot \sigma(0_0^+ \rightarrow J_K^\epsilon) + 0.08 \cdot \sigma(1_0^+ \rightarrow J_K^\epsilon) \tag{5.5}$$

For excitation of the 1_0^+ state an additional correction is made for scattering out of this initially populated state. The measured cross section is:

$$\sigma(p \rightarrow 1_0^+) = 0.92 \cdot \sigma(0_0^+ \rightarrow 1_0^+) - 0.08 \cdot \sum_{i \neq 1_0^+} \sigma(1_0^+ \rightarrow i) \tag{5.6}$$

For para-NH$_3$ a similar correction has to be made for the slightly populated 1_1^+ state. The measured cross section now is:

$$\sigma(p \rightarrow J_K^\epsilon) = 0.95 \cdot \sigma(1_1^- \rightarrow J_K^\epsilon) + 0.05 \cdot \sigma(1_1^+ \rightarrow J_K^\epsilon) \tag{5.7}$$

In Tables 5.3 and 5.4 we compare the measured cross sections with the corresponding composite theoretical cross sections. The results are not strikingly different from the conclusions obtained when studying the single theoretical cross sections of Tables 5.1 and 5.2 and hence it is a reasonably good assumption to neglect in first instance the contribution from these 1_0^+ and 1_1^+ states. However, for ortho-NH$_3$ a relatively strong effect due to these corrections is observed for excitation to the 1_0^+ state. For the unscaled potential V_I the corrected values for $\sigma(0_0^+ \rightarrow 1_0^+)$ are definitely better in agreement with the experiment. This indicates that a substantial amount of scattering takes place out of the 1_0^+ state. As a result of this the 'pure' cross section $\sigma(0_0^+ \rightarrow 1_0^+)$ as obtained from Equation (5.1), is measured too weak, which can be seen in Table 5.1. For the scaled potential V_{II} this correction changes the cross section $\sigma(0_0^+ \rightarrow 1_0^+)$ drastically and the agreement with experiment is even worse.

	Ortho NH$_3$; $\sigma(0_0^+ \to J_K^\epsilon)$ $E = 282$ cm^{-1}				Ortho NH$_3$; $\sigma(0_0^+ \to J_K^\epsilon)$ $E = 451$ cm^{-1}		
J_K^ϵ	Experiment	Theory unscaled	Theory scaled	J_K^ϵ	Experiment	Theory unscaled	Theory scaled
1_0^+	6.07	7.41	0.87	1_0^+	4 33	4.33	2 04
2_0^+	6.73	8.42	12.49	2_0^+	5 72	9 76	10.42
3_0^+	2 19	4.12	2 94	3_0^+	2 38	3.94	2.14
4_0^+	0.48	0.49	2.40	4_0^+	1.73	0.59	2 91
6_0^+	-	-	-	6_0^+	1.01*	0.07	0 13
3_3^-	12.23	8.56	9.96	3_3^-	14 23	10 93	12.21
3_3^+	3.43	2 17	1.53	3_3^+	1 68	2 07	1.92
4_3^-	5.77	3 29	1 91	4_3^-	4.90	2.59	2.15
4_3^+	1 31	0.32	0.50	4_3^-	2.70	0.75	0.87

Table 5.3 : *Same as Table 5 1   The theoretical data are corrected for the impure initial state preparation for ortho-NH$_3$ The theoretical cross sections are now composed of two state-to-state cross sections 0 92 $\sigma(0_0^+ \to J_K^\epsilon) + 0\ 08$ $\sigma(1_0^+ \to J_K^\epsilon)$ For $\sigma(1_0^+ \to J_K^\epsilon)$ a correction is made for out-scattering 0 92 $\sigma(0_0^+ \to 1_0^+) - 0\ 08$ $\sum_{i \neq 1_0^-} \sigma(1_0^+ \to i)$*

5.4   Conclusions

In this paper we report parity resolved state-to-state cross sections for rotational excitation of NH$_3$ upon collisions with Ar at two different collision energies. In a crossed molecular beam experiment the NH$_3$ initial state preparation is achieved by expanding an NH$_3$/Ar,Xe gas mixture into vacuum followed by an electrostatic state selection process In this way we succeeded in preparing almost exclusively the 0_0^+ state for ortho-NH$_3$ and the 1_1^- state for para-NH$_3$. Before and after the scattering event the rotational state distribution in the vibronic ground state of the ammonia molecule was probed by means of 2+1 REMPI spectroscopy via the electronic $\tilde{B}$ state of NH$_3$.

In comparison with previously obtained results for scattering by He we found a relatively strong $\Delta J = 1$ excitation for ortho-NH$_3$ and $|\Delta K| = 3$ excitation for both para and ortho species. In addition similar parity propensities were observed.

The experimentally determined inelastic cross sections were compared with theoretical values obtained from quantum scattering calculations. We used the quantum mechanical close coupling formalism in order to solve the scattering equations. The intermolecular potential for the NH$_3$-Ar system was obtained from ab initio calculations. Furthermore we performed a scattering calcula-

Para NH$_3$; $\sigma(1_1^- \to J_K^\epsilon)$ E = 282 cm^{-1}				Para NH$_3$; $\sigma(1_1^- \to J_K^\epsilon)$ E = 451 cm^{-1}			
J_K^ϵ	Experiment	Theory unscaled	Theory scaled	J_K^ϵ	Experiment	Theory unscaled	Theory scaled
2_1^+	6.49	4.39	10.33	2_1^+	3.84	4.35	7.45
2_1^-	4 82	4.23	3.21	2_1^-	5.62	3 66	2.50
3_1^+	0.91	2.06	1.66	3_1^+	1.38	1 73	1.43
3_1^-	1.39*	3.28	3.18	3_1^-	1 40	3 17	4.39
2_2^+	13.29	12.85	12.65	2_2^+	7.86	10 03	11.55
2_2^-	1.22	1.61	1 11	2_2^-	1.53	1.12	1 03
3_2^+	3.33	2.70	2.96	3_2^+	4.35	2.06	1.46
3_2^-	2.63	3.84	1.15	3_2^-	1.99	3.84	1.55
4_2^+	-	0.58	0 76	4_2^+	-	0 71	1.54
4_2^-	1.00	0.52	0.96	4_2^-	1.21*	0 79	0 75
4_4^+	2.49	1 23	2.07	4_4^+	2.15*	1 66	2.97
4_4^-	0.82*	0 72	0.60	4_4^-	1.27	0.62	0 62
5_4^+	0.45*	0.39	0.38	5_4^+	1.28*	0.45	0.37
5_4^-	-	0.42	0.23	5_4^-	0.77	0.48	0.31

Table 5.4 : *Same as Table 5 2   The theoretical data are corrected for the impure initial state preparation for para-NH$_3$ The theoretical cross sections are now composed of two state-to-state cross sections 0 95 $\sigma(1_1^- \to J_K^\epsilon) + 0\ 05\ \sigma(1_1^+ \to J_K^\epsilon)$*

tion in which this potential was scaled to spectroscopical data. This scaled potential however did not reproduce the experimental scattering data adequately. The unscaled, 'true' ab initio potential is therefore preferred to describe the NH$_3$-Ar collision process. We also used a potential without inclusion of the inversion coordinate. The collision cross sections obtained that way showed only minor differences with the ones derived using the tunneling potential The comparison between experiment and theory showed good agreement as far as pure rotational energy transfer is concerned. For ortho-NH$_3$ the close coupling technique has proven to be an adequate device to predict also the correct parity propensity rules. For para-NH$_3$ the experimentally determined parity propensities deviate from the theoretically predicted propensity rules. In comparing theoretical and experimental parity averaged cross sections for para-NH$_3$ the agreement is reasonably good.
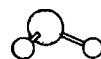
5.5   Acknowledgement

Chapter 6

Close Coupling Calculations On Rotational Excitation And Inversion Of NH$_3$ By Collisions With Ar

G.C.M. van der Sanden, P.E.S. Wormer and A. van der Avoird
Institute of Theoretical Chemistry, University of Nijmegen,
Toernooiveld, 6525 ED Nijmegen, The Netherlands

J. Schleipen and J.J. ter Meulen
Department of Molecular and Laser Physics, University of Nijmegen,
Toernooiveld, 6525 ED Nijmegen, The Netherlands

State-to-state total cross sections for rotational excitation and inversion of NH$_3$ by collisions with Ar have been calculated within the accurate close coupling framework. The inversion motion in NH$_3$ was included both via a delta function model and by taking the inversion coordinate explicitly into account. We used an ab initio potential and a potential in which one term in the angular expansion of the ab initio potential is scaled in order to reproduce spectroscopic data. At the energies used in these calculations the delta function model is found to be in nearly quantitative agreement with the exact tunneling results. A comparison with experiment shows the ab initio potential to be better than the scaled one. The results of the calculations for ortho- NH$_3$ are in general accord with the measurements. For para- NH$_3$ the relative magnitudes of the cross sections to the two inversion states are not reproduced correctly for all levels.
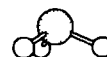
6.1 Introduction

The last few years it has become possible to obtain state-to-state cross sections for transitions between rotation-inversion states of NH_3, induced by collisions with various perturbers Advances in molecular beam techniques have made it experimentally feasible to distinguish between the symmetric and antisymmetric states of the inversion doublets The close coupling (CC) method for the accurate quantum mechanical treatment of the problem has been well established theoretically for quite some time However, computer systems that meet the computational demands have only recently become available

In this chapter we consider collisions of NH_3 with Ar This study was undertaken mainly for two reasons Firstly, comparison of theoretical results with experimental data enables us to determine the accuracy of the intermolecular potential energy surface [86], in the region that is probed in scattering experiments In addition we used a somewhat different potential in order to gain some understanding of the sensitivity of the cross sections to variations in the potential surface The second potential contains a scaling parameter that was chosen to account for spectroscopic bound states data In particular, we wanted to see whether a variation that improved bound state results would also improve the outcome of the scattering calculations

Secondly, we investigate how the description of the umbrella inversion of NH_3 influences the cross sections Until now, the monomer inversion has been included in scattering calculations on NH_3 only via a model in which the wavefunction is a linear combination of two delta functions centered at the equilibrium positions (Davis and Boggs [50], Green [29]) Although the model seemed to have its justification in the fact that the period for inversion is much longer than the duration of a collision, it was not clear whether deviations from predicted propensity rules could be attributed to the neglect of the inversion motion in the description of the intermolecular potential [62, 89] Here we take the inversion degree of freedom explicitly into account in order to assess exactly how severe an approximation is made in neglecting it

Finally, we have performed some calculations using the much cheaper coupled states (CS) approximation to find out how this approximation affects the calculated cross sections as compared to the CC results In the calculations on He–NH_3 using the CS method [15] certain theoretical cross sections are found to be equal or almost equal to zero, whereas the experimental cross sections are significantly different from zero [41] By applying the CS approximation, together with our Ar–NH_3 potential surface, we can establish to what extent deviations are caused by the method

6.2 Theory

The coordinate system used in the CC method is the space-fixed frame [40] The vector $\vec{R}$, with polar angles (β, α) in this frame, points from the NH_3 center of mass to the Ar nucleus The orientation of NH_3 is given by the Euler angles $(\gamma, \vartheta, \varphi)$, where γ and ϑ are the usual spherical polar angles of the symmetry axis of NH_3 with respect to the space fixed frame and φ is the third Euler angle describing a rotation of the symmetric top around its symmetry axis In the geometry $\gamma = \vartheta = \varphi = 0$, the nitrogen is on the positive z-axis and one of the protons is in the xz plane with a positive x-component The inversion coordinate ρ is defined as the angle between the C_3 axis and one of the N–H bonds

The rotation-inversion scattering Hamiltonian can be written as

$$\hat{H} = \hat{H}_{umb}(\rho) + \hat{H}_{vdw}(\gamma, \vartheta, \varphi, R, \beta, \alpha, \rho) \tag{6 1}$$

The Hamiltonian for the umbrella motion of the NH$_3$ monomer which depends only on the internal coordinate ρ is designated by $\hat{H}_{\text{umb}}$. It describes both the fast umbrella vibration (ν_2) and the slow inversion tunneling. If the threefold symmetry is retained and the N–H distance is kept fixed at r_0, $\hat{H}_{\text{umb}}$ is given by [30, 90]

$$\hat{H}_{\text{umb}} = -\tfrac{1}{2}\hbar^2 g(\rho)^{-1/2} \frac{\partial}{\partial\rho} I_{\rho\rho}^{-1}(\rho) g(\rho)^{1/2} \frac{\partial}{\partial\rho} + V_{\text{umb}}(\rho) \,, \tag{6.2}$$

where

$$
\begin{aligned}
g(\rho) &= I_{xx}(\rho)I_{yy}(\rho)I_{zz}(\rho)I_{\rho\rho}(\rho) \,, \\
I_{xx}(\rho) &= I_{yy}(\rho) = 3m_H r_0^2(\tfrac{1}{2}\sin^2\rho + \zeta\cos^2\rho) \,, \\
I_{zz}(\rho) &= 3m_H r_0^2 \sin^2\rho \,, \\
I_{\rho\rho}(\rho) &= 3m_H r_0^2(\cos^2\rho + \zeta\sin^2\rho) \,, \\
\zeta &= m_N/(3m_H + m_N) \,.
\end{aligned}
\tag{6.3}
$$

Here $g(\rho)$ is the determinant of the metric tensor $\vec{\vec{g}} = \text{diag}(I_{xx}, I_{yy}, I_{zz}, I_{\rho\rho})$ in a curvilinear coordinate system; m_H and m_N are the masses of the hydrogen and nitrogen nuclei. The quantities I_{xx}, I_{yy} and I_{zz} are the moments of inertia of NH$_3$, which depend on the inversion coordinate ρ. The generalized moment of inertia $I_{\rho\rho}$ is associated with the umbrella motion and depends also on the inversion coordinate. The double well potential $V_{\text{umb}}(\rho)$ is represented by a harmonic force field augmented by a Gaussian

$$V_{\text{umb}}(\rho) = \tfrac{1}{2}k(\rho - \tfrac{1}{2}\pi)^2 + a\exp\left[-b(\rho - \tfrac{1}{2}\pi)^2\right] \,. \tag{6.4}$$

The parameters k, a and b are chosen such that the measured inversion tunneling splitting in the ν_2 ground state and both transitions to the ν_2 first excited state are reproduced to an accuracy better than 0.1% . The form of the resulting potential is shown in Figure 6.1.

The associated eigenvalue problem is solved in Ref. [91] using a basis of functions $\sin m\rho$ ($m = 1,\ldots,100$). Here we consider only the lowest two eigenfunctions $|\nu\rangle$, also shown in Figure 6.1. They describe the lower and upper inversion states that are separated by 0.8 cm^{-1}. The lowest of the two, which is designated by $\nu = +$, is symmetric with respect to $\rho \to \pi - \rho$. The upper level , designated by $\nu = -$, is antisymmetric with respect to this operation.

The Van der Waals Hamiltonian can be written as

$$
\begin{aligned}
\hat{H}_{\text{vdw}}(\gamma, \vartheta, \varphi, R, \beta, \alpha, \rho) = \; & B(\rho)\hat{j}^2 + [C(\rho) - B(\rho)]\hat{j}_z^2 - \frac{\hbar^2}{2\mu R}\frac{\partial^2}{\partial R^2} R \\
& + \frac{\hat{l}^2}{2\mu R^2} + V_{\text{int}}(\gamma, \vartheta, \varphi, R, \beta, \alpha, \rho) \,.
\end{aligned}
\tag{6.5}
$$

The first two terms in $\hat{H}_{\text{vdw}}$ represent the symmetric top Hamiltonian of NH$_3$. The rotational constants are related to the moments of inertia given in Equation (6.3): $B(\rho) = [2I_{xx}(\rho)]^{-1}$ and $C(\rho) = [2I_{zz}(\rho)]^{-1}$. The third and fourth term give the kinetic energy of the "diatom", with $\hat{l}$ being the relative angular momentum. The intermolecular potential V_{int} is expanded in spherical harmonics $Y_{\lambda\mu}$:

$$V_{\text{int}}(R, \Theta, \Phi, \rho) = \sum_{\lambda\mu} v_{\lambda\mu}(R, \rho)Y_{\lambda\mu}(\Theta, \Phi) \,, \tag{6.6}$$

105
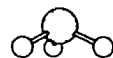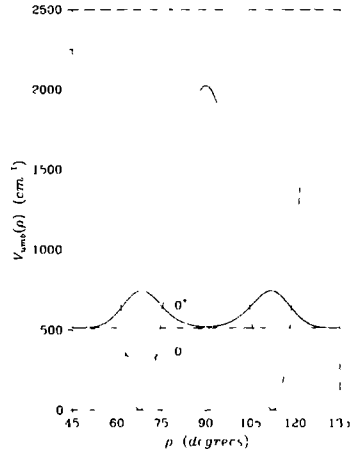
Figure 6.1 : *Double well potential $V_{umb}(\rho)$ for the NH$_3$ umbrella motion, cf Equation (6 4), and the two lowest eigenfunctions of $\hat{H}_{umb}(\rho)$, cf Equation (6 2) Wavefunctions in arbitrary units and zero coinciding with the corresponding energy*

where Θ and Φ are the polar angles of the Ar projectile with respect to the principal axes frame of the NH$_3$ rotor. In the space fixed frame $Y_{\lambda\mu}(\Theta, \Phi)$ becomes

$$Y_{\lambda\mu}(\Theta, \Phi) = \sum_{\nu} D_{\nu\mu}^{(\lambda)}(\gamma, \vartheta, \varphi) Y_{\lambda\nu}(\beta, \alpha) , \qquad (6.7)$$

where $D_{\nu\mu}^{(\lambda)}(\gamma, \vartheta, \varphi)$ is the usual Wigner rotation matrix [92]. The expansion coefficients $v_{\lambda\mu}(R, \rho)$ have been taken from Bulski et al. [86], who calculated the ab initio potential for four different umbrella angles ρ, and expanded it in tesseral harmonics. Due to the threefold symmetry of the ammonia only terms with $m = 0, 3, 6, \ldots$ are present. The first 15 terms with $l \leq 7$ have been included leading to an accuracy of about 0.6% in the convergence of the expansion. The expansion coefficients are written as a sum of a short and a long range contribution:

$$v_{\lambda\mu}(R, \rho) = v_{\lambda\mu}^{SR}(R, \rho) + v_{\lambda\mu}^{LR}(R, \rho) , \qquad (6.8)$$

where

$$
\begin{aligned}
v_{\lambda\mu}^{SR}(R, \rho) &= F_{\lambda\mu}(\rho) \left[1 + \delta_{\lambda\mu}(\rho)R\right] \ \exp\left[-\alpha_{\lambda\mu}(\rho)R - \beta_{\lambda\mu}(\rho)R^2\right] , \\
v_{\lambda\mu}^{LR}(R, \rho) &= -\sum_{n=6}^{10} f_n^{\lambda\mu}(R, \rho) C_n^{\lambda\mu}(\rho) R^{-n} .
\end{aligned}
\qquad (6.9)
$$

106

The $C_n^{\lambda\mu}(\rho)$ are the induction and dispersion coefficients, the $f_n^{\lambda\mu}(R,\rho)$ are Tang and Toennies type damping functions. The values of all coefficients are given in Ref. [86]. The rotational constants for a given tunneling state ν are given by

$$B_\nu = \langle \nu \mid B(\rho) \mid \nu \rangle \quad \text{and} \quad C_\nu = \langle \nu \mid C(\rho) \mid \nu \rangle \qquad (6\,10)$$

Their values are listed in Table 6.1

ν	calculated values [90]		values used [94]	
	B_ν	C_ν	B_ν	C_ν
+	10 000	6 337	9 9402	6 3044
-	9 998	6 337	9 9402	6 3044

Table 6.1 : *Rotational constants (in cm^{-1}) for the lowest two inversional states of NH₃*

In the CC method the angular basis functions are usually formed by Clebsch-Gordan coupling of the relative angular momentum functions $Y_{lm_l}(\beta,\alpha) = \mid lm_l \rangle$ and the symmetric top functions $\mid jkm \rangle$ to a total angular momentum J with space fixed z-component M. In the case of permutation-inversion symmetry PI(D₃ₕ), which we have here, it is convenient to take linear combinations $\mid jkm\epsilon \rangle$ of the symmetric top functions, defined by

$$\mid jkm\epsilon \rangle = (2\,[1 + \delta_{k0}])^{-1/2}\,(\mid jkm \rangle + \epsilon\mid j - k\,m \rangle)\,, \qquad (6\,11)$$

where $k \geq 0$ and $\epsilon = \pm 1$, except for $k = 0$ when obviously only $\epsilon = +1$ is allowed.

Since we take the umbrella motion explicitly into account, the basis has to be extended by taking the tensor product with the tunneling functions $\nu(\rho)$

$$\mid jklJM\epsilon\nu \rangle = \sum_{m\,m_l} \mid jkm\epsilon \rangle \mid lm_l \rangle \mid \nu \rangle \langle jmlm_l \mid JM \rangle\,, \qquad (6\,12)$$

where $\langle jmlm_l \mid JM \rangle$ is a Clebsch-Gordan coefficient [92]. From symmetry considerations it follows [29] that the symmetric (antisymmetric) inversion function can combine to a state adapted to PI(D₃ₕ) with only one of the two $\mid jkm\epsilon \rangle$ functions, so that $\epsilon = \mp(-1)^j$ for $\nu = \mid \pm \rangle$. We can therefore omit the quantum number ν and label the basis functions by $\mid jklJM\epsilon \rangle$, instead of using the labeling given in Equation (6.12). In the CC equations the noninteracting blocks for different J are separated into two parity blocks, each containing channels $(jkl\epsilon)$ having different values of $\epsilon(-1)^{j+k+l}$. States of the free NH₃ can be designated by j_k^ϵ, thereby uniquely specifying the inversion function.

The coupling between the channels that comes from the potential matrix elements is given by

$$V_{j'k'l'\epsilon'}^{jkl\epsilon} = \sum_{\lambda\mu}\langle jklJM\epsilon \mid v_{\lambda\mu}(R,\rho)Y_{\lambda\mu}(\Theta,\Phi) \mid j'k'l'JM\epsilon'\rangle \qquad (6\,13)$$

107
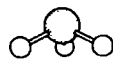
In order to calculate the matrix elements between the two tunneling states we obtained an analytical representation of the ρ-dependence of the expansion coefficients $v_{\lambda\mu}(R,\rho)$ by fitting, for each value of R, a fifth order polynomial in $\rho - \frac{1}{2}\pi$ through the ab initio values of the coefficients for different ρ. The fit contains only even or only odd powers depending on whether $\lambda + \mu$ is even or odd. The matrix elements can then be evaluated as follows:

$$\langle \nu \mid v_{\lambda\mu}(R,\rho) \mid \nu' \rangle = \sum_{n=0}^{5} c_n^{\lambda\mu}(R) \langle \nu \mid (\rho - \tfrac{1}{2}\pi)^n \mid \nu' \rangle , \qquad (6.14)$$

where the $c_n^{\lambda\mu}(R)$ are the polynomial expansion coefficients. The above relationship between the values of ϵ and ν is used to insert the correct (ν,ν') combination into Equation (6.13).

According to Ref. [93] the ab initio potential has to be scaled to give good agreement with spectroscopic data of the bound Ar–NH$_3$ complex. This scaling consists of multiplying the short range parameter F_{33} in Equation (6.9) by a factor of 1.43. Here, calculations have been performed using both the original ab initio potential and a modified potential in which the same scaling was applied for all values of the inversion coordinate.

In addition to the calculation with the inversion averaged matrix elements in the way we have just described (henceforth referred to as the 'exact' inversion method), we have used the model developed by Davis and Boggs [50] and Green [29]. In this model the inversion functions are taken to be delta functions: $\mid \pm \rangle = [\delta(\rho - \rho_e) \pm \delta(\rho - \pi + \rho_e)]/\sqrt{2}$, where ρ_e is the value of the inversion coordinate in the equilibrium configuration. In this case the intermolecular potential needs to be known only for the equilibrium angle, since the expansion coefficients, averaged over the inversion functions, are now given by

$$\langle \pm \mid v_{\lambda\mu}(R,\rho) \mid \pm \rangle = \begin{cases} v_{\lambda\mu}(R,\rho_e), & \text{for } \lambda + \mu \text{ even} \\ 0, & \text{for } \lambda + \mu \text{ odd} \end{cases}$$

$$\langle \pm \mid v_{\lambda\mu}(R,\rho) \mid \mp \rangle = \begin{cases} 0, & \text{for } \lambda + \mu \text{ even} \\ v_{\lambda\mu}(R,\rho_e), & \text{for } \lambda + \mu \text{ odd} . \end{cases} \qquad (6.15)$$

Using this model for the inversion functions, together with the neglect of the inversion splitting, the scattering equations for para- NH$_3$ are invariant to a simultaneous change of parity in the incoming and outgoing channels, i.e.

$$\sigma(j_k^\epsilon \to j'^{\epsilon'}_{k'}) = \sigma(j_k^{-\epsilon} \to j'^{-\epsilon'}_{k'}) . \qquad (6.16)$$

In the CS method the scattering equations are expressed in a body-fixed coordinate system. The fourth term in the Van der Waals Hamiltonian, Equation (6.5), is approximated by putting $\hat{l}^2$ $(= \hat{J}^2 + \hat{j}^2 - 2\vec{\hat{j}} \cdot \vec{\hat{J}})$ equal to $\hat{J}^2$. This implies that the Coriolis interactions are neglected and that Ω, the projection of both $\vec{j}$ and $\vec{J}$ on the vector $\vec{R}$, is a good quantum number, i.e. there is no coupling between channels with different Ω. The molecular symmetry group of the dimer is thus enlarged from PI(D$_{3h}$) to the semi-direct product of C$_\infty$ and PI(D$_{3h}$).

6.3 Computational aspects

The calculations were carried out with the HIBRIDON inelastic scattering code [94]. The total collision energy E, the maximum value of the total angular momentum J and the values of j and k

at which the rotational basis set is to be truncated, are input parameters of the program. The values for l are then given by triangular inequalities, cf. Equation (6.12). The program has the possibility of further reducing the size of the basis set as the overall rotation takes up more and more of the available energy. So, from a chosen value of J onwards, the program includes only open channels. To keep the calculations feasible even at higher energies, an interpolation scheme for the total cross sections as a function of J can be used, leading to a substantial reduction of the required CPU time.

J_k^ϵ	basis set (J_{max}, k_{max})			J_k^ϵ	basis set (J_{max}, k_{max})		
	(9,9)	(10,9)	(11,9)		(9,9)	(10,9)	(11,9)
1_0^+	7 92	7 43	7 42	5_3^+	0 10	0 10	0 10
2_0^+	10 10	10 50	10 47	5_3^-	0 63	0.60	0 61
3_0^+	3 94	3 84	3 87	6_3^-	0 06	0 07	0 07
4_0^+	0 46	0 52	0 54	6_3^+	0 01	0 02	0 02
5_0^+	0 13	0 13	0 13	6_6^-	0 04	0 04	0 04
6_0^+	0.07	0 07	0 07	6_6^+	0.41	0.42	0 42
3_3^+	1.32	1.25	1.25	7_6^+	0 11	0.13	0 13
3_3^-	11.70	11 96	11.98	7_6^-	0 01	0 01	0.01
4_3^-	2 52	2 27	2 26				
4_3^+	0 65	0.72	0 72				

Table 6.2 : *Effect of the maximum (J, k) values in the basis set on the cross sections $\sigma(0_0^+ \rightarrow J_k^\epsilon)$ (in Å²) for ortho NH₃-Ar at an energy of 485 cm⁻¹ ('exact' inversion, ab initio potential)*

The values of the total energies are determined by the two relative kinetic energies attained in the experiment, 280 cm⁻¹ and 485 cm⁻¹. The ortho- NH₃ with initial state $J = k = 0$ has zero internal energy, so the total energies are equal to the relative kinetic energies. The initial $J = k = 1$ state of para- NH₃, which is the ground state of this species, has an internal energy of 16 245 cm⁻¹. The total energies are consequently set equal to 296.245 cm⁻¹ and 501.245 cm⁻¹. The molecular levels in the basis set are retained up to $J = 9$ inclusive, with all allowed values of k. This means that for ortho- NH₃ 34 levels are included (with a maximum energy of 895 cm⁻¹) 11 of which are asymptotically accessible in the lower, and 19 in the higher energy case. Out of the 66 levels for para- NH₃ (with a maximum energy of 891 cm⁻¹) 24 and 40 levels are accessible, respectively. The J value at which we start to neglect closed channels is 78. The interpolation step size ΔJ is taken to be six, so that calculations are actually performed for $J = 0, 6, 12, \ldots, 150$. As explained in section 2, the NH₃ inversion is taken into account by calculation of the matrix elements according to the 'exact' inversion method, given in Equation (6.14) or according to the model inversion, given in Equation (6.15).

Convergence with respect to relevant parameters in the propagator, such as the step size ΔR,

j_k^ϵ	$\Delta J = 1$	$\Delta J = 4$	$\Delta J = 6$	$\Delta J = 8$
1_0^+	10.83	10.93	11.35	9.06
2_0^+	9.02	9.00	8.74	9.63
3_0^+	4.43	4.32	4.34	4.29
4_0^+	0.42	0.40	0.39	0.38
3_3^+	1.64	1 63	1.62	1.59
3_3^-	9.26	9 25	9.33	8.42
4_3^-	3.21	3.33	3.25	3.34
4_3^+	0.25	0.22	0.25	0.24
5_3^+	0.06	0.05	0.05	0.05
5_3^-	0.34	0.36	0.36	0.34

Table 6.3 : *Effect of the interpolation step size ΔJ on the cross sections $\sigma(0_0^+ \rightarrow j_k^\epsilon)$ (in $\mathring{A}^2$) for ortho NH_3 at an energy of 280 cm^{-1} (delta function model inversion, ab initio potential).*

was better than 1%. Table 6.2 shows the dependence of the cross sections on the magnitude of the rotational basis set. Going from a maximum j value of 9 to a maximum value of 11 in the rotational basis set induced changes in the cross sections of about 6%. The neglect of closed channels for $J > 78$ did not affect the results. The effect of interpolation step size ΔJ on the cross sections is shown in Table 6.3. The error due to the step size used here is found to be smaller than 5%.

Since the averaging of the rotational constants over the inversion wave functions has a small effect (cf. Table 6.1), we have taken the same value for both inversion states [45]: $B = 9.9402$ cm^{-1} and $C = 6.3044$ cm^{-1}. The maximum number of channels used in the calculation was 219 per parity block for ortho- NH_3 taking about 24 CPU hours for a full calculation and 441 per parity block for para- NH_3, taking about 241 CPU hours on an IBM RS/6000 model 320 workstation.

In the CS calculation we used only the 'exact' inversion method. The value of Ω ranged from 0 to 7 for ortho NH_3 and from 0 to 8 for para NH_3; the maximum j value in the rotational basis set was 9 and J was varied from 0 to 150 at an energy of 485 cm^{-1}, resp. 501.245 cm^{-1}. The interpolation step size ΔJ was six as well. The ortho NH_3 calculation took 45 minutes on the same workstation, with a maximum of 34 channels per Ω-block, the para NH_3 calculation took 4 hours with a maximum of 66 channels per Ω-block.

6.4   Results and discussion

The results of the calculations reported here are compared with the results of the crossed molecular beam experiment, which was described in Chapter 5. Only differences in population of a specific rotation-inversion state $| \imath \rangle \equiv j_k^\epsilon$ before and after the collision are measured. The signal is

proportional to

$$\Delta n(j) = \sum_{i \neq j} \{ n(i) \ \sigma(i \to j) - n(j) \ \sigma(j \to i) \} \ , \tag{6 17}$$

where $n(j)$ stands for the initial population of state j and $\Delta n(j)$ for the collision induced change in that population For the experiment to yield pure state-to-state cross sections, only a single state must be initially populated This requirement, however, cannot be completely met For ortho-NH₃ the initial state consists of 92% 0_0^+ and 8% 1_0^+ and for para- NH₃ of 95% 1_1^- and 5% 1_1^+ The state-to-state cross sections obtained from the calculations therefore have to be put into Equation (6 17) in order to enable comparison with the observed quantities

j_k^ϵ	V_I	V_{II}	V_{III}	V_{IV}	experiment
1_0^+	11 35 (7 64)	4 03 (1 09)	11 06 (7 41)	3 82 (0 87)	6 07
2_0^+	8 74 (8 69)	13 35 (12 65)	8 45 (8 42)	13 20 (12 49)	6 73
3_0^+	4 34 (4 29)	2 56 (2 98)	4 16 (4 12)	2 51 (2 94)	2 19
4_0^+	0 39 (0 53)	2 41 (2 37)	0 35 (0 49)	2 44 (2 40)	0 48
3_3^+	1 62 (2 24)	0 75 (1 53)	1 54 (2 17)	0 70 (1 53)	3 43
3_3^-	9 33 (8 84)	10 10 (9 47)	9 04 (8 56)	10 65 (9 96)	1 23
4_3^-	3 25 (3 18)	1 94 (1 97)	3 38 (3 29)	1 87 (1 91)	5 77
4_3^+	0 25 (0 33)	0 45 (0 51)	0 23 (0 32)	0 44 (0 50)	1 31
5_3^+	0 05 (0 06)	0 39 (0 40)	0 06 (0 07)	0 41 (0 42)	-
5_3^-	0 36 (0 36)	0 28 (0 28)	0 34 (0 35)	0 31 (0 31)	-

Table 6.4 : *State-to state cross sections $\sigma(0_0^+ \to j_k^\epsilon)$ for ortho NH₃ Ar in Å² at an energy of 280 cm⁻¹ The cross sections given in parentheses are corrected for the incomplete initial state preparation in the measurement, as follows (cf Equation (6 17))*

$$\sigma(\to 1_0^+) = 0 \ 92 \ \sigma(0_0^+ \to 1_0^+) - 0 \ 08 \sum_{i \neq 1_0^+} \sigma(1_0^+ \to i) \ , \ ,$$

$$\sigma(\to j_k^\epsilon) = 0 \ 92 \ \sigma(0_0^+ \to j_k^\epsilon) + 0 \ 08 \ \sigma(1_0^+ \to j_k^\epsilon), \ \text{for } j_k^\epsilon \neq 1_0^+$$

A dash ( ) in the last column indicates that the corresponding cross section has not been measured

V_I	*delta function model inversion, ab initio potential*
V_{II}	*delta function model inversion, scaled potential*
V_{III}	*'exact' inversion, ab initio potential*
V_{IV}	*'exact' inversion, scaled potential*

Only relative values for the cross sections can be derived from the experiment To facilitate comparison, the sum of the experimental cross sections over all states is set equal to the sum of the cross sections calculated with the original ab initio potential and the 'exact' inversion method
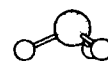
The sum contains only cross sections to levels j_k^ϵ that are experimentally different from zero for one or two values of ϵ This sum hardly differs for the scaled and the original ab initio potential The experimental results thus acquired are given in Tables 6 4, 6 5 and 6 6 and Figures 6 2 and 6 3, together with the corresponding theoretical values The results for ortho- NH$_3$ are given both for the model and for the 'exact' inversion treatment The experimental error is between 10% and 20 %

Both for ortho and para- NH$_3$ the scaling in the potential has a large effect In the case of ortho- NH$_3$ this effect is about the same for the various cross sections at both energies Especially transitions to 1_0^+, 2_0^+, 3_0^+ and 4_0^- are strongly affected in the lower energy case, and in the higher energy case transitions to 1_0^+, 3_0^+ and 4_0^+ energy case Use of the delta function model for inversion does not affect the influence of the scaling For para- NH$_3$ the cross sections obtained by use of the scaled potential, are sometimes smaller for the lower and larger for the higher energies, or vice versa For the lower energy the scaling reduces the size of most of the para NH$_3$ cross sections, except for the 2_1^+, 4_4^+ and 4_1^- states The scaling induces large changes in the relative magnitudes of the inversion states for transitions to the 2_1, 3_2 and 4_4 states

Comparison with the experiment shows that the calculations using the original ab initio potential give a better overall agreement than calculations using the scaled potential Particularly, cross sections to the 1_0^+, 2_0^- and $2_1^\pm$ states come out better In a few cases, however, the scaled cross sections are closer to the experimental ones

It has been a subject of discussion whether it is necessary to include a v_{33} term in the description of the intermolecular potential, since the observed far-infrared Ar–NH$_3$ spectrum could also be explained with a potential that contained only terms up to v_{20} [80] When we look at the results of the scattering calculations, we see that in the case of ortho- NH$_3$ the experimental cross sections $\sigma(0_0^+ \rightarrow 3_3^\pm)$ are reproduced fairly well In the first Born approximation these transitions are solely due to the v_{33} term in the potential It seems unlikely that the agreement between experiment and theory can be maintained when this important first order contribution is zero as is the case when v_{33} is zero

Inspection of the influence of the scaling on the cross sections of ortho- NH$_3$ shows that not only $\Delta j = \Delta k = 3$ transitions are affected, but other transitions as well The latter would not be affected in the first Born approximation This means that the higher Born approximations also contribute significantly The importance of higher order effects in the interaction between Ar and NH$_3$ is confirmed by calculations on bound states Although the v_{33} term does not contribute in a first order perturbation theory, which has the isotropic Hamiltonian as its zeroth order Hamiltonian, it proves to be one of the dominant terms in determining the energy levels of the Ar–NH$_3$ complex [93]

At the energies used here, application of the model for the inversion of NH$_3$ has only a small effect on the cross sections as compared to the 'exact' calculations, in the order of 5% The parity propensities, which are defined as the ratio between the difference and the sum of the cross sections to the two inversion states [74], are hardly affected The suggestion that deviations of theoretical propensities from experimental ones can be accounted for by taking the inversion motion explicitly into account [62, 89] is wrong

Our calculations show further that the invariance to a simultaneous change of parity in the incoming and outgoing channels (cf Equation (6 16)) for para- NH$_3$ holds to an accuracy of about 0 2% when the inversion is fully included but the inversion splitting of 0 8 cm^{-1} is neglected When this splitting is included also, the deviations are of the order of 3% Billing [42] has found in He–

$\jmath_k^\epsilon$	V_I	V_{II}	V_{III}	V_{IV}	experiment
1_0^+	7 90 (4 30)	5 94 (2 40)	7 92 (4 33)	5 53 (2 04)	4 33
2_0^+	10 20 (9 85)	10 73 (10 17)	10 10 (9 76)	11 02 (10 42)	5 72
3_0^+	4 07 (4 07)	1 84 (2 18)	3 94 (3 94)	1 77 (2 14)	2 38
4_0^+	0 50 (0 63)	3 00 (2 87)	0 46 (0 59)	3 04 (2 91)	1 73
5_0^-	0 13 (0 19)	1 07 (1 06)	0 13 (0 18)	1 06 (1 04)	-
6_0^+	0 07 (0 07)	0 13 (0 14)	0 07 (0 07)	0 12 (0 13)	1 01
3_3^+	1 39 (2 11)	0 88 (1 96)	1 32 (2 07)	0 83 (1 92)	1 68
3_3^-	12 14 (11 35)	12 83 (11 96)	11 70 (10 93)	13 12 (12 21)	14 23
4_3^-	2 47 (2 56)	2 14 (2 21)	2 52 (2 59)	2 07 (2 15)	4 90
4_3^+	0 66 (0 76)	0 87 (0 92)	0 65 (0 75)	0 82 (0 87)	2 70
5_3^+	0 11 (0 13)	0 25 (0 28)	0 10 (0 12)	0 22 (0 25)	
5_3^-	0 66 (0 71)	1 18 (1 16)	0 63 (0 69)	1 17 (1 15)	-
6_3^-	0 06 (0 09)	0 27 (0 26)	0 06 (0 09)	0 26 (0 26)	-
6_3^+	0 01 (0 02)	0 04 (0 05)	0 01 (0 02)	0 04 (0 05)	-
6_6^-	0 04 (0 07)	0 06 (0 11)	0 04 (0 06)	0 06 (0 11)	-
6_6^+	0 38 (0 39)	0 91 (0 87)	0 41 (0 43)	0 96 (0 91)	-
7_6^+	0 12 (0 12)	0 12 (0 11)	0 11 (0 12)	0 11 (0 11)	-
7_6^-	0 01 (0 01)	0 02 (0 02)	0 01 (0 01)	0 02 (0 02)	-

Table 6.5 : *State-to state cross sections $\sigma(0_0^+ \rightarrow \jmath_k^\epsilon)$ for ortho NH_3-Ar in $\mathring{A}^2$ at an energy of 485 cm^{-1} The corrected cross sections given in parentheses are obtained as indicated in Table 6 4 A dash (-) in the last column indicates that the corresponding cross section has not been measured*

V_I *delta function model inversion, ab initio potential*
V_{II} *delta function model inversion, scaled potential*
V_{III} *'exact' inversion, ab initio potential*
V_{IV} *'exact' inversion, scaled potential*

113
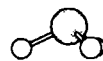
j_k^ϵ	V_{III}	V_{IV}	exp.	j_k^ϵ	V_{III}	V_{IV}	exp.
2_1^-	4.22 (4.23)	2.82 (3.21)	4.70	2_1^-	3.62 (3.66)	2.23 (2.50)	5.51
2_1^+	4.40 (4.39)	10.73 (10.33)	6.32	2_1^+	4.39 (4.35)	7.72 (7.45)	3.76
3_1^+	2.00 (2.06)	1.57 (1.66)	0.89	3_1^+	1.65 (1.73)	1.26 (1.43)	1.35
3_1^-	3.35 (3.28)	3.27 (3.18)	1.35	3_1^-	3.24 (3.17)	4.55 (4.39)	1.37
4_1^-	0.57 (0.56)	1.42 (1.37)	-	4_1^-	1.10 (1.06)	0.93 (0.92)	-
4_1^+	0.33 (0.34)	0.50 (0.55)	-	4_1^+	0.27 (0.32)	0.78 (0.79)	-
2_2^-	0.99 (1.61)	0.47 (1.11)	1.19	2_2^-	0.62 (1.12)	0.44 (1.03)	1.50
2_2^+	13.48 (12.85)	13.30 (12.65)	12.94	2_2^+	10.52 (10.03)	12.13 (11.55)	7.70
3_2^+	2.64 (2.70)	3.06 (2.96)	3.24	3_2^+	1.96 (2.06)	1.46 (1.46)	4.26
3_2^-	3.90 (3.84)	1.05 (1.15)	2.56	3_2^-	3.94 (3.84)	1.56 (1.55)	1.95
4_2^-	0.52 (0.52)	0.97 (0.96)	0.97	4_2^-	0.79 (0.79)	0.71 (0.75)	1.19
4_2^+	0.59 (0.58)	0.75 (0.76)	-	4_2^+	0.71 (0.71)	1.58 (1.54)	-
5_2^+	0.12 (0.12)	0.22 (0.22)	-	5_2^+	0.36 (0.35)	0.63 (0.61)	-
5_2^-	0.03 (0.04)	0.09 (0.10)	-	5_2^-	0.14 (0.15)	0.25 (0.27)	-
4_4^-	0.69 (0.72)	0.52 (0.60)	0.80	4_4^-	0.56 (0.62)	0.49 (0.62)	1.24
4_4^+	1.25 (1.23)	2.15 (2.07)	2.43	4_4^+	1.72 (1.66)	3.10 (2.97)	2.11
5_4^+	0.39 (0.39)	0.39 (0.38)	0.44	5_4^+	0.44 (0.45)	0.37 (0.37)	1.25
5_4^-	0.42 (0.42)	0.22 (0.23)	-	5_4^-	0.49 (0.48)	0.31 (0.31)	0.75
5_5^+	0.22 (0.24)	0.25 (0.27)	-	5_5^+	0.40 (0.43)	0.19 (0.23)	-
5_5^-	0.54 (0.52)	0.67 (0.65)	-	5_5^-	0.94 (0.92)	0.94 (0.90)	-

Table 6.6 : *State-to-state cross sections $\sigma(1_1^- \rightarrow j_k^\epsilon)$ for para NH_3-Ar in Å^2. The relative kinetic energies are as indicated. The cross sections given in parentheses are corrected for the incomplete initial state preparation in the measurement, as follows (cf. Equation (6.17)):*

$$\sigma(\rightarrow j_k^\epsilon) = 0.95 \, \sigma(1_1^- \rightarrow j_k^\epsilon) + 0.05 \, \sigma(1_1^+ \rightarrow j_k^\epsilon).$$

A dash (-) in the last column indicates that the corresponding cross section has not been measured.

V_{III}	*'exact' inversion, ab initio potential*
V_{IV}	*'exact' inversion, scaled potential*
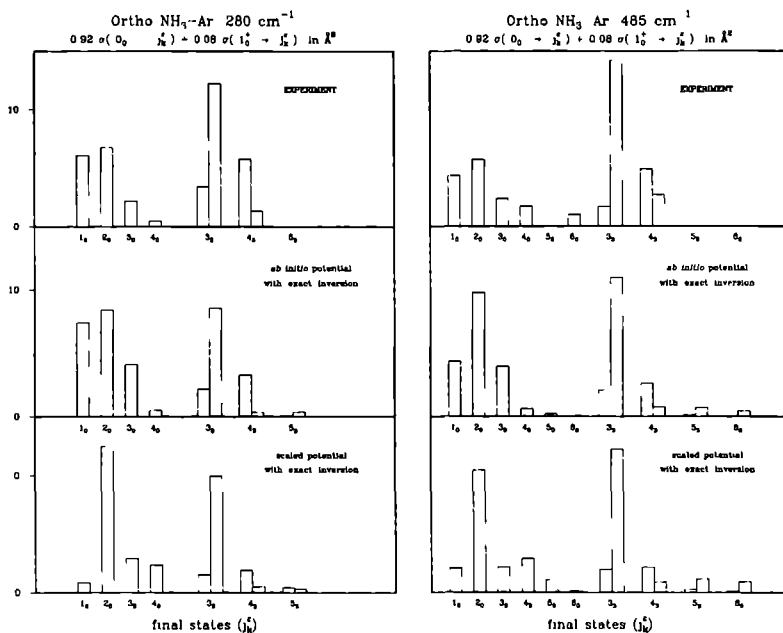
Figure 6.2 : *Experimental and theoretical cross sections for ortho NH₃–Ar scattering at a relative kinetic energy of 280 cm^{-1} (Figure 6 2 a) and 485 cm^{-1} (Figure 6 2 b) The theoretical values are given in parentheses in Tables 6 4 and 6 5 respectively, for the 1_0^+ state we have used the expression given in Table 6 4*

NH$_3$ calculations at an energy of 525 cm^{-1}, using a semiclassical approach, that the invariance is accurate to within 5% when the splitting of the inversion doublet is taken into account The effect of including the tunneling splitting on the invariance is therefore larger than the effect of averaging over the inversion wavefunctions

The limited influence of the delta function model for inversion seems surprising at first sight because the wavefunctions in Figure 6 1 do not resemble delta functions This means, however, as is noted by Davis and Boggs [50], that the $v_{\lambda\mu}(R,\rho)$ are functions of ρ varying slowly enough for the delta function approach to be valid

Application of the CS approximation gives a reasonable agreement for para- NH$_3$ (Table 6 7) For ortho- NH$_3$, however, there are strong deviations, both from the CC method and from experiment The CS calculation gives zero cross sections to the 3_3^+ and 4_3^+ states, whereas both experimental and CC cross sections to these states are different from zero This means that these transitions come from the Coriolis terms in the Hamiltonian Even though these terms are small, their long range apparently gives rise to significant transition probabilities
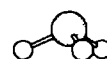
Ortho-NH$_3$ – Ar				Para-NH$_3$ – Ar			
j_k^ε	CC	CS	exp	j_k^ε	CC	CS	exp
1_0^+	7 92	9 24	4 33	2_1^-	3 62	3 30	5 62
2_0^+	10 10	8 17	5 72	2_1^+	4 39	3 39	3 84
3_0^+	3 94	5 17	2 38	3_1^+	1 65	1 31	1 38
4_0^+	0 46	0 71	1 73	3_1^-	3 24	3 35	1 40
5_0^+	0 13	0 13	-	4_1^-	1 10	0 91	-
6_0^+	0 07	0 08	1 01	4_1^+	0 27	0 28	
3_3^+	1 32	0	1 68	2_2^-	0 62	0 37	1 53
3_3^-	11 70	8 71	14 23	2_2^+	10 52	12 16	7 86
4_3^-	2 52	3 23	4 90	3_2^+	1 96	2 26	4 35
4_3^+	0 65	0	2 70	3_2^-	3 94	4 93	1 99
5_3^+	0 10	0	-	4_2^-	0 79	0 44	1 21
5_3^-	0 63	0 61	-	4_2^+	0 71	0 54	-
6_3^-	0 06	0 06	-	4_4^-	0 56	0 62	1 27
6_3^+	0 01	0	-	4_4^+	1 72	1 08	2 15
6_6^-	0 04	0	-	5_4^+	0 44	0 41	1 28
6_6^+	0 41	0 39	-	5_4^-	0 49	0 58	0 77
7_6^+	0 11	0 12	-	5_5^+	0 40	0 23	-
7_6^-	0 01	0	-	5_5^-	0 94	0 99	-

Table 6.7 : *Results of CC and CS calculations ('exact' inversion, ab initio potential, without correction for initial state preparation, at a relative kinetic energy of 485 cm^{-1}) and experimental results The cross sections are in $\mathring{A}^2$ A dash (-) in the last column indicates that the corresponding cross section has not been measured*

In calculations on He–NH$_3$ scattering at an energy of 792 cm^{-1} using the CS method Meyer et al have found the cross sections into the 3_3^+ and 4_3^+ to be exactly zero and the cross section to the 2_2^- state to be extremely small [29] The fact that the 3_3^+ and 4_3^+ cross sections come out zero is an artifact of the CS method The smallness of the 2_2^- cross section however cannot be attributed to the method

6.5 Conclusions

We have calculated close coupling cross sections for the scattering of NH$_3$ with Ar at two different collision energies and compared them with experimentally derived cross sections For the first time, the inversion motion of NH$_3$ has been taken into account explicitly Comparison with calculations in which use is made of a delta function model description of the inversion motion, shows that this model works quite well at the energies used here We find that deviations from experimentally
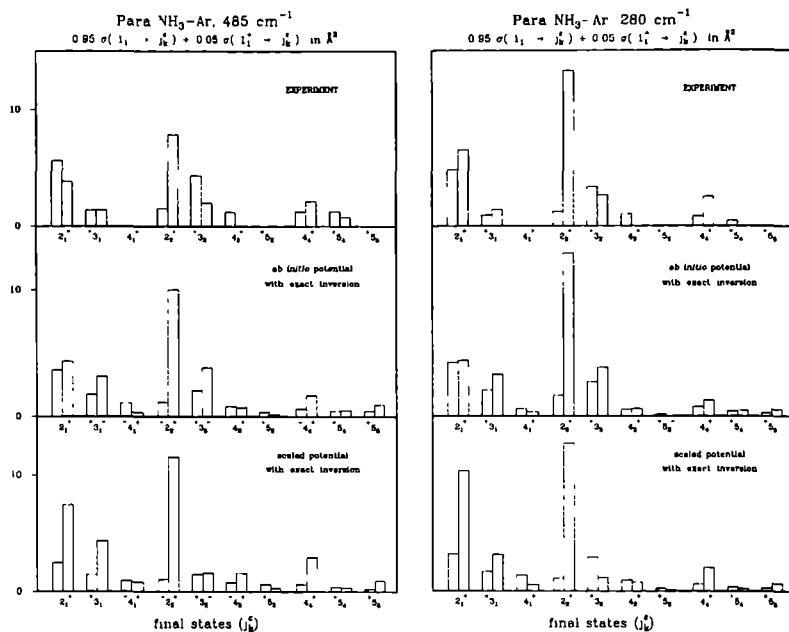
Figure 6.3 : *Experimental and theoretical cross sections for para NH_3-Ar scattering at a relative kinetic energy of 280 cm^{-1} (Figure 6.3.a) and 485 cm^{-1} (Figure 6.3.b) The theoretical values are given in parentheses in Table 6 6.*

determined parity propensities cannot be attributed to use of the delta function model. It is more likely that the discrepancies arise from shortcomings of the intermolecular potential.

In calculations on bound states use of the scaled potential, in which one single term in the expansion of the ab initio potential was scaled by a factor of 1.43, gave better agreement with experimental data than use of the ab initio potential itself. We find that for scattering calculations the opposite is true. This can be seen as a manifestation of the fact that scattering states and bound states probe different regions of the intermolecular potential surface. The applied scaling is too crude to obtain a realistic potential. For ortho- NH_3 the calculated ab initio cross sections reproduce the experimental ones fairly well. For para- NH_3 differences remain between theoretical and experimental parity propensities, indicating that the ab initio potential needs further improvement.

Comparison of the results for the two potentials also shows the cross sections to be very sensitive to variations in the potential surface. The changes induced in transitions to the various rotation-inversion states by the scaling lead to conclude that higher order effects play a role in the scattering
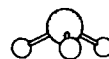
process, just as they do in bound state interactions

Application of the coupled states approximation introduces selection rules that do not have a physical justification. For ortho- NH_3 the agreement with close coupling results is poor, for para-NH_3 it is reasonable

6.6 Acknowledgement

Chapter 7

State-to-State Cross Sections for Rotational Excitation of OH by collisions with He, Ar and H_2

J. Schleipen, A. Eppink and J.J. ter Meulen
Department of Molecular and Laser Physics, University of Nijmegen,
Toernooiveld, 6525 ED Nijmegen, The Netherlands

Parity resolved state-to-state cross sections for rotational excitation of $OH(X^2\Pi)$ colliding with He, Ar and H_2, have been obtained in a crossed molecular beam experiment. The OH radicals were produced in a pulsed DC discharge in a H_2O/Ar gas mixture. State preparation for the OH radicals is achieved by adiabatic expansion into vacuum followed by electrostatic state selection in a hexapole electric field. As a result only the upper parity component ($p = +$) of the $X^2\Pi_{3/2}, J = \frac{3}{2}$ Λ-doublet is initially populated in the primary beam. The OH rotational state distribution is probed, before and after the collision event, by means of LIF spectroscopy of the $A \leftarrow X$ electronic band at 308 nm. For the OH-H_2 system the experimental values for the relative cross sections compare well with the results from close coupling scattering calculations. The OH-Ar and OH-He scattering experiments behave very similar with the exception of the $J = \frac{3}{2}$ Λ-doublet transition which is induced much weaker by the He collisions. For the OH-He system the relative state-to-state cross sections can be compared with other experimental data and also here the agreement is good. For both OH-He and OH-Ar scattering a weak oscillatory behaviour of the spin-orbit multiplet conserving, parity changing transitions is observed.
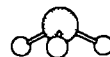
7.1 Introduction

The OH radical has been the subject of many experimental and theoretical studies in various scientific fields such as molecular physics, chemistry or astrophysics From a spectroscopical point of view the OH radical probably is the most frequently studied and consequently best understood free radical From a molecular and chemical point of view the radical reveals interesting features since the unpaired π-electron is responsible for various interactions such as a coupling between electronic spin and electronic orbital angular momentum and the breakdown of the Born-Oppenheimer approximation yielding the well-known 'Λ-doubling' of $^2\Pi$ electronic states

Many astronomical studies report the observation of OH spectral lines arising from stellar and interstellar objects containing the hydroxyl radical The very intense and often polarized character of the observed OH emissions presumes some kind of maser activity of the emitting object The first astronomical OH masers were observed in the middle 1960's [95] and many others were reported since then [96, 97] Several models were constructed in order to explain this interstellar maser activity Guibert et al [98] developed a model for OH excitation in interstellar clouds involving radiative transfer of population, collisional excitation by neutral species (H_2, H) or ions (C^+), and interaction with the surrounding (black body and IR) radiation field The model was used for explaining the 1720 MHz and 1612 MHz maser lines in several galactic objects

In 1986 Andresen published a paper [99] in which he discussed the population inversion in the OH $X^2\Pi_i$ electronic ground state in terms of two complementary pump mechanisms In Figure 7 1 this is illustrated schematically The photodissociation of H_2O molecules by VUV radiation, arising from e g new born stars, preferentially populates the antisymmetric (A'') Λ-doublet states in OH, resulting in an inversion in the $^2\Pi_{3/2}$ state and an anti-inversion in the $^2\Pi_{1/2}$ state [100, 101] On the other hand, inelastic collisions of OH($X^2\Pi_{3/2}, J = \frac{3}{2}$) with molecular hydrogen preferentially populate the symmetric (A') Λ-doublet states and produce an inversion in the $^2\Pi_{1/2}$ and an anti-inversion in the $^2\Pi_{3/2}$ state [18, 102] [The experiments leading to this conclusion evoked a discussion on the correct assignment of the overall parity of the OH molecular wavefunction In references [101, 102] it was shown that the assignment of the Λ-doublet states of OH indeed were wrong Alexander and Dagdigian [38] performed a careful analysis of the parity assignment of the OH Λ-doublet states and their assignment has been confirmed since then by many experimental and theoretical studies] Due to dipole induced, parity changing infrared decay of rotational populations in each $^2\Pi_i$ state the population inversion (or anti-inversion) in a specific rotational level J is transferred to the lowest rotational state $J = \frac{3}{2}$ in the $^2\Pi_{3/2}$ spin-orbit multiplet or $J = \frac{1}{2}$ in the $^2\Pi_{1/2}$ multiplet The population inversion (or anti-inversion) in the $^2\Pi_{1/2}, J = \frac{1}{2}$ state is then transferred by IR relaxation to the $J = \frac{3}{2}$ state of the $^2\Pi_{3/2}$ multiplet Now hyperfine selection rules have different impact on this population transfer to the $^2\Pi_{3/2}, J = \frac{3}{2}$ state whether the population is transferred from the $^2\Pi_{3/2}, J = \frac{5}{2}$ state, or from the $^2\Pi_{1/2}, J = \frac{1}{2}$ state Andresen showed that pumping by means of photodissociation of H_2O favours the $(^2\Pi_{3/2}, J = \frac{3}{2}, F' = 2 \rightarrow F'' = 1)$ 1720 MHz maser line, whereas the collisional excitation of OH by H_2 is preferentially pumping the $(^2\Pi_{3/2}, J = \frac{3}{2}, F' = 1 \rightarrow F'' = 2)$ 1612 MHz maser

From this it may be clear that the interpretation of the observed interstellar maser emission requires accurate rate constants for the different pump mechanisms involved in the maser action In this chapter we focus our attention to the rotational population transfer in the electronic ground state of the OH molecule upon collisions with the astrophysically important H_2, and the rare gases He and Ar Recently Andresen et al [18] published the results from a crossed beam collision exper-

iment in which they initially prepared both $|{}^2\Pi_{3/2}, J^p = \frac{3}{2}^\pm\rangle$ Λ-doublet substates in their primary beam. The rotational state of the molecule is indicated by its rotational angular momentum J and the overall parity of the molecular wavefunction p (see Chapter 2, section 4 1) They obtained parity averaged cross sections $\sigma^\pm$ for rotational excitation to states $|{}^2\Pi_{\Omega'}, J'^{p'}\rangle$ by collisions with H_2 and D_2 Since these cross sections are averaged over both initial parity substates, no information could be derived on the important $X{}^2\Pi_{3/2}, \frac{3}{2}^+ \to \frac{3}{2}^-$ Λ-doublet transition However, for the $v = 1$ vibrationally excited state in the electronic ground state of OH they obtained rate constants for this Λ-doublet transition which indicated that the Λ-doublet transitions are faster compared to rotational transitions. Wysong et al [17] studied the energy transfer in the electronic ground state of OH by collisions with He Their double resonance relaxation measurements yielded parity resolved rate coefficients for the OH$({}^2\Pi, v = 2)$-He system for rotational energy transfer in the $v = 2$ vibrational state of electronic ground state OH
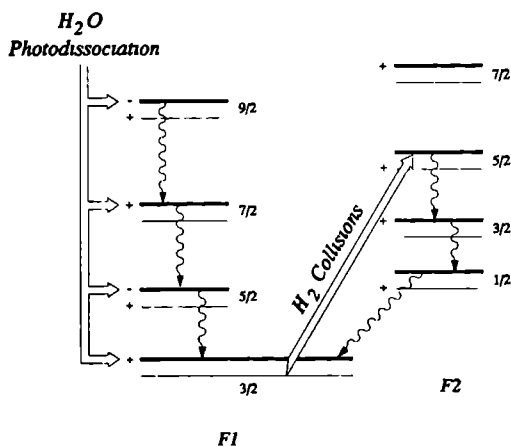
Figure 7.1 : *Diagram showing two important complementary inversion mechanisms for the OH maser, as proposed by Andresen [99] Photodissociation of H_2O leads to inversion in the F1 spin-orbit manifold, whereas inelastic collisions with the interstellar very abundant H_2 molecules result in an inversion in the F2 multiplet Population inversion or anti-inversion is transferred to the lowest rotational levels in each spin orbit multiplet by radiative infrared decay, indicated by the wavy arrows Each rotational state is indicated by its rotational angular momentum and the parity of the overall molecular wavefunction*

Theoretical scattering results are available for the collision system OH-H_2 from several authors Close coupled calculations for OH–para-H_2 ($j_2 = 0$) scattering were performed by Dewangan and Flower [103] at relatively low collision energies ($E_{coll} \stackrel{<}{\sim} 300$ cm^{-1}), using the ab initio potential energy surface of Kochanski and Flower [104] Schinke and Andresen [105] performed a coupled states calculation on the OH-H_2 system and recently Offer and Flower [106] reported results from

close coupling calculations for rotational excitation of OH by both para-H_2 ($j_2 = 0$) and ortho-H_2 ($j_2 = 1$)

No theoretical data are available at the moment for $OH(X^2\Pi)$-He or Ar scattering Quantum scattering calculations for these systems are necessary for a comparison between experiment and theory Since the measured relative state-to-state cross sections can be compared directly with the computed values, information is obtained about the intermolecular potential for the $OH(^2\Pi)$-He and $OH(^2\Pi)$-Ar systems Accurate potentials for these systems are also required for calculating the stationary states and energy levels of e g the OH-Ar van der Waals complex [107] A potential calculation for $OH(X^2\Pi)$-He is performed by Vegiri and Farantes [108] Because of its importance for chemical kinetics and temperature measurements in combustion processes, rotational relaxation rates in the $A^2\Sigma^+$ state of OH are calculated by Jorg et al for OH-He [109] and by Degli Esposti and Werner for the system OH-Ar [110]

In this study we discuss the results of a crossed molecular beam experiment in which the OH radical is prepared in a single parity substate of the $X^2\Pi_{3/2}, J = \frac{3}{2}$ Λ-doublet Parity resolved relative state-to-state cross sections $\sigma(^2\Pi_{3/2}, \frac{3}{2}^+ \rightarrow \ ^2\Pi_{\Omega'}, J'^{p'})$ are obtained for OH-He, OH-Ar and OH-H_2 scattering at collision energies of 394 cm^{-1}, 451 cm^{-1} and 596 cm^{-1} respectively Our experimental results are compared with experimental and theoretical data for OH-H_2 scattering [105, 106] and with experimental data for OH-He rotational relaxation [17]

7.2 Experimental

7.2.1 Experimental set-up

In the present scattering experiment use is made of a crossed molecular beam set-up The molecular beam machine has been described in full detail in Chapter 3 of this thesis Two pulsed molecular beams are crossed at right angles, using two modified Bosch-type fuel injectors with a pulse width (FWHM) of about 1 millisecond The primary beam contains the OH radicals which are rotationally excited by collisions with secondary beam targets He, Ar or H_2 The OH radicals are produced in an electrical discharge just downstream the primary valve exit hole (see Chapter 2) For this purpose a 24 mbar H_2O in Ar mixture is expanded into vacuum at a total backing pressure of 1 5 bar A small electrode ring is positioned 3 mm downstream the nozzle exit hole The ring is 6 mm in diameter and is made of 1 mm thick stainless steel A negative high voltage of typically 4-5 kV is applied to the electrode and as soon as the expansion takes place a discharge occurs between the electrode and the pulsed valve, which is on earth potential In the expansion the water molecules dissociate and the OH radicals are produced very efficiently The secondary beam is produced in a differentially pumped vacuum chamber, separated from the scattering chamber by a 5 mm skimmer As a result the scattering region is geometrically confined to within a volume of about 8x8x8 mm^3

During operation of both molecular beam valves the pressure inside the vacuum chamber does not exceed 10^{-5} mbar We measured the velocity of the primary and secondary beams by means of a fast ionization gauge positioned on the beam axis By varying the distance from the nozzle to the ionization gauge and measuring the corresponding flight times we estimated the velocities to be $v_{OH} = 670$ m/s and for the secondary beam $v_{He} = 1560$ m/s, $v_{Ar} = 670$ m/s and $v_{H_2} = 2720$ m/s Knowing the beam velocities it is possible to calculate the center-of-mass collision energies in the different scattering events $E_{coll}(OH-He) = 394$ cm^{-1}, $E_{coll}(OH-Ar) = 451$ cm^{-1} and $E_{coll}(OH-H_2) = 596$ cm^{-1}

After the expansion the OH molecular pulse is shaped into a primary beam by a 5 mm diameter skimmer about 20 mm downstream from the nozzle orifice. Next, the OH radicals travel through an electrostatic state selector positioned on the primary beam axis. Use is made of a hexapole which acts as an electrostatic positive lens for molecules in an antisymmetric Λ-doublet state and as a negative lens for molecules being in a symmetric Λ-doublet state. The state selector is 230 mm long and consists of six 2 mm diameter rods at a distance of 2 mm from each other. The hexapole is operated at voltages up to 30 kV, well below electrical breakdown. The focus of the state selector occurs about 40 mm behind the exit opening of the hexapole and coincides with the scattering volume and detection region.

In the discharge producing the OH radicals also ions and electrons are produced inside the molecular beam, which give rise to an electrical current of several 100 μA through the hexapole rods. Since the high voltage power supply for the state selector is not able to accept these high currents, a diaphragm, with an opening of 6 mm in diameter, is positioned between the primary beam skimmer and the hexapole. Putting the diaphragm on earth potential and applying a voltage of typically 100 V to the skimmer results in an efficient shielding of the hexapole from incoming ions or electrons. Consequently the current through the hexapole device is reduced to 10 μA or less, yielding a stable high voltage output and constant focusing efficiency.

Before and after the collision process the rotational state distribution of the OH radicals is probed state selectively by means of LIF spectroscopy of the $A^2\Sigma^+(v' = 0) \leftarrow X^2\Pi_i(v'' = 0)$ electronic transition at ≈ 308 nm, which is discussed in Chapter 2 of this thesis. For this purpose the frequency doubled output of a XeCl excimer laser pumped dye laser is guided into the scattering region. The dye laser operates at Rhodamine-B dye, lasing between 600 and 640 nm. The output of the dye laser is frequency doubled in a KDP crystal yielding tunable UV radiation in the 308 nm wavelength region with a bandwidth of ≈ 0.4 cm^{-1}. The output power is ≈ 3 mJ/15 nsec pulse. The resulting LIF signal is imaged onto the first cathode plate of a photon multiplier tube by means of collecting optics using a spatial filtering diaphragm. A Schott color filter (UG11) in front of the photon multiplier is used to suppress scattered laser light and scattered light arising from the discharge. The resulting signal is then processed by a boxcar averager and directed to a strip-chart recorder and AT computer. Simultaneously the UV power is monitored by means of a photodiode.

7.2.2 Initial state preparation

Initial state preparation of the OH radicals is achieved by the supersonic expansion of the OH molecular pulse, followed by electrostatic state selection in the hexapole electric field. During the expansion rotational and vibrational energy of the radical is converted into translational energy which results in cooling of the internal degrees of freedom of the OH radicals. In Figure 7.2 a Boltzmann plot is shown of the rotational state distribution in the $X^2\Pi_{3/2}$ ($F1$) and $X^2\Pi_{1/2}$ ($F2$) states of OH with no high voltage applied to the state selector. About 75 % of the OH electronic ground state population is contained in the lowest rotational state $J = \frac{3}{2}$ of the $X^2\Pi_{3/2}$ state. The rest of the population is distributed among the higher rotational states and the $^2\Pi_{1/2}$ spin-orbit multiplet of OH. About 10 % of the population in the prepared $F1, J = \frac{3}{2}$ state is still contained in the $J = \frac{5}{2}$ state of the $F1$ multiplet. Although the Boltzmann plot indicates a non-thermal behaviour of the population distribution in the higher rotational states, an effective rotational temperature can be ascribed to the two lowest rotational states of the $X^2\Pi_{3/2}$ state, yielding $T_{rot} \approx 49$ K.

123
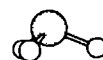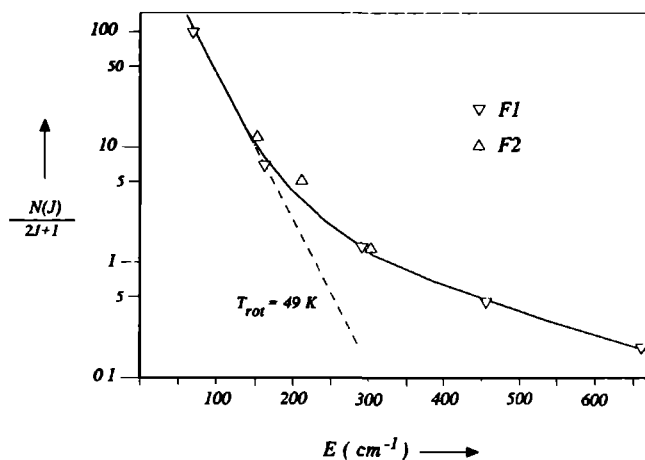
Figure 7.2 : *Boltzmann plot showing the rotational population distribution of the electronic ground state OH, directly after the expansion without electrostatic state selection A rotational temperature of ≈ 49K can be associated with the lowest rotational states For higher J-values the rotational cooling is less efficient, resulting in a non-thermal Boltzmann distribution*

In the OH radical an interaction between the electronic angular momentum $\vec{L}$ and the nuclear rotational angular momentum $\vec{R}$, known as 'Λ-doubling', is responsible for a doubling of each rotational level in the electronic ground state into two components with opposite parity p (see Chapter 2) The energy difference between these two Λ-doublet components is only 0 05 cm^{-1} for the $J = \frac{3}{2}$ rotational state in the $X^2\Pi_{3/2}$ state Consequently both $J = \frac{3}{2}$ Λ-doublet substates are equally populated in the supersonic expansion Theory predicts parity propensity rules for collisional excitation into a rotational state $|X^2\Pi_1, J \rangle$, i e a preference exists for either parity conserving or parity changing transitions In order to investigate these parity propensity rules only one component J^p ($p = \pm$) of the $|X^2\Pi_{3/2}, J = \frac{3}{2}\rangle$ Λ-doublet is initially prepared in the primary beam For this purpose the hexapole is used to focus the OH molecules in the upper Λ-doublet state $|X^2\Pi_{3/2}, J^p = \frac{3}{2}^+\rangle$ towards the molecular beam axis

As can be seen from Figure 2 7 molecules in the initially prepared $F1, \frac{3}{2}^+$ state are probed by the $Q_1(1)$ transition in the $A \leftarrow X$ electronic band, whilst molecules in the $F1, \frac{3}{2}^-$ state are probed by the $P_1(1)$ and $R_1(1)$ transitions In Figure 7 3 the focusing efficiency of the hexapole state selector is illustrated The $Q_1(1)$ and $P_1(1)$ LIF signals are given as a function of the high voltage applied to the hexapole rods The high voltage was limited to a maximum value of 30 kV in order to avoid electrical breakdown From the figure it follows that the focusing efficiency for the $\frac{3}{2}^+$ state reaches a value of ≈ 8 at a maximum voltage of 30 kV At this voltage the $\frac{3}{2}^-$ state OH radical density is decreased by a factor of ≈ 3 The net effect of the electrostatic state selection is an overpopulation of the $J = \frac{3}{2}$ positive parity component by a factor of 25 with respect to the $J = \frac{3}{2}$ negative parity component Since the $J = \frac{5}{2}^-$ state is also affected by the electrostatic

124

state selection process, its initial population increases as a function of state selector voltage At a voltage of 30 kV about 10 4 % of the $J = \frac{3}{2}^-$ state population is contained in this $J = \frac{5}{2}^-$ state With regard to the experimental accuracy of ≈ 20 % we obtained an adequate initial parity substate preparation for performing a real state-to-state collision experiment

The initial state preparation obtained in this study is however not perfect Since the OH radicals are produced in a relatively 'hot' discharge environment, the rotational temperature of the molecular beam after the expansion has taken place is about 50 K and after state selection still 10 % of the OH $^2\Pi_{3/2}, \frac{3}{2}^+$ population is contained in the $^2\Pi_{3/2}, J^p = \frac{5}{2}^-$ state Consequently, the measured cross section $\sigma(\imath \to f)$ is made up of two contributions

$$\sigma(\imath \to f) = 0\ 9\ \ \sigma(^2\Pi_{3/2}, \frac{3}{2}^+ \to f) + 0\ 1\ \ \sigma(^2\Pi_{3/2}, \frac{5}{2}^- \to f) \tag{7 1}$$

A similar correction should be made for scattering into this $^2\Pi_{3/2}, \frac{5}{2}^-$ state Since any scattering out of this 10 % initially prepared state results in a decrease of the scattering signal, the measured cross sections for collisional excitation into this state are equal to

$$\sigma(\imath \to\ ^2\Pi_{3/2}, \frac{5}{2}^-) = 0\ 9\ \ \sigma(^2\Pi_{3/2}, \frac{3}{2}^+ \to\ ^2\Pi_{3/2}, \frac{5}{2}^-) - 0\ 1 \sum_{\jmath \neq\ ^2\Pi_{3/2}\ \frac{5}{2}^-} \sigma(^2\Pi_{3/2}, \frac{5}{2}^- \to \jmath) \tag{7 2}$$
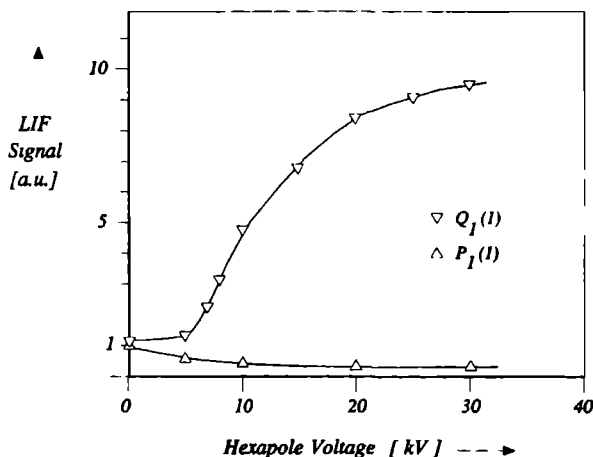
Figure 7.3 : *Diagram showing the focusing efficiency of the hexapole state selector for the $F1, J^p = \frac{3}{2}^+$ state (probed by the $Q_1(1)$ transition), and the $F1, J^p = \frac{3}{2}^-$ state (probed by the $P_1(1)$ transition) At a voltage of 30 kV the separation factor of both Λ doublet states is ≈ 25*

125

7.3 Results and interpretation

As shown in Chapter 3 for the NH_3 scattering experiment the state-to-state collision cross section $\sigma(i \rightarrow f)$ for scattering out of the initially prepared state $|i\rangle$ into a final state $|f\rangle$ can be extracted from the scattering spectra in a rather straightforward manner if single collision conditions are fulfilled. The final state in the scattering process $|f\rangle$ is probed by some rotational transition $|f\rangle \rightarrow |f'\rangle$ in the electronic $A \leftarrow X$ band, giving a LIF signal $S_{ff'}$. The scattering signal $\delta S_{ff'}$ represents the change in signal $S_{ff'}$ upon collisions with the secondary beam molecules. From these scattering signals $\delta S_{ff'}$ the relative cross sections $\sigma(i \rightarrow f)$ are deduced via the following formula:

$$\sigma(i \rightarrow f) \propto \frac{\delta S_{ff'}}{n(i) \cdot \mathcal{L}_{ff'} \cdot P_{ff'} \cdot F} \tag{7.3}$$

In this formula $\mathcal{L}_{ff'}$ represents the rotational linestrength of the transition, $P_{ff'}$ is the laser power at the specific transition frequency and F represents the flux-density transformation relating the measured particle densities with the incoming and scattered particle fluxes [59]. This transformation F contains the particle velocity and consequently its value depends on the scattered state $|f\rangle$ of the OH radical. However, since the laboratory velocity of the OH molecules is mainly determined by the center-of-mass velocity, which does not change during the collision, the outcome of the flux-density transformation is nearly the same for all probed $|f\rangle$ states. Because we are studying relative integral cross sections the factor F can be omitted from Equation (7.3) .

The relation between the relative cross section $\sigma(i \rightarrow f)$ and the scattering signal $\delta S_{ff'}$, as expressed in Equation (7.3), is only valid if single collision conditions are obeyed [62]. Careful checks have been performed in order to be sure that collisional effects are linear with secondary beam density. Several scattering spectra are recorded at different backing pressures of the secondary beam collision partners. For low pressures the scattering spectra grow stronger with increasing secondary beam pressure and they all show a one to one correspondence. However, above a certain critical value for the secondary beam stagnation pressure the scattering spectra show a deviating behaviour from the low pressure spectra, indicating that higher order collision processes come into play. Under these circumstances the relation between scattering signal $\delta S_{ff'}$ and cross sections becomes too complex to derive a state-to-state cross section $\sigma(i \rightarrow f)$ from the scattering spectra. In order to avoid these secondary or higher order collisions the secondary beam backing pressure was kept below 300 mbar for all three scattering partners He, Ar and H_2.

The state-to-state cross sections reported here are all obtained by probing the rotational population distribution in the electronic ground state by means of the Q_1, P_1, Q_2 and P_2 branches in the $A^2\Sigma^+, v' = 0 \leftarrow X^2\Pi_i, v'' = 0$ band of OH. The upper Λ-doublet levels are probed by the Q_1 and P_2 transitions, whilst the Q_2 and P_1 branches probe the lower Λ-doublet levels. The laser power of typically 3 mJ/15 nsec was enough to saturate these strong transitions. Since we are determining only relative cross sections the linestrength $\mathcal{L}_{ff'}$ and laser power $P_{ff'}$ in Equation (7.3) can be omitted. For some transitions such as $Q_1(1)$ and $Q_2(1)$ the main line in the spectrum is overlapped by a satellite line arising from a transition from the same ground state level to a different ρ-doublet component in the excited state. For these transitions the collision induced changes in density of molecules is determined from the LIF signals by calculating the composite line shape from the individual line profile and the frequency difference between the main and satellite lines.

In Table 7.1 the relative state-to-state cross sections $\sigma(^2\Pi_{3/2}, J^p = \frac{3}{2}^+ \rightarrow {}^2\Pi_{\Omega'}, J'^{p'})$ obtained from Equation (7.3) are given for the three collision partners He, Ar and H_2. These data are

$^2\Pi_{3/2} \rightarrow$	$^2\Pi_{3/2}$			$^2\Pi_{3/2} \rightarrow$	$^2\Pi_{1/2}$		
J',p'	σ, He 394 cm^{-1}	σ, Ar 451 cm^{-1}	σ, H$_2$ 596 cm^{-1}	J',p'	σ, He 394 cm^{-1}	σ, Ar 451 cm^{-1}	σ, H$_2$ 596 cm^{-1}
$3/2,-$	1 1	5 6	3 4	$1/2,+$	1 6	0 33	0 39
$5/2,+$	3 0	3 6	2 6	$1/2,-$	<0 3	0 53	0 89
$5/2,-$	0 63	0 72	4 3	$3/2,+$	0 51	0 38	0 60
$7/2,+$	0 24	0 44	0 96	$3/2,-$	0 60	0 41	1 34
$7/2,-$	0 60	0 92	1 1				
$9/2,+$	0 15	0 28	0 45				
$9/2,-$	0 05	0 24	0 58				

Table 7.1 : *Relative state-to-state cross sections $\sigma(^2\Pi_{3/2}, 3/2^+ \rightarrow {}^2\Pi_{\Omega'}, J'^{p'})$ for rotational excitation of ground state OH by collisions with He, Ar and H$_2$ The experimental error is 20%*

obtained by averaging the results from several scattering measurements As the OH scattering measurements are still going on, these data represent preliminary results The experimental error for the listed values is estimated to be 20 % For some cross sections only an upper limit could be determined due to a poor signal-to-noise ratio for the corresponding lines in the LIF scattering spectra More accurate values for these cross sections have to await the outcome of the present measurements For scattering in the $F1$ spin-orbit multiplet ($F1 \rightarrow F1$) cross sections could be determined with J'-values up to $\frac{9}{2}$, whereas for the spin-orbit multiplet changing $F1 \rightarrow F2$ transitions only excitations into the lowest two rotational states were measured The decrease of population in the initially prepared state $F1, \frac{3}{2}^+$ is compared with the sum of populations scattered into all other rotational states Within the experimental accuracy this balance showed a canceling of the collisionally excited population by the de-excitation of the initially prepared state As a result we may conclude that elastic scattering effects are not detected as many molecules in the $J = \frac{3}{2}^+$ state are scattered out of the probe region as there are scattered into this area

Due to coinciding $Q_2(2)$ and $Q_2(3)$ lines in the LIF spectra the scattering signal measured at these transitions in fact represents the sum cross section $\sigma(i \rightarrow F2, \frac{3}{2}^-) + \sigma(i \rightarrow F2, \frac{5}{2}^+)$ In the case of OH – H$_2$ scattering theoretical data are available and this sum cross section can be compared with the corresponding theoretical value

The He and Ar scattering experiments indicated that a substantial amount of scattering occurs out of the 10% initially populated $F1, \frac{5}{2}^-$ state Since no theoretical data were available for scattering out of this state, we made the following assumption In order to obtain a value for the sum $\sum_j \sigma(F1, \frac{5}{2}^- \rightarrow j)$ in Equation (9 2), we assume that the total inelastic cross sections for the $\Pi_{3/2}, J = \frac{3}{2}^+$ and $\Pi_{3/2}, J = \frac{5}{2}^-$ state are equal This would result in an equal percentual decrease of the $Q_1(1)$ and $Q_1(2)$ signals due to out-scattering This value for the total inelastic scattering

out of the $\Pi_{3/2}, J = \frac{3}{2}^{+}$ state is known from the experiment and yields 9% for He, 11% for Ar and 17% for H_2 scattering Since the initial population in the $F1, \frac{5}{2}^{-}$ state with respect to the $F1, \frac{3}{2}^{+}$ state is well known, the measured cross sections for excitation into the $F1, \frac{5}{2}^{-}$ state are corrected for out-scattering and the resulting values are given in Table 7 1 In order to get an impression of the possible error due to the assumption of equal inelastic cross sections for $J = \frac{3}{2}^{+}$ and $\frac{5}{2}^{-}$ we considered also the case where the $J = \frac{5}{2}^{-}$ inelastic cross section is a factor 2 smaller than the $J = \frac{3}{2}^{+}$ cross section The effect of varying this correction factor from 50 % to 100% of the total inelastic $F1, \frac{3}{2}^{+}$ scattering is indicated by the error bars in Figures 7 4 and 7 5, giving the cross sections for OH – He, Ar and OH – H_2 scattering respectively It must be noted that despite of the large effect of this correction it is not taken into account by Andresen et al [18] in a similar crossed beam experiment Also in their experiment the $J = \frac{5}{2}$ state was occupied for about 10 % and a considerable amount of out-scattering must have taken place

7.4 Discussion

7.4.1 OH – He, Ar scattering

In Figure 7 4 the cross sections from Table 7 1 are presented graphically for the OH – He and OH – Ar collisions The relative cross section is given as a function of final angular momentum J' and parity p' With the exception of the $F1, J = \frac{3}{2}$ Λ-doublet transition, the overall behaviour of the cross sections looks very similar for OH-Ar and OH-He scattering For OH – He scattering the cross sections for spin-orbit changing transitions $(F1 \rightarrow F2)$ are in the same order of magnitude as those for scattering in the F1 spin-orbit manifold This is in agreement with the relaxation measurements of Wysong et al [17] To our knowledge no quantum scattering calculations have been performed for rotational excitation of OH in its electronic ground state by collisions with rare gas atoms He or Ar Consequently no theoretical data are available for comparison with the experimental values

At the time when this thesis was prepared we were informed on scattering calculations for the $OH(^2\Pi)$ – Ar system performed by Prof Dr H -J Werner and coworkers [121] In Figure 7 4 their preliminary cross sections are indicated by the shaded squares and circles Comparing their data with our state-to-state cross sections for OH Ar scattering shows a good agreement for the low-lying rotational states The relative strength of the $F1, J = \frac{3}{2}$ Λ-doublet transition and the spin-orbit conserving versus spin-orbit changing transitions is in agreement with our experiment Also the calculated parity propensity for excitation to the $F1, J = \frac{5}{2}$ Λ-doublet compares well with the observed propensity For excitation to higher rotational states their cross sections decrease faster due to the relatively small collision energy of 300 cm^{-1} used in their calculations

The potential governing the interaction between an open shell Π-state diatomic and a closed shell atom can be thought as being composed of two potential energy surfaces $V_{A'}$ and $V_{A''}$, having reflection symmetry A' and A'' respectively in a plane containing the diatomic and the interacting partner Alexander [111] showed that for a pure Hund's case (a) molecule the sum potential, $V_{A'} + V_{A''}$, governs the collisional excitation within each spin-orbit multiplet $(F1 \leftrightarrow F1, F2 \leftrightarrow F2)$, whereas the difference potential, $V_{A'} - V_{A''}$, controls the multiplet changing $(F1 \leftrightarrow F2)$ transitions Due to symmetry considerations the sum and difference potentials can be expanded as [112]

$$V_{A'} + V_{A''} = \sum_{l} V_{l0}(R) \ P_l(cos\ \theta) \tag{7 4}$$

and

$$V_{A'} - V_{A''} \;=\; \sum_l V_{l2}(R) \; P_l^{(2)}(\cos\theta) \tag{7 5}$$

with $P_l(\cos\theta)$ and $P_l^{(2)}(\cos\theta)$ the regular and associated Legendre polynomials and $V_{l0}(R)$ and $V_{l2}(R)$ the expansion coefficients for the sum and difference potentials respectively For the lowest J-values the OH molecule can be considered as a Hund's case (a) molecule In case of scattering by Ar the cross sections for spin-orbit multiplet conserving transitions are stronger than those for multiplet changing transitions, when compared to the OH-He results This may be the result of a larger ratio V_{l2}/V_{l0} for the OH – Ar potential, where this ratio represents a measure of the efficiency of multiplet changing transitions

Figure 7 4 also shows that scattering by Ar is more effective in inducing the 'pure' Λ-doublet transition $^2\Pi_{3/2}, \frac{3}{2}^+ \rightarrow {}^2\Pi_{3/2}, \frac{3}{2}^-$ in the OH radical, than scattering by He The term in the potential which is directly responsible for this Λ-doublet transition, is the V_{l0} term Consequently, for scattering by Ar the V_{l0} term should be stronger relative to the higher order odd l potential terms than for the OH-He interaction

Wysong et al [17] studied the rotational energy transfer in the $v = 2$ vibrationally excited state of the electronic ground state of OH scattered by He Their experiment was performed in bulk circumstances and consequently they obtained rate coefficients in stead of cross sections They found a pronounced parity propensity effect conservation of total parity is favored in collisions which change in spin-orbit multiplet This observation is in agreement with our results for OH $(^2\Pi_{3/2}, v = 0)$-He scattering a clear propensity for parity conserving transitions to the $F2$ $J = \frac{1}{2}$ state is observed (see Figure 7 4 b) For excitation to the $F2, J = \frac{3}{2}$ state this parity propensity is less clear The cross section in Figure 7 4 b for excitation to the $F2, J = \frac{3}{2}^-$ state in fact represents the sum cross section for scattering into the $F2, J = \frac{3}{2}^-$ and $\frac{5}{2}^+$ state The actual value for $\sigma(i \rightarrow F2, \frac{3}{2}^-)$ will be smaller than the number indicated in the figure and consequently the parity propensity for excitation to the $F2, J = \frac{3}{2}$ state is also in agreement with the observations of Wysong et al When this thesis was prepared the OH scattering experiment was still going on and cross sections for scattering into the $J' = \frac{5}{2}$ and $\frac{7}{2}$ states of the $F2$ spin-orbit multiplet were not available yet Measurement of these cross sections are necessary for a positive confirmation of this parity propensity rule also for the higher rotational states No such parity propensity was observed however for scattering by Ar

For both OH-rare gas collision experiments there seems to be a weak oscillatory behaviour of the cross sections for spin-orbit multiplet conserving transitions, as a function of angular momentum transfer For OH-Ar $F1 \rightarrow F1$ scattering, and to less extent for OH-He $F1 \rightarrow F1$ scattering, a preference for parity changing transitions is observed when ΔJ is even In the case of odd ΔJ parity conserving transitions are preferred As a result an anti inversion is achieved in the rotational states of the $F1$ multiplet when starting from the upper $J = \frac{3}{2}$ state Further measurements of higher J' rotational states are necessary to confirm this observation and to see whether this oscillatory behaviour is also present for multiplet changing transitions A similar oscillatory behaviour of cross sections was reported by Joswig et al [58] for scattering of $NO(X^2\Pi_{1/2})$ with rare gas atoms He, Ne and Ar Their experiment yielded relative cross sections $\sum_p \sigma(^2\Pi_{1/2}, \frac{1}{2}^p \rightarrow {}^2\Pi_{\Omega'}, J'^{p'})$ averaged over both initial $J = \frac{1}{2}$ parity substates For the multiplet conserving transitions they observed an oscillatory behaviour for scattering by Ar, He and Ne transitions with $\Delta J = 2n$ are preferred over transitions with $\Delta J = 2n - 1$ In the case of NO-Ar scattering these oscillations are
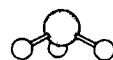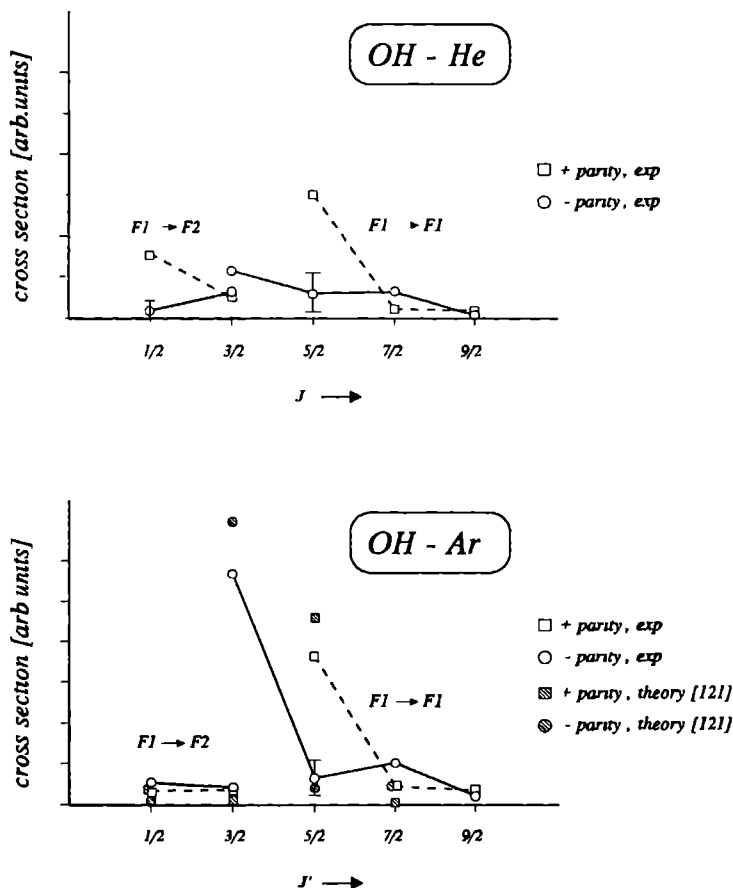
Figure 7.4 : *Relative state-to-state cross sections* $\sigma(^2\Pi_{3/2}, \frac{3}{2}^+ \rightarrow\ ^2\Pi_\Omega, J'^{p'})$ *for OH-Ar (Figure 7 4 a) and OH-He (Figure 7 4 b) scattering The multiplet conserving transitions are indicated with* $F1 \rightarrow F1$, *the multiplet changing transitions with* $F1 \rightarrow F2$ *The data indicated by the open squares represent the cross sections for rotational excitation into the Λ-doublet component with positive parity (i e parity conserving transitions) The open circles show the cross sections for collisional excitation into the Λ-doublet component with negative parity The error bar for the $J = \frac{5}{2}^-$ state illustrates the effect of correcting the measured cross section for inelastic scattering out of this $\frac{5}{2}^-$ state (see text) For OH-Ar scattering preliminary results of Werner et al [121] are indicated by the shaded squares and circles*

130

well understood [113] and arise from a dominant V_{20} term in the expansion of the sum potential $V_{A'} + V_{A''}$ This potential term is responsible for a 'direct' $\Delta J = 2$ coupling between initial and final rotational states in the scattering calculations and thereby causes the oscillatory behaviour of the multiplet conserving transitions Our observations indicate that for OH – Ar scattering the V_{20} potential term plays a more dominant role in the collision process than for OH – He scattering
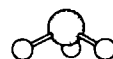
7.4.2 OH – H₂ scattering

In Figure 7 5 the cross sections from Table 7 1 are presented graphically for OH – H₂ collisions In this case the experimental cross sections can be compared with theoretical data obtained from quantum scattering calculations by Offer and Flower [106] Schinke and Andresen [105] reported the results of a coupled states calculation for scattering of OH by para-H₂ ($j_2 = 0$) at a collision energy of 670 cm⁻¹ , which is close to our experimental energy of 590 cm⁻¹ Offer and Flower performed close coupling calculations for OH para H₂ ($j_2 = 0$) and OH -ortho-H₂ ($j_2 = 1$) scattering at a collision energy of 680 cm⁻¹ In our experiment we used normal-H₂ as a collision partner which consists of 25 % para-H₂ ($j_2 = 0$) and 75 % ortho-H₂ ($j_2 = 1$) The calculations of Offer and Flower show that collisions with para-H₂ ($j_2 = 0$) behave very differently from collisions with ortho-H₂ ($j_2 = 1$) For some transitions the cross section for collisions with para-H₂ is small and the rotational excitation is mainly driven by interactions with ortho-H₂ Consequently, the collision cross sections for scattering with normal-H₂ are strongly influenced by the OH – ortho-H₂ interaction Since Schinke and Andresen only performed a calculation for OH – para-H₂ ($j_2 = 0$) scattering, these data cannot be used for a realistic comparison with the present experiment In order to compare theory with experiment the computed values of Offer and Flower for the para-H₂ and ortho-H₂ scattering are averaged with statistical weights of 1 3 for para ortho H₂ In Table 7 2 these weighted values are compared with the experimental values from Table 7 1 The cross sections are normalized such that the sum of the enlisted experimental cross sections is equal to the sum of the corresponding theoretical values For excitation to the $^2\Pi_{1/2}, J = \frac{3}{2}^-$ state only a sum cross section could be determined for scattering into the $^2\Pi_{1/2}, J = \frac{3}{2}^-$ and $^2\Pi_{1/2}, J = \frac{5}{2}^+$ states Consequently this value is compared with the sum of the corresponding theoretical cross sections from Offer and Flower Also the relative parity averaged cross sections

$$\bar{\sigma}(^2\Pi_{3/2}, \frac{3}{2}^+ \rightarrow {}^2\Pi_{\Omega'}, J') \equiv \frac{1}{2} \sum_{p'=\pm} \sigma(^2\Pi_{3/2}, \frac{3}{2}^+ \rightarrow {}^2\Pi_{\Omega'}, J'^{p'})$$

are given in Table 7 2 These cross sections can be considered as the cross sections for 'pure' rotational excitation

The potential energy surfaces they used for describing the OH-H₂ interaction are the ab initio surfaces of Kochanski and Flower [104] The results of Offer et al are illustrated in Figure 7 5 by the shaded squares and circles On the overall the agreement between theory and experiment is reasonably good Clearly the spin- orbit conserving transitions are preferred over spin-orbit changing collisional excitations, indicating that the sum potential, $V_{A'} + V_{A''}$, plays a more important role in the OH-H₂ collision process than the difference potential $V_{A'} - V_{A''}$ For the parity averaged cross sections, defined in section 7 3 , the agreement between theory and experiment is also good for the lowest rotational states

The cross section for the $^2\Pi_{3/2}, J = \frac{3}{2}^+ \rightarrow {}^2\Pi_{3/2}, J = \frac{3}{2}^-$ Λ-doublet transition in OH is in the same order of magnitude as the rotational transitions The theoretical value for the cross section
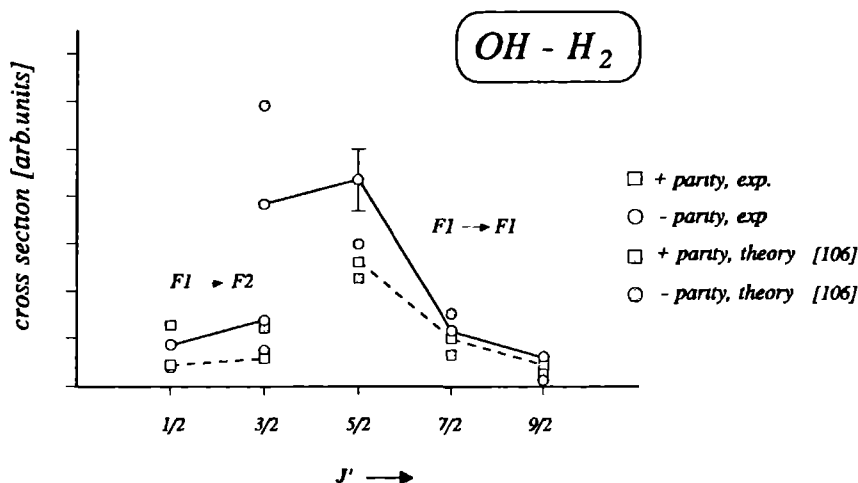
Figure 7.5 : *Relative state-to-state cross sections $\sigma(^2\Pi_{3/2}, \frac{3}{2}^+ \rightarrow \ ^2\Pi_{\Omega'}, J'^{p'})$ for $OH - H_2$ scattering The multiplet conserving transitions are indicated with $F1 \rightarrow F1$, the multiplet changing transitions with $F1 \rightarrow F2$ The data indicated by the open squares represent the cross sections for rotational excitation into the Λ-doublet component with positive parity (i e parity conserving transitions) The open circles show the cross sections for collisional excitation into the Λ-doublet component with negative parity The theoretical values from reference [106] are represented by the shaded squares and circles The error bar for the $J = \frac{5}{2}^-$ state illustrates the effect of correcting the measured cross section for inelastic scattering out of this $\frac{5}{2}^-$ state (see text)*

for this Λ-doublet transition became available from a private communication with Dr A Offer and appears to be stronger than our experimental value Andresen et al [18] measured the rate constant k_Λ for this $^2\Pi_{3/2}, \frac{3}{2}^+ \rightarrow \ \frac{3}{2}^-$ Λ-doublet transition in the $v = 1$ vibrationally excited state in the electronic ground state of OH In comparing with the total rate constant k_R for rotational transitions, they obtained $k_\Lambda/k_R = 0\ 7 \pm 0\ 5$ This may be compared with the present ratio of the cross sections for Λ-doublet and rotational transitions $\sigma_\Lambda/\sigma_R = 0\ 26$ So it seems that their value for k_Λ is somewhat overestimated

For the multiplet conserving $F1 \rightarrow F1$ transitions a weak parity propensity is observed Parity changing collisional excitations are slightly preferred over parity conserving transitions, leading to inversion for $\Delta J = $ odd transitions and to anti-inversion for even ΔJ transitions Except for excitation to the $J = \frac{9}{2}$ doublet, this is in agreement with the calculations of Offer and Flower Some more higher rotational states have to be measured for the multiplet changing $F1 \rightarrow F2$ transitions for drawing conclusions about a general parity selection rule For excitation to the $J = \frac{1}{2}$ state in the $F2$ multiplet a propensity for the parity conserving transitions is observed, in agreement with the theoretical data

$^2\Pi_{3/2} \to {}^2\Pi_{3/2}$					$^2\Pi_{3/2} \to {}^2\Pi_{1/2}$				
J',p'	$\sigma^{a)}$	$\sigma^{b)}$	$\bar{\sigma}^{a)}$	$\bar{\sigma}^{b)}$	J',p'	$\sigma^{a)}$	$\sigma^{b)}$	$\bar{\sigma}^{a)}$	$\bar{\sigma}^{b)}$
3/2, −	5 23	8 60							
5/2, +	4 00	3 22			1/2, +	0 60	1 82		
5/2, −	6 60	4 38			1/2, −	1 37	0 61		
5/2			5 30	3 80	1/2			0 98	1 22
7/2, +	1 48	0 98			3/2, +	0 92	1 75		
7/2, −	1 69	2 25			3/2, −	2 10	1 65		
7/2			1 59	1 62	3/2			1 51	1 70
9/2, +	0 69	0 51							
9/2 −	0 89	0 23							
9/2			0 79	0 37					

Table 7.2 : *State-to-state cross sections $\sigma({}^2\Pi_{3/2}, 3/2, + \to {}^2\Pi_\Omega, J', p')$ and parity averaged cross sections $\sigma({}^2\Pi_{3/2}, 3/2, + \to {}^2\Pi_\Omega, J')$ for OH H_2 collisions The experimental error is 20% The experimental values are compared with theoretical absolute values (in $\mathring{A}^2$) from Offer and Flower [106]*
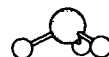
a) Present experimental results
b) Theoretical results from Offer and Flower [106]

Recently, Andresen et al [18] published the results of a similar crossed beam experiment on OH-H_2 scattering as the one described in this chapter However, they weren't able to separate the two $J = \frac{3}{2}$ Λ-doublet components in their initial state preparation both the $F1, \frac{3}{2}^p$ ($p = \pm$) parity substates were equally populated in the primary beam Consequently they reported 'parity averaged' cross sections $\sigma^\pm$ for collisional excitation out of both parity substates $|X^2\Pi_{3/2}, \frac{3}{2}^+\rangle$ and $|X^2\Pi_{3/2}, \frac{3}{2}^-\rangle$

$$\sigma^\pm(J', \Omega') = \frac{1}{2} \sum_{p=\pm} \sigma({}^2\Pi_{3/2}, \frac{3}{2}^p \to {}^2\Pi_{\Omega'}, J'^\pm) \tag{7 6}$$

Their collision energy was the same as in our experiment and they also used normal-H_2 as a scattering partner They obtained the interesting result that collisions with H_2 produce an anti-inversion in the $X^2\Pi_{3/2}$ state and an inversion in the $X^2\Pi_{1/2}$ multiplet, which has important astrophysical relevance, as is pointed out in the introduction of this chapter

It would be interesting to compare our results to the data of Andresen et al However, this is only possible if we would know the cross sections for scattering out of the $|X^2\Pi_{3/2}, \frac{3}{2}^-\rangle$ state also For this purpose the results of a scattering experiment with both $F1, J = \frac{3}{2}$ Λ-doublet components populated, are underway On the overall our experimental results are in reasonable agreement with the results from Offer and Flower [106] Since their parity averaged cross sections, as defined in

Equation (7.6) are in reasonable agreement with the crossed beam results of Andresen et al., our experimental results probably will not differ drastically from Andresen's results. However, a full comparison with their data is only possible if the cross sections $\sigma(^2\Pi_{3/2}, \frac{3}{2}^- \rightarrow {}^2\Pi_{\Omega'}, J'^{p'})$ become available from future measurements.

7.5 Conclusions

In this chapter we report preliminary results for the parity resolved relative state-to-state cross sections for rotational excitation of OH ($X^2\Pi$) by collisions with He, Ar and H_2. In a crossed molecular beam apparatus the OH radicals are produced by generating an electrical discharge in a molecular pulse, containing an H_2O in Ar gas mixture. Initial state $|^2\Pi_{3/2}, J^p = \frac{3}{2}^+\rangle$ preparation is achieved by rotational cooling of the OH molecules in a supersonic expansion, followed by electrostatic state selection in a hexapole electric field. After state preparation the primary beam is colliding with the target beam, containing molecular hydrogen or the rare gas He or Ar. Checks have been performed in order to be sure that single collision conditions are fulfilled, facilitating the data reduction. The rotational energy transfer in both spin-orbit multiplets of the OH ($X^2\Pi_i$) radical is studied by means of LIF spectroscopy of the $A \leftarrow X$ electronic transition of the molecule.

For OH – He collisions the cross sections for spin-orbit conserving rotational excitation are in the same order of magnitude as those for multiplet changing transitions. Remarkable is the weakness of the Λ-doublet transition induced by He scattering. Scattering by Ar or H_2 causes preferentially $\Delta J = 0$ (Λ-doublet) and $\Delta J = 1$ spin-orbit conserving transitions. For OH–H_2 scattering a weak propensity for parity changing transitions is observed for spin-orbit conserving collisional excitations. For OH–He and OH–Ar scattering a weak oscillatory behaviour is observed for the multiplet conserving cross sections.

The obtained cross sections are compared with theoretical values from quantum scattering calculations (OH-H_2 and OH-Ar) and show good agreement. Observed parity propensities for OH–He scattering are also in agreement with experimental data from double resonance relaxation measurements. A complete comparison with theory has to await quantum scattering calculations for the OH- He and OH- Ar collision systems at the experimental energies of 394 cm^{-1} and 451 cm^{-1} respectively.

As mentioned earlier the state-to-state cross sections for OH – H_2 scattering are strongly dependent on the H_2 species. Offer and Flower showed that in the case of para-H_2 scattering, strong parity propensity rules show up for certain collisional excitations. In order to test these theoretical predictions an experiment will be performed in which para-H_2 is prepared as collision partner.

7.6 Acknowledgement

Chapter 8

High Resolution Electronic Spectroscopy on the OH-Ar Van der Waals Complex

J. Schleipen, J. Heinze and J.J. ter Meulen
Department of Molecular and Laser Physics, University of Nijmegen
Toernooiveld, 6525 ED Nijmegen, The Netherlands

L. Nemes
Hungarian Academy of Science
Budapest, Hungary

In this study we report high resolution measurements on the electronic transition OH($A^2\Sigma^+$, $v'_{OH} = 0$)-Ar(^1S), $v'_{stretch} = 4$ and $5 \leftarrow$ OH($X^2\Pi$, $v''_{OH} = 0$)-Ar(^1S), $v''_{stretch} = 0$ using pulsed dye amplification of cw laser radiation. Rotational line splittings were observed which are attributed to hyperfine structure in the excited state. Accurate values have been determined for the rotational constants in the ground and excited states.
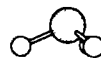
8.1 Introduction

The first observations of the electronic spectrum of the open shell Van der Waals complex OH-Ar by Lester and coworkers [114] and Fawzy and Heaven [115] has given rise to a rapidly expanding experimental and theoretical activity on this topic. A manifold of transitions starting from the vibrational ground state of $OH(X^2\Pi)$-Ar to various bending and stretching vibrational states in the excited state $OH(A^2\Sigma^+)$-Ar has been observed. The spectra could be analyzed assuming a linear or bent rigid rotor geometry of the complex. Theoretical models [116] do not exclude the possibility of large amplitude motions although these have not been included in the models so far. It is generally hoped that high resolution measurements can clarify this intriguing problem by an accurate analysis of rotational and possibly finer structures.

One of the questions to be solved concerns the change of the coupling of the non-zero electronic spin and angular momentum with the molecular rotation and vibration by the complex formation. In the OH radical these couplings give rise to the well-known Λ-doubling in the $X^2\Pi$ state and the spin-rotation splitting (ρ-doubling) in the $A^2\Sigma^+$ state. Because of the nearly pure case (a) character of the $OH(X^2\Pi)$-Ar state due to the small B rotational constant of the complex the Λ-doubling will be very small in the $\Pi_{3/2}$ state. In case of a bent geometry a Renner-Teller type splitting of this state is expected instead. With respect to the excited state $OH(A^2\Sigma^+)$-Ar it is generally assumed that the spin-rotation interaction constant γ scales down by the ratio of the rotational constants ($\sim$130). In contrast, the hyperfine interaction is probably not influenced much by the complex formation, as observed for Ar-NO [117]. As a result, the hyperfine splittings may exceed the spin-rotation splitting in the $OH(A^2\Sigma^+)$-Ar state.

The experiments reported so far have been performed with a resolution of ≥ 0.1 cm^{-1}, which is too low for the observation of possible hyperfine features in the spectra. In the present experiment we have performed LIF measurements on the OH-Ar complex with a resolution of 0.017 cm^{-1}, using pulsed dye amplification of single frequency cw laser radiation. We observed line splittings which can be explained by hyperfine interactions in the $OH(A^2\Sigma^+)$-Ar state. Precise values were obtained for the rotational and centrifugal distortion constants in the ground and excited states. When we started writing this paper we learned about a similar high resolution experiment by Miller and coworkers [118].

8.2 Experimental

In the present experiment OH radicals are produced by photodissociation of HNO_3. For this purpose the seeding gas argon was led through a 96% pure solution of nitric-acid. The gas mixture thus obtained is expanded in vacuum through a home-rebuilt Bosch-type pulsed valve. The valve is operated with a repetition rate of 10 Hz and a backing pressure of 2 atmosphere. The pulse duration is a few hundred microseconds. During operation the pressure in the vacuum chamber was about 10^{-5} Torr.

On top of the nozzle a quartz capillary (10 mm long and 1 mm in diameter) is mounted through which the gas is expanded. Before the expansion takes place, the HNO_3/Ar gas mixture is irradiated by the focused [f=50 cm] output of an ArF excimer laser (Lambda Physik EMG 150MSC, 193 nm, 80 mJ/15 nsec) in order to photodissociate the nitric-acid into smaller products, amongst which the OH radical is strongly represented. The focus of the photolyzing laser lies about 100 mm behind the capillary in order not to damage the quartz windows of the capillary and to irradiate the gasflow in the capillary over the largest possible area.
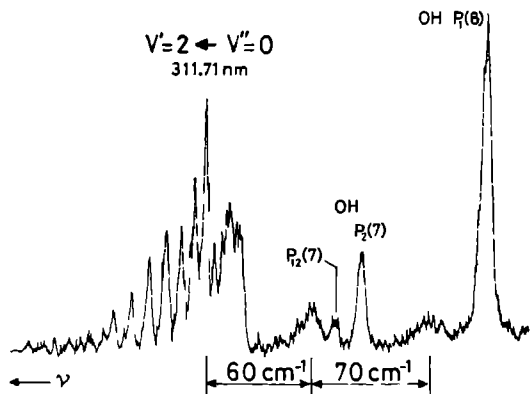
Figure 8.1 : *Low resolution spectrum of the $OH(A^2\Sigma^+, v'_{OH} = 0) - Ar, v'_{stretch} = 2 \leftarrow OH(X^2\Pi, v''_{OH} = 0) - Ar, v''_{stretch} = 0$ transition in the neighbourhood of the OH $P_1(8)$ rotational line Two satellite bands, shifted towards smaller frequencies, can clearly be distinguished They can probably be attributed to bending vibrations in the OH Ar electronic ground state*

After dissociation the gas mixture is expanded into the vacuum chamber and during collisions of the OH with the surrounding Ar atoms in the beginning of the expansion, the Van der Waals complex OH-Ar is formed The molecules are probed by laser induced fluorescence For this purpose the probe laser crosses the molecular beam about 5 cm downstream A mirror and lens assembly, collecting the fluorescence signal, image the probe volume onto the entrance slit of a 1/8 m monochromator (Oriel) The latter can be used either as a broad-band filter, eliminating any stray light sources, or as a narrow-band filter for recording a dispersion spectrum The output of the monochromator is registered by a photon multiplier tube

In this experiment we probe the $A^2\Sigma^+, v' = 0 \leftarrow X^2\Pi, v'' = 0$ transition of OH in the 308 nm wavelength region and the associated red-shifted bands of the Van der Waals complex OH-Ar In a low-resolution experiment the probe laser radiation is produced by frequency-doubling the output of a XeCl excimer laser (Lambda Physik EMG 201MSC) pumped dye laser (Lambda Physik, FL2002) operating with DCM dye The bandwidth of the frequency doubled radiation is about 0 5 cm^{-1} Frequency calibration is done by measuring several OH rotational lines during each scan In order to resolve possible structures underlying these 0 5 cm^{-1} broad line profiles, we performed a high-resolution experiment This time a home-built pulsed dye amplifier is applied, pumped by a Nd YAG laser (Quantel, 532 nm, 500 mJ/5 nsec) The PDA is locked by the 100 mW, narrowband (0 5 MHz) output of a cw ring dye laser (Spectra Physics 380 D) The output of the PDA is then frequency-doubled in a KDP crystal The bandwidth of the PDA radiation is merely
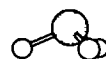
determined by the Fourier limit of the pulsed pump laser and yields ≈ 150 MHz for the fundamental output. Frequency calibration is achieved by recording simultaneously the absorption spectrum of the iodine molecule and the transmission fringes of a stabilized 299.4 MHz FSR interferometer. The output power of both probe lasers is attenuated in order to avoid saturation and line broadening effects.
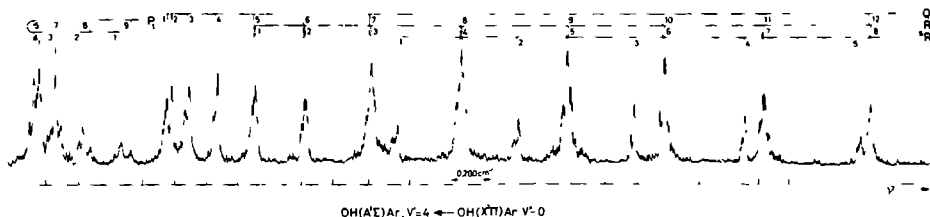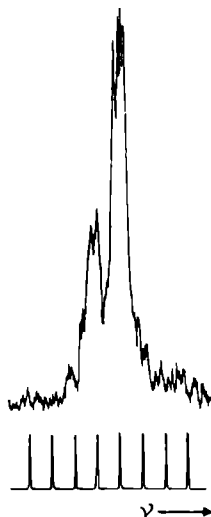

Figure 8.2 : *High resolution spectrum of the $OH(A^2\Sigma^+, v'_{OH} = 0) - Ar, v'_{stretch} = 4 \leftarrow OH(X^2\Pi, v''_{OH} = 0) - Ar, v''_{stretch} = 0$ transition. The spectrum is constructed from several overlapping frequency scans, which results in an irregular intensity ratio for some neighbouring rotational lines.*

8.3 Results and interpretation

The OH-Ar production was optimized applying low resolution LIF detection. In addition to the known transitions to the stretching vibrational states $v' = 2$ upto $v' = 6$ of $OH(A^2\Sigma^+)$-Ar we observed some red-shifted satellite features as shown in Figure 8.1. These unresolved satellite bands have been reported recently also by Bramble and Hamilton [25]. They attributed these bands to transitions from low-lying bending vibrational levels in the electronic ground state. For $v' = 2$ we observed a weak second satellite band, red-shifted about twice as much as the stronger first one. The satellite bands were too weak to be investigated with high resolution.

v"=0		v'=4		v'=5	
		ν_0	32291.686(2)	ν_0	32371.330(2)
B	0.10244(15)	B	0.13691(14)	B	0.12634(23)
D	0.0000079(13)	D	0.0000050(11)	D	0.0000094(25)

Table 8.1 : *Molecular constants (in cm^{-1}) for the groundstate $OH(X^2\Pi, v''_{OH} = 0) - Ar, v''_{stretch} = 0$ and the vibronic excited states $OH(A^2\Sigma^+, v'_{OH} = 0) - Ar, v'_{stretch} = 4$ and 5.*

Figure 8.3 : *Observed line splitting of the $^S R_{21}(3)$ transition The frequency distance between the markers is 598 8 MHz*

High resolution spectra were recorded for the $v'_{stretch} = 4 \leftarrow v''_{stretch} = 0$ and $v'_{stretch} = 5 \leftarrow v''_{stretch} = 0$ transitions at 309 7 and 308 9 nm, respectively A typical excitation spectrum for the transitions to $v' = 4$ is shown in Figure 8 2 Due to the limited continuous scan range of the cw laser several overlapping scans were required to cover the full spectrum The individual line width is about 500 MHz and is determined mainly by Doppler broadening caused by the divergence of the jet A further reduction of the linewidth by enlarging the distance between the detection region and the pulsed valve would cause too large a reduction of sensitivity

As can be seen from Figures 8 2 and 8 3, all single rotational lines are split into a doublet with an intensity ratio of approximately 1 2 for the two lines, the weak line being situated always at the low frequency side The splittings, which are typically about 0 024 cm^{-1} are observed for all siolated rotational lines in both the transition to $v' = 4$ and to $v' = 5$ In the rotational analysis the strongest line of each doublet was taken into account

8.3.1 Rotational analysis

The rotational lines could be assigned easily by making use of combination differences Similar to the OH $A^2\Sigma^+ \leftarrow X^2\Pi$ transitions six branches can be distinguished, namely P_1, Q_1, $^Q P_{21}$, R_1, $^R Q_{21}$ and $^S R_{21}$, where the same notation is used as for OH The Q_1 and $^Q P_{21}$ branches, and similarly the R_1 and $^R Q_{21}$ branches could not be resolved from each other as a result of the small spin-rotation splitting in the excited state Unfortunately for the $v' = 4 \leftarrow v'' = 0$ transition the
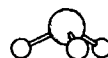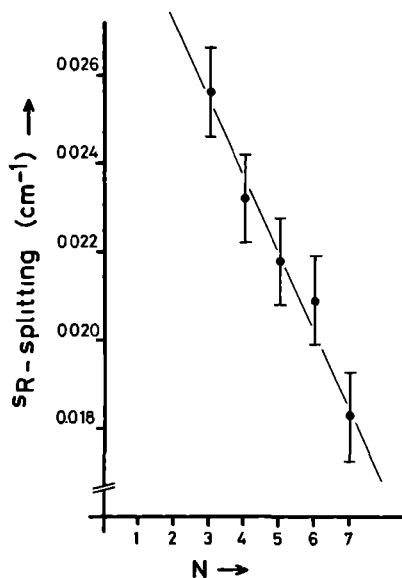
Figure 8.4 : *Observed splittings in the $^S R$-rotational lines due to hyperfine structure in the excited state OH($A^2\Sigma^+$) Ar,v'=4, N'   The splitting is decreasing with increasing rotational quantumnumber N'   This probably results from the growing importance of the spin rotation interaction in the excited state, with increasing N'*

R_1 and Q_1 branches are accidentally nearly coincident

The line frequencies were fitted to an effective Hamiltonian for a rigid linear molecule

$$H_{rot} = B'' J''(J'' + 1) - D'' J''^2(J'' + 1)^2 \qquad (8\ 1)$$

for OH ($X^2\Pi$)-Ar, and

$$H_{rot} = B' N'(N' + 1) - D' N'^2(N' + 1)^2 \qquad (8\ 2)$$

for OH ($A^2\Sigma^+$)-Ar

Here, J'' is the total angular momentum quantum number of the complex in the ground state and N' the end-over-end rotation quantum number in the excited state No parity splitting in the ground state or spin-rotation splitting in the excited state was taken into account The values for the rotational and centrifugal distortion constants obtained in a least squares fit, including 52 line frequencies, are given in Table 8 1 The quoted accuracy corresponds to one standard deviation and is an order of magnitude higher than previous results The absolute line frequencies and their deviations from the fitted values are given in Table 8 2

140

8.3.2 Hyperfine structure
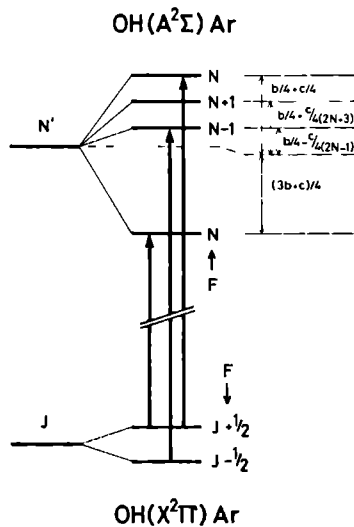
Figure 8.5 : *Hyperfine components of a $^S R$ rotational transition of the OH-Ar complex Due to practically zero spin-rotation interaction, the hyperfine levels in the excited state split into a triplet and a singlet with F'-quantumnumbers as denoted in the figure The $F' = N' + 1$ and $F' = N' - 1$ levels belong to $J' = N' + \frac{1}{2}$ and $J' = N' - \frac{1}{2}$, respectively The $J' = N' \pm \frac{1}{2}$, $F' = N'$ states are strongly mixed*

The observed rotational line splittings are only slightly larger than the present resolution making a detailed analysis impossible Although more structure can be expected to be present, we can draw some conclusions from the overall size of the splittings and the 1 2 intensity ratio of the two doublet lines As shown in Figure 8 4 for the $^S R_{21}$ transitions to the $v' = 4$ excited state, the splitting tends to decrease for larger N' values A similar dependence was also observed for the Q_1 transitions Averaging all splittings observed, a value of 720 MHz was obtained

The splittings can be explained by the hyperfine structure in the excited state which is caused by the interaction between the electron spin $\vec{S}$ and the nuclear spin $\vec{I}$

$$H_{hyp} = b\vec{I} \cdot \vec{S} + cI_z S_z \tag{8 3}$$

with $b + \frac{c}{3} = b_F$, the Fermi contact term. In case of OH $(A^2\Sigma^+)$ each N' state is split into two doublet states with $J' = N' \pm \frac{1}{2}$, due to the spin-rotation interaction The hyperfine interaction splits each of these states again into two doublet states with the quantum numbers $F' = N'$ and $F' = N' + 1$ in the upper ρ-doublet state $(J' = N' + \frac{1}{2})$ and $F' = N'$ and $F' = N' - 1$ in the lower ρ-doublet state $(J' = N' - \frac{1}{2})$ The hyperfine interaction constants for OH $(A^2\Sigma^+)$ are [119] $b_F = 775.1(1\ 1)$ MHz and $c = 166\ 4(2\ 8)$ MHz which give a hyperfine splitting of typically about
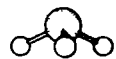
Transition	$v' = 4 \leftarrow v'' = 0$		$v' = 5 \leftarrow v'' = 0$	
	Frequency	Obs -Calc	Frequency	Obs -Calc
$P_1(1)$	32291 2947(50)	-0 0077	32370 9458(50)	-0 0003
$P_1(2)$	32291 0625(50)	-0 0020	32370 6898(50)	0 0028
$P_1(3)$	32290 8977(50)	0 0014	32370 4758(50)	-0 0005
$P_1(4)$	32290 8032(50)	0 0051	32370 3188(50)	0 0046
$P_1(5)$	32290 7724(50)	0 0019	32370 2068(50)	0 0059
$P_1(6)$	32290 8138(50)	-0 0003	-	-
$P_1(7)$	32290 9263(50)	-0 0031	-	-
$P_1(8)$	32291 1061(50)	-0 0112	-	-
$P_1(9)$	-	-	32370 2448(50)	0 0069
$P_1(10)$	-	-	32370 3738(50)	0 0039
$P_1(11)$	-	-	32370 5498(50)	-0 0013
$Q_1(1)$	32291 5780(50)	0 0018	-	-
$Q_1(2)$	32291 6128(50)	0 0008	32371 1918(50)	-0 0002
$Q_1(3)$	32291 7160(50)	-0 0012	32371 2318(50)	-0 0015
$Q_1(4)$	32291 8912(50)	-0 0009	32371 3188(50)	-0 0037
$Q_1(5)$	32292 1324(100)	0 0047	32371 4578(50)	-0 0018
$Q_1(6)$	32292 4426(100)	-0 0101	32371 6408(50)	-0 0036
$Q_1(7)$	32292 8172(200)	-0 0221	32371 8768(50)	-0 0002
$Q_1(8)$	-	-	32372 1548(50)	-0 0023
$Q_1(9)$	-	-	32372 4808(50)	-0 0038
$R_1(1)$	-	-	32371 7008(50)	-0 0029
$R_1(2)$	32292 4426(100)	0 0097	32371 9488(50)	-0 0002
$R_1(3)$	32292 8172(100)	0 0060	32372 2398(50)	-0 0018
$R_1(4)$	32293 2530(100)	-0 0057	-	-
$R_1(5)$	32293 7770(50)	0 0012	-	-
$R_1(6)$	32294 3721(50)	0 0095	-	-
$R_1(7)$	32295 0258(50)	0 0061	-	-
$R_1(8)$	32295 7515(50)	0 0040	-	-
$R_1(9)$	32296 5512(50)	0 0048	-	-
$R_1(10)$	32297 4154(50)	-0 0019	-	-
$R_1(11)$	32298 3598(50)	-0 0008	-	-

Table 8.2 : *Measured line positions (in cm^{-1}) for the OH-Ar,v'=4 and 5 $\leftarrow$ OH-Ar,v''=0 transition and deviations from a least squares fit The transitions are denoted by the 'near' quantumnumber $N'' = J'' - \frac{1}{2}$ in the $X^2\Pi_{3/2}$ correlated electronic state*

Transition	$v' = 4 \leftarrow v'' = 0$		$v' = 5 \leftarrow v'' = 0$	
	Frequency	Obs Calc	Frequency	Obs -Calc
$^S R_{21}(1)$	32292 9454(50)	0 0008	-	-
$^S R_{21}(2)$	32293 5326(50)	0 0057	-	-
$^S R_{21}(3)$	32294 1777(50)	-0 0001	-	-
$^S R_{21}(4)$	32294 8972(50)	-0 0001	-	-
$^S R_{21}(5)$	32295 6815(50)	-0 0042	-	-
$^S R_{21}(6)$	32296 5392(50)	0 0038	-	-
$^S R_{21}(7)$	32297 4658(50)	-0 0037	-	-
$^S R_{21}(8)$	32298 4664(50)	0 0007	-	-

Table 8.2 : *continued*

400 MHz Since this is at least an order of magnitude smaller than the spin-rotation splitting, the two $F' = N'$ states interact only slightly with each other

For OH($A^2\Sigma^+$)-Ar the spin-rotation interaction is probably much smaller than the hyperfine interaction, in which case a strong mixing is present between the two $F' = N'$ states Diagonalization of the Hamiltonian $H_{rot} + H_{hyp}$ gives a splitting of each N' state into three closely spaced hyperfine states with $F' = N' - 1$, N', $N' + 1$ and one more isolated state, $F' = N'$, at a lower energy as shown in Figure 8 5 If the spin-rotation interaction constant γ is set equal to zero the splitting between the two $F' = N'$ states is equal to $b + \frac{c}{2}$ This is equal to about 800 MHz, when it is assumed that the hyperfine interaction is not influenced by the complex formation The magnitude of this splitting is comparable to the observed one The intensity ratio of 1 2 can be understood from the normal electric dipole transition strengths, implying that the transitions with $\Delta J = \Delta F$ are the strongest ones As a result, three strong components are expected for each transition Two of these belong to transitions from both hyperfine states of the initial rotational state to two of the three upper hyperfine states of the excited state ($F' = N'$ and $F' = N' - 1$ or $N' + 1$, depending on the P, Q or R character of the transition) Since the hyperfine splittings in the ground state are small (of the order of 10 MHz for OH) we expect that these two transitions cannot be resolved with the present resolution The third strong component arises from a transition from one of the hyperfine states in the initial state to the lower $F' = N'$ state in the excited state This is illustrated in Figure 8 5 for the case of a $^S R_{21}$ transition Since both hyperfine states in the initial rotational state are nearly equally populated, an intensity ratio of 1 2 is expected with the weakest line at the low-frequency side

The observed tendency towards a smaller splitting for larger N'-values can only be understood if a non-zero spin-rotation constant γ is considered In that case the mixing of the two $F' = N'$ states becomes smaller for larger N' values due to a larger separation of both states As a result
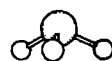
the relative intensities of the three strong components change. From calculated mixing coefficients we expect that already for values of γ around 200 MHz a doublet will appear with nearly equal line intensities and a splitting of about 400 MHz. An exact analysis of the hyperfine splittings has to await ultra-high resolution measurements.

8.4   Conclusions

The present high resolution spectra of the transition to the excited $v' = 4$ and $v' = 5$ stretching vibrational states in OH($A^2\Sigma^+$)-Ar could be analyzed well, using the rigid linear rotor model. This, however, does not exclude the possibility of large amplitude motions of the complex. Analysis of the observed red-shifted features either by ultra-high resolution LIF spectroscopy or far infrared absorption could provide a possible clue to unravel this mystery.

The observed line splittings can be explained by hyperfine structure in the excited state. The determination of the hyperfine and spin-rotation interaction constants requires a resolution that is at least a factor of 2 to 3 higher than in the present experiment. This might be obtained by a reduction of the Doppler broadening by collimation of the molecular beam.

8.5   Acknowledgement

Outlook

In this thesis single state-to-state cross sections for rotational excitation of NH_3 and OH by collisions with He, Ar and H_2 are presented Advanced molecular beam techniques made it possible to prepare a single initial quantum state of the NH_3 and OH molecules before collisions take place Pulsed laser sources, tunable in the visible and ultra violet region of the electromagnetic spectrum, can be used to detect the NH_3 and OH species with great sensitivity and in addition probe individual vibrational and rotational states of the molecules The combination of pulsed molecular beams and spectroscopical detection methods made the collision experiments described in this thesis to a success In the near future these techniques can be applied and further developed for similar collision experiments, studying the process of rotational or vibrational energy transfer in small molecules

- In this study only relative state-to-state collision cross sections could be determined Accurate beam density measurements are required for primary and secondary beam in order to obtain absolute state-to-state cross sections These data can be compared with theoretical values and provide information on the strength of the collision interaction

- The collision energies obtained with the present experimental set-up are in the order of 300-800 cm^{-1} From an astrophysical point of view and for calculational reasons it will be interesting to reduce this collision energy Interstellar collisions of NH_3 and OH with surrounding H_2 molecules occur with typical energies of less than 100 cm^{-1} and cross sections at these energies are required Lowering the collision energy further reduces the number of allowed collision entrance channels, facilitating quantum scattering calculations In order to obtain a smaller collision energy one can reduce the primary beam velocity This was done in the NH_3-Ar scattering experiment described in Chapter 5 and yielded a collision energy of 285 cm^{-1} For smaller collision energies, the molecular beam set-up has to be changed and two merged molecular beams have to be used By reducing the angle between primary and secondary beam, collision energies can be obtained down to a minimum value of 15 cm^{-1}, 70 cm^{-1} and 150 cm^{-1}, for NH_3 Ar, NH_3 – He and NH_3 – H_2 scattering, respectively Further reduction of the collision energy can be achieved by cooling the pulsed valves, yielding smaller beam velocities

- Recently much research has been done on the NH_3 dimer Infrared and microwave spectroscopical data provide important information on the intermolecular potential for the electronic ground state of this complex State-to-state collision experiments and calculations studying NH_3 NH_3 or NH_3 - ND_3 scattering may lead to a more complete picture of the intermolecular potential energy surface

- As was done for NH_3 scattering in Chapter 4 of this thesis, the OH collision experiment may

145
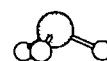
be repeated with the astrophysically important para-H_2 as a collision partner Considerable differences in the collisional behaviour of para H_2 and ortho-H_2 are expected from theoretical arguments and the experimental cross sections for these collision systems are a sensitive probe for the OH–para-H_2 and OH–ortho-H_2 potential energy surfaces

- In order to examine vibration-rotation interactions during vibrational and/or rotational energy transfer in $NH_3 - H_2$ and OH $- H_2$ scattering, the collision partner H_2 can be vibrationally excited by stimulated Raman pumping to the v=1 vibrational state (at 4395 cm^{-1}) of the electronic groud state

- The experimentally determined cross sections represent integral state-to-state cross sections, averaged over all centre of mass scattering angles Additional information on the anisotropy of the potential enery surface can be obtained from differential state-to-state cross sections Differential scattering measurements may be performed where the laser probes the final state distribution of the scattered primary beam molecules as a function of scattering angle This technique has been succesfully applied in a cw scattering experiment on formaldehyde by van Hulst et al [120], using a carefully designed rotatable LIF detector A strong angular dependence was observed for some rotational transitions when colliding with H_2 The REMPI technique should be a good candidate for differential detection in the case of NH_3 scattering The high detection efficiency of ions and the absence of any laser radiation background result in a high detection sensitivity In addition no collection optics is necessary to detect the ions which simplyfies the differential detection and keeps the molecular beams undisturbed

- In the present investigation only one rotational state for ortho-NH_3 (0_0^+), para-NH_3 (1_1^-) and OH ($F 1, \frac{3}{2}^+$) could be initially populated in the primary beam An additional microwave (MW) or infrared (IR) pump directly behind the hexapole state selector can induce dipole transitions in the prepared molecules The scattering data obtained from such MW/IR–UV double resonance experiments may result in state-to-state cross sections $\sigma(i_{MW/IR} \to f)$ for scattering out of the the microwave or infrared labeled rovibrational states in the electronic ground state of the NH_3 or OH molecules

- The combination of single initial state preparation in a pulsed molecular beam set-up and the complete state and species selective spectroscopical detection techniques may also be used in reactive scattering Plans are made to investigate the reaction

$$H_2(X^1\Sigma_g^+, i, j) \; + \; O(^1D_2) \;\; \to \;\; OH(X^2\Pi_i, v, J) \; + \; H$$
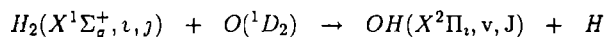
where the OH product state distribution is studied with the differential LIF detection technique The OH product vibrational and rotational state distribution can be studied as a function of collision energy and initial vibrational and rotational energy of the molecular hydrogen The experiment may reveal information on the reaction path across the different potential energy surfaces describing the interaction and on the intermolecular potential itself

Bibliography

[1] A C Cheung, D M Rank, C H Townes, D D Thornton and W J Welch, Phys Rev Lett 21 (1968) 1701

[2] M Morris, B Zuckerman, P Palmer and B E Turner, Astrophys J 186 (1973) 501,
P R Schwartz, A C Cheung, J M Bologna, M F Chui, J A Waak and D Matsakis, Astrophys J 218 (1977) 671,
G Winnewisser, E Churchwell and C M Walmsley, Astron Astroph 72 (1979) 215,
T Oka, F O Shimizu, T Shimizu and J K G Watson, Astrophys J 165 (1971) 15,
W T Sullivan, Astrophys J 157 (1969) 13,
P T P Ho and C H Townes, Ann Rev Astron Astrophys 21 (1983) 239

[3] S Weinreb, A H Barrett, M L Meeks and J C Henry, Nature 200 (1963) 829,
H F Weaver, D R Williams, N H Dieter and W T Lum, Nature 208 (1965) 29,
B J Robinson and R X McGee, Ann Rev Astron Astroph 5 (1967) 183
B E Turner, J Roy Astron Soc Canada 64 (1970) 221

[4] M M Litvak, A L McWorther, M L Meeks and H J Zeiger, Phys Rev Lett 17 (1966) 821,
M M Litvak, Astroph J 156 (1969) 471

[5] A C Cheung, D M Rank, C H Townes, S H Knowles and W T Sullivan III, Astroph J 157 (1969) L13

[6] R Howard and W V Smith, Phys Rev 79 (1950) 128,
R L Legan, J A Roberts E A Rinehart and C C Lin, J Chem Phys 43 (1965) 4337,
B Bleany and R P Penrose, Proc Phys Soc London 60 (1948) 540,
T Amano, T Amano and R H Schwendeman, J Chem Phys 73 (1980) 1238

[7] G Bachet, J Quant Spectr Rad Transf 13 (1973) 1305

[8] J S Margolis, J Quant Spectr Rad Transf 15 (1975) 637,
J S Margolis and S Sarangi, J Quant Spectr Rad Transf 16 (1976) 405

[9] M Broquier, A Picard-Bersellini and J Hall, Chem Phys Lett 136 (1987) 531,
M Broquier, A Picard-Bersellini, H Aroui and G D Billing, J Chem Phys 88 (1988) 1551

[10] T Oka, J Chem Phys 48 (1968) 4919, 49 (1968) 3135,
P W Daly and T Oka, J Chem Phys 53 (1970) 3272,
A R Fabris and T Oka, J Chem Phys 56 (1972) 3168

[11] A Das and C H Townes, J Chem Phys 85 (1986) 179

[12] B Abel, S L Coy, J J Klaassen and J I Steinfeld, to be published

[13] M J Shultz and J Wei, J Chem Phys 92 (1990) 5951

[14] J M H Reynders, Ph D Thesis, Katholieke Universiteit Nijmegen, 1978,
D B M Klaassen, Ph D Thesis, Katholieke Universiteit Nijmegen, 1982,
D B M Klaassen, J M H Reynders, J J ter Meulen and A Dymanus, J Chem Phys 77 (1982) 4972, 78 (1983) 767
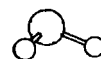
References

[15] H Meyer, U Buck, R Schinke and G H F Diercksen, J Chem Phys 84 (1986) 4976

[16] G Ebel, R Krohne, U Buck and R Schinke, J Phys Chem 95 (1991) 8232

[17] G A Raiche, J B Jeffries, K J Rensberger and D R Crosley, J Chem Phys 92 (1990) 7258,
I J Wysong, J B Jeffries and D R Crosley, J Chem Phys 94 (1991) 7547

[18] P Andresen, N Aristov, V Beushausen, D Hausler and H W Lulf, J Chem Phys 95 (1991) 5763

[19] *Atomic and molecular beam methods, vol I*, Eds G Scoles, D Bassi, U Buck and D Lainé, Oxford University
Press, Oxford, 1988

[20] J J ter Meulen, Ph D Thesis, Katholieke Universiteit Nijmegen, 1976

[21] W Ubachs, Ph D Thesis, Katholieke Universiteit Nijmegen, 1986

[22] T Bercess and S Forgeteg, Trans Farad Soc 66 (1970) 633, 66 (1970) 640,
T Bercess, S Forgeteg and F Marta, Trans Farad Soc 66 (1970) 648

[23] H S Johnston, S G Chang and G Whitten, J Phys Chem 78 (1974) 1

[24] A T Droege and P C Engelking, Chem Phys Lett 96 (1983) 316

[25] S K Bramble and P A Hamilton, Chem Phys Lett 170 (1990) 107

[26] P R Bunker, *Molecular symmetry and spectroscopy*, Academic Press, New York, 1979

[27] M N R Ashfold, R N Dixon, R J Stickland and C M Western, Chem Phys Lett 138 (1987) 201,
M N R Ashfold, R N Dixon, R J Stickland and C M Western, Chem Phys 98 (1984) 463,
C M Western, private communications

[28] A R Edmonds, *Angular momentum in quantum mechanics*, Princeton Univ Press, Princeton, 1960

[29] S Green, J Chem Phys 73 (1980) 2740

[30] D Papoušek and M R Aliev, *Molecular vibrational - rotational spectra*, Studies in physical and theoretical
chemistry, vol 17, Elsevier Science Publishers, Amsterdam, 1982

[31] E B Wilson, J C Decius and P C Cross, *Molecular vibrations*, McGraw-Hill, New York, 1955

[32] G Herzberg, *Molecular spectra and molecular structure, II Infrared and Raman spectra of polyatomic molecules*,
Van Nostrand Rheinhold, Princeton, 1945

[33] K Chen and E S Yeung, J Chem Phys 69 (1978) 43

[34] G Herzberg, *Molecular spectra and molecular structure, I Spectra of diatomic molecules*, Van Nostrand Rhein-
hold, Princeton, 1950

[35] G H Dieke and H M Crosswhite, J Quant Spectrosc Radiat Transfer 2 (1962) 97

[36] M Mizushima, *The theory of rotating diatomic molecules*, Wiley Interscience, New York, 1975

[37] E L Hill and J H van Vleck, Phys Rev 32 (1923) 250

[38] M H Alexander and P J Dagdigian, J Chem Phys 80 (1984) 4325

[39] G C Dousmanis, T M Sanders, Jr and C H Townes, Phys Rev 100 (1955) 1735

[40] S Green, J Chem Phys 64 (1976) 3463

[41] Th Seelemann, P Andresen, J Schleipen, B Beyer and J J ter Meulen, Chem Phys 126 (1988) 27

148

[42] G D Billing, L L Poulsen and G H F Diercksen, Chem Phys 98 (1985) 397,
G D Billing, Cross sections for NH₃-He, private communication

[43] G H F Diercksen, B O Roos and A J Sadlej, Intern J Quantum Chem Quantum Chem Symp 17 (1983) 265

[44] G Ebel, R Krohne, H Meyer, U Buck, R Schinke, T Seelemann, P Andresen, J Schleipen, J J ter Meulen and G H F Diercksen, J Chem Phys 93 (1990) 6419

[45] G Danby, D R Flower, P Valiron, E Kochanski L Kurdi and G H F Diercksen, J Phys B At Mol Phys 19 (1986) 2891, J Phys B At Mol Phys 20 (1987) 1039

[46] A Offer and D R Flower, J Phys B At Mol Opt Phys 22 (1989) L439

[47] A Offer and D R Flower, J Chem Soc Faraday Trans 86 (1990) 1659

[48] G D Billing and G H F Diercksen, Chem Phys 105 (1986) 145,
G D Billing and G H F Diercksen, Chem Phys 118 (1987) 161

[49] G D Billing, L L Poulsen and G H F Diercksen, Chem Phys 98 (1985) 397

[50] S L Davis and J E Boggs, J Chem Phys 69 (1978) 2355

[51] W R Gentry and C F Giese, Rev Sci Instrum 46 (1975) 104

[52] J Stutzki and G Winnewisser, Astron Astrophys 144 (1985) 13

[53] R J Stanley, O Echt and A W Castleman, Appl Phys B 32 (1983) 35

[54] A J Grimley and B D Kay, Chem Phys Lett 98 (1983) 359,
B D Kay and A J Grimley, Chem Phys Lett 127 (1986) 303,
B D Kay and T D Raymond, J Chem Phys 85 (1986) 4140

[55] W E Conoway, R J S Morrison and R N Zare, Chem Phys Lett 113 (1985) 429,
R J S Morrison, W E Conoway, T Ebata and R N Zare, J Chem Phys 84 (1986) 5527

[56] G C Niemann and S D Colson, J Chem Phys 71 (1979) 571

[57] J H Glownia, S J Riley and S D Colson, J Chem Phys 72 (1980) 5998,
J H Glownia, S J Riley, S D Colson and G C Niemann, J Chem Phys 73 (1980) 4296,
J H Glownia, S J Riley, S D Colson, J C Miller and R N Compton, J Chem Phys 77 (1982) 68

[58] H Joswig, P Andresen and R Schinke, J Chem Phys 85 (1986) 1904

[59] P J Dagdigian, in 'Atomic and Molecular Beam Methods',vol 1, edited by G Scoles, Oxford University Press, Oxford, 1988

[60] D M Sonnenfroh and K Liu, Chem Phys Lett 176 (1991) 183

[61] N Dam, C Liedenbaum, S Stolte and J Reuss, Chem Phys Lett 136 (1987) 73

[62] J Schleipen and J J ter Meulen, Chem Phys 156 (1991) 479

[63] G D Billing and G H F Diercksen, Chem Phys 124 (1988) 77

[64] G Danby and P Valiron, Chem Phys Lett 163 (1989) 75

[65] A C Cheung, D M Rank, C H Townes, D D Thornton and W J Welch, Nature 221 (1969) 917,
S H Knowles and A C Cheung, Astroph J 164 (1971) L19,
N Kaifu, M Morris, P Palmer and B Zuckerman, Astroph J 201 (1975) 98

149

References

[66] R Mauersberger, C Henkel and T L Wilson, Astron Astrophys 173 (1987) 352

[67] C M Walmsley and H Ungerechts, Astron Astrophys 122 (1983) 164

[68] S Guilloteau, T L Wilson, R N Martin, W Batrla and T A Pauls, Astron Astrophys 124 (1983) 322

[69] K J Johnston, S R Stolovy, T L Wilson, C Henkel and R Mauersberger, Astrophys J 343 (1989) L41

[70] S C Madden, W M Irvine, H E Matthews, R D Brown and P D Godfrey, Astroph J 300 (1986) L79

[71] J S Schweitzer, Astroph J 225 (1978) 116

[72] D R Flower and G D Watt, Mon Not R Astr Soc 209 (1984) 25

[73] E Roueff, H Abgrall, J Le Bourlot and Y Viala, In *Rate Coefficients in Astrochemistry*, eds T J Millar and D A Williams, Kluwer, Dordrecht, 1988

[74] J Schleipen, J J ter Meulen, G C M van der Sanden, P E S Wormer and A van der Avoird, Chem Phys 163 (1992) 161

[75] G C M van der Sanden, P E S Wormer, A van der Avoird, J Schleipen and J J ter Meulen, submitted for publication in J Chem Phys

[76] I F Silvera, Rev Mod Phys 52 (1980) 393

[77] D A Long, *Raman Spectroscopy*, McGraw-Hill London, 1977

[78] P Valiron, private communications 1989

[79] J M Hutson and S Green, MOLSCAT computer code version 9, CCP6 (Daresbury Laboratory, UKSERC, 1986)

[80] E Zwart, H Linnartz, W L Meerts, G T Fraser, D D Nelson Jr and W Klemperer, J Chem Phys 95 (1991) 793

[81] D H Gwo, M Havenith, K L Busarow, R C Cohen, C A Schmuttenmaer and R J Saykally, Mol Phys 71 (1990) 453

[82] G T Fraser, D D Nelson Jr , A Charo and W Klemperer, J Chem Phys 82 (1985) 2535

[83] D D Nelson Jr , G T Fraser, K I Peterson, K Zhao, W Klemperer, F J Lovas and R D Suenram, J Chem Phys 85 (1986) 5512

[84] M Alexander, J Chem Phys 77 (1982) 1855
M Alexander and S L Davis, J Chem Phys 79 (1983) 227

[85] N F Ramsey, 'Molecular Beams', Clarendon Press, Oxford, 1956

[86] M Bulski, P E S Wormer and A van der Avoird, J Chem Phys 94 (1991) 491

[87] J W I van Bladel, A van der Avoird and P E S Wormer, J Chem Phys 94 (1991) 501

[88] S Green, J Chem Phys 70 (1979) 816

[89] C Rist, Ph D Thesis, Université Joseph Fourier, Grenoble, 1991

[90] E Olthof, Student Thesis, Katholieke Universiteit Nijmegen, 1991

[91] J W I van Bladel, A van der Avoird, and P E S Wormer, Chem Phys , in press

[92] D M Brink and G T Satchler, *Angular Momentum*, Clarendon Press, Oxford, 1968

[93] J W I van Bladel, A van der Avoird, and P E S Wormer, J Phys Chem 95 (1991) 5414

[94] HIBRIDON is a package of programs for the time-independent quantum treatment of inelastic collisions and photodissociation written by M H Alexander, D Manolopoulos, H-J Werner, and B Follmeg, with contributions by P F Vohralik, G Corey, B Johnson, T Orlikowski and P Vahron

[95] H Weaver, D R Williams, N H Dieter and W T Lum, Nature 208 (1965) 29,
S Weinreb, M L Meeks, J C Carter, A H Barrett and A E Rogers, Nature 208 (1965) 440,
B Zuckerman, A E Lilley and H Penfield, Nature 208 (1965) 441,
R X McGee, B J Robinson, F F Gardner and J G Bolton, Nature 208 (1965) 1193,
R D Davies, D de Jager and G L Verschuur, Nature 209 (1966) 974
A H Barrett and A E Rogers, Nature 210 (1966) 188

[96] M Elitzur, Rev of Mod Phys 54 (1982) 1225

[97] M J Reid and M J Moran, Ann Rev Astron Astrophys 19 (1981) 231

[98] J Guibert, M Elitzur and Ngyuen-Q Rieu, Astron Astrophys 66 (1978) 395

[99] P Andresen, Astron Astrophys 154 (1986) 42

[100] P Andresen, G S Ondrey and B Titze, Phys Rev Lett 50 (1982) 486

[101] P Andresen, G S Ondrey, B Titze and E W Rothe, J Chem Phys 80 (1984) 2548

[102] P Andresen, D Hausler and H W Lulf, J Chem Phys 81 (1984) 571

[103] D P Dewangan and D R Flower, J Phys B At Mol Phys 14 (1981) 2179,
D P Dewangan and D R Flower, J Phys B At Mol Phys 16 (1983) 2157

[104] E Kochanski and D R Flower, Chem Phys 57 (1981) 217

[105] R Schinke and P Andresen, J Chem Phys 81 (1984) 5644

[106] A Offer and D R Flower, J Phys B At Mol Opt Phys 23 (1990) L391,
A Offer, Ph D Thesis, University of Durham, 1990,
A Offer, private communications

[107] W Fawzy and M C Heaven, J Chem Phys 89 (1988) 7030,
M T Berry, M R Brustein and M I Lester, Chem Phys Lett 17 (1988) 153,
M T Berry, M R Brustein, J R Adamo and M I Lester, J Phys Chem 92 (1988) 5551,
J Schleipen, L Nemes, J Heinze and J J ter Meulen, Chem Phys Lett 175 (1990) 561,
B Chang, L Yu, D Cullin, B Rehfuss, J Williamson, T A Miller, W Fawzy, X Zheng, S Fei and M Heaven, J Chem Phys 95 (1991) 7086
C Chakravarty, D C Clary, A Degli Esposti and H-J Werner, J Chem Phys 93 (1990) 3367

[108] A Vegiri and S Farantos, J Phys Chem 92 (1988) 2723,
S Farantos and A Vegiri, J Phys Chem 92 (1988) 2719

[109] A Jorg, A Degli Esposti and H J Werner, J Chem Phys 93 (1990) 8757,
A Jorg, U Meier and K Kohse-Hoinghaus, J Chem Phys 93 (1990) 6453

[110] A Degli Esposti and H-J Werner, J Chem Phys 93 (1990) 3351

[111] M H Alexander, J Chem Phys 76 (1982) 5974

[112] M H Alexander, Chem Phys 92 (1985) 337

[113] T Orlikowski and M H Alexander, J Chem Phys 79 (1983) 6006
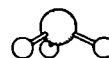
[114] M T Berry, M R Brustein, J R Adamo and M I Lester, J Phys Chem 92 (1988) 5551,
M T Berry, M R Brustein and M I Lester, Chem Phys Lett 153 (1988) 17

[115] W M Fawzy and M C Heaven, J Chem Phys 89 (1988) 7030, J Chem Phys 92 (1990) 909

[116] W M Fawzy and J T Hougen, J Mol Spectr 137 (1989) 154,
C Chakravarty, D C Clary, A Degli-Esposti and H J Werner, J Chem Phys 93 (1990) 3367

[117] P D A Mills, C M Western and B J Howard, J Phys Chem 90 (1986) 4961

[118] B C Chang, D W Cullin, J M Williamson, B D Rehfuss, L Yu and T A Miller, 45th Symposium on Molecular Spectroscopy, June 11 15 (1990), Ohio, USA

[119] J J ter Meulen, W A Majewski, W L Meerts and A Dymanus, Chem Phys Lett 94 (1983) 25

[120] N F van Hulst, Ph D Thesis, Katholieke Universiteit Nijmegen, 1986

[121] Prof Dr H J Werner, private communications

Summary

In this thesis we study the rotational energy transfer in the vibronic ground state of the NH_3 and the OH molecule upon collisions with target particles He, Ar and H_2 In a molecular beam machine two pulsed molecular beams are crossed at right angles, the primary beam containing the NH_3 or OH molecules and the secondary beam containing the He, Ar or H_2 scattering targets Rotational state preparation of the primary beam molecules is obtained by rotational cooling in a supersonic expansion into vacuum, followed by electrostatic state selection in a hexapole electric field Rotational state analysis of the NH_3 and OH molecules, before and after the collision process, is achieved by laser spectroscopical methods For the NH_3 molecule the 2+1 REMPI spectroscopy of the $\tilde{B} \leftarrow \tilde{X}$ electronic transition proved to be a very accurate and sensitive tool for probing individual rotational states in the vibronic ground state of NH_3 For the OH radical LIF spectroscopy of the A $\leftarrow$ X electronic transition yielded a complete rotational state analysis of the OH vibronic ground state.

Single initial state $|i\rangle$ preparation and complete state selective final state $|f\rangle$ detection of the NH_3 and OH molecules finally results in the determination of relative parity resolved rotational state-to-state cross sections $\sigma(i \rightarrow f)$ The collision energies are typically 300-800 cm^{-1}, depending on the collision system under study Carefull checks have been performed in order to be sure that single collision conditions are fulfilled, facilitating the data analysis As a result the secondary beam stagnation pressure is restricted to a maximum value, depending on the primary and secondary beam species The experimentally determined cross sections are compared with theoretical values obtained from quantum scattering calculations for the different collision systems In general the agreement between experiment and theory is good as far as 'pure' rotational energy transfer is concerned Also theory predicts strong 'parity propensity rules' a strong preference exists for either parity-conserving or parity-changing rotational excitations For most rotational transitions these propensities are confirmed, although less pronounced as predicted by theory

In Chapter 3 we study the NH_3 – He and NH_3 – H_2 scattering The collision experiment is repeated in Chapter 4, but now with the astrophysically important para-H_2 as scattering partner Chapters 5 and 6 deal with the collisional excitation of NH_3 by Ar In Chapter 5 the crossed molecular beam experiment yields state-to-state cross sections $\sigma(i \rightarrow f)$ at two different collision energies of 285 cm^{-1} and 485 cm^{-1} respectively In Chapter 6 we perform a quantum scattering calculation for the NH_3 - Ar collision system using an ab initio potential energy surface and a potential scaled to spectroscopical data The intermolecular potential contained the inversion coordinate explicitly and solving the close coupled scattering equations involved integration over this inversion coordinate The calculations predict a strong propensity for parity-index changing rotational transitions for ortho-NH_3 and for some $|\Delta K = 3|$ transitions in para-NH_3, when the scattering takes place by the rare gas atoms He and Ar or by the para-H_2 species This propensity for parity-index changing transitions is verified by the crossed beam experiments, although the
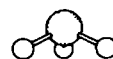
observed propensities are less strong than the corresponding theoretical predictions

We showed that the rotational excitation of NH_3 in collision with para-H_2, behaves different from NH_3 – He scattering, which has important astrophysical relevance since the NH_3 – He collision cross sections are often taken as a reference for NH_3 – para-H_2 collisions For NH_3 – Ar scattering the calculations showed that discrepancies with the experiment most probably arise from shortcomings of the ab initio potential energy surface Furthermore, the use of the coupled states approximation in the quantum scattering calculations yield predictions for the parity propensity rules which are inconsistent with the experimentally obtained propensities Consequently, the (computer-)time consuming exact close coupling formalism should be used for an accurate description of the collision process

Chapter 7 describes the OH scattering experiment. The OH radicals are produced in an electric discharge in the H_2O/Ar molecular pulse Subsequent rotational cooling and electrostatic state selection prepared the $\frac{3}{2}^+$ state in the $^2\Pi_{3/2}$ spin-orbit multiplet of the vibronic ground state of OH. Parity resolved rotational state-to-state cross sections are obtained for OH – He, OH – Ar and OH – H_2 scattering Spin-orbit multiplet conserving, as well as spin-orbit changing transitions are observed in the collision process For He and Ar scattering a weak $\Delta J = 2$ oscillatory behaviour is observed for spin-orbit conserving, parity changing rotational excitations The state-to-state cross sections thus obtained are compared with data from other experiments and quantum calculations and show good agreement

In Chapter 8 we report a spectroscopical study on the OH-Ar van der Waals molecule The OH radical is produced in the molecular beam machine using flash photolysis of nitric acid Subsequent collisions with the Ar atoms inside the primary beam expansion result in the OH-Ar complex formation The complex is studied by means of LIF spectroscopy using the narrow band output of a pulsed dye amplifier laser system The spectra can be analyzed assuming a linear geometry for the OH-Ar bound system and yield accurate rotational and centrifugal distortion constants for the ground and first electronic excited states of the complex

Samenvatting

Toestandselectieve botsingsdoorsneden voor rotationele excitatie van NH_3 en OH door botsingen met He, Ar en H_2

In dit proefschrift bestuderen we het proces van rotationele energieoverdracht in de electronische en vibrationele grondtoestand van het NH_3- en OH-molecule ten gevolge van botsingen met de edelgasatomen He en Ar, en met het di-atoom H_2 Hiertoe worden twee gepulste moleculaire bundels gekruist in een vacuumopstelling In de primaire bundel bevinden zich de NH_3- of OH-moleculen en de secundaire bundel bevat de botsingspartner helium, argon of moleculair waterstof Door middel van een supersone expansie van de moleculen in een vacuumomgeving, gevolgd door electrostatische toestandsselectie in een zespool-electrisch veld, zijn we in staat één enkele rotatietoestand van het NH_3- en OH-molecule te prepareren voordat de moleculaire bundel het strooicentrum bereikt De rotationele toestandsverdeling van de primaire bundel moleculen wordt voor en na het botsingsproces bepaald met behulp van laser-spectroscopische methoden Bij het NH_3-molecule maken we gebruik van 2+1 REMPI spectroscopie aan de $\tilde{B} \leftarrow \tilde{X}$ electronische overgang in het molecule Deze zeer gevoelige multi-foton-ionisatietechniek maakt het mogelijk elke rotatietoestand van het molecule individueel te bestuderen Bij de detectie van het OH-radicaal wordt LIF spectroscopie aan de $A \leftarrow X$ electronische overgang toegepast, hetgeen eveneens een complete rotationele toestandsanalyse van het molecule mogelijk maakt

Het prepareren van slechts één rotatietoestand van het NH_3- en OH-molecule, in combinatie met de rotatietoestand-selectieve detectiemethode voor beide moleculen, stelt ons in staat volledig toestandsopgeloste botsingsdoorsneden $\sigma(\imath \to f)$ te bepalen voor het betreffende verstrooiingsexperiment De botsingsenergieen bedragen 300-800 cm^{-1}, afhankelijk van de snelheid en massa van de botsingspartners Om er zeker van te zijn dat secundaire botsingen geen bijdrage leveren aan het gemeten verstrooiingssignaal worden zorgvuldige testmetingen verricht De experimentele botsingsdoorsneden kunnen vervolgens worden vergeleken met de resultaten van quantumberekeningen voor de diverse verstrooiingssytemen In het algemeen is de overeenkomst met de theoretische waarden goed wat betreft de pure rotationele energieoverdracht De theorie voorspelt tevens 'pariteitsvoorkeurregels' er bestaat een sterke voorkeur voor ofwel pariteitsbehoudende dan wel pariteitsveranderende rotationele toestandsexcitaties Voor de meeste rotatie-overgangen zijn deze pariteitsvoorkeurregels bevestigd, ofschoon de experimentele voorkeur minder sterk is gebleken dan de theoretische voorspellingen doen vermoeden

Het proefschrift is als volgt ingedeeld Hoofdstuk 1 geeft een algemene inleiding tot het botsingsexperiment Hierbij worden verschillende meetmethodes besproken die in het verleden gebruikt zijn om botsingsdoorsneden voor rotationele energieoverdracht te bepalen In Hoofdstuk 2 wordt het huidige botsingsexperiment besproken, waarbij de REMPI- en LIF-spectroscopische technieken kort worden toegelicht In Hoofdstuk 3 van dit proefschrift bestuderen we de verstrooiing van NH_3

155

aan He en H_2 Het experiment is herhaald in Hoofdstuk 4, maar nu voor het astrofysisch belangrijke para-H_2 als botsingspartner De Hoofdstukken 5 en 6 behandelen de rotatto nele excitatie van het NH_3-molecule ten gevolge van botsingen met Ar In Hoofdstuk 5 worden experimentele toestandsopgeloste botsingsdoorsneden verkregen met de moleculaire bundel opstelling In Hoofdstuk 6 wordt een quantumberekening uitgevoerd aan dit NH_3-Ar verstrooiingssyteem, waarbij enerzijds gebruik wordt gemaakt van een zuivere ab initio intermoleculaire potentiaal en anderzijds van een geschaalde potentiaal, geijkt op spectroscopische data In deze berekening wordt de 'tunnel'-beweging van het NH_3-molecule expliciet meegenomen De intermoleculaire potentiaal bevat de inversie-coordinaat van het NH_3-molecule en tijdens de 'close coupling'-quantum verstrooiingsberekeningen wordt geintegreerd over deze coordinaat De berekeningen voorspellen een sterke voorkeur voor pariteitsindex-veranderende rotatie-overgangen voor ortho-NH_3 en voor enkele $|\Delta K = 3|$-overgangen in para-NH_3, wanneer deze excitaties plaatsvinden door botsingen met de edelgassen He en Ar, of met para-H_2 Deze pariteitsvoorkeur wordt tevens waargenomen in het verstrooiingsexperiment, ofschoon minder sterk dan de theoretische voorspelling

We laten zien dat de rotationele botsingsexcitatie van NH_3 door para-H_2 zich anders gedraagt dan in NH_3-He verstrooiing, hetgeen belangrijke consequenties heeft voor de interpretatie van astrofysische waarnemingen De berekeningen voor NH_3 – Ar verstrooiing tonen aan dat de discrepanties met het experiment waarschijnlijk een gevolg zijn van een onvolledige kennis van de intermoleculaire potentiaal die deze botsingsinteractie beschrijft Het gebruik van de 'coupled states'-benadering in deze verstrooiingsberekeningen resulteert in pariteitsvoorkeurregels die niet overeenkomen met de waarnemingen Dit heeft tot gevolg dat het (computer-)tijdverslindende, doch quantum mechanisch exacte, 'close coupling'-formalisme gehanteerd moet worden teneinde een nauwkeurige beschrijving van het botsingsproces te verkrijgen

In Hoofdstuk 7 wordt het OH-verstrooiingsexperiment beschreven De OH-radicalen worden geproduceerd in een electrische ontlading tijdens de expansie van een H_2O in Ar bevattende moleculaire puls in vacuum Rotationele koeling en electrostatische toestandsselectie hebben tot gevolg dat de $\frac{3}{2}^+$ rotatietoestand in de $^2\Pi_{3/2}$ electronische grondtoestand wordt geselecteerd voordat de botsingsexcitatie plaatsvindt Toestandsopgeloste botsingsdoorsneden worden bepaald voor rotationele excitatie van het OH-molecule ten gevolge van verstrooiing aan He, Ar en H_2 Spinbaan multiplet-behoudende als ook multiplet-veranderende overgangen worden waargenomen in het botsingsproces De botsingsdoorsneden voor OH – He, Ar verstrooiing vertonen een zwak oscillerend $\Delta J = 2$ gedrag voor spin-baan multiplet-behoudende, pariteitsveranderende rotationele excitaties De experimentele botsingsdoorsneden worden vergeleken met data van overige experimenten en quantum-verstrooiingsberekeningen en vertonen een goede overeenstemming

In Hoofdstuk 8 beschrijven we een spectroscopische studie aan het OH-Ar van der Waalsmolecule Het OH-radicaal wordt geproduceerd door fotolyse van HNO_3 in een moleculaire bundel opstelling Ten gevolge van botsingen met Ar-atomen in de primaire bundel tijdens de expansie van de moleculaire puls ontstaat er complexvorming Het gebruik van een 'pulsed dye amplifier' laser-systeem stelt ons in staat middelhoge resolutie (150 MHz) LIF metingen te verrichten aan het complex De spectra kunnen vervolgens worden geanalyseerd door te veronderstellen dat het OH-radicaal en het Ar-atoom in de gebonden van der Waals-toestand op een lijn liggen Deze analyse levert nauwkeurige waarden voor de rotatieconstanten en centrifugale distorsieconstanten met betrekking tot de grondtoestand en de eerste electronisch aangeslagen toestand van het complex

Curriculum Vitae

Johannes Joseph Hubertina Barbara Schleipen

Op 8 april 1964 ben ik geboren te Born (L) Gedurende de periode 1976–1982 bezocht ik het Bisschoppelijk College 'St Jozef' te Sittard alwaar ik in 1982 het VWO diploma – Gymnasium β behaalde Vervolgens startte ik mijn studie Natuurkunde aan de Katholieke Universiteit te Nijmegen, met als specialisatierichting Experimentele Natuurkunde Mijn studie werd afgesloten met de afstudeerstage 'Productie van en spectroscopie aan het OD radicaal' aan de afdeling 'Molecule- en Laserfysica' onder begeleiding van Prof J Reuss Op 10 december 1987 mocht ik het doctoraal diploma Natuurkunde in ontvangst nemen Aansluitend begon ik met mijn promotie-onderzoek aan dezelfde afdeling onder directe begeleiding van Dr J J ter Meulen Het resultaat van dit onderzoek is in dit proefschrift vastgelegd Tijdens mijn studie- en promotietijd heb ik studenten Natuurkunde en Scheikunde geassisteerd bij het Practicum Natuurkunde In het kader van een samenwerkingsverband met het 'Max Planck Institut fur Stromungsforschung' te Gottingen (Dld), ben ik van januari 1987 tot maart 1987 gast-medewerker geweest aan de afdeling van Prof P Andresen Per 1 september 1992 ben ik als wetenschappelijk medewerker verbonden aan het Philips Natuurkundig Laboratorium te Eindhoven

Publications

Part of the contents of this thesis is based on the following publications

Chapter 3 :
State-to-state cross sections for rotational excitation of ortho- and para- NH_3 by He and H_2
J Schleipen and J J ter Meulen,

Chapter 4 :
State-to-state cross sections for rotational excitation of NH_3 colliding with ortho- and para- H_2
J Schleipen, J J ter Meulen and A Offer,
to be published

Chapter 5 :
State-to-state cross sections for rotational excitation of ortho- and para- NH_3 by Ar at different collision energies, theory vs experiment,
J Schleipen, J J ter Meulen, G C M van der Sanden, P E S Wormer and A van der Avoird,
Chem Phys 163 (1992) 161

Chapter 6 :
Close coupling calculations on rotational excitation and inversion of NH_3 by collisions with Ar,
G C M van der Sanden, P E S Wormer, A van der Avoird, J Schleipen and J J ter Meulen,
accepted for publication in J Chem Phys , expected issue september 1992

Chapter 7 :
State-to-state cross sections for rotational excitation of OH $(X^2\Pi)$ by H_2, He and Ar,
J Schleipen, A Eppink and J J ter Meulen,
to be published

Chapter 8 :
High resolution electronic spectroscopy on the OH-Ar van der Waals complex,
J Schleipen, L Nemes, J Heinze and J J ter Meulen,
Chem Phys Lett 175 (1990) 561

Further publications
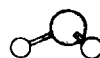
- *State-to-state collisional excitation of NH_3 by He and H_2 studied in a laser crossed molecular beam experiment* ;
  Th. Seelemann and P. Andresen, MPI Göttingen, W-Germany,
  J. Schleipen, B. Beyer and J.J. ter Meulen, KUN Nijmegen, The Netherlands;
  Chem. Phys. 126 (1988) 27.

- *Rotationally inelastic scattering of NH_3 with H_2: molecular beam experiment and quantum calculations* ;
  G. Ebel, R. Krohne, H. Meyer, U. Buck, R. Schinke, Th. Seelemann and P. Andresen, MPI Göttingen, W-Germany,
  J. Schleipen and J.J. ter Meulen, KUN Nijmegen, The Netherlands,
  G.H.F. Diercksen, MPI Garching, W-Germany;
  J. Chem. Phys. 93 (1990) 6419.

- *New vibronic states of NH_2 observed in ammonia photolysis* ;
  J. Schleipen and J.J. ter Meulen, KUN Nijmegen, The Netherlands,
  L. Nemes, Hungarian Academy of Sciences, Budapest, Hungary,
  M. Vervloet, Université de Paris-Sud, Orsay Cedex, France;
  Accepted for publication in Chem. Phys. Letters.

Chapters 5 and 6 of this thesis will also be part of the Ph D. thesis of G C M van der Sanden, KUN, Nijmegen.